University of Huddersfield Repository

Anyakwo, Arthur

Condition monitoring of curve squeal based on analysis of acoustic and vibration data

Original Citation

Anyakwo, Arthur (2020) Condition monitoring of curve squeal based on analysis of acoustic and vibration data. Doctoral thesis, University of Huddersfield.

This version is available at http://eprints.hud.ac.uk/id/eprint/35286/

Condition monitoring of curve squeal based on analysis of acoustic and vibration data

BY

ARTHUR ANYAKWO

A thesis submitted to the University of Huddersfield in partial fulfilment of the requirements for the degree of Doctor of Philosophy

March 2020

TABLE OF CONTENTS

List of Figures

List of Tables

List of Notations

Symbol	Unit	Definition
a	mm	Semi-axis of the contact area (longitudinal direction)
a'	mm	Approximate semi-axis of the contact area (longitudinal direction)
b	mm	Semi-axis of the contact area (lateral direction)
b'	mm	Approximate semi-axis of the contact area (lateral direction)
C_{ij}	-	Kalker' creep coefficients
c_w	N.s/m	Modal damping constant
D	1/m	Combined principal radius of curvature
E'	Pa	Combined elasticity modulus
E	Pa	Elasticity modulus
$E(m)$	m	Elliptical integral of the first kind of modulus
F_N	N	Normal contact force
F_L	N	Lateral force
F_V	N	Vertical force
f	Hz	Frequency
G	1/Pa	Modulus of rigidity
H	1/m	Combined radii of curvature
$K(m)$	m	Elliptical integral of the second kind of modulus
k_w	N/m	Modal stiffness
m	-	Modulus
m_w	kg	Modal mass of wheel roller
n	-	Number of nodal diameters
P_m	MPa	Maximum contact pressure
P	MPa	Normal contact pressure
R_{x1}	m	Wheel rolling radius (longitudinal direction)
R_{y1}	m	Wheel rolling radius (lateral direction)
R_{x2}	m	Rail rolling radius (longitudinal direction)
R_{y2}	M	Rail rolling radius (lateral direction)
u		Reduced radius of curvature ratio

v_x	-	Lateral creepage
v_y	-	Longitudinal creepage
v_{spin}	-	Spin creepage
ψ		Angle of attack
γ		Ratio of contact ellipse
μ	-	Adhesion coefficient
ξ	-	Damping ratio
x	m	Longitudinal/rolling direction
y	m	Lateral/transverse direction
z	m	Vertical direction

Abstract

The railway industry is currently investing in condition monitoring techniques to be able to compete with other transportation mediums. One of the reasons for this investment is to be able to identify the incipient development of curve squeal in railway systems. The annoying high-pitched tonal noise produced because of curve squeal has necessitated the need for mitigation measures to be taken by railway operators. However, noise from the surroundings and other trains has affected the conventional use of microphones for monitoring curve squeal in tight curves. It is imperative that the railway industry introduce additional sensors to help in the characterization and identification of curve squeal in railway track as the train negotiates the curve.

The objective of this research is focused on the evaluation of condition monitoring performances using vibrations obtained from the wheel/rail roller and sound obtained remotely close to the wheel-rail interface to identify and characterize curve squeal. By the completion of the comparative studies, this research has resulted in a number of new findings that illustrate the significant contributions to knowledge. This research presents the application of correlation method to establish a reliable relationship between acoustic and sound for the detection and characterization of curve squeal on the twin disc rig. The sensors used to detect and characterize curve squeal are microphone and two accelerometers installed laterally on the wheel and rail roller rims. The contact conditions taken into consideration are dry contact, wet contact and friction modifier contacts. A MATLAB model was developed to detect and characterize curve squeal. The results of the simulated model showed some disparities between the simulated transition yaw angles and measured transition yaw angles for which curve squeal occurs. Time and frequency domain were employed to extract the features from the sensors. Correlation method was employed to classify the features extracted from the microphone and accelerometer data. The results obtained showed that a negligible or weak correlation coefficient value indicates the development of curve squeal on the twin disc rig in dry contact conditions. A moderate or strong correlation coefficient values   is an indication of no curve squeal occur or curve squeal mitigation when contaminants (water and friction modifiers are introduced to the wheel-rail interface). The performance of the Correlation method for determining and classifying fault feature (curve squeal) extracted from the microphone and wheel/rail accelerometers has presented some useful qualities that makes it suitable in a real condition monitoring application system.

Acknowledgement

Declaration

No portion of the work presented in this thesis has been submitted in support of an application for another degree or qualification of this or any other university or other institute of learning.

Chapter 1 – Introduction

This chapter presents an overview of curve squeal monitoring and methods that used to mitigate this phenomenon. Condition monitoring of the wheel-rail contact is important in other to understand, model, measure and mitigate curve squeal. Most condition monitoring systems developed to monitor curve squeal have been applied in the railway industry today. These systems focus on measuring and characterising sound, vibration and wheel-rail contact forces emanating from the wheel-rail contact especially as the railway vehicle negotiates the curve. Some of the advantages and disadvantages of the condition monitoring systems developed are presented and discussed in this chapter. The research conducted in this thesis presents an opportunity to address some of the difficulties encountered in actually measuring and mitigating curve squeal. In addition, the placement accelerometers on the wheel web rather than the rail track as is used in the industry is discussed. The aims and objectives of the thesis is presented and arranged to study the research problem. The thesis layout is also presented.

1.1   Background on noise generation in the railway industry

In recent times, railway is regarded as one of the most convenient methods for transporting goods and people. Due to their low carbon dioxide (CO_2) emission levels, railways are considered as an ecologically welcoming means of transportation compared with other forms of transportation in the world today. According to the latest EU-28 report conducted in 2017, railways account for 0.5% of greenhouse gas (GHG) emissions from transportation mode alone in 28 European Union member states making it the one of the greenest form of transportation (European Environment Agency, 2017).
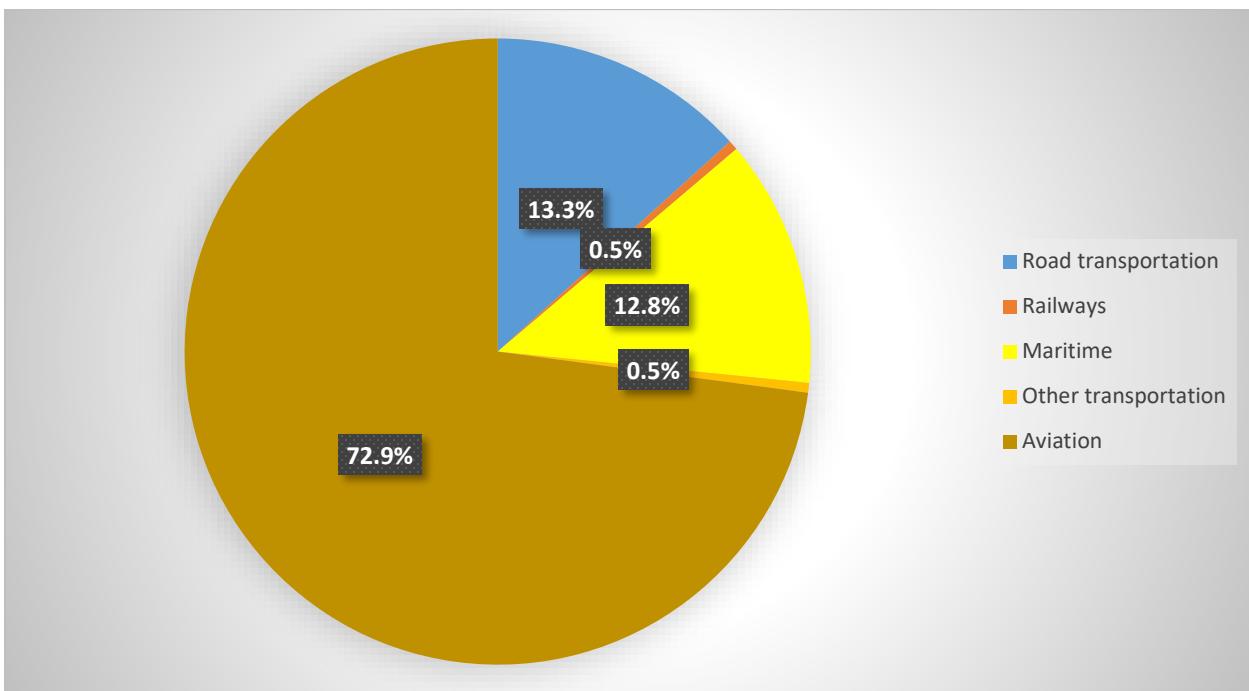
Figure 1.1: Breakdown of greenhouse gas (GHG) emissions transportation in Europe (European Environment Agency, 2017).

Despite the low GHG emissions associated with railways when compared with other means of transportation, noise is regarded as an important phenomenon to study and mitigate in present railway systems environment. With the growing development of railways systems (metro systems and trams) in areas of high population density, it is imperative that the underlying theory and mechanisms of railway noise is studied and investigated. Railway noise could be regarded as environmental pollution due to its impact on public health (WHO, 2011). Several researches have given understanding to the theories that lead to railway noise and ways to mitigate it. However,

the cost and maintenance of railway operations further increase with addition of noise mitigation measures. Higher costs are incurred because there are different sources of noise. However, wheel-rail contact forces are known to lead to different types of noise such as rolling noise, flanging noise, curve squeal, and ground borne noise. Other sources of noise in railways include, power unit noise and aerodynamic noise. It is imperative to note there is no universal standard for mitigating any these noise hence each type of noise must be studied individually (Thompson, 2009).

Rolling noise is the most prevalent type of railway noise in the industry. It is caused by excitation of wheel-rail contact forces due to wheel-rail roughness. As roughness develops on the wheel and rail, vertical force oscillations develop which then sets the wheel and rail into vibration. The vibrations of the wheel and rail lead to radiation of sound. This kind of noise illustrated in Figure 1.2 can be mitigated by applying wheel dampers, re-profiling the wheel and rail grinding. However no matter how much mitigation measures that are applied, rolling contact noise is always predominant in railway vehicles as long as it is moving on the track (Thompson, 2009).
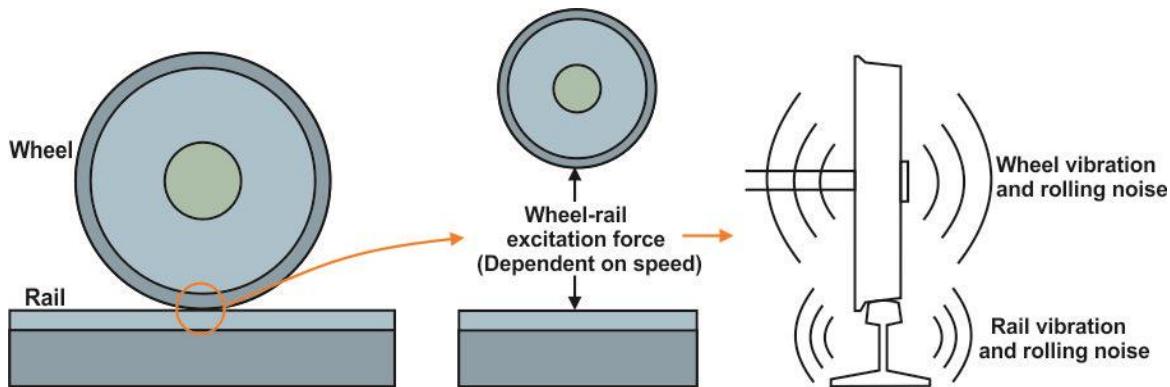
Figure 1.2: Rolling noise produced from rail and wheel roughness

Another important type of railway noise that is the concern of this thesis is curve squeal. Curve squeal, is a high-pitched tonal screech noise that originates in curve sections of the track. Unlike the wheel-rail rolling noise, curve squeal is caused by tangential wheel-rail contact forces developed on the wheel-rail contact point. These forces excite the bending oscillations of the wheels which is responsible for large wheel amplitude vibrations that are radiated into the environment as high pitched sound (Railway noise Technical Measures Catalogue, 2013).

Mitigation measures for curve squeal is increasing becoming an important point of discussion for railway vehicles, railway operators, administrators, and traffic operators. However, the necessary tools to validate new railway designs and tracks by manufacturers is necessary to understand the prediction of sound (Thompson, 2009). One of the most widely used commercial tools available in the railway industry today is Track-Wheel Interaction Noise Software (TWINS) software (Thompson et al., 1999). This software is based on the frequency-domain approach; hence, it is limited in processing time information for wheel and rail cases that do not have discrete irregularities.

Despite the plethora of commercial models developed to model curve squeal, the results obtained from these models do not usually coincide with experimental results due to several uncertainties and non-linearities. It is therefore necessary to develop a robust condition monitoring system targeted towards understanding curve squeal phenomenon and methods of mitigating this phenomenon. This would enable policy makers in the railway industry to set limits on curve squeal levels and enable better curve squeal simulation tools to be developed.

1.2   Introduction to curve squeal phenomenon

Curve squeal is one of the most annoying form of rolling noise that occurs in a typical railway system. It is defined as the high-pitched tonal noise observed when the train negotiates a tight curve. The term 'tight curve' is defined in accordance to the curve radius-wheelbase (R-W) of the railway vehicle. The R-W bogie ratio is a good indicator to detect curve squeal. Although the recommended R-W ratio for curve squeal occurrence is R-W < 200, it has been observed that curve squeal occurs for ratios of R-W greater than 200 (Remington, 1987) (Rudd, 1976) although sparingly. Table 1.1 show the occurrence of curve squeal for various radius track sections as defined (Thompson, 2009):

Table 1.1: Guide for occurrence of curve squeal in railways

$R \geq 500$ m	No curve squeal
200 m $< R <$ 500 m	Intermittent occurrence
$R \leq 200$ m	Common occurrence

Despite the fact that the mechanism and theory or curve squeal has been studied for several years now, its underlying cause is still yet to be fully understood. Some research carried out concluded the self-excited vibration of the wheel modes in its dominant mode produces curve squeal. From literature, it has been observed that there are two major causes of curve squeal, mode coupling and negative slope friction. It is established that the leading wheelset on a train when negotiating a sharp curve has a very large yaw angle relative to its forward motion. When this occurs, curve squeal is observed due to the developed lateral sliding velocity at the wheel-rail contact (Thompson, 2009).

The radiated sound because of curve squeal is dominated by a single frequency usually ranging from 250 Hz – 10 kHz. With very high sound pressure levels of up to 130 dB, curve squeal is regarded as one of the loudest types of railway noise. Also, with the large number of sharp curves in urban areas, a considerable proportion of the population are exposed to squeal noise. This could be detrimental to public health in the society (Thompson, 2009), (Glocker et al., 2009), (Koch et al., 2006). In addition, the tonal nature of curve squeal leads to excitation of the modal frequencies of the axial wheel modes and higher harmonics of the corresponding wheel modes.

These scenarios define the non-linear nature of curve squeal (Koch et al., 2006). The wheel radiates the highest amount of sound since it has a higher vibration response than the rail. Several factors lead to or cause curve squeal and they are regarded as energy input to the system (Thompson and Jones, 2002), (Thompson, 2009). These factors include lateral creepage, differential longitudinal slip and flange rubbing (Rudd, 1976). However, in several field observations and laboratory measurements, it was discovered that flange rubbing and differential longitudinal slip are not responsible for curve squeal. According to (Liu and Meehan, 2013), the wheel can actually squeal due to the presence of lateral creepage. This singles out lateral creepage as the main cause of curve squeal and the main energy input source.

The normalized relative velocity between the wheel and the rail divided with the rolling velocity is defined as creepage. The three creepages developed in the wheel-rail contact include the longitudinal creepage (v_{long}), lateral creepage (v_{lat}) and spin creepage (v_{spin}). They can be defined as:

$$v_{long} = \frac{v_x^W - v_x^R}{v} \tag{1.1}$$

$$v_{lat} = \frac{v_y^W - v_y^R}{v} \qquad (1.2)$$

$$v_{spin} = \frac{\omega_z^W - \omega_z^R}{v} \qquad (1.3)$$

where the superscript index W represents the wheel and superscript R represents the rail. Spin creepage arises because of the wheel-rail contact angle (wheel conicity) and the yaw velocity of the railway vehicle during negotiation of the curve. Longitudinal creepage occurs as a result of the acceleration, braking and longitudinal differential slip during negotiation of wheelsets on the curve. The lateral creepage is generated because of angle of attack (yaw angle) formed by the wheelset on a curved track in the rolling direction. The longitudinal and lateral creepage are responsible for the building up of the tangential wheel-rail contact forces necessary for curving, braking and acceleration (Kalker, 1990).

In railway curves, it is observed that the leading wheelset tends to run into the flange contact on the outer wheel. This hypothesis was previously propounded as the major cause of curve squeal due to the rubbing of the outer wheel flange on the outer rail gauge corner. However, laboratory tests carried out on a roller rig observed that curve squeal reduces by 10 dB at flange contact. This effect was noticed as wheel in a laboratory test on the twin disc rig. Hence it was concluded that the outer wheel does not lead to curve squeal as a result of lateral flange contact while the inner wheel is regarded as the largest radiator of curve squeal (Liu and Meehan, 2013). This was also confirmed by (Kim et al., 2019) through field experiments on curved sections of the track that squeal noise is generated from the inner wheel tread/rail head contact and flange noise is produced from the outer wheel flange/rail gauge corner contact as illustrated in Figure 1.3.
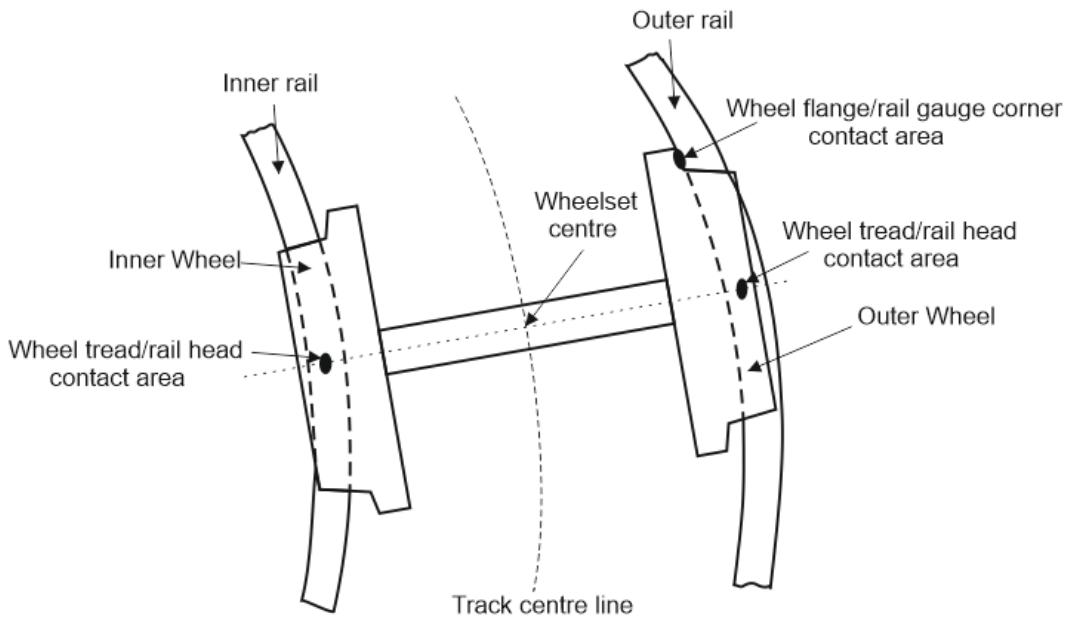
Figure 1.3: Contact locations of a typical wheelset on a curved track

Hence it is agreed in literature that lateral creepage is the main cause of curve squeal at the wheel-rail contact (Thompson, 2009), (Liu and Meehan, 2013). When the bogie negotiates the curve track, misalignment is observed between the wheel and rolling velocity. This leads to the development of angle of attack (yaw angle). As a result of the angle of attack (yaw angle) developed between the tangential direction of the rail and the rolling velocity, the inner wheel experiences a significant lateral creepage leading to the development of lateral force developed on the inner rim of the wheel. The oscillating lateral force developed causes the wheel to vibrate in resonance. This results in radiation of large sound of which the consequence is curve squeal.

Despite the fact that lateral creepage is the main cause of curve squeal, other mechanisms that influence curve squeal generation include local kinematic parameters of the wheel-rail contact, wheel modal parameters and wheel-rail contact friction (Liu and Meehan, 2013). They would be discussed in the next section.

1.2.1 Other causes of curve squeal

For curve squeal to occur, some other mechanisms interplay together. The most common mechanisms of curve squeal include wheel modes geometric coupling and creepage dependent on friction curve.

7

Geometric coupling is regarded as one of the mechanism responsible for development and persistence of curve squeal. It occurs between the degrees of freedom of the system thus leading to stick-slip oscillation in the system. In geometric coupling, two stiffness are at least required to model the couple of for example a single degree of freedom system. These stiffness are used to describe the coupling of the vertical and lateral displacements and the development of the corresponding forces (Jiang et al., 2015). The coupling ability of the system is affected by instability and the friction coefficient especially if it is above the required set point value. This mechanism was investigated and simulated by (Pieringer, 2014), (Glocker et al., 2009) and (Brunel et al., 2006). For railway wheels, several geometric couplings could be present for a single mode, which could arise because of close proximity of modal frequencies, and more wheel modes. The number of wheel modes depends on the properties of the wheel, friction and contact position of the wheel on the rail. According to the investigation carried out by (Glocker et al., 2009) three modes were discovered to be present with similar modal frequencies for curve squeal to occur or be present. (Pieringer, 2014) found out that the geometric coupling leads to asymmetry in the stiffness matrix of the system.

Creepage dependent on friction curve has been investigated in literature as a major mechanism responsible for curve squeal. The phenomenon was discovered by (Rudd, 1976). In his paper, he proposed that the falling friction curve is the main cause of curve squeal. He described this phenomenon as negative damping that leads to self-induced stick-slip oscillations in the wheel rail contact thus resulting in curve squeal. This implies that the falling friction slope is a function of the slip velocity and the friction coefficient. Also measurement results taken in (Remington, 1987), (Thompson, 2009) shows a decrease in the friction coefficient with increasing creepage. When the tangential forces reach the static friction limit $\mu_m F_z$, where F_z is the vertical contact force and μ_m is the maximum friction coefficient. As observed in Figure 1.3, as the slip (s) increases, the friction coefficient (μ) decreases. This process continues until a restoration force of the wheel decreases below the value of the frictional force. When this occurs, stick is re-established in the wheel-rail contact and the friction force increases until it reaches the static friction limit.
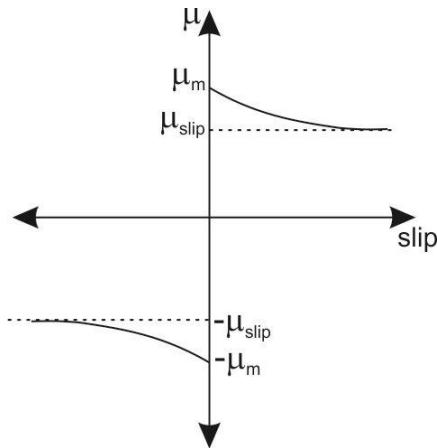
Figure 1.3: Illustration of friction law dependent on slip velocity for increasing slip velocity for decreasing friction coefficient

1.2.2 Measures for mitigating Curve squeal

Several measures for mitigating curve squeal have been applied in railways. They include the use of lubricants, design of asymmetric rail profiles, narrowing rail gauge, special bogie design and wheel damping.

Lubricants are one of the most widely used measures for mitigation of curve squeal. They are used to either lower the friction coefficient or change the shape of the friction curve (Railway noise Technical Measures Catalogue, 2013). Care is usually taken when using lubricants to avoid making the friction coefficient too low, which could affect traction and braking performance of the railway vehicle. In the railway industry, friction modifiers are used to control the shape the adhesion curve. They are usually applied either on the wheel and rail surfaces to mitigate curve squeal, minimize wheel flanging noise, reduce wheel-rail wear and minimize rail corrugation in curves (Railway noise Technical Measures Catalogue, 2013), (Arias-Cuevas et al., 2010), (Curley et al., 2015).

According to (Kim et al., 2019) as the wheelset passes the curved track, lateral creep force is generated. The relationship between the friction coefficient and the lateral creep ratio based on the contact between the railway track and the train is illustrated in Figure 1.4. The characteristics of the wheel and the rail based on the material and geometry results is observed. The friction coefficient increases with increase lateral creep. In dry contact conditions, when the friction coefficient reaches its maximum value, it decreases as the creepage increases.
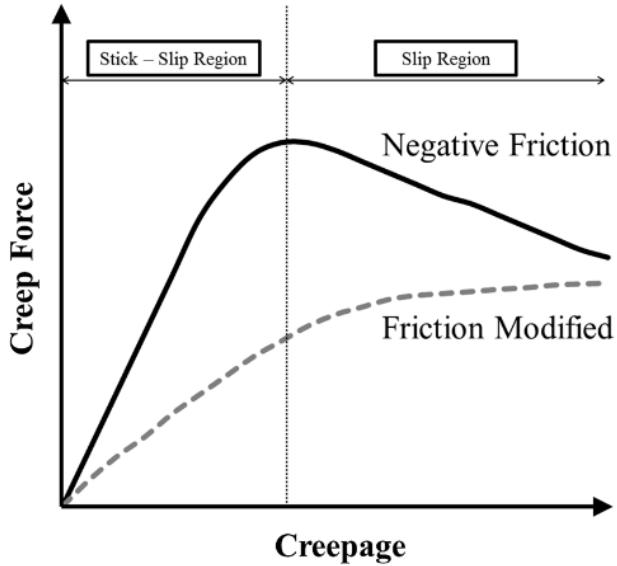
Figure 1.4: Creep force-creepage characteristic curve (Kim et al., 2019)

Special bogie designs are used for also for improving the curving behaviour of railway vehicles, thus reducing lateral creepage and mitigating curve squeal. Several designs such as independent wheel axles, steerable axles, active steering and tilt control have been applied (Thompson, 2009), (Railway noise Technical Measures Catalogue, 2013).

Wheel damping (see Figure 1.7) have been used previously to reduce rolling noise of the wheel and mitigate curve squeal. It involves applying materials (aluminium plates, cast iron plates) on the wheel web to minimize geometric coupling of the wheel modes, minimize wheel vibrations amplitudes. (Thompson, 2009) proposed that wheel damping could mitigate curve squeal. However, several control field tests carried out observed that wheel damping did not eliminate squeal. (Squicciarini et al., 2015) and (Cigada et al., 2008) concluded that the use of resilient wheels (damped wheels) did not minimize curve squeal as a result of the vibro-acoustic nature of damped wheels. In the study, it was discovered that the wheel mode amplitudes where not damped enough to mitigate curve squeal. This study showed that the correct determination of the wheel damping value is necessary since small values lead to high variations of the radiated sound for small variation and large values of wheel damping do not affect the radiated sound from the wheel. (Thompson, 2009).

Tuned dampers installed on
the wheel web

Constrained layer damping
installed on both sides of the
wheel web
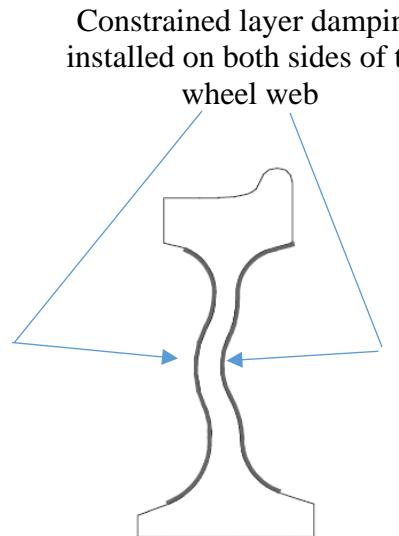
(a) **(b)**

**Figure 1.7: Different types of wheel damping treatments for curve squeal (a) Wheel
tuned damper (b) Wheelset section fitted with constrained layer damping (Thompson,
2009)**

1.3 Introduction to condition monitoring for railway vehicles

Condition monitoring in used to investigate the performance of a system while it is functioning. It also entails the periodic or continuous valuation of a machinery component or vibratory system while it is in operation. Condition monitoring allows scheduled maintenance or other steps to be carried out to prevent results of failure in a system. It is therefore, more cost effective than to allow the system to fail in operation. Some of the main aims of condition monitoring are for fault diagnosis, fault prediction, ensure safety at work place, improve production by reducing downtime, and encourage improved management of spare parts required for systems.

Noise and vibration signal obtained from a vibratory system usually contain crucial information about the running condition of the system. While noise is measured by proximity to the external surface of the material at a distance, vibration is measured on the surface of the vibratory system. The advantage of noise measurements over vibration is that acoustic signals can be measured at sufficient distances far from the vibratory system using microphones while vibratory sensors would need to be mounted on the surface for vibration measurement. It is therefore beneficial in some situations to measure the sound emanating from the system without having contact with the system and then correlate it with the health of the system, which would not have been possible using vibration sensors. However, the disadvantage of using acoustic sensors for measurement is

11

that they pick up spurious noise very easily from the environment. Therefore, special care must be taken to ensure that only the acoustic sound from the vibratory system is measured and analysed and any unwanted noise identified and removed using signal processing methods.

Condition monitoring is defined as the process of monitoring certain parameters in a system so as to identify drastic change that is indicative of developing fault. Condition monitoring allows scheduled maintenance, and other actions to be taken to avert damages to a system. In a typical condition monitoring system, sensors are used to acquire data about the parameters of the system. There are several types of sensors which include strain gauges, microphones, accelerometers, ultrasonic transducers and so on. Measured data from these sensors are processed to aid in better comprehension of the system conditions. Signal processing techniques differ depending on the data acquired from the sensors. The next phase of a condition monitoring system is to provide strategy for maintenance depending on the signal processing results obtained (Ngigi et al., 2011). In the railway industry, the strategy for maintenance depends on the type of condition monitoring system. The condition monitoring systems differ depending on the sensor types utilized. Sensors could either be installed inside the railway vehicle or on the wayside. (Ngigi et al., 2011) highlighted the key signal processing techniques that are used in railway industry. A summary of the techniques mentioned include visual inspection, acoustic emission, noise and vibration and ultrasonic methods.

Visual inspection of the wheels and rails was usually carried out by trained industrial. This method relied on the expertise of the personnel to characterize and identify anomalies in the wheel and rail. Noise and vibration spectra are widely used in railway industry to identify faults in the wheelset, curve squeal, wheel flats, out of roundness of the wheel and cracks in the wheel rim. The vibration sensors are usually installed on the rail track while noise is monitored using microphones installed at strategic locations close to the track. This method provides better advantages compared to the visual inspection method. Acoustic emission is utilized in the industry to monitor faults in the axle box and wheel bearing. Measurements conducted on the wheelset without faults is used as a baseline to compare with faulty wheelset. Ultrasonic methods are widely used in the railway industry to identify cracked wheelset axles and to characterize the size and shape of the wheel-rail contact patch area. They have also been applied to monitor railway track faults (Ngigi et al., 2011).

1.3.1   Introduction to condition monitoring of curve squeal

Curve squeal is one of the most disturbing and loudest noise in railways. It is usually a strong tonal high frequency noise dominated by a single frequency that occurs in curved sections of the track. It is a consequence of intense vibrations of the wheel and the rail structure interaction resulting in radiation of sound. Condition monitoring of curve squeal in the railway industry involves the use of sensors installed at certain locations on the trackside. Microphones and accelerometers are the most widely used sensors used to monitor curve squeal. Microphones are installed at defined locations on the curved trackside to measure curve squeal as the railway vehicle negotiate the track. Accelerometers in some cases are installed on the rail to monitor its lateral vibrations and thereby identify curve squeal.

However, due to the random nature of curve squeal, it is difficult to predict which wheel will squeal in any given train pass on the curved track as a result of interaction of several variables. To tackle this problem, accelerometers are installed underside each rail. By comparing the levels of vibration for each wheel, the difference in 10dB proved to be a reliable indicator to determine which rail curve squeal occurs in the curved track. In addition, optical sensors installed on the wheel and matched with noise measurements from the microphone proved useful in the identification of which wheel is squealing in the railway vehicle. According to (Squicciarini et al., 2015), if curve squeal is not monitored and mitigated, it can result to wear in the wheel rail interface as well as noise pollution. Poor wheel and rail profiles produced as a result of excessive curve wheel can result in high stresses that can cause other kinds of defects to occur such as rail corrugation and wheel flats. The consequence of these problems is increase in emissions and fuel consumption of the railway vehicle.

1.4   Aim and scope of research work

The aims of this research work are to develop a reliable relationship between vibration and sound measurements in characterizing and identifying curve squeal using Correlation method. The developed method would mainly address curve squeal developed on the wheel and identify how it can be mitigated. To ascertain the suitability of the Correlation method, employed in a condition monitoring system, its performance would be investigated using a scaled Twin disc rig operated at varying contact conditions. The contact conditions include dry, wet and friction modifier

contacts. The condition monitoring system would be investigated and simulated using four variable wheel speeds and one loading conditions.

1.5   Objectives of research work

To achieve the aims mentioned in the previous section, the following objectives are stated with emphasis on the main research aim:

(1)   Gain understanding of condition monitoring of curve squeal using vibration and acoustic based signal processing tools.

(2)   To further detail the disadvantages of traditional signal processing and methods for analysis of in time and frequency domains and identify which method is most suitable for analysing vibration and acoustic signals from the wheel rail interface.

(3)   Investigate acoustic and vibration generation and its characteristics in identification of curve squeal on the twin disc rig.

(4)   Develop a realistic experimental method in situ with adequate system to study acoustic and vibration signals for curve squeal characterization.

(5)   Investigate the condition monitoring performance of acoustic and vibration signals using time and frequency domain analysis.

(6)   identify suitable condition monitoring indicators in time and frequency domain that can be used to predict the incipient development of curve squeal.

(7)   Investigate the effect of water and friction modifiers using acoustic and vibration data for curve squeal mitigation.

(8)   Investigate the condition monitoring performance of using vibration and acoustic signals using Correlation method for curve squeal identification.

(9)   Propose a condition monitoring system based on the developed Correlation method for curve squeal identification.

1.6   Outline of thesis

This thesis is divided into seven main chapters:

Chapter 2 introduces the topic of curve squeal and problems associated with it. The required conditions necessary for curve squeal to occur and its general characterization is presented. The underlying mechanism associated with curve squeal are also discussed in detail.

Chapter 3 presents the experimental facilities for curve squeal monitoring. A complete description of parts of the test rig, including the data acquisition system, microphones for curve squeal measurement, accelerometers, and strain gauges are presented and discussed in detail in this chapter

Chapter 4 presents the development of an engineering curve squeal model for the test rig. Detailed study on Hertz contact theory, creep force modelling, contact area estimation, curve squeal vibration model and several other vital topics are discussed and investigated in this chapter.

Chapter 5 presents the vibration methods for monitoring curve squeal in the test rig. Time domain, frequency domain and time frequency domain methods are used to identify the onset development and mitigation of curve squeal on the test rig.

Chapter 6 presents acoustic methods for monitoring curve squeal on the test rig. Time domain, frequency domain and time frequency domain methods are used to study and characterize curve squeal under different contact conditions and four varying average wheel speeds.

Chapter 7 presents the development of the correlation method for characterizing and development of curve squeal in the twin disc rig.

Chapter 8 presents conclusions and future work.

Chapter 2 – Literature review

This chapter presents a detailed literature review on curve squeal. An introduction that covers the main methods that have been used to study curve squeal is first presented. After the introduction, the review on curve squeal is then broken down into two main parts; mathematical models that have been developed to study curve squeal and condition-monitoring methods for curve squeal. Each of these parts is reviewed in detail especially in line with the aims and objectives of this project report. The advantages and disadvantages of each part is addressed. The depth of research work that has been conducted in identifying curve squeal and ways to mitigate it are stated and a direction for the research work is therefore stated.

2.1   Introduction

Curve squeal is an important phenomenon in the railway industry. It is imperative that adequate research is carried out to understand the underlying mechanisms associated with curve squeal and how these can be mitigated especially in curve sections of the track. As has already been introduced in Chapter 1, curve squeal occurs in sections of the curved track most frequently where the radius is less than or equal to 200 m. It is well documented that as the radius increases from this value, the likelihood of curve squeal occurring is limited. However due to the complexity in understanding the various cause of curve squeal in the railway industry, several research works have focused on developing a robust condition monitoring system for identifying and characterizing curve squeal. Based on the measurements conducted on the railway track using various sensors, an engineering mathematical model for curve squeal is then developed by various research groups. The models developed help the railway industry in understanding the mechanisms associated with curve squeal and then scheduling a suitable maintenance strategy to mitigate its effect (Thompson, 2009).

In literature, it has been observed that curve squeal study is grouped into two main parts; mathematical models for curve squeal, and condition monitoring methods for curve squeal. Mathematical models developed for curve squeal in literature is classified into two main parts, time and frequency domain. It is unfortunate that most of the frequency domain methods developed in literature are derived from simplistic linear models of the wheel-rail contact system. Their simplicity is not sufficient to comprehend the underlying causes of curve squeal. It is well established that non-linearities are prevalent in most wheel-rail contact systems. The time domain method is therefore developed in Chapter 4 to be able to characterize and determine curve squeal amplitude as it varies with time in other to the determine its severity (Zenzerovic et al., 2015), (Thompson et al., 1999).

There is a plethora of different condition monitoring methods used to characterize curve squeal. However, the challenge is to ensure that the right measuring method is used for condition monitoring of the wheel-rail contact. The selection of the appropriate method is a requirement for determining the right signal processing technique that can be applied to study and identify curve squeal. Signal processing techniques are a crucial part of a condition monitoring system application. There are several signal-processing methods available for investigating curve squeal. The suitability of each method depends on the application and the result required.

One of the main methods for characterising curve squeal is the time domain method. Time-domain methods are easy to implement, and are better suited for characterizing curve squeal using several statistical parameters. Frequency domain methods have advantages over the time domain methods in its ability to study the frequency range necessary for curve squeal to occur. In addition to this merit, the curve squeal frequency and the wheel-excited modes can also be easily identified. Frequency domain methods however, do not have the ability to show the signal time resolution. While it is true that most signals are non-stationary in nature, signal-processing method that can identify curve squeal frequency at any particular time instant is of paramount importance. Time-frequency signal processing method is therefore used to show curve squeal characteristics in a two-dimensional plane. This is one of the main advantages of using this signal processing technique over the conventional time and frequency domain methods (Pieringer et al., 2018). All the aforementioned curve squeal methods have been at some stage applied in the railway industry to investigate and characterise curve squeal. The next section focuses on the mathematical models that have been used to study curve squeal.

2.2   Review on contact model domains

This section presents a comprehensive review on the domains used for curve squeal model. These include time and frequency domain models.
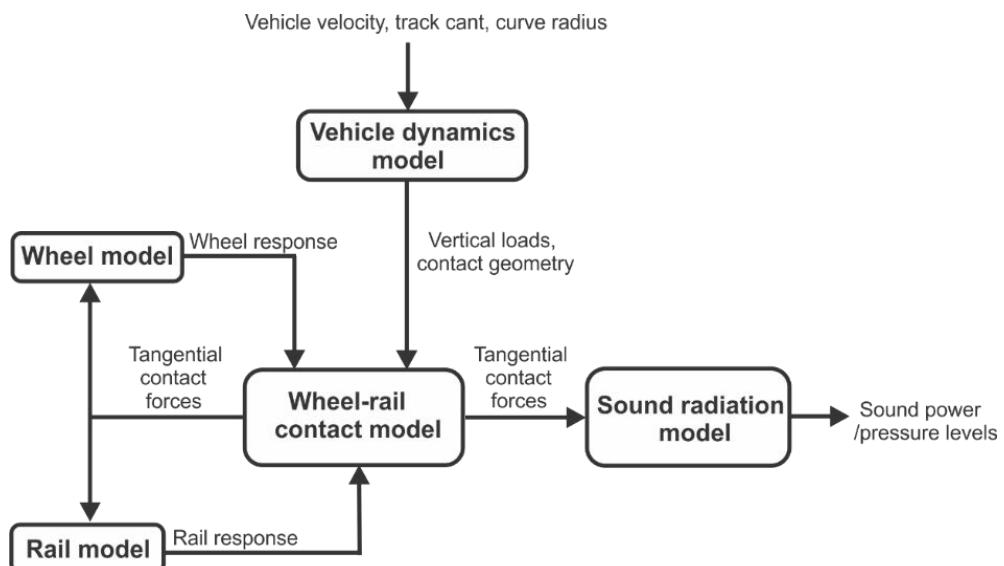
Figure 2.1: Conventional structure used for curve squeal model

The structure of the curve squeal model does not depend on whether the model is in the time or frequency domain. Most of the blocks in the structure contain two or more sub models but the most important model block is the wheel-rail contact model. This block contains the rolling contact sub-models and the wheel and rail dynamics. The wheel and rail models generate the wheel and rail vibration response for the curve squeal model. The sound radiation model is extended in most cases to simulate the sound power and pressure levels generated from the wheel-rail contact model. Going back to the two groups of curve squeal model, each of the models blocks in the general curve squeal model would be discussed and general conclusions are then given for some of the models described.

2.2.1 Time domain models for curve squeal

Time domain models add several characteristics to the wheel rail system such as non-linearities, ability to determine curve squeal amplitude and its severity. Higher harmonic components of the system response and squeal amplitudes can be easily determined. Amongst the first squeal models formulated in the time domain, (Schneider et al., 1988) model is the most widely used to simulate curve squeal. Non-linear differential equations that describe the system model was solved using Rung-Kutta routine. Finite Element (FE) model was used to obtain the modal parameters for the wheel, while the rail was considered as rigid. The wheel displacement response was determined using modal transformation methods. Kraft's falling friction model was used to describe the friction model assuming point contact between the wheel and rail. Finally, Rayleigh integral was used to determine the radiated sound from a typical baffled plate.

A more detailed wheel-rail model was developed by (Fingberg, 1990) which includes semi-transient rolling contact model and evaluation of the sound radiated model. The semi-transient model was implemented to take into consideration transient contact conditions that occur during curve squeal. Only half of the wheelset was modelled using FE while the rail was built using two models: one for the longitudinal dynamics and one for the lateral dynamics.

Wheel and rail response functions and were also determined as in the case of (Schneider et al., 1988) using modal expansion methods. This later technique combined with boundary element method was used to determine the radiated sound from the wheel. Each wheel mode contribution to the radiated sound was computed separately and then the added up obtain to cumulative sound radiation.

(Fingberg, 1990) model was extended by (Periard, 1998). The modal parameters of the rail was obtained using FE model and included with its differential equations (Vermeulen and Johnson, 1964) and (Kalker, 1982) with falling friction characteristics was used to extend the model. Simulations of the radiated sound and vehicle curving behaviour was calculated using Rayleigh integral. The contribution of each mode to the overall sound model was evaluated in the sound radiation model. The model developed by (Periard, 1998) is a combination of (Fingberg, 1990) approach and (Schneider et al., 1988) approach to the evaluation of radiated sound.

(Huang et al., 2008) also modelled and simulated sound radiation in the curve squeal model. His sound radiation model was based on the (Thompson and Jones, 2002) and (Fingberg, 1990). Considerations of the wheel and rail contact mobilities were taken and solved using (Kalker, 1982). Different falling friction models were used to simulate the influence of creepages on the lateral force. The model also used convolution instead of integration to determine the response of the system. Green functions were used to represent the circular disc with Green's functions (impulse response) obtained from the superposition of the disc modes. Only the lateral dynamics was considered and the rail was not included in the model. The tangential contact force and Green's function was convolved together to obtain the wheel response (Zenzerovic et al., 2015).

2.2.2 Frequency domain models for curve squeal

In curve squeal models, frequency domain models are one of the most widely used models since they can be either obtained by linearization of non-linear equations from time domain models or from simplified linear wheel-rail contact models. However, the accuracy of the developed models depends on the attention to modelling details. Several curving situations and parameters influence on curve squeal have been investigated in the past using frequency domain models. For instance, the stability of wheel modes that are prone to curve squeal was studied in (Koch et al., 2006) and (Heckl, 2000) while the influence of wheel damping on mitigation of curve squeal was investigated in (Rudd, 1976), (van Ruiten, 1988). Also frequency domain models to determine the stability of wheels in a bogie and its effects on bogie was developed in (Glocker et al., 2009), (Monk-Steel and Thompson, 2003) and (Xie et al., 2006). Models to investigate the effect of kinematic parameters such as curve radius (Rudd, 1976), lateral contact position (de Beer et al., 2003), and curve squeal developed in the presence of two wheel-rail contact points (Squicciarini et al., 2015).

Out of the mentioned frequency domain models, one of the first squeal noise model was developed by (Rudd, 1976). The wheel system was modelled as a single degree of freedom. (Rudd, 1976) determined the impedance of the system experimentally and considered the lateral dynamics of the system. The rail was assumed rigid; hence, the rail dynamics was not included in the model. The vertical forces and the lateral forces were assumed to be coupled by the law of friction. Rudd interpreted the falling friction function as negative damping. He concluded that curve squeal is caused by falling friction otherwise called negative damping.

Several frequency domain models emanated from (Rudd, 1976) model. For instance, (van Ruiten, 1988) used (Rudd, 1976) model to study the effect of wheel damping and rolling speed on curve squeal. He compared the simulation results obtained from the mathematical model with experimental results to investigate how curve squeal occurrence could be mitigated. The results he obtained compared well with (Rudd, 1976) model.

The second most widely used frequency domain model from where other models have been developed was (Fingberg, 1990) model. The wheel, rail and the contact was used as three sub-models. From the time domain developed and eventually the frequency domain model, de Beer et al developed a frequency domain based on the three sub-models. The contact spring mobility, the wheel and rail dynamics was included in the TWINS software. The wheel-rail contact problem was solved using (Kalker, 1990) linear theory. The measured falling friction function was used to define the model, developed using Kraft's friction law. The vertical and lateral dynamics was coupled together and used to develop the model. This was regarded as an important contribution to the development of the wheel-rail contact model. The wheel-rail contact position was taken into consideration since it influences the vertical and lateral coupling dynamics. He also came to the conclusion by (Rudd, 1976) that falling friction is responsible for the development of curve squeal. The conventional stability method; Nyquist Criterion was applied to develop the model.

(Xie et al., 2006), simulated the effect of curve squeal on vehicle curving behaviour. The falling friction model developed by Kraft and (Kalker, 1982) algorithm was used for the simulations while different curving scenarios was studied.

A simplified version of (de Beer et al., 2003) model was simulated by (Hsu et al., 2007). The model assumed that the normal force is constant. Test measurements were carried out and considerations were made based on (de Beer et al., 2003) model through a simplified version of it that was used. (Monk-Steel and Thompson, 2003) adopted the same method similar to (Hsu et al.,

2007). A finite element (FE) model of the wheel was used to obtain its modal parameters. The rail was described using two models one for the vertical dynamics and another for the lateral dynamics. The falling friction portion of the curve was modelled using (Vermeulen and Johnson, 1964) while (Kalker, 1990) was used to model the increasing portion of the friction curve. From the time domain models already discussed, (Heckl and Abrahams, 2000) developed a frequency domain model based on finding out the wheel modes prone to curve squeal. Integro-differential equations of the linear system was used to determine the complex Eigen-values of the system. Finally (Squicciarini et al., 2015) developed a frequency domain model similar to (Hsu et al., 2007) model to account for two point contact on the wheel. This was regarded as a major contribution as the effect of two-point contact on curve squeal was studied. Mobilities of the wheel and the wheel parameters was included and used to tune the measurements. Kraft's falling friction model and (Kalker, 1982) was used to model the friction curve of the system. The unstable frequencies of the wheel and the rail was determined using a parameter space.

2.3   Review on wheel-rail contact models

Wheel-rail contact forces (lateral, longitudinal and vertical forces), tangential traction, normal pressure and contact area size and shape can be determined using wheel-rail contact model. From vehicle dynamic simulations, curve squeal and evaluation of rolling contact noise, the knowledge of contact forces developed in the wheel-rail contact can be investigated. Also, of importance is the tangential tractions and normal pressure along with the displacements observed in the contact area. The variables of the wheel-rail contact depend on several parameters such as geometric and kinematic parameters that influence wheel-rail relative motion, wheel-rail material parameters, geometry of the wheel-rail surfaces and contact position. In addition, environmental variables play a vital role in influencing friction in wheel-rail contact models. All the parameters mentioned are used as input to the wheel-rail contact model.

Material behaviour and parameters are crucial for the determination of displacements in the wheel-rail contact area. Since the rail and wheel is made of from the same material (steel), they are regarded as linear elastic materials in wheel-rail contact models used for curve squeal modelling. In literature, therefore all the wheel-rail contact models used for force displacement relations assume linear elasticity. With emphasis on wheel rail geometry, non-conformal and conformal contacts are differentiated as shown in Figure 2.2. Non-conformal wheel-rail contact in wheel-rail

contact context occurs in the rail head/wheel tread contact (Figure 2.2(a)) while conformal contact occurs when the rail gauge corner and the wheel flange are in contact (Figure 2.2(b). When the contact area is in characteristic dimensions of the contact bodies, the contact is said to be conformal. The curvature radius of the rail and wheel and the flange contact at the point of contact can be compared with the contact size. X are of the opinion that the conformal contact solutions require the application of numerical methods. Paul and Hashemi used boundary-element approaches and finite element models to solve this kind of problem.

Compared to conformal contacts, non-conformal wheel-rail contacts are easy to model. The reason for this is that the stresses developed in the contact are concentrated close to the region of contact thereby not having any effect on the complete body stress distributions. In most literature, the contact stresses are determined by the assumptions that the bodies in contact are semi-infinite and bounded by a surface plane. This corresponds to the definition of elastic half-space. In addition, there are two types of contact, Hertzian contact and non-Hertzian contact. Hertzian contact are represented by second order polynomials in the contact area region to equate the deformation distance. Hertzian contact assumes that the surface does not have friction, is smooth, the material is linearly elastic and the half space approximation holds. Hertz contact results in ellipsoidal normal contact pressure distribution and elliptical contact area. Hertzian contacts are strictly non-conformal contacts. However, non-conformal contacts can be either non-Hertzian or Hertzian. Non-Hertzian contacts unlike Hertzian contacts do not result in the use of second order polynomials. This is because the curvature radius of the wheel and rail can significantly change on the wheel tread for small lateral displacements. For worn rail and wheel contacts, the curvature change is obvious. However, curvature radius discontinuities can result in multiple contact areas aside the non-elliptical contact patch formed. Another cause of non-Hertzian contact is surface roughness. In reality, however, most surfaces have some level of surface roughness resulting in contact occurring at distinct locations in the contact patch region. The asperities due to the contact surfaces result in contact pressures that are much larger than Hertzian maximum contact pressure. In this thesis, curve squeal models are limited to non-conformal contacts. This is motivated by the fact that curve squeal happens when the rail head and the wheel tread are in contact.

2.3.1 Curve squeal contact conditions

A review on the general process that occur in the wheel-rail contact area would be reviewed in this section. The discussion would be based on the processes that result in curve squeal. Creepages are developed in the contact to describe the overall relative motion between the rail and the wheel. Two conditions are required for relative motion to occur. They include the local deformations that happen in the rail and wheel-rail contact as a result of rail and wheel elasticity and the relative motion generated by particles in the wheel-rail contact. In the stick area, the rail and wheel particles don't relatively move with each other due to the fact that the limit of the tangential tractions defined by the normal pressure and the coefficient of friction has not been reached. The traction builds up from the leading edge of the contact area to the trailing edge. The longitudinal traction at some point approaches the traction limit. When this happens, the particles don't stick together anymore and relative motion occurs. This is regarded as the slip region of the contact area. The presence of creepage in the contact area results in the occurrence of slip in the contact area. Tangential forces arise as a result of the relative motion between the rail and the wheel. When longitudinal creepage is involved, the forces generated are called the braking or traction forces. According to (Zenzerovic et al., 2015), the particles in slip as a result of contacting particles is defined as:

$$s_\tau = \omega_\tau - v\frac{\partial u_\tau}{\partial x} + \frac{\partial u_\tau}{\partial t}, \qquad \tau = 1,2 \qquad (2.1)$$

Where ω_τ is the creepage to slip velocity contribution (rigid slip), v is the rolling velocity, s_τ is the local slip between the contacting particles, and u_τ is the difference in displacement between the rail and the wheel. The rigid slip depends on creepages developed at the contact patch:

$$\omega_1 = (\gamma_x - \gamma_\omega y)v, \qquad \omega_2 = (\gamma_y - \gamma_\omega x)v \qquad (2.2)$$

where γ_x is the longitudinal creepage, γ_y is the lateral creepage, and γ_ω is the spin creepage. The direction x and number 1 denotes the longitudinal direction when the y direction with number 2 denotes the lateral direction. Equation (2.1) is required to be solved to compute the stick and slip distributions in the contact area. This equation is used to illustrate transient rolling. The time depending in equation 2.1 ($\partial u_\tau/\partial t$) vanishes for steady state problems (KALKER, 1979).

Carter studied the effect of tractive steady state rolling on a cylinder. He was the first to find the solution for traction in rolling contact problems. This assumption may not hold for curve squeal models. This is because during curve squeal, the distributions of the slip and stick in the contact area vary with time, resulting in instability in the slip-stick process. For a proper understanding of

the slip-stick process, it is imperative to define global and local motion. According to Carter on the global level, the continuous variation of the slip and stick regions between the wheel and the rail occur at the contact. The regions are illustrated in Figure 2.4. Stick-slip oscillations happen with the oscillations of the periods with full contact slip in the contact area. On the stick phase, the deformations of the wheel increase. This deformation is limited by the tangential force in the contact region. This is defined as the product of the coefficient of friction and the normal load. At the deformation limit, the potential energy developed is transformed to kinetic energy. The wheel and rail inertia also affect the stick-slip process. In the lateral force time history, stick-slip contact regions can be observed as shown in Figure 2.4. The traction limit remains constant throughout the stick and slip phases.

(Knothe and Groß-Thebing, 2008) used the L/ax ratio of the characteristic motion wavelength L and the length of the contact region on the rolling direction to investigate contact conditions. Transient conditions was characterized with a ratio less than ten. Although the authors took into account rail corrugation in their study, the method applied can be used for curve squeal. This is because contact conditions are transient for curve squeal. The authors suggested the need for a transient model to be developed and applied to other wheel-rail contact problems.

2.3.2 Contact models used for curve squeal: A review

The contact models that have been commonly used for curve squeal are reviewed in this section. Tangential contact models for wheel-rail contact would be reviewed since they are important for curve squeal models. The main contact models used in literature include point contact, Kalker's variational theory, Kalker's simplified theory, Kalker's linear theory.

Point contact models are simplified models of the of the wheel-rail contact. They describe the contact process on a global scale. They assume point contacts for the normal and tangential contacts. One of the main advantages of using point contact model is their fast-computational speed, especially in solving tangential contact problem. They are derive using simple analytical equations to represent the creep force/creepage relationship. They are formulated in some cases in terms of the friction model. Point contact models employ Hertz contact theory to solve the normal contact problem. They are normally applied to rail head/wheel tread contact. Further details of the analytical expressions for Hertz contact theory would be discussed subsequently. Point contact models employ the relationship between the tangential and normal contact forces.

$$F_\tau = \mu(s)F_z, \qquad \tau = x, y \tag{2.3}$$

where F_z is the vertical force in the z direction, and F_τ is the longitudinal and lateral force in the x and y directions respectively. This equation is valid for one tangential direction that is when $\tau = x$ or $\tau = y$. The tangential contact model depends on whether the two directions are taken into consideration. If the longitudinal and lateral directions are considered, then the slip velocity (s), is determined as:

$$s = (s_1^2 + s_2^2)^{1/2} \tag{2.4}$$

If only a single tangential direction is taken into consideration, then the point contact model is simplified and easy to solve. The disadvantage of point contact models arise from the assumption of global contact. They also prevent further study on local contact process that occur in the contact area.

Kalker's linear theory includes information about local contact process apart from the conventional friction model. Kalker developed his theory from the linearization of Carter's theory. Carter's theory is based on the assumption of a cylinder on a rolling plane. The plane is assumed to be two-dimensional and non-linear. The force/creepage relationship is expressed as:

$$\frac{F_1}{\mu F_z} = \begin{cases} -c\gamma_x + 0.25k^2\gamma_x|\gamma_x| & if \ c|\gamma_x| \leq 2, \\ -sign(\gamma_x) & if \ c|\gamma_x| > 2 \end{cases} \tag{2.5}$$

given that $c = 4R/(\mu A)$ represents creepage coefficient, R is the radius of the cylinder, and a is the contact width half length. Equation 2.5 illustrates the transition from full stick to slip contact. Carter's theory is illustrated in Figure 2.5:

Kalker's linear theory provides the solution of the tangential contact problem for the stick region. Kalker's linear theory is expressed as follows:

$$F_x = abGC_{11}\gamma_x \tag{2.6}$$

$$F_y = abGC_{22}\gamma_y - (ab)^{3/2}GC_{23}\gamma_w \tag{2.7}$$

where a and b are the semi axes of the elliptical contact area, C_{11}, C_{22}, C_{23} rely on the elliptical contact ratio a/b. G is the shear modulus of the contacting materials.

Finberg extended Kalker's linear theory to solve semi-transient contact problem in curve squeal. This model depended on creepage coefficients dependent on frequency and developed by (Knothe and Groß-Thebing, 2008). (Vermeulen and Johnson, 1964) developed a non-linear approximation model that is valid for elliptical contact areas. This makes it suitable for the inclusion of Hertz contact theory. However, the assumption of the non-slip (stick) region as elliptical lead to errors

in the contact model. The disadvantage of using this model is that is does not taken into consideration spin creepage. To include the effects of spin.

(SHEN et al., 1983) extended the Johnson and Vermeulen model to include spin creepage in the tangential contact problem. However, this model according to the authors permits small spin creepages.

(Polach, 2005) developed a tangential contact model for the scenario of large creepages. He assumed that the slip region is fully encompassed leading to tangential force near the traction limit. The effects of spin creepage and contact shear stiffness was applied by Polach. This model is however strictly confined to steady state contact and elliptical contact conditions.

(Piotrowski and Chollet, 2005) addressed multiple contact patch scenarios. They developed the approximate multi-Hertzian method for the solution of normal contact problem. Finite element (FE) methods produce the most precise solution to the contact problem. However due to the large computational cost, they are seldomly used in solution of contact problems

Kalker's variation contact theory is dependent on the complementary energy principle. The theory comprised of two algorithms, NORM and TANG. NORM is used to solve the normal contact problem while TANG is used to solve the tangential contact problem. Kalker's variational contact theory uses the active set algorithm. The theory discretizes the potential contact region and then calculates the pressures and traction at each point in the discretized region. The contact area size, shape and normal contact problem is solved using the NORM algorithm. TANG algorithm solves the transient rolling contact for each element that is discretized in the contact. The division of the contact area into slip and stick areas is computed. Kalker's variational contact theory is application to non-Hertzian and Hertz contacts, steady state and transient process, cases of variation in creepages and normal force and contact bodies with different materials. The disadvantage of using Kalker's variational contact theory is the high computational cost required to solve the NORM and TANG algorithm. To reduce the computation cost and provide efficiency, Kalker introduced a simplified theory called the FASTSIM algorithm. However according to Kalker the FASTSIM algorithm does not provide accurate solution of the normal contact provide. He suggests that Hertz contact theory is most suited for normal contact problem (Kalker, 1990).

To improve the problems associated with the FASTSIM algorithm, (Spiryagin et al., 2013) developed a falling friction law for curve squeal models. (Xie et al., 2006) applied this model to compute creepages for curve squeal model.

2.3   Review on condition monitoring methods for curve squeal

In the previous section, a detailed literature review on curve was discussed. Most of these models was implemented based on trials and measurements conducted on the railway system. However, the difficulties encountered in obtaining measurements from the railway track, such as the cost of installation of condition monitoring systems and the uncertainty in predicting which wheel squeals in a curved track has necessitated the need for trials to be conducted in controlled laboratory conditions. Despite the challenges encountered in investigating the underlying cause of curve squeal, some measurements have been conducted experimentally with the permission of railway industry to identify and characterize curve squeal.

(Stefanelli et al., 2006) investigated the cause of curve squeal using a measurement setup constructed and placed in a 200 m curve radius section of the track where there is busy train traffic. The measurement system for curve squeal comprised of two microphones placed on either side of the railway track. Vibration was monitored using two accelerometers installed on the flange of the rail. The railway vehicle speed was measured using axle counters. The microphones and the accelerometers produced a signal that was converted to digital and stored on a hard drive for further signal processing. In other to different between break squeal and curve squeal, only departure trains was used for this experiment. The measurement results showed that curve squeal depended on the type of train and that the curve squeal frequencies ranged from 3 to 5 kHz. The accelerometers placed on the flange of the rail provided accurate information on the actual emanation of curve squeal. Using the Doppler Effect, the position of the wheel was determined before the curve squeal was measured. The results concluded that the wheel is the main source of squeal and it results from the vibration of the wheels. In addition, the trials conducted showed that the damping ration, direction of excitation, driving direction and train speed are all influential to the generation of curve squeal.

(Fourie et al., 2016) conducted an experiment to characterise curve squeal in 1000m large radius curve section of an export line located in South Africa. The measurement system was setup in such a way as to be able to locate the curve squeal source, frequency of curve squeal, and the actual wheel in the bogie where curve squeal emanates from. Two microphones were installed at a distance of 7.5 m from the railway track line of centre to measure curve squeal. The lateral and vertical forces was measured using installed strain gauge bridges at both rails. Due to the Doppler Effect, two microphones were installed at both inner and outer rail to characterise the difference

between their curve squeal amplitudes and then compare the results simultaneously with sampled force signals. Two triangulation laser sensors were used to measure wheelset lateral displacement. The surprising results obtained from this experiment showed that the inner wheels are more prone to curve squeal than the outer wheels due to longitudinal creepage and very little or no lateral creepage. This study disagrees with the study carried out by (de Beer et al., 2003), (Pieringer, 2011) and (Glocker et al., 2009) where it was concluded that lateral creepage was responsible for curve squeal rather than longitudinal creepage.

(Hanson et al., 2014) in a recent study presented a detailed overview of the study conducted by Transport for New South Wales (TfNSW) Freights and Regional development, Australia on curve squeal measurement. In the results of the trials, and measurements conducted, they identified wheel-rail interface, wheel squeal and rolling stock to be the major contributing factors to curve squeal. A detailed investigation on measurement of curve squeal from noise measurements using wayside noise measurements, determination of actual wheel that contributes to curve squeal and the wheel-rail contact area involved was carried out. They encountered difficulties in determination of which wheel is responsible for curve squeal. To solve this problem, the noise was measured very close to the railway track to differentiate it from individual noise from other wheels. In addition, the curve squeal frequency was obtained and compared with the wheel modal frequencies, and lastly, accelerometers were on the underside of each rail. The difference in the vibration amplitudes for each wheel squeal was used as a benchmark to differentiate the rail for which curve squeal occurs. Mitigation measures for curve squeal was also conducted in the trial using top-of-rail friction modifiers for a period of six months over a 300 m curve radius. The results obtained from three different locations showed that for gauge face lubrication of both rails, 90% reduction in curve squeal amplitude was observed from two locations.

Despite the fact that these trials were conducted in the railway track, it is necessary to conduct the experiment also in controlled conditions. This would help proffer solutions for improving the efficiency of wheel-rail maintenance and performance, and reduce the costs that would be required for identifying and diagnosing faults on the wheel and rail systems. In addition, most of the mathematical models for curve squeal predict accurately the relationship between the creepages and tangential creep forces leading to curve squeal. Experimental verification and validation of these models is therefore required to characterize the falling friction coefficient that is envisaged to happen in theory during unsteady curve squeal.

(Hsu et al., 2007) developed a complete validation of mathematical model for curve squeal from experiments. The experiment was conducted on a twin disc rig. The dynamic response of the wheel and rail rollers and the lateral force was measured for changing values of the creepages during curve squeal. The results obtained compared well with developed theoretical models they developed for curve squeal.

(Liu and Meehan, 2013), (Liu and Meehan, 2014) and (Meehan and Liu, 2018) developed a rolling contact two disc test rig to identify and characterise curve squeal. Strain gauges was installed on the rig to measure the lateral force developed between the upper and lower rollers. The yaw angle of the roller was measured using a special digital later distance meter. Microphone placed at a distance of 50 mm in line with the upper and lower roller contact was used to measure curve squeal amplitude. The results obtained from the experimental two-disc rig compared well with the mathematical model developed to predict theoretically the vibration amplitude of curve squeal. In addition, the authors concluded that curve squeal is developed when the curve squeal amplitude reaches a steady state leading to the crabbing velocity especially for high angle of attack.

(Kim et al., 2019) analysed wheel squeal and flange noise developed in sharp curve track sections. In their study, they used a roller test rig to measure and investigate noise characteristics produced when a real wheel and curved railway section track are in contact. Results obtained from the study showed that curve squeal is generated in the high frequency region while flange contact noise happens depending on the radial wheel modes. The authors in addition to their study measured the vibration and noise in a typical curved track section. Accelerometers were installed on at strategic points under the rail head while microphones were mounted in line with the accelerometers at optimal proximity from the wheel-rail interface. The natural frequency and frequency analysis of the noise in the real urban railway curve sectioned track was compared. The results obtained from this further study showed that curve squeal is generated as a consequence of the interaction of the inner wheel with the rail while flange noise is generated as a result of the interaction between the outer wheel and the outer rail. However, their study did not investigate the effect of contaminants (water and friction modifiers) in mitigation of curve squeal. Their study, however proved beyond all reasonable double that curve squeal noise is significantly louder than flange noise for the various sections of the curved track.

2.3   Review on mitigation measures for curve squeal

Noise emanating from the curved sections of the track or switch is a major problem in railways. The high tonal frequency noise (curve squeal) attributed to the negotiation of railway vehicles as they transverse the curve causes annoyance for people living in the environment of the curve squeal railway track as well as passengers waiting to enter the trains at these points on the track.

Several researches have been conducted to mitigate curve squeal on the railway track. One of the foremost projects developed is the Combating Curve Squeal project proposed by the International Union of Railways (UIC) to combat curve squeal. The study was grouped phases named phase 1 and 2. In the first phase, the tools required to mitigate curve squeal was developed and introduced. The challenges of the phase 1 project were the inability to predict when these methods are to be applied to combat curve squeal. Some of the measures for mitigating curve squeal in phase 1 includes using wheel-based solutions (resilient wheels, ring dampers), lubricants and friction modifiers, coatings, and track-based solutions (rail dampers). The second phase of the UIC project was conducted in Switzerland, France and UK. Emphasis was centred on the combating curve squeal so as to improve confidence level, costs and safety in the railway system (Muller and Oertli, 2006).

The mitigation measures for curve squeal was introduced in the previous chapter. Some of the methods include using asymmetric rail profiles /narrower track gauges, wheel and rail dampers, friction modifiers, lubricants, improving bogie design etc.

Asymmetrical rail profiles have been proposed to mitigate curve squeal, reduce wear in track curves and improve railway vehicle curving capacity. According to (Thompson, 2009) the main concept of this method is the shifting of the inside wheel closer to the flange to improve the wheelset rolling radius difference and hereby allow the railway vehicle negotiate the curve smoothly. A special asymmetrical rail profile was designed and tested on a 200m curved radius section. The results obtained showed that the curve squeal was reduced by 3dB. The conclusion was the asymmetric rail profiles do not sufficiently mitigate curve squeal. In a similar test conducted on the same rail profile but with the application of tungsten carbide on the profile, a significant reduction in curve squeal was achieved from 74% to 26%. However the disadvantage of using advanced method is the need to review the application of the element every 5 years (Thompson, 2009). (Zeng et al., 2017) proposed an optimization method for asymmetric rail grinding in tight curves to minimize wear and curve squeal. The optimized target rail profile was

proposed to include a non-uniform B-spline rational curve having tuneable weight factors. Wheel and rail dampers do not readily provide the benefit of curve squeal mitigation as is the case with asymmetric rail profiles. For example in a recent study carried out by (Setsohhonkul and Kaewunruen, 2016), it was concluded that rail and wheel damper do not benefit from reduction of curve squeal when compared with other mitigation methods although they have lower maintenance cost and longer life cycle. The next viable method that is well researched in literature for mitigating curve squeal is friction modifiers.

(Eadie et al., 2002), (Eadie et al., 2003), (Eadie et al., 2005), (Eadie and Santoro, 2006), (Eadie et al., 2008) showed from field trials and tests, application of friction modifiers can be used to mitigate curve squeal and change the main friction creep-curve characteristics. It was discovered in the experimental study on several curve sections in the track that negative characteristics of the slope of the friction curves caused by increased lateral creepage led to stick-slip oscillations in the wheel-rail contact. The application of friction modifiers on the top-of the rail was observed to not only reduce the adhesion coefficient, but also transform the creep curve characteristics (from negative to positive). Thus, the name positive friction modifiers can be used to interchangeably with the conventional name to stress its particular role and function. However, most of the work carried out was done using oil-based friction modifiers or water-based friction modifiers only. No comparisons were made between the two types of friction modifiers.

(Liu and Meehan, 2016) investigated the effect of applying water and oil-based friction modifiers on a rolling contact twin disc rig to mitigate wheel squeal. Its effect on the friction-creep curves was also investigated. The main components of the twin disc rig comprised of an upper and lower roller. The upper roller was driven by a constant speed vector-controlled motor. The lower wheel was driven by the longitudinal creepage generated from the upper and lower roller contact. Lateral and vertical forces was measured using strain gauges mounted a leaf spring top while a laser guided meter was used to measure the yaw angle of the upper roller to simulate angle of attack. To measure curve squeal, microphone was placed sufficiently close to the wheel-rail roller contact at a distance of 5 cm. Water and oil-based modifiers was applying by spraying on the top of the rail roller contact. The test rig was run for several speeds. The friction coefficient and the curve squeal was then measured for various yaw angles. The results obtained for all speeds show that there is a significant reduction in the lateral force and the friction coefficient when the friction modifiers were applied unlike the dry contact case. The decrease in these parameters was more conspicuous

with oil-based friction modifiers. However, at very large speeds and large yaw angles the friction modifiers did not mitigate curve squeal completely. The authors developed a simplified time domain model to understand this new development. They concluded that curve squeal might still be present in high speeds and yaw angles due to increased temperature in the contact region.

2.4   Summary of main points

This chapter presented detailed literature review on modelling and monitoring curve squeal for railway vehicles. The first section presented an introduction to curve squeal review and highlighted the important difference between monitoring and modelling methods for curve squeal. A comprehensive review on the models developed for curve squeal was then presented and discussed. It was observed that most of these models was designed based on trials and experimental results conducted on the railway systems over the years. These models have helped in understanding the underlying causes of curve squeal although the mechanism behind it is still unknown. In most models developed in literature, it was discovered that lateral creepage is the most dominant cause of curve squeal although several other causes such as mode-coupling and longitudinal creepage have been proposed as major causes.

In addition, an extensive literature review on condition monitoring methods for curve squeal was discussed in detail. It was discovered that difficulties exist in conducting measurements and trials on the railway track due to the challenge in determining the wheelset that is prone to curve squeal and the added cost of installation of condition monitoring systems for this purpose. Despite these challenges, several trials was conducted by organizations in the railway industry to monitor curve squeal. The results obtained from these experiments concluded that the main cause of cause squeal was due to the development of large wheel-rail contact forces especially lateral contact forces resulting in unsteady vibration of the wheel and curve squeal. In the studies conducted, lubricants using friction modifiers was discovered as one of the viable methods for mitigating curve squeal. The difficulties encountered by most railway operators for identifying and characterising curve squeal as already mentioned was minimized by adopting other means of investigation. Controlled laboratory conditions were adopted in several research labs to study and understand curve squeal phenomenon. Scaled test rigs was used for this purpose to ensure that only noise from the wheel-rail contact is measured and monitored unlike when compared with track conditions. The results obtained from the measurement of curve squeal using test rigs further strengthened the fact that

curve squeal is caused mainly by stick-slip oscillations of the contact patch area resulting in the development of large lateral forces at the wheel-rail contact area in curves. As the yaw angle increases, the lateral force increases and the result of this effect is excessive vibration of the wheels thus leading to curve squeal development.

Chapter 3 – Scaled test rig facility for modelling and monitoring curve squeal

This chapter presents the Scaled twin disc rig that will be used to study and validate the research project aims and objectives. Although there are differences between the test rig and the railway system, their appropriateness in helping understand the condition monitoring tools required are presented. The measurement systems and the instruments used for monitoring curve squeal are also presented. In this project, a strain gauge amplifier has been designed to measure the normal, vertical and lateral forces developed in the test rig. A detailed description of the circuit design is presented and discussed. Impact hammer tests to extract the wheel and rail roller modal frequencies is illustrated and presented. To differentiate between the modes obtained from hammer tests, modal analysis of the wheel and rail roller is illustrated using ANSYS Workbench. Comparisons are made between the results obtained and conclusions are drawn.

3.1 Twin Disc rig facility at Huddersfield University

The Twin disc rig facility located in Institute of Railway Research (IRR), University of Huddersfield is used to investigate the curve squeal phenomena. Figure 3.1 shows the schematic of the Twin disc rig.
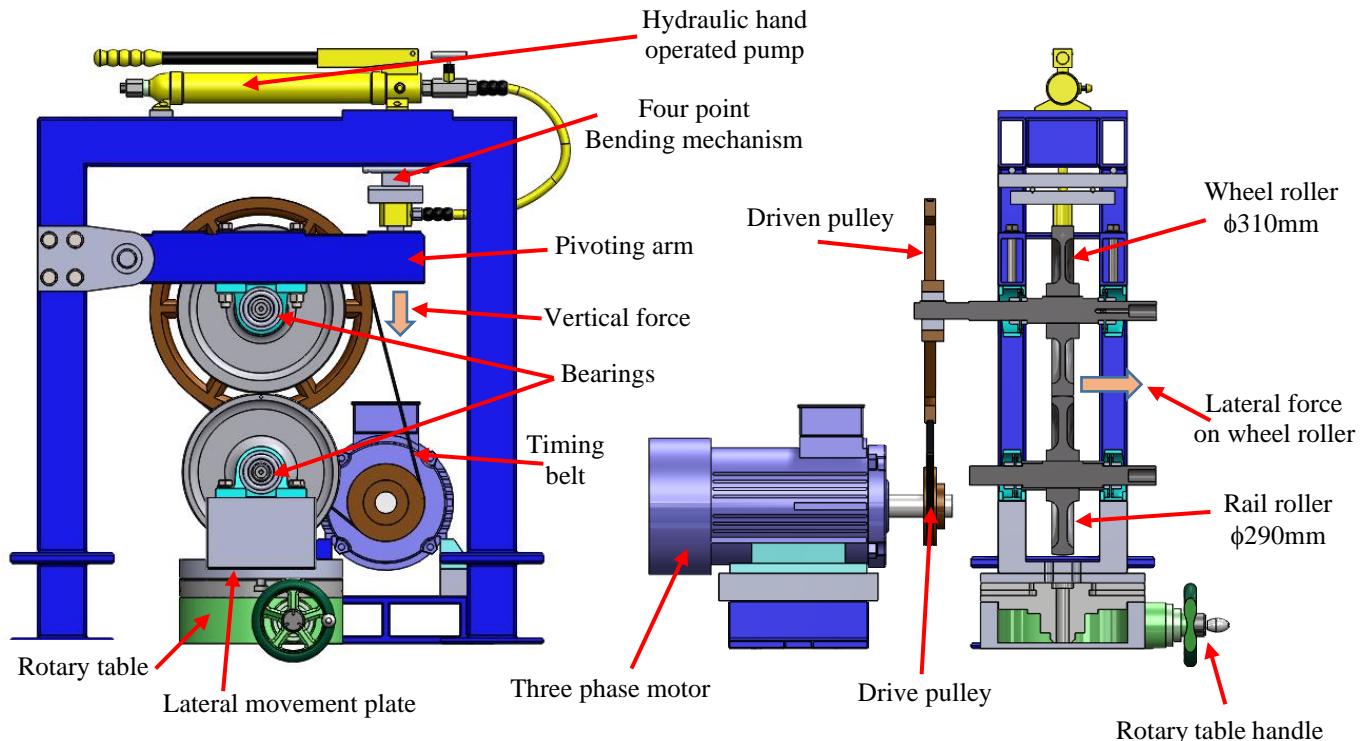
Figure 3.1: Twin disc rig schematic

The twin disc rig is a scaled electromechanical system used as alternative means of recreating wheel-rail interaction of the train under controlled laboratory conditions. The upper roller (wheel roller with diameter equal to 310 mm) is a scaled version (one-third) of the locomotive railway wheel, while the lower roller (rail roller with diameter 290 mm) represents the one-third of scaled rail track. The rail roller is mounted on its own shaft supported with bearings mounted on a U-block (Iron frame) fixed onto the lateral movement plate and the rotary table. The rail roller is free to rotate about its axis. The wheel roller is mounted on a long stub shaft held together with two bearings on either side mounted at the centre of the pivoting arm. The pivoting arm is fixed to the rigid frame to hold it together. Also attached to the long stub shaft is the belt and pulley system, which is driven by a 10 KW, 3500 rpm, three-phase induction motor. An inverter is used to power

the three-phase induction motor and to ensure that the wheel speeds are maintained under any loading condition.
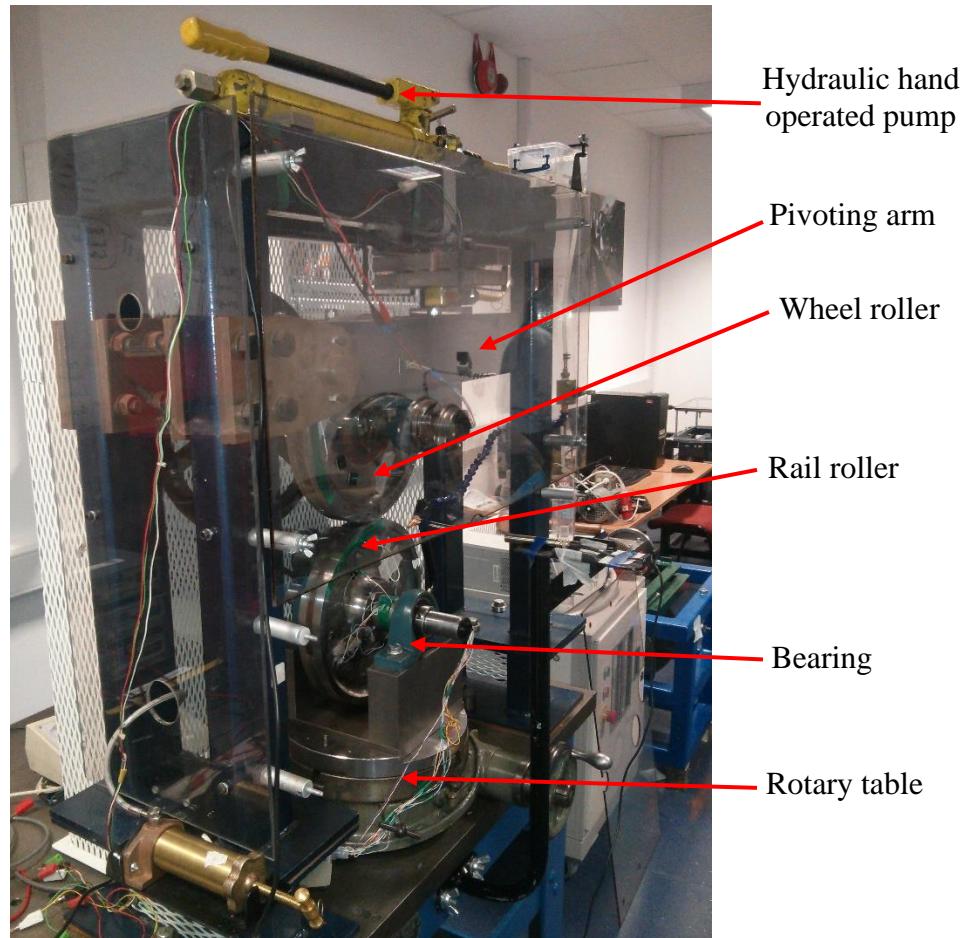
Figure 3.2: Overview of the twin disc rig

The pivoting arm provides the vertical force acting on the wheel roller through the hydraulic hand operated jacking mechanism mounted on the frame. The rig is loaded using a hydraulic hand operated actuator, which provides the hydraulic force acting on the pivoting arm. Since the ratio of the distance from one end of the pivoting arm to the distance of the axis of the rollers is two is to one, the vertical force acting on the rollers is twice that of the applied hydraulic force.

A rotary table is fitted to the twin-disc rig with a rotary table handle to aid adjustments of the rail roller relative to the wheel roller, creating yaw angle. Markings on the handle of the rotary table are used to indicate the yaw angle with resolution of 1/60 of a degree. Improved yaw angle measurement can be achieved using displacement transducers. The ability to adjust the yaw angle

is important to replicate train movements along curves. The rotary table also houses the rotary damping plate, used to minimize vibrations on the rotary table assembly. Lateral alignment can be made by adjusting and clamping the damping plate on which the bearings of the rail roller shaft is mounted. An overview of the twin disc rig is shown in Figure 3.2. The general description of the twin disc rig would be discussed in subsequent sub-sections.

3.2   Detailed description of the twin disc rig

Detailed description of the twin disc rig would be discussed in this section. The main parts of the twin disc rig include the inverter, three phase induction motor, belt and pully drive system, bearings, wheel roller assembly and rail roller assembly.

3.2.1   Inverter

The inverter is used to supply steady AC voltage and rotation frequency to the 3-phase induction motor irrespective of the load applied such as yawing the rail rollers. Powerflex 753 inverter shown in Figure 3.3 was used to provide power to the twin disc rig.

Figure 3.3: PowerFlex 753 inverter (Rockwell Automation Allen-Bradly, 2013).

Some parameters of the inverter are shown in Table 3.1. Other parameters of the inverter can be found in reference PowerFlex 750-Series AC drives Technical Data manual (Rockwell Automation Allen-Bradly, 2013).

Table 3.1: PowerFlex 753 inverter specifications

Parameters of the Inverter	
Input voltage range/Nominal motor voltage	380V – 480 V
Frequency range	47 – 63 Hz
Efficiency	97.5%
Digital input voltage (DC)	24V – 30 V
Digital input voltage (AC)	120V – 132V
Output frequency range	0 – 325 Hz @ 2 kHz carrier 0 – 590 Hz @ 4 kHz carrier
Frequency control	Speed regulation with 0.5% base speed across 40:1 speed and operation range.

3.2.2   Three phase induction motor

The three-phase induction motor was used to drive the wheel roller through the pulley system consisting of the drive pulley and the driven pulley. The driver pulley was connected to the shaft of the induction motor and a pulley belt was used to link the driven pulley. The pulley system ensures a one-third reduction of the speed generated by the three-phase induction motor. The scaled down speed at the driven pully is used to drive the wheel roller. Figure 3.4 shows the typical three-phase induction motor, while Figure 3.5 shows the pulley system.

Figure 3.4: IMB3 VDF Three phase induction motor (ABB, 2010)

The parameters of the three-phase induction motor are shown in Table 3.2.

Table 3.2: IMB3 VDF VEM CLASS F three-phase induction motor parameters

Parameters of the 3-phase Induction Motor	
Voltage	400/690 V
Power	10 kW
Speed range	0 – 3500 RPM
Frequency	50/60 Hz
Motor type	Asynchronous motor with cage rotor
Ambient temperature	-20°C – 40°C
Type of Construction	IMB3

3.

Figure 3.5 shows the Belt and pully drive system used for scaled down reduction of the wheel speed.

Driven pulley (Connected to the wheel roller shaft)

Belt

Drive pulley (Connected directly to the rotor of the induction motor)
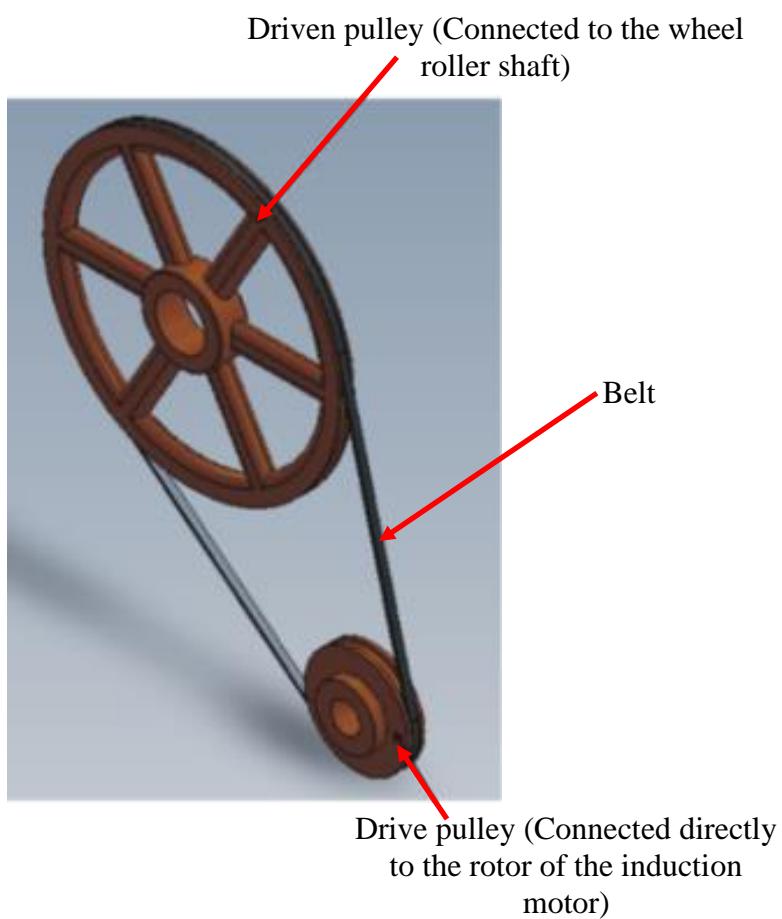
Figure 3.5: Belt and pulley drive system

3.2.3   Bearings

Bearings are mounted on the twin disc rig to support the wheel and rail roller shafts. The inner ring of the bearing is press fit unto the rotating shafts so that there is no relative movement between the two while the shaft is in motion. The outer ring of the bearing is carefully press fit into the bearing house for assembly reasons to allow small axial movement and provide differential thermal expansion, manufacturing tolerances between the shafts and bearing house (Robert and Tata, 2014). The type of bearings used are the NTN (P207) pillow block bearings shown in Figure 3.6.

Figure 3.6: NTN (P207) pillow block bearing (Robert and Tata, 2014)

3.2.4   The wheel roller system

The wheel roller system comprises of the pivoting arm, driven pulley, bearings and the long stub shaft. The main component of the wheel roller system is the wheel roller. The wheel roller is a large cylindrical wheel scaled down to one-third of a typical UK class 91 locomotive wheel. It is made up of EN24T steel material with nominal yield strength equal to 650 MPa, young modulus equal to 2.09×10^5 and Poisson's ratio equal to 0.3. The pivoting arm, driven pulley and the bearings make up the surrounding components that are used to hold the wheel roller in position as shown in Figure 3.7
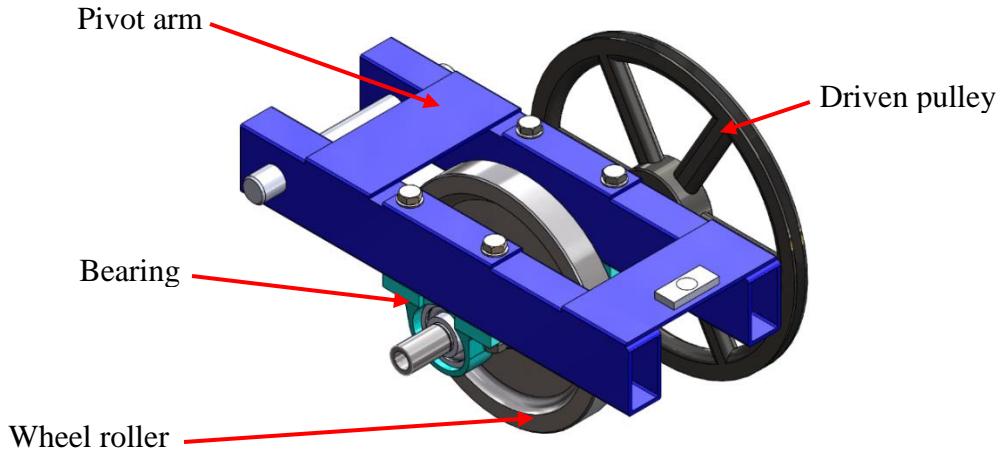
Figure 3.7: Wheel roller system (a) Isometric drawing (b) Side view

The wheel roller is directly press fit to the centre of the shaft while two bearings are mounted on both sides of the shaft unto the pivoting arm. Hydraulic fore is applied to the wheel roller through the rectangular block located on top of the pivoting arm using the four-point bending mechanism (details of this would be discussed in subsequent sections). The force experienced at the wheel roller central axis is twice the force applied at the right end of the pivoting arm according to the principle of moments. The revolute joint located on the left end of the pivoting arm controls its motion. Detailed description of the wheel roller is illustrated in Table 3.3

Table 3.3: Parameters of the wheel roller

Description	Value
Thickness of the wheel and rail roller rim	40 mm
Longitudinal radius of wheel and rail roller	155 mm
Lateral radius of wheel and rail roller	∞
Wheel rail rolling speed range used	75 – 175 RPM
Normal load on pivoting arm	0 – 4 kN
Young modulus of wheel roller	2.09×10^5 MPa
Density	7850 kg/m^3
Poisson ratio	0.3
Mass	13.59 kg

Material	EN24T Steel

3.2.5 Rail roller system

The rail roller system comprises of the rail roller, its shaft, bearings mounted at both sides of the shaft, rotary base table, rotary base handle, U-block and lateral movement damping plates. The main component of the rail roller system is the rail roller. The rail roller represents a one-third scaled version of the railway track in a typical railway system infrastructure. It has the same material properties with the wheel roller. The rail roller assembly shown in Figure 3.8 comprises of the rail roller, shaft, bearings, u-block, damping plates and the rotary table. The rail roller is press fit to the centre of the shaft while two bearings are used to support the rail roller on a u-block material made of steel. The rail roller is free to rotate about its axis. Underneath the u-block is the damping plates.
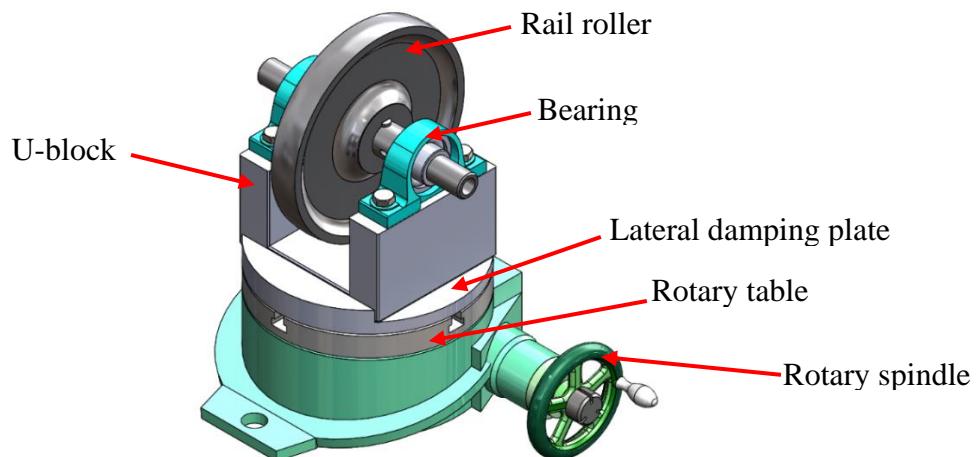
Figure 3.8: Rail roller system

The lateral movement damping plates are used to reduce vibrations during operations. They are also used to introduce lateral displacement to the rail roller assembly system. They are rigidly fixed to the rotary table whereby manual yaw angle adjustments of the rail roller assembly could be done. Yaw angle resolution was set to $1/60^{th}$ of a degree. The parameters of the rail roller are illustrated in Table 3.4.

Table 3.4: Parameters of the Rail roller

Description	Value
Thickness of the rail roller rim	40 mm
Longitudinal radius of rail roller	145 mm
Lateral radius of rail roller	100 mm
Wheel rail rolling speed range used	75 – 175 RPM
Angle of attack (yaw angle) range	0 – 2 degrees
Young modulus of wheel and rail roller	2.09×10^5 MPa
Density	7850 kg/m^3
Poisson ratio	0.3
Mass	12.98 kg
Material	EN24T Steel

3.2.6 Hydraulic hand operated pump

The hydraulic hand operated pump mounted on top of the twin disc rig is used to apply normal load to the wheel-rail roller assembly. The normal load is applied through the four-point bending mechanism to the end of the pivoting arm. The normal force applied at this point on the pivoting arm is twice the force applied on the wheel-rail roller using the principle of moments. Figure 3.9 shows the hydraulic hand operated pump.
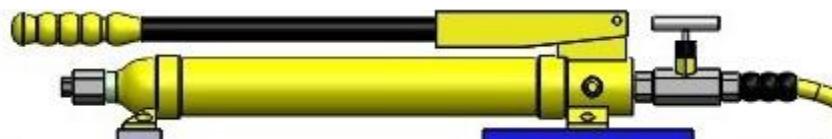
Figure 3.9: Hydraulic hand operated pump

3.3 Devices used for monitoring curve squeal on the Twin disc rig

Devices used for monitoring curve squeal on the twin disc rig include microphone and accelerometers.

3.3.1   Integrated Circuit Piezoelectric (ICP) microphone

Integrated Circuit Piezoelectric (ICP) microphone contains built in impedance conversion electronics and integrated amplifiers. The advantage of using this microphone is that it does not require additional amplifier circuitry as is the case of other kinds of microphones. The optimal distance between the microphone and the wheel rail contact is important to be able to accurately measure curve squeal from the twin disc rig. The closer the microphone is to the wheel-rail contact, the less surrounding noise the microphone would be pick and the better the measurements. In this thesis, a distance of 50 mm was deemed sufficient to measure curve squeal. It is important to note that if the microphone is installed too close (less than 50 mm) to the wheel-rail contact, water and friction modifier can easily splash on the microphone thus affecting the measurements. Placing the microphone farther than the distance used introduced unwanted noise from the laboratory surroundings. However, despite the close proximity of the microphone to the wheel-rail contact, filtering of the signal is still required to process the sound pressure data because of noise picked up from other sources such as the pulley belt, 3-phase induction motor noise and other unknown sources. Figure 3.10 shows the ICP microphone, YG-201.

Figure 3.10: ICP microphone, YG-201 (Global Sensor Technology, 2007)

Some parameters of the ICP microphone, YG-201 is tabulated in Table 3.5

Table 3.5: Parameters of ICP microphone, YG-201

ICP Microphone specifications	
Frequency response	16Hz to 100 kHz
Maximum output voltage	5.0V rms corresponding to 134dB SPL)
Sensitivity	50mV/Pa
Connector type	BNC

The ICP microphone was hoisted on its stand as shown in Figure 3.11 to hold it in position for sound measurements from the wheel-rail interface.
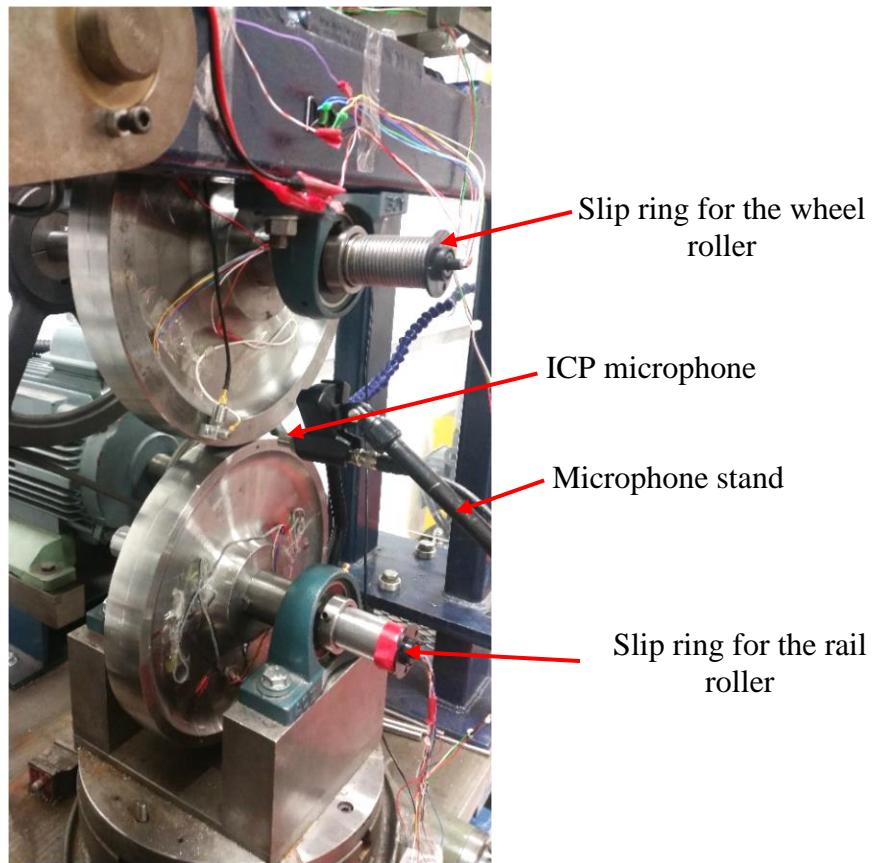
Figure 3.11: ICP microphone positioning on the Twin disc rig

Further information on ICP microphone, YG-201 can be found in (Global Sensor Technology, 2007).

3.3.2   Slip rings

Slip rings allow the transmission of electrical signals and power from a stationary to a rotating structure. It is an electromechanical device that needs continuous rotation to be able to transmit electrical signals. The slip ring using for this experiment is a commercial slip ring with a maximum speed of 250RPM. Figure 3.11 show the locations for the installation of the slip rings on the wheel and rail roller shafts. These accelerometers and strain gauge wires are connected through the slip rings to the Data Acquisition System (DAS).

3.3.3 Dytran 3035B accelerometer

Because of the noise that can be easily picked up during curve squeal measurements, accelerometers were required to be mounted on the wheel and rail roller rim to measure lateral vibration of the rollers and therefore monitor curve squeal. Integrated electronic piezoelectric (IEPE) accelerometer series, Dytran 3035B (see Figure 3.12) was used for modal analysis and lateral vibration measurements due to its light weight, small size, low cabling costs, robustness and integrated electronics. The parameters of the accelerometer are shown in Table 3.6:

Table 3.6: Parameters of Dytran 3035B accelerometer

Dytran 3035B accelerometer	
Sensitivity	100mV/g
Acceleration measurement range	50g
Frequency range	0.5 to 10 kHz
Connectors	5-44 radial connector
Weight	2.5g
Material	Stainless steel
Type of accelerometer	IEPE

Figure 3.12: Dytran 3035B accelerometer

The installation of the wheel and rail accelerometers is displayed in Figure 3.13. As can be observed, the accelerometers are installed on the wheel and rail rims for both impact hammer tests and vibration measurements. The choice of accelerometer location enabled comparisons to be made between the natural frequency analysis obtained from the rollers and the actual dynamic vibration measurements. Although the accelerometers can be installed on the wheel or rail web to investigate its effect in characterizing and identifying curve squeal, this was not investigated in this thesis.

Wheel accelerometer

Slip ring

Rail accelerometer

(a) **(b)**
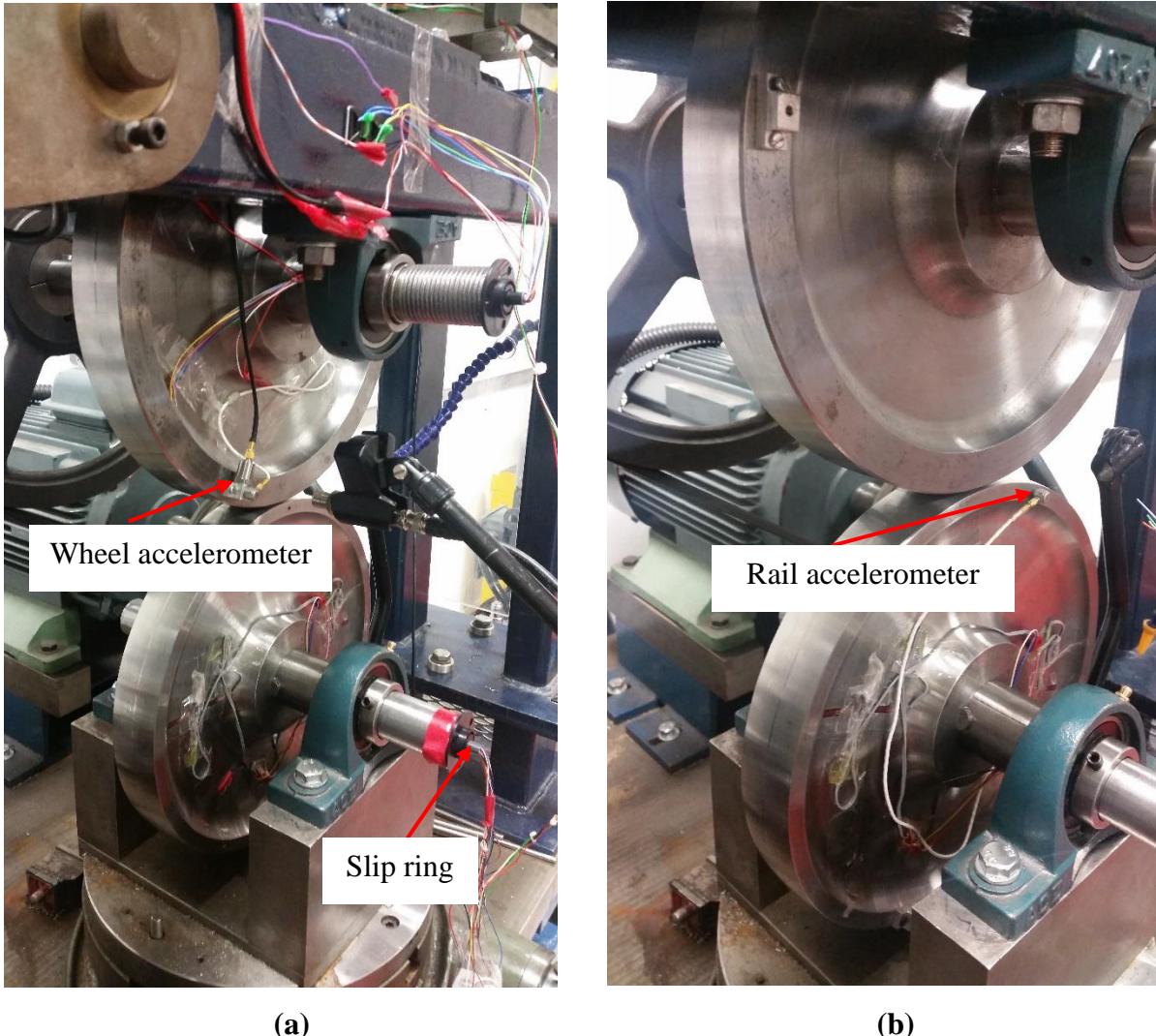
Figure 3.13: Dytran 3035B accelerometer (a) wheel accelerometer (b) rail accelerometer

3.3.4 Data acquisition system

Sinocera YE6232B data acquisition (DAQ) system (see Figure 3.14) was used to acquire measurement data for curve squeal. Details of the DAQ system is listed in Table 3.7.

Table 3.7: Specifications of Sinocera YE6232B

Sinocera YE6232B DAQ	
Input range	±10V
Number of channels	16
Sampling rate	96 kHz/channel

ADC conversion resolution	16 bits
Programmable gain	1,10 or 100
Temperature range	$0^oC - 60^oC$
Software	YE7600
Interface	USB 2.0

The DAQ operates using the YE7600 software. This software is used for analysis and signal processing of the measurement data.

Figure 3.14: Sinocera YE6232B

Sinocera LC-02A impact hammer was used to conduct impact hammer tests on the rollers. Impact hammer test, otherwise known as modal testing was used to extract the natural frequencies (modes) of the wheel and rail roller over the frequency range of 0 to 9 kHz. This range was chosen from modal analysis results of the wheel and rail roller simulated in ANSYS (will be discussed in next section) as the dominant modes where curve squeal is likely to occur. Sinocera LC-02A impact hammer series (see Figure 3.15) with nylon tip was used to excite the rollers laterally due to its structural flexibility and the narrow range of modal frequencies anticipated before testing.

Figure 3.15: Sinocera LC-02A impact hammer

Finally, *FLA-3-11* (Hannah, R. L. and Reed S. E., 1992) strain gauges (see specifications on Table 3.8 and Figure 3.16) was set up in full-Wheatstone bridge configuration to measure the normal forces (installed on the wheel roller assembly), vertical forces and lateral forces (strain gauges installed on the rail roller).
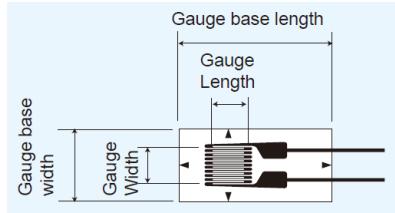
Figure 3.16: FLA-3-11 Strain gauge (Hannah, R. L. and Reed S. E., 1992)

Further details on the placement of the strain gauges would be discussed in the next section.

Table 3.8: FLA-3-11 strain gauge specifications

Gauge base length	Gauge base width	Gauge length	Gauge width	Resistance
8.8 mm	3.5 mm	3 mm	1.7 mm	120 Ω

3.4 Experiments conducted on the Twin disc rig

Impact hammer testing and calibration tests on the rail roller for normal, vertical and lateral force measurement are the two experiments used to establish the test rig parameters. Details of the impact hammer test (experimental modal analysis) and vertical and lateral force calibration would be discussed in subsequent sections.

3.4.1 Experimental modal analysis of the wheel and rail assembly

Experimental modal analysis has grown progressively in popularity over the years since the introduction in 1970's of digital Spectrum analyzer. To characterize vibration resonance, natural modes of a structure are used. Most structures exhibit what is called resonant vibration on their natural modes depending on the excitation force applied to them. Therefore in experimental modal analysis, it is imperative that the resonances of the wheel and rail roller is identified in other to understand its vibration structure (Schwarz and Richardson, 1999).

It is necessary to note that the structure resonances of the test rig are due to the force vibrations and resonances. These integral vibrations and forced resonances affect the dynamic behaviour of the test rig. Since curve squeal is of importance in this study, only the individual resonances vibrations of the rollers have been considered and undertaken. There is a possibility that these structural vibrations of the rollers would affect the performance of the overall test rig structural system.

The experimental modal analysis of the wheel and rail roller was carried out to determine their natural frequencies. This would provide an insight to the identification of the dominant natural

frequency associated with curve squeal. The wheel and rail roller was excited axially to determine the natural frequencies linked with generation of curve squeal. (Kim et al., 2019) confirmed that curve squeal generation is a consequence of excitation of the dominant wheel natural frequency in the axial (lateral) direction

Two accelerometers (Dytran 3035B) was installed laterally on the wheel and rail roller rim for the impact hammer tests as shown in Figure 3.17(a) and Figure 3.17(b) respectively. The wheel and rail rollers were fixed to the bearings through their respective shafts for the tests. Two separate tests; one for wheel and rail roller was carried out. The first test involved the wheel roller isolation from the rail roller prior to measurements to extract its natural frequencies and mode shapes. The second test involved the isolation of the rail roller assembly from the twin disc rig before measurements was carried out.

Sinocera LC-02A impact hammer with nylon tip was used to ensure that the only the wheel and rail roller natural frequencies are excited. The accuracy of the test is dependent on the impact force quality. Therefore, to eliminate bad hits from the impact and average only the good hits remaining, five hits for each test was carried out. The accelerometers and impact hammer were then connected the Computer system through the DAQ and then the YE7600 software was used to identify the modal shapes and natural frequencies of the wheel and rail roller. Accelerance frequency response function (FRF) (ratio of the acceleration to the excitation force) was then computed for each roller based on the extracted hammer test results.
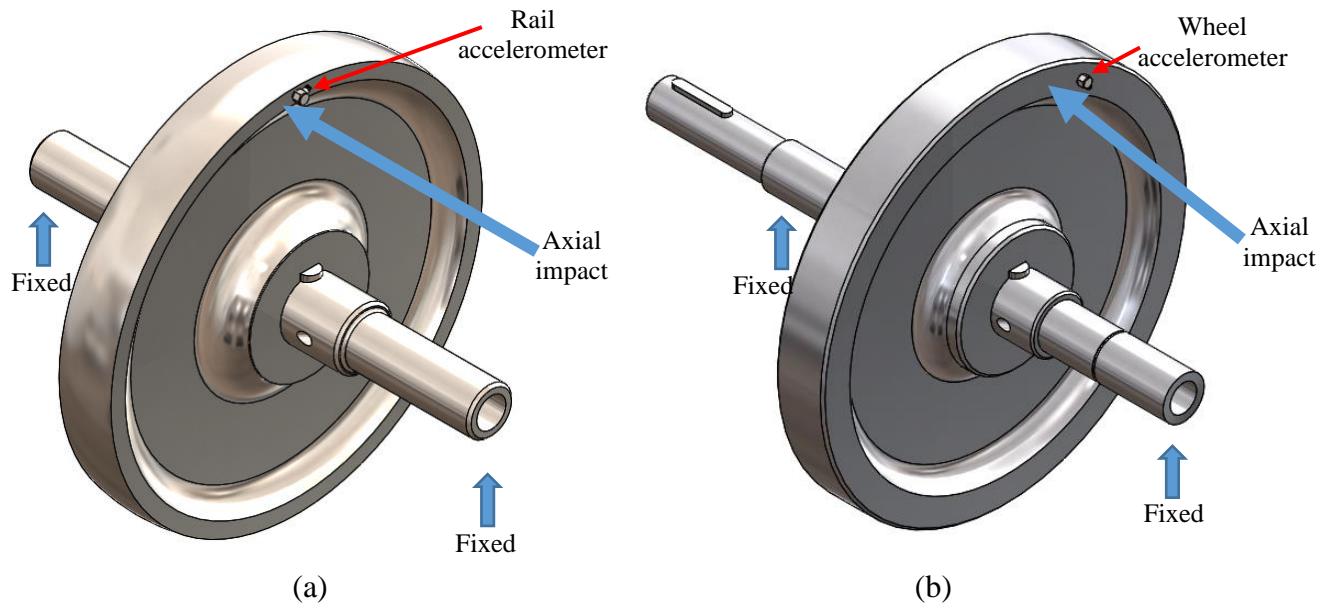
Figure 3.17: Setup for tests on the (a) rail roller assembly (b) wheel roller assembly

The frequency response functions/phase response in the axial directions on the side face of the wheel and rail rollers is shown in Figure 3.18 and Figure 3.19 respectively.

(a)
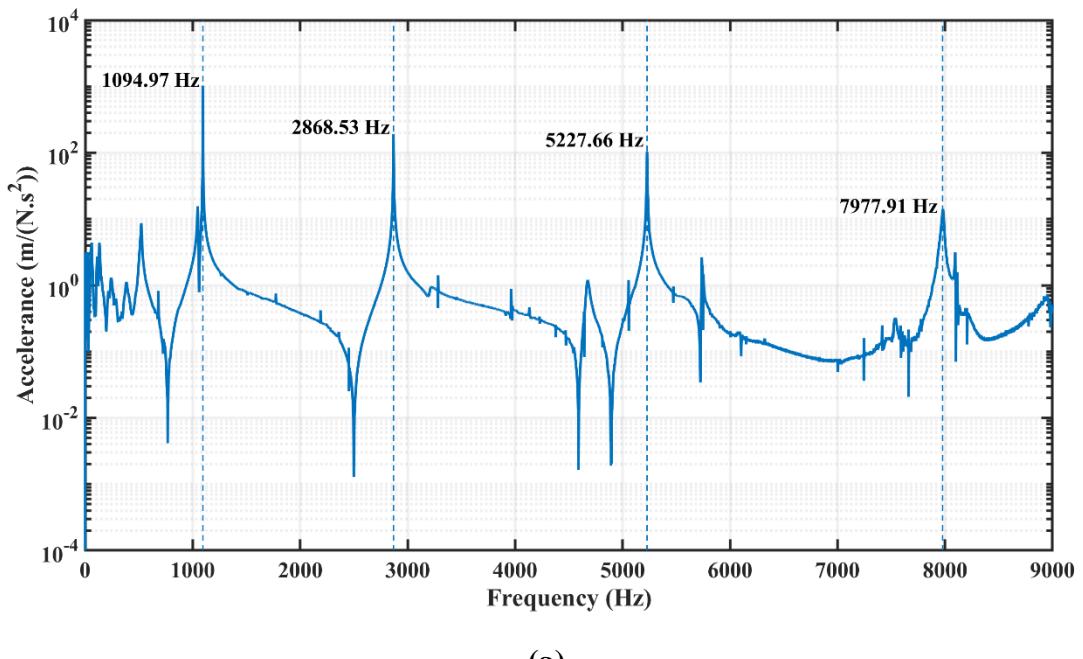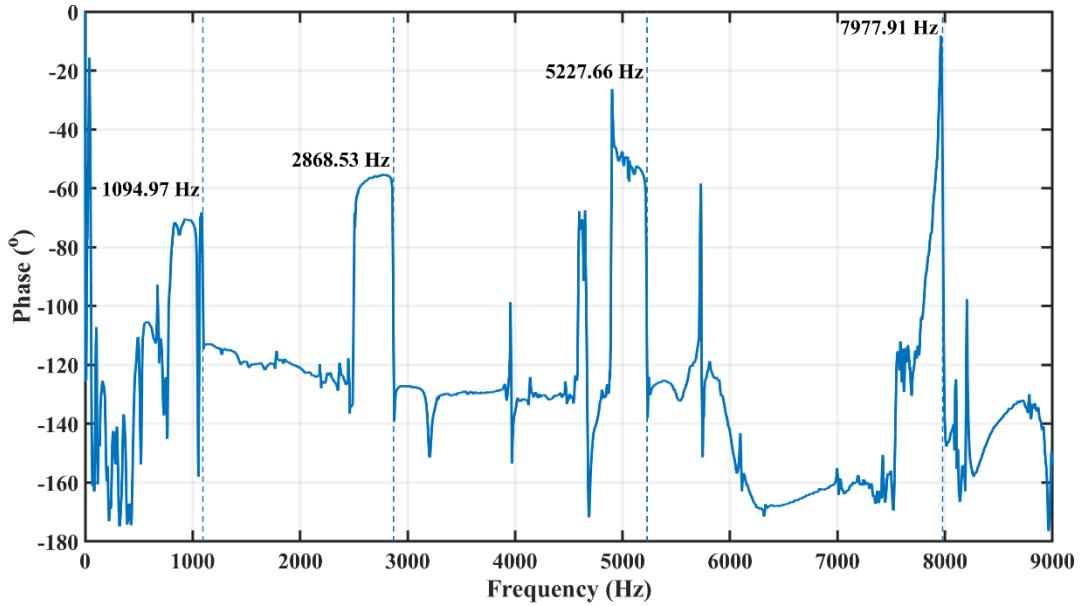
(b)

Figure 3.18: Frequency response function (a) and phase response (b) of the wheel roller assembly

The natural frequencies of the wheel roller can be observed from the Accelerance plot in Figure 3.18(a). The corresponding phase response of the wheel roller indicating the natural frequencies is observed in Figure 3.18(b).

Similarly, the natural frequencies and the mode shapes obtained from the Accelerance plot for the rail roller can be observed in Figure 3.19(a). In addition, the phase response of the rail roller (Figure 3.19(b)) indicates the regions where the natural frequencies on the rail roller occurs. The wheel and rail roller natural frequencies are observed to be slightly different from each other in other to be able to identify which the dominant frequency responsible for curve squeal. These results correlate with the results obtained in (Hsu et al, 2007).
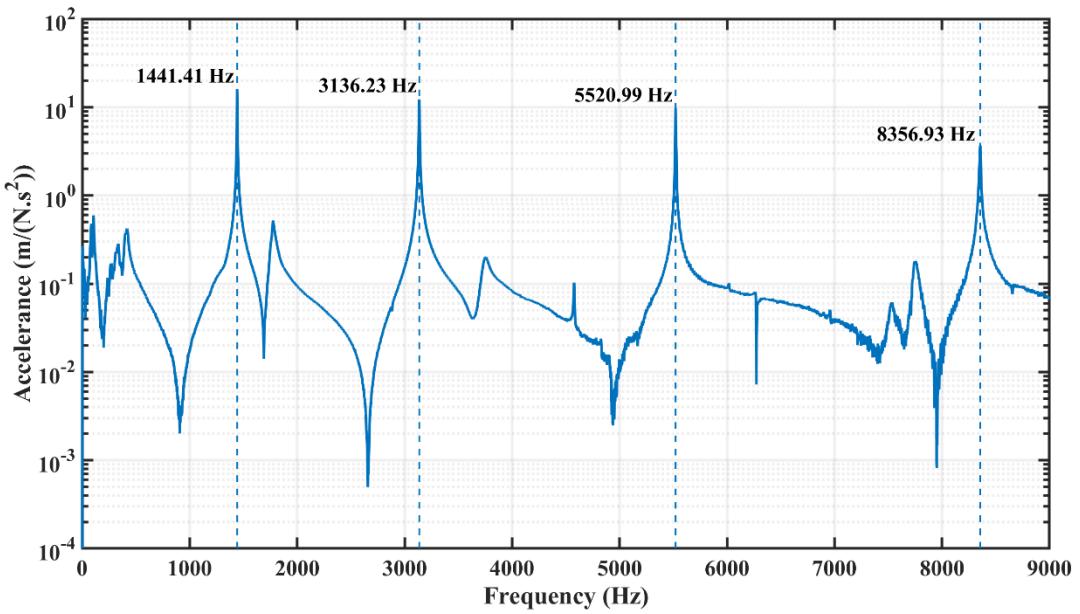
(a)
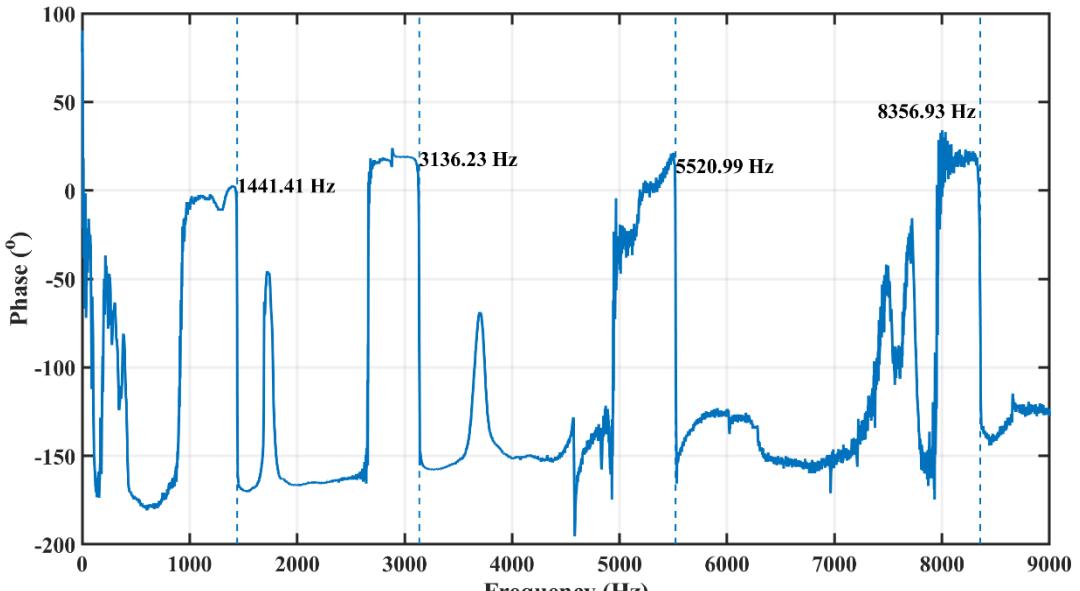
(b)

Figure 3.19: Frequency response function (a) and phase response (b) of the rail roller assembly

The impact hammer test conducted on the Twin disc rig provided understanding of the wheel and rail roller natural frequencies and mode shapes. However, it did not provide sufficient information

about which of the natural frequencies in the wheel and rail roller are excited during curve squeal. This information would be observed in dynamic measurements conducted on the twin disc rig.

3.5   Finite element model (FEM) of the wheel and rail assembly

Finite element model (FEM) of the wheel and rail roller assembly (with their respective shafts) was performed with ANSYS workbench to examine in detail the modes of vibration. In the FEM model, modal and harmonic response analysis of the wheel and rail roller assembly would be implemented. In this next section modal analysis of the wheel and rail assembly would be discussed in detail while the harmonic analysis of the wheel and rail assembly would be discussed in the next section.

3.5.1   Modal analysis of the wheel and rail roller assembly

Modal analysis is required to determine the natural frequencies, mode shapes and modal damping parameters of the wheel and rail roller. The determination of these parameters would help to discover the dominant mode and natural frequencies that are responsible for curve squeal. In addition, comparisons would be made with the results obtained from the impact hammer tests.

ANSYS Workbench was the preferred choice to ANSYS mechanical for modal analysis of the rollers due to its relative easy interface, ability to interact easily with other CAD (Computer aided design) packages, stepwise solving scheme, easy rectification of errors, ability to update geometries and boundary conditions, ability to integrate two or more solvers, and its vast analysis capabilities (Chen and Liu, 2014). 3D CAD model of the wheel/rail roller attached to their respective shafts was generated in SolidWorks to replicate the actual geometry and exported to ANSYS Workbench to develop the FEM model. The material properties of the wheel/rail rollers including the shafts is displayed in Table 3.9:

Table 3.9: Material properties of the wheel/rail rollers and their respective shafts

Material	Density	Poisson's ratio	Young Modulus	Tensile Yield strength
EN24T steel	7850kg/m^3	0.3	2.09 x 10^5 MPa	650MPa

Further details on the geometrical properties of the wheel and rail roller can be found in Table 3.3.

The wheel and rail roller assembly were fixed at the shafts ends as shown in Figure 3.20. This is to replicate the actual test rig scenario where the bearings are press fit to the same locations on the shafts of the wheel/rail system. Multizone and Hex Dominant mesh algorithms was applied to the wheel/rail roller and the shafts respectively so as to be optimal for the circular shape. 345,157 nodes and 99,027 elements was generated for the wheel roller assembly, while 226,301 nodes and 58,885 elements generated for the rail roller assembly using the described mesh method.

(a)   (b)
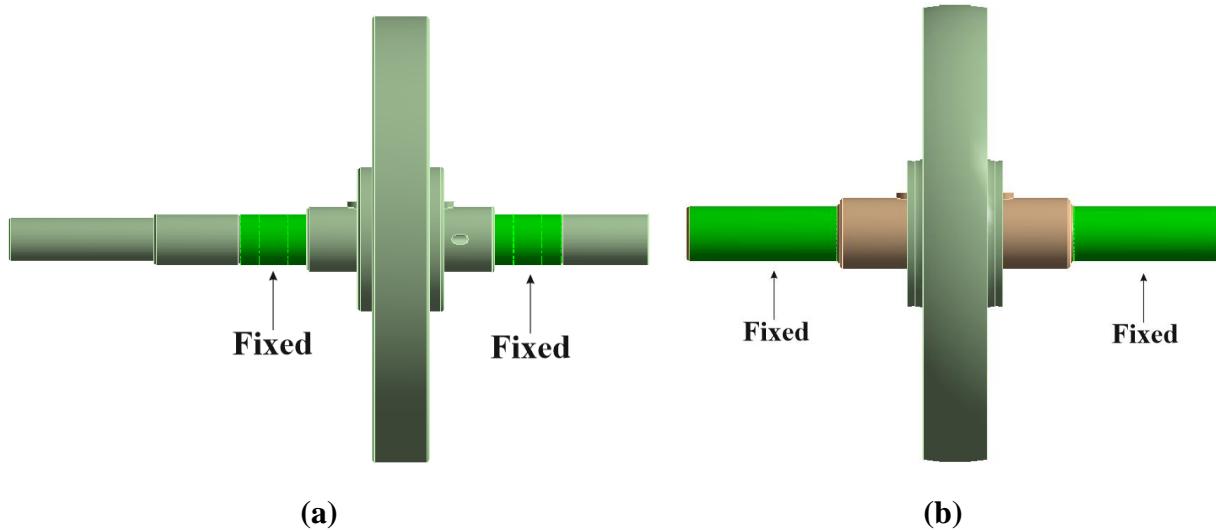
Figure 3.20: Boundary conditions for the wheel (a) and rail (b) roller assembly

Figure 3.21 shows the mesh applied on the wheel and rail roller assembly

(a)   (b)
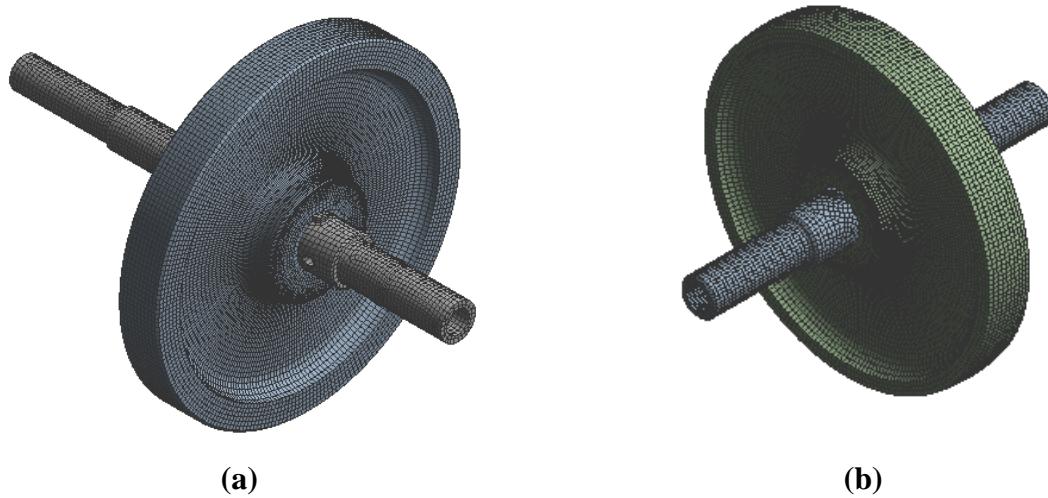
Figure 3.21: Meshed wheel (a) and rail (b) rollers

The modal shapes of the wheel roller assembly from the FEM model are displayed in Figure 3.22.

56

(a)

(b)

(c)

(d)
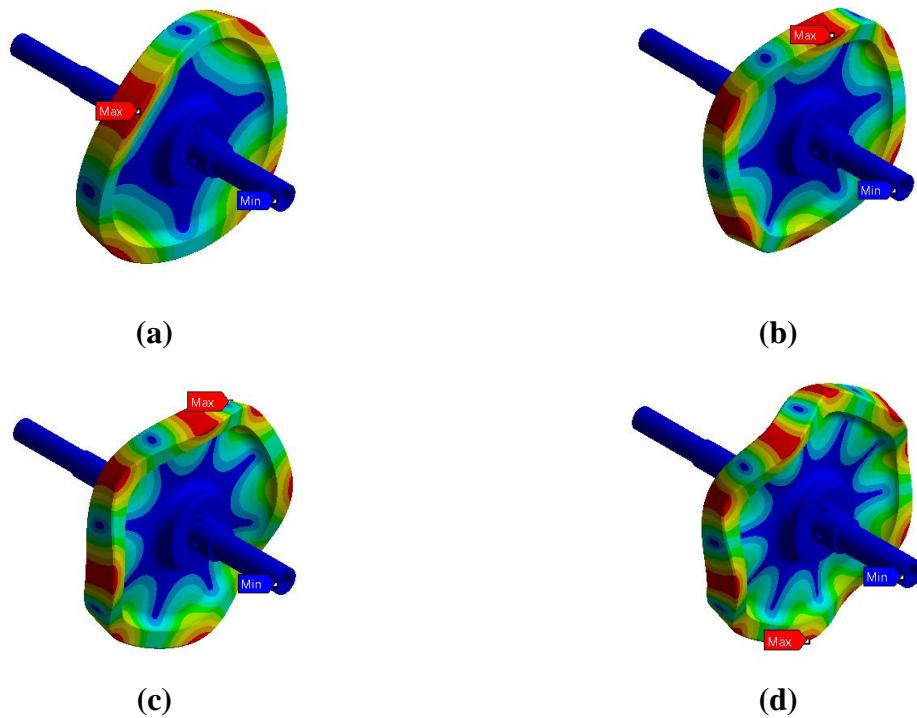
Figure 3.22: Mode shapes for the wheel roller assembly (a) 1095.1Hz, (b) 2869.1Hz, (c) 5223.5Hz, (d) 7956.4Hz.

It can be observed that the mode shapes of the wheel roller assembly generated in the axial direction are characterized by nodal diameters (n). The nodal diameters represent the vibration amplitudes created in the circumferential direction of the rollers for which the maximum response is on the wheel roller rim. Figure 3.22(a), Figure 3.22(b), Figure 3.22(c) and Figure 3.22(d) has nodal diameters 2, 3, 4 and 5 respectively.

Similarly, the modal shapes of the rail roller are displayed in Figure 3.23.

(a)

(b)
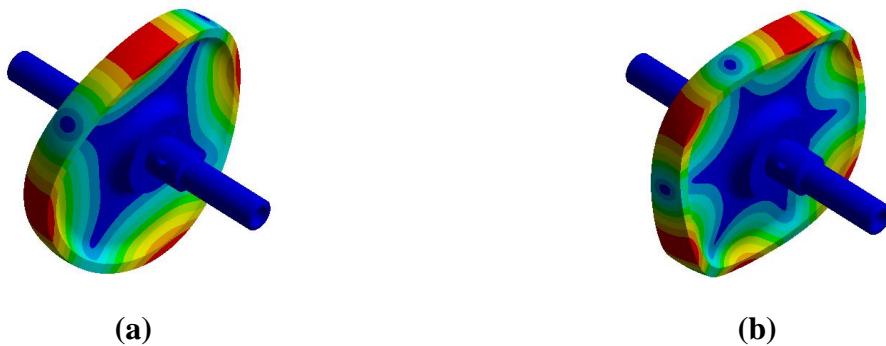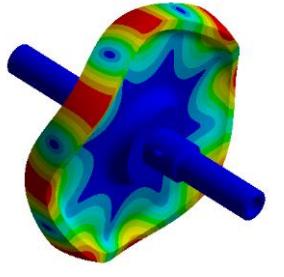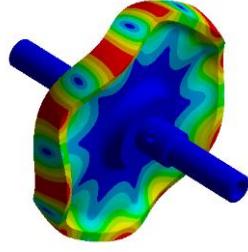
<div align="center">(c)   (d)</div>

Figure 3.23: Mode shapes for the rail roller assembly (a) 1454.9Hz, (b) 3127.1Hz, (c) 5521Hz, (d) 8360.1Hz.

Similar observations of the nodal diameters of the rail roller are observed. However, the natural frequencies locations of the rail roller can be observed to be slightly difference from that of the wheel rollers. This was intentionally done from the 3D model of the rollers to differentiate which modes are responsible for curve squeal.

3.5.2 Harmonic response analysis of the wheel and rail roller assembly

To further determine the resonance of the wheel and rail roller assembly, and study the forced vibration response, harmonic response analysis is required to be conducted based on the modal analysis results. Harmonic response analysis of the wheel and rail roller assembly FEM model was conducted using a range of 0Hz to 9kHz at 6.25Hz intervals. The boundary conditions were imported from the modal analysis results and the wheel and rail roller was divided in the axial directions by a force of 1kN. From the impact hammer test results, the modal damping of the wheel and rail assembly was predicted to be about 0.0001 and used to perform the harmonic analysis. The frequency response function (FRF) with the corresponding mode shape of the wheel roller is shown in Figure 3.24.
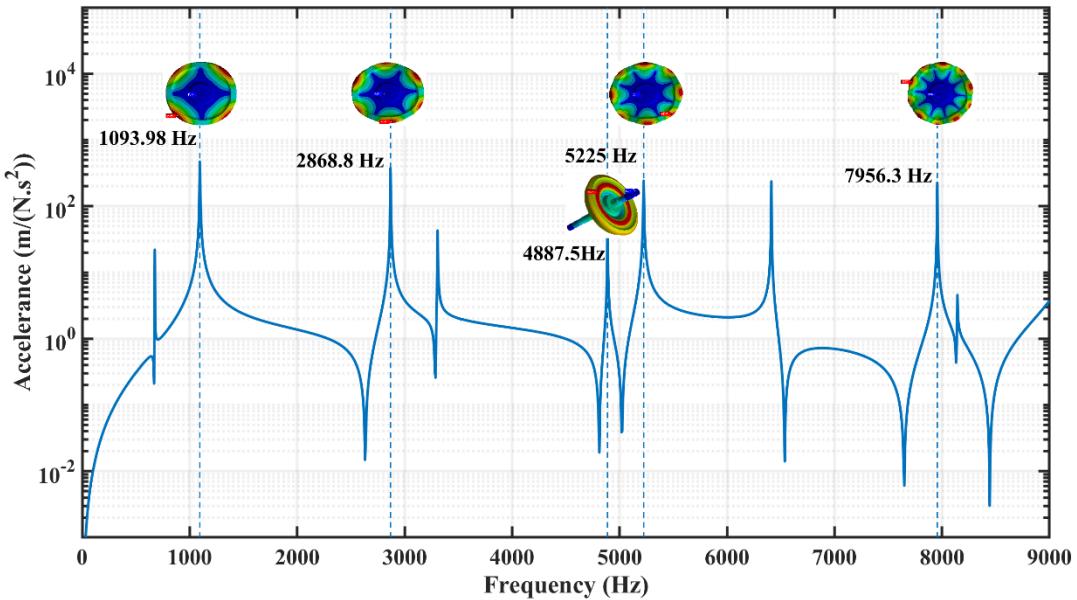
(a)
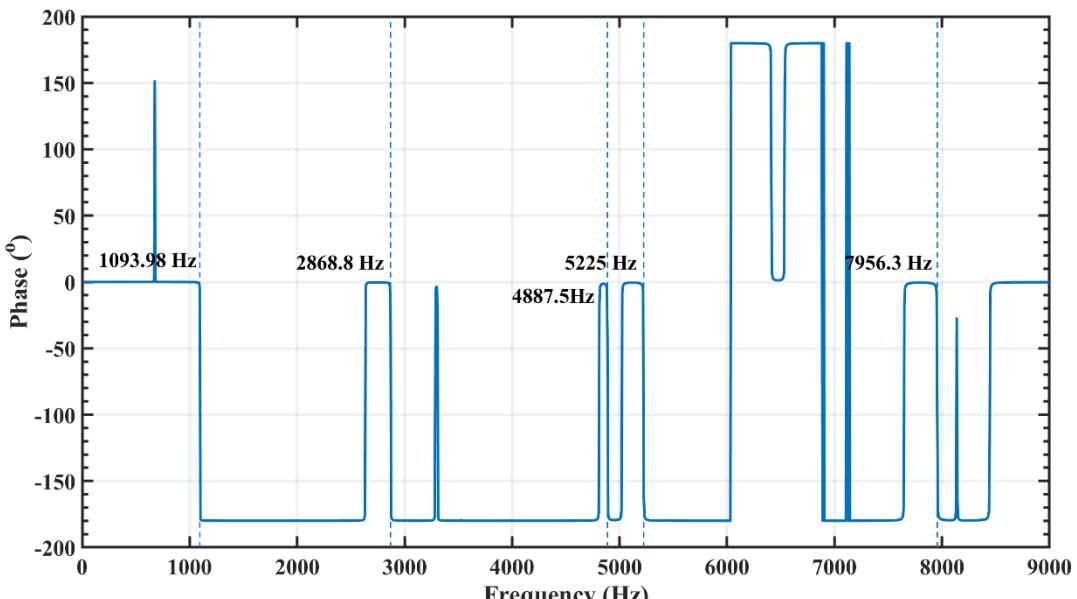
(b)

Figure 3.24: Frequency response function (a) and phase response (b) of the wheel roller assembly from harmonic analysis

Similarly, the frequency response function (FRF) with the corresponding mode shape of the rail roller assembly is shown in Figure 3.25.
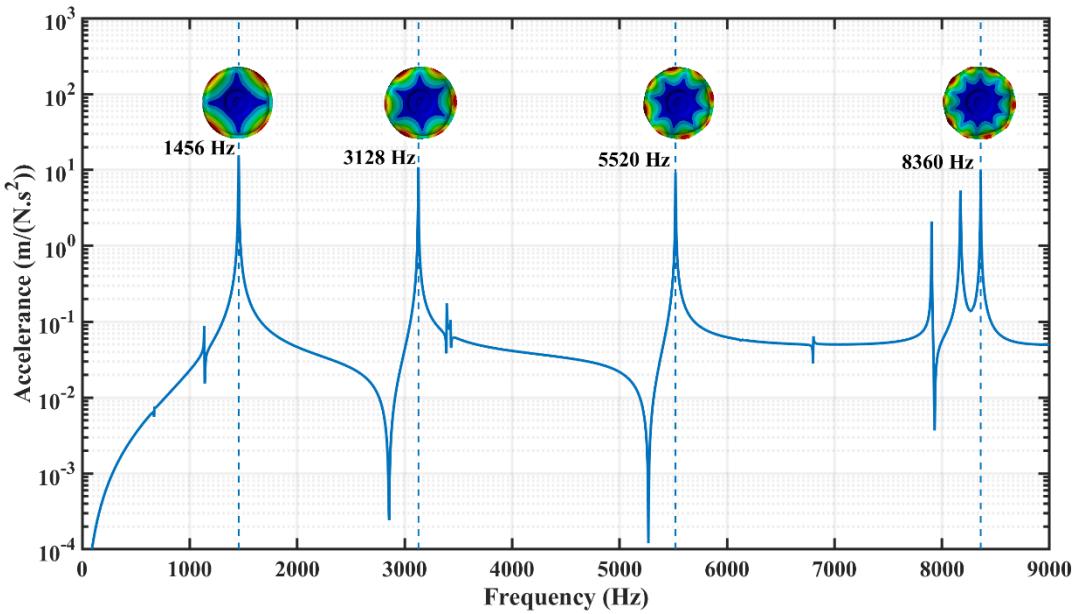
(a)
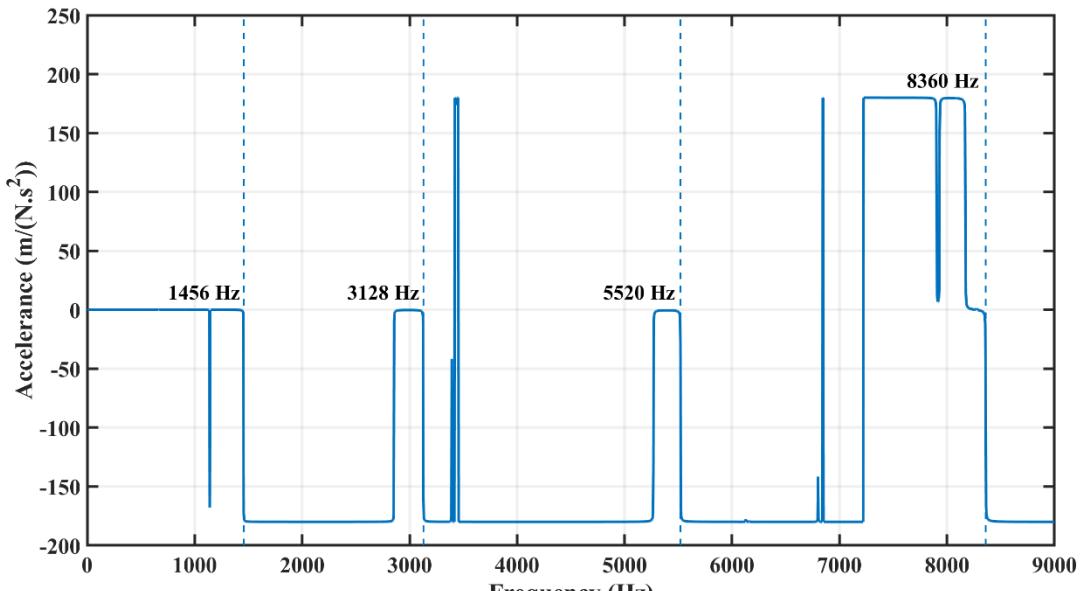
(b)

Figure 3.25: Frequency response function (a) and phase response (b) of the rail roller assembly from harmonic analysis

The axial modes of the wheel and rail roller assembly was successfully extracted using harmonic analysis. The phase response of the wheel and rail roller assembly is the imaginary part of the frequency response function which is complex.
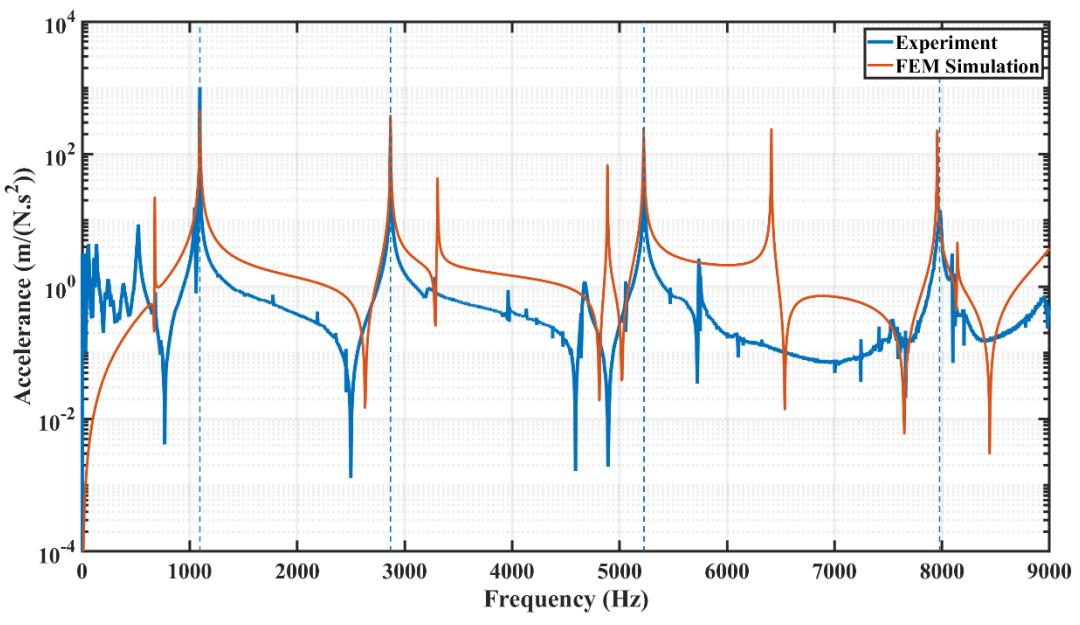
(a)
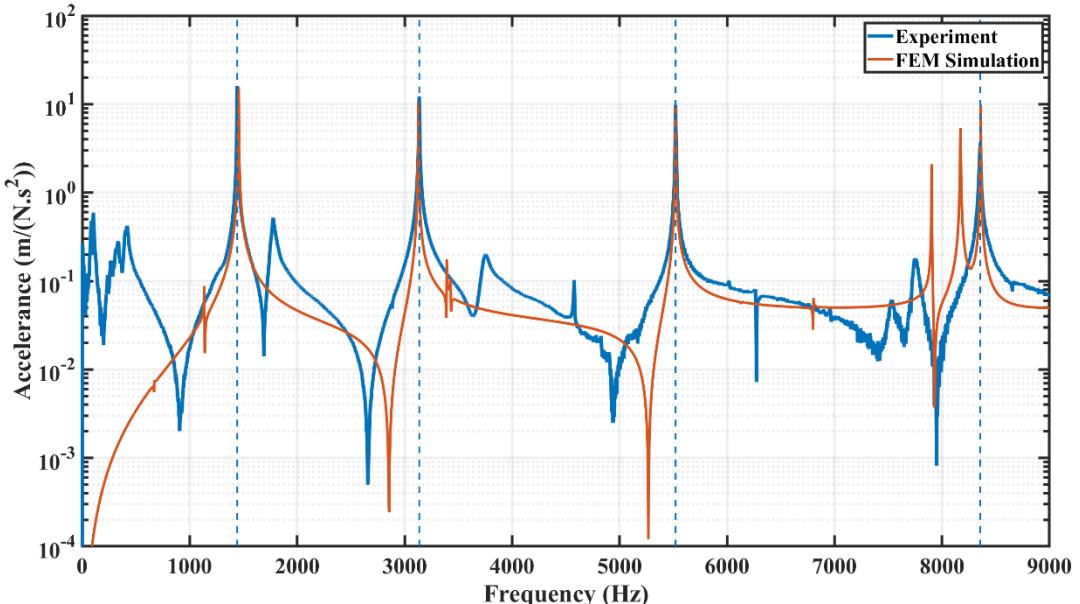
(b)

Figure 3.26: Frequency response function comparison of (a) wheel roller assembly and (b) rail roller assembly.

Figure 3.25(a) and Figure 3.26(b) shows the comparison between the wheel roller assembly and rail roller assembly respectively. The experiments and the simulated results obtained from the

FEM model showed good agreement with each other in the axial direction. The difference in the total frequency response for the wheel and rail roller assembly was under 2% as shown in Table 3.10.

Table 3.10: Comparison between experiment and FEM (Wheel roller assembly)

Wheel roller assembly				
Mode	FEM (Hz)	Experiments (Hz)	Difference (%)	Mode shape
1	1093.98	1094.97	0.091	Axial
2	2868.8	2868.53	0.0094	Axial
3	5225	5227.66	0.051	Axial
4	7956.30	7977.91	0.27	Axial
Rail roller assembly				
Mode	FEM (Hz)	Experiments (Hz)	Difference (%)	Mode shape
1	1456	1441.41	1.01	Axial
2	3128	3136.23	0.032	Axial
3	5520	5520.99	0.018	Axial
4	8360	8356.93	0.037	Axial

3.6   Lateral force measurement on the Twin disc rig

Lateral force in the Twin disc rig was determined through the bending moment by a strain gauge array installed on two different circular arrays on the rail roller as shown in Figure 3.27(a). The lateral force on the wheel is calculated as:

$$F_Y = \frac{M_1 - M_2}{r_1 - r_2}$$
(3.1)

Where r_1 and r_2 are the optimized radii of the two circumferences for which the strain gauges are installed on the rail roller web and M_1 and M_2 are the two bending moments on two radius measurements. The radii for the strain gauges must be optimized to minimize sensitivity against other forces (vertical and normal) and increase the sensitivity of the strain gauges to lateral forces.
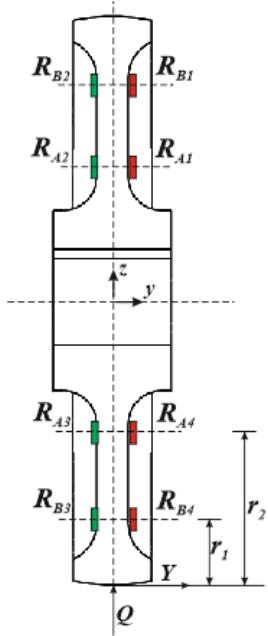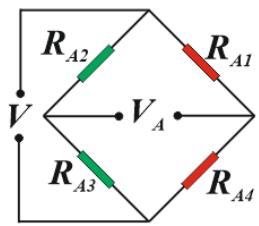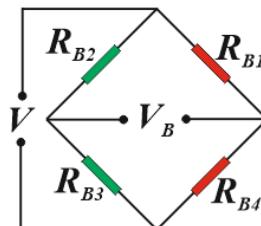
Figure 3.27: Layout of the strain gauge for the measurement of lateral force on the Twin disc rig (a) Strain gauge layout locations on the rail roller (b) Strain gauge layout 1 connection (c) Strain gauge layout 2 connection

The method for lateral force measurement was derived from (Papini et al., 2013). This method is effective in the estimation of lateral force through bending moment using strain gauge arrays mounted on two dissimilar circular arrays. The rationale for this approach is to be able to minimize the effects of other forces applied on the wheel such as the lateral and vertical forces. This method of lateral force measurement uses full bridge configuration (all four strain gauges connected together), rather than half or quarter bridge configuration to ensure that the output voltage is directly proportional to the applied force. They provide twice the sensitivity of half bridge configurations and provide temperature compensation during measurements. Finally, full bridge

configurations provide less complexity in circuitry for lateral force measurement than half bridge configurations used by (Hsu et al., 2007).

3.6.1 Optimal positioning determination using rail roller FEM model

A complete FEM model was required to determine the effect of strain gauge position on measurement was developed in Ansys Workbench. The optimization for the measurement of the lateral forces was simulated using one loading and contact position on the Twin disc rig. The vertical and lateral forces was selected based on realistic operating conditions. For example, assuming that the coefficient of friction at the wheel rail contact in central position is 0.3, vertical force was assumed to be 2.5 kN while the lateral force was assumed to be 2.5 kN x 0.3 = 750 N. Longitudinal forces on the test rig was negligible and was therefore not considered in the FEM simulation. Figure 3.29 shows the generated mesh for the rail roller using Multizone mesh method. This method decomposes the rail roller geometry into pure hexahedral mesh. The advantage of using multizone mesh is its ability to handle problems associated with complex geometry compared with other mesh methods. The resultant mesh yielded 128,291 nodes and 98,123 elements.

Figure 3.29: Mesh results for the rail roller

The result of the FEM simulation with the corresponding optimal radii for the placement of the strain gauges are r_1 =73.20 mm and r_2 =113.10 mm as shown in Figure 3.30.
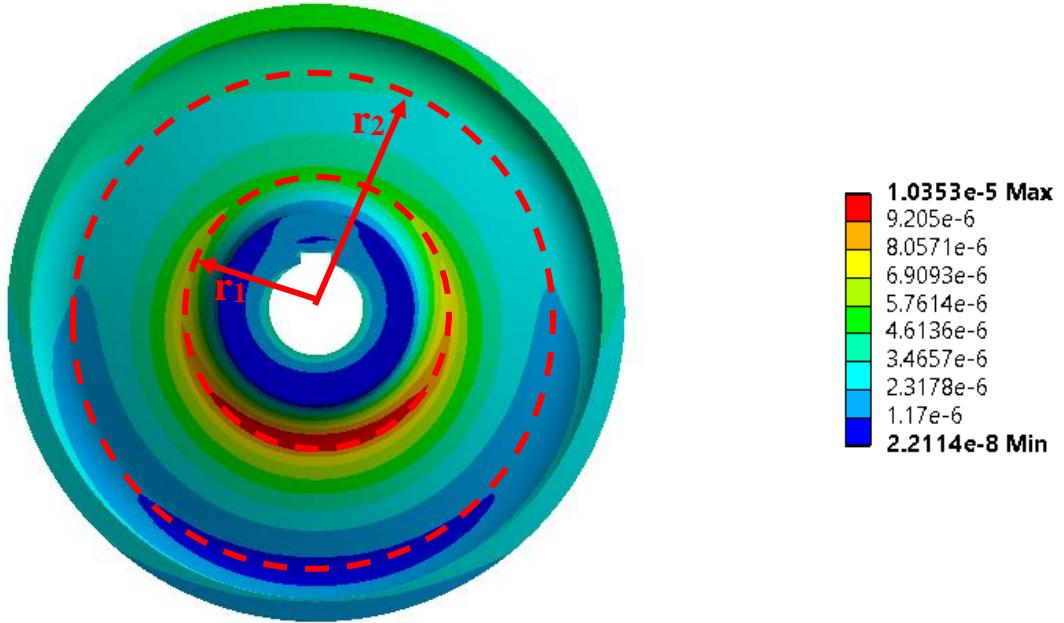
Figure 3.30: FEM model showing radial strain on the rail roller for the assumed loading condition

Maximum radial strain occurs at the radii location r_1 as expected compared to radii location r_2. This is due to the fact that when lateral force is applied, more lateral bending is experienced at this radii circumference location. Strain gauges mounted at r_1 circumference would therefore produce much higher strain compared to strain gauges installed at r_2. However, the installation of strain gauge at r_2 is necessary to eliminate all wheel-rail contact forces to ensure that only lateral force is taken into consideration.

3.6.2 Calibration of lateral force using Intron 3369 Table top system

Using the determined optimal strain gauge location, calibration of the lateral force on the rail roller was performed using Instron 3369 tabletop system (see Appendix for detailed specification of the instron 3369 tabletop system) to determine the relationship between voltage and lateral force. Specially designed test piece was constructed for the application of lateral force on the rail roller rim. The Instron 3369 tabletop system is used to apply lateral force to the test piece. The system has the capability of applying force up to 50 kN. Considering the twin disc rig design constraints, 4 kN lateral force was sufficient for lateral force calibration on the rail roller (see Figure 3.31).
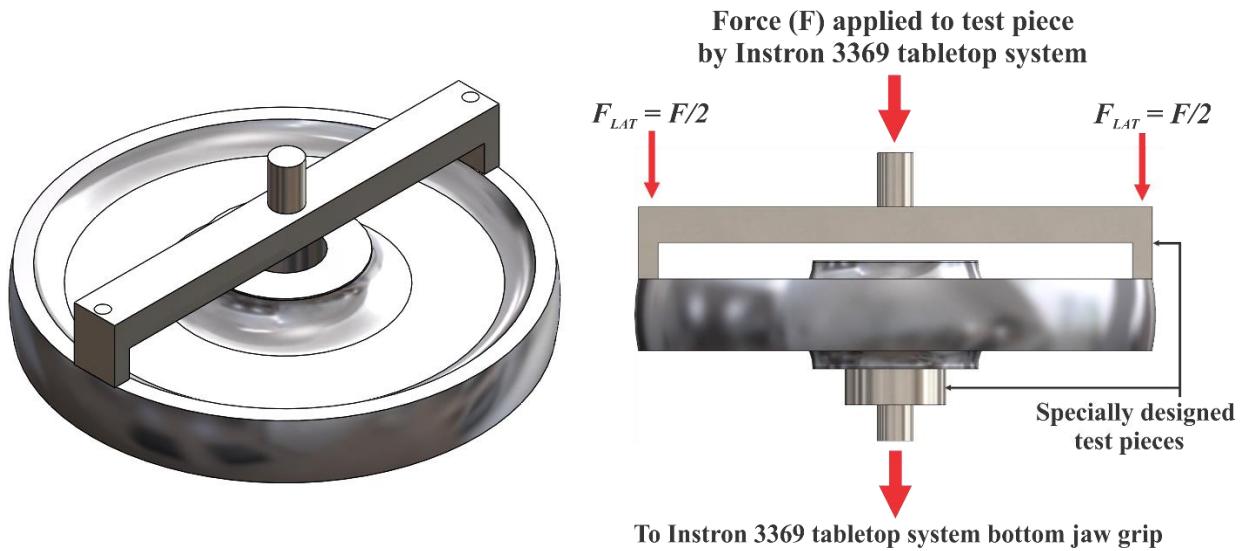
Figure 3.31: Lateral force measurement on the rail roller

Lateral force applied by Instron 3369 tabletop system was in the range of 0 to 4 kN in increments of 0.25 kN. Since the lateral force is only possible at one position in the rail roller rim, the applied lateral force. Strain gauge amplifier circuit (details in Appendix) was designed to measure the corresponding voltages of the strain gauge (V_A and V_B as shown in Figure 3.32 and Figure 3.33 respectively).
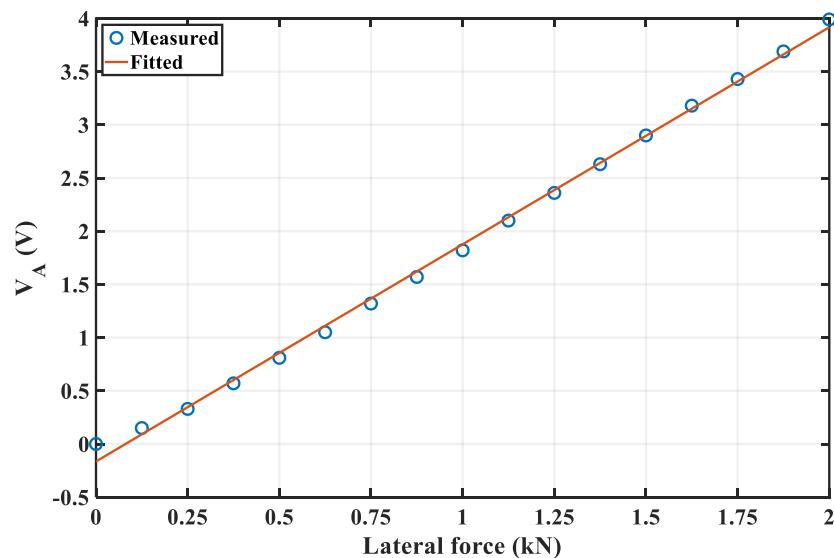
Figure 3.32: Calibration results for the lateral force on the rail roller (Voltage V_A versus lateral force)

The expression for the line of best fit in Figure 3.30 is expressed as follows:

$$V_A = 2.04F_L - 0.164 \qquad (3.2)$$

Where the slope is given as 2.04V/kN, and the voltage intercept is -0.164V.

Figure 3.33 shows the calibration results for the lateral force versus the lateral voltage (V_B).
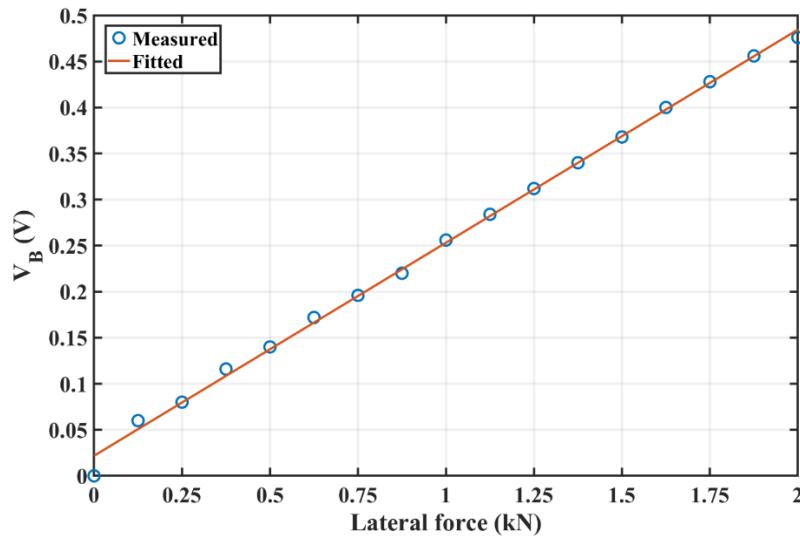
Figure 3.33: Calibration results for the lateral force on the rail roller (Voltage V_B versus lateral force)

The equation for the line of best fit in Figure 3.31 is expressed as follows:

$$V_B = 0.23F_L + 0.0218 \qquad (3.3)$$

As expected, the lateral voltage (V_B) plot obtained from the strain gauges installed at the radii r_2 has slope that is much lesser than the slope obtained in equation (3.2). The full bridge configuration installed at radii r_1 has a sensitivity that is approximately ten times greater than the full bride configuration installed at radii location r_2. These observations correlate with the FEM results obtained in Figure 3.30.

3.7   Calibration of normal force using Intron 3369 Table top system

Normal force is one of the components of measured force on the wheel-rail contact. In the twin disc rig, normal force is directly applied perpendicular to the wheel rail interface. Four-point bending mechanism is used to produce the required normal force for the Twin disc rig. Although in railway vehicles, the normal force differs from the vertical force as a result of the cant angle and the location of the contact point location, in the twin disc rig, the normal force is approximately

equal to the vertical force. The reason for this assumption is that the wheel and rail roller are aligned at central position always in the twin disc rig for dynamic measurements. Therefore, with no lateral displacement and cant angle, the normal force is equal to the vertical force.

To calibrate the normal/vertical force, Instron 3369 system was used to apply the respective load to the four-point bending system along with the designed test pieces (see Figure 3.35).
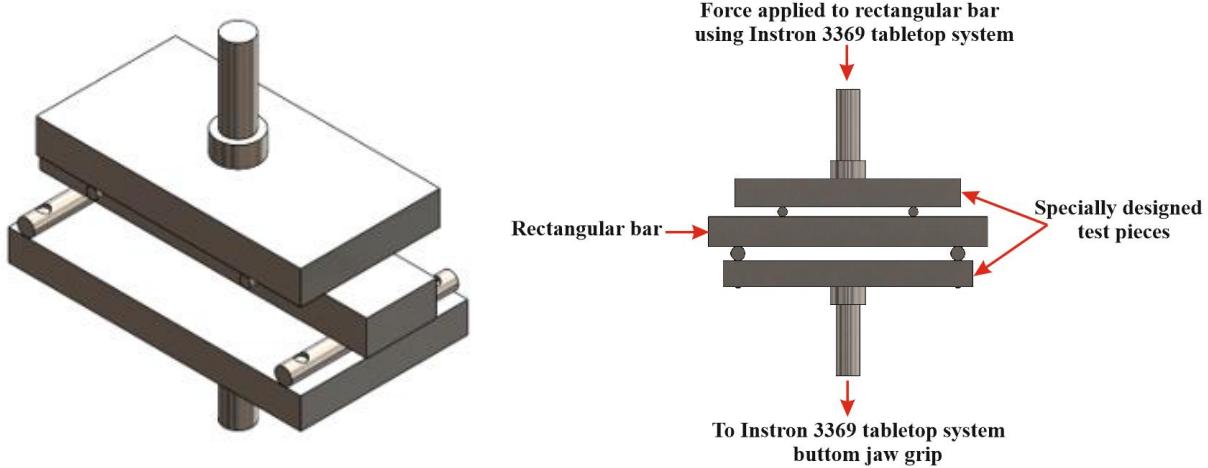
Figure 3.35: Vertical/Normal force calibration on the Twin disc rig

For best sensitivity results, full bridge configuration was installed centrally on the rectangular bar (See Figure 3.36).
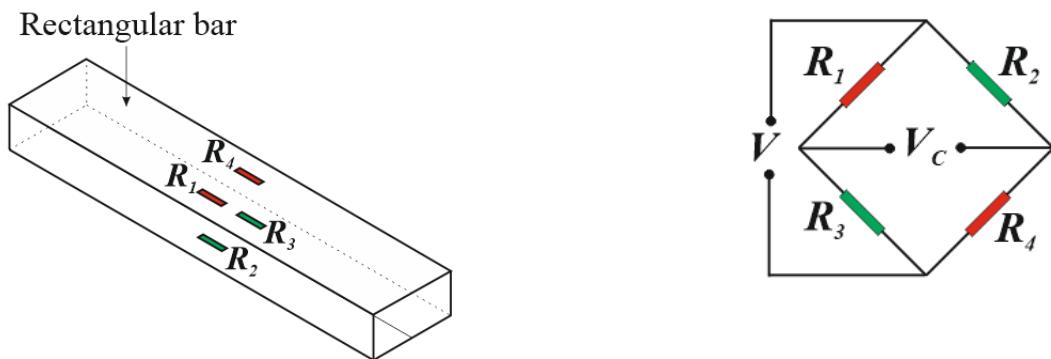
Figure 3.36: Strain gauge layout for measurement of vertical/normal force

Figure 3.37 shows the plot of the voltage versus the normal force/load:
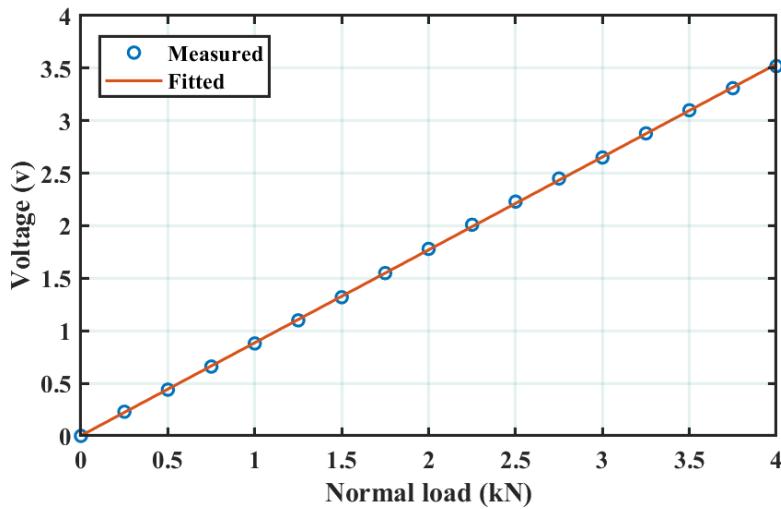
Figure 3.37: Vertical/normal force calibration results

The sensitivity of the full bridge configuration from Figure 3.34 was obtained as 0.89V/kN. The results obtained show that the normal force is directly proportional to the voltage obtained from the full bridge configuration.

Figure 3.38 shows the location of the four-point bending mechanism on the twin disc rig. The hydraulic hand operated pump in Figure 3.9 is used to apply normal force to the wheel roller. Assuming that the hydraulic force is given as F_H, then the normal force F_N can be determined using the principle of moments:

$$(F_H)(2L) = (F_N)(L) \tag{3.4}$$

$$F_N = 2F_H \tag{3.5}$$

This implies that the normal force is twice the hydraulic force obtained from the hydraulic hand operated pump. For a specified normal load of 2.5kN, the hydraulic force from the calibration tests must be equal to 1.25kN to satisfy equation (3.5).
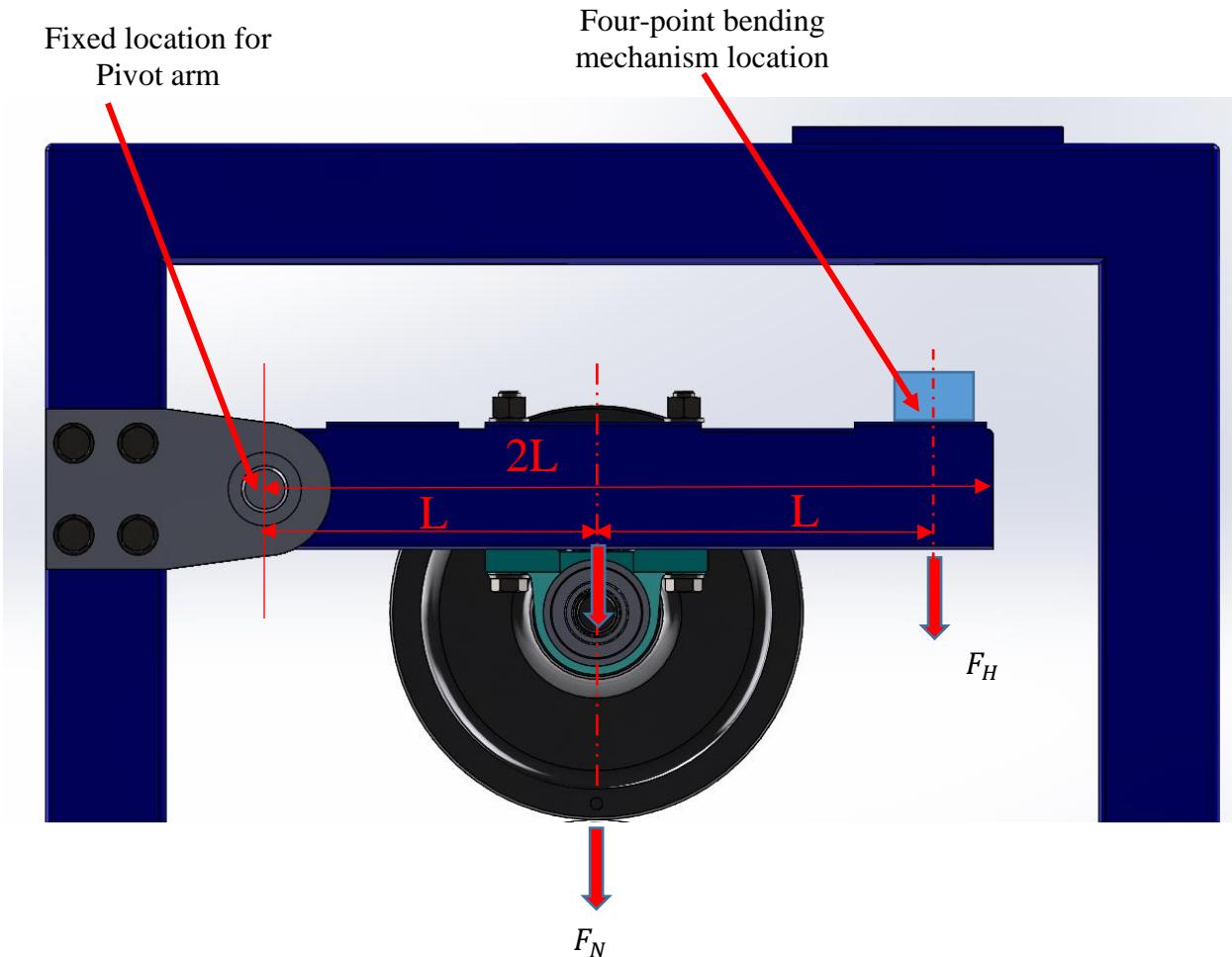
Figure 3.38: Hydraulic and normal force determination in the twin disc rig.

3.8   Experimental set-up for curve squeal measurement on Twin disc rig

Experimental measurement for curve squeal measurement on the twin disc rig was the next objective after the wheel-rail contact force calibrations. Figure 3.39 shows the experimental set-up for monitoring curve squeal.
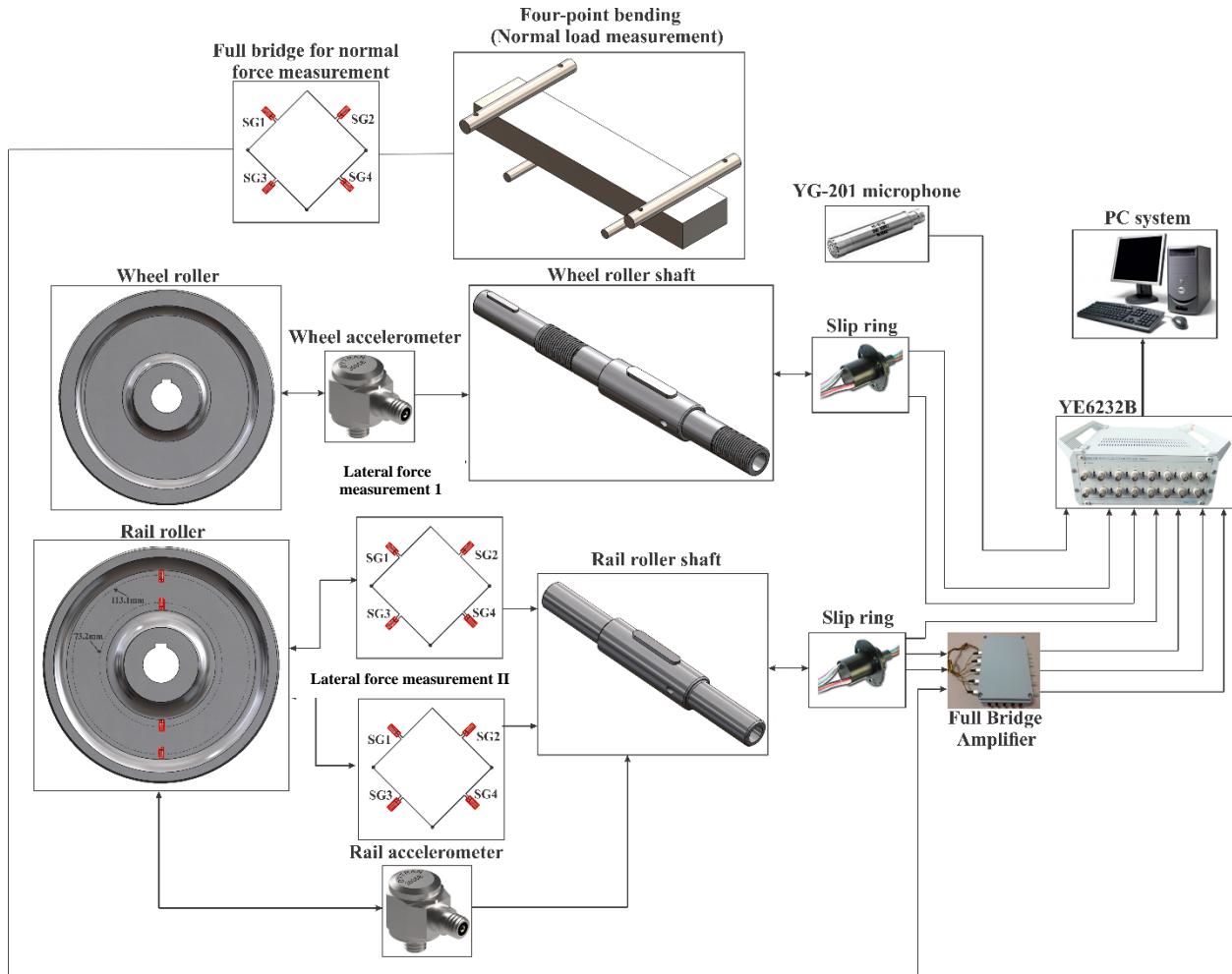
Figure 3.39: Experimental setup for curve squeal measurement on the Twin disc rig

Two full bridge circuits; lateral force measurement I and lateral force measurement II was connected through the slip ring installed on the rail roller shaft to the full bridge amplifier. The full bridge amplifier is used to amplify the voltage from bridge circuits. The amplified voltages using the calibrated results was connected to two channels of Sinocera YE6232B data acquisition system in other to measure the dynamic lateral force developed on the wheel-rail interface.

The full bridge configuration installed on the four-point bending mechanism was connected through the full bridge amplifier to the data acquisition system for measurement of vertical forces developed on the wheel-rail interface. The normal force 1.25kN was set on the hydraulic arm to yield the required normal force for all tests conducted on the twin disc rig (see previous section for details of the hydraulic and normal force). Dytran 3035B accelerometers were mounted on the wheel roller connected through the wheel's shaft to the slip ring and DAQ to measure the rollers

71

lateral acceleration. Curve squeal was measured using YG-201 microphone. The unit of squeal measurement is pascal. All measurements from the DAQ was sent to the PC system using for further data analysis such as conversion of pascals to decibels and so on. The sampling rate for all measurements was chosen to be 24 kHz to account for Nyquist sampling rate since the maximum modal frequencies do not exceed 9 kHz.

Digital hand held laser Tachometer was used to measure the wheel speed as the yaw angle is manually changed from central position (zero degrees) to the maximum yaw angle. At dry contact conditions the experiment was discontinued after 1.4 to 1.5 degrees because of the large tonal squeal noise and wear observed at the wheel and rail rollers. The average wheel speed was calculated from four sets of wheelset speeds. The average wheel speeds calculated are approximately 100RPM, 125RPM, 150RPM and 175RPM. For wet, FM1 and FM2 contact conditions, the yaw angles were extended up to 2 degrees. The average wheel roller speed was calculated using as approximately equal to the wheel speeds obtained for dry contact conditions.

Finally, before tests were carried out on the test rig, it was necessary to ensure that the rig complies with relevant health and safety standards. Health and safety regulation compliance was carried out to ensure that the rig is safe for experiments. Front and rear guards were installed to the test rig to minimize the risk of entrapment especially at high wheel and rail roller speeds. The rear guard was manufactured from a metal mesh that has a removal guard to enable observation of experiments conducted on the test rig. Figure 3.40 shows the installed front and rear guards for the test rig.
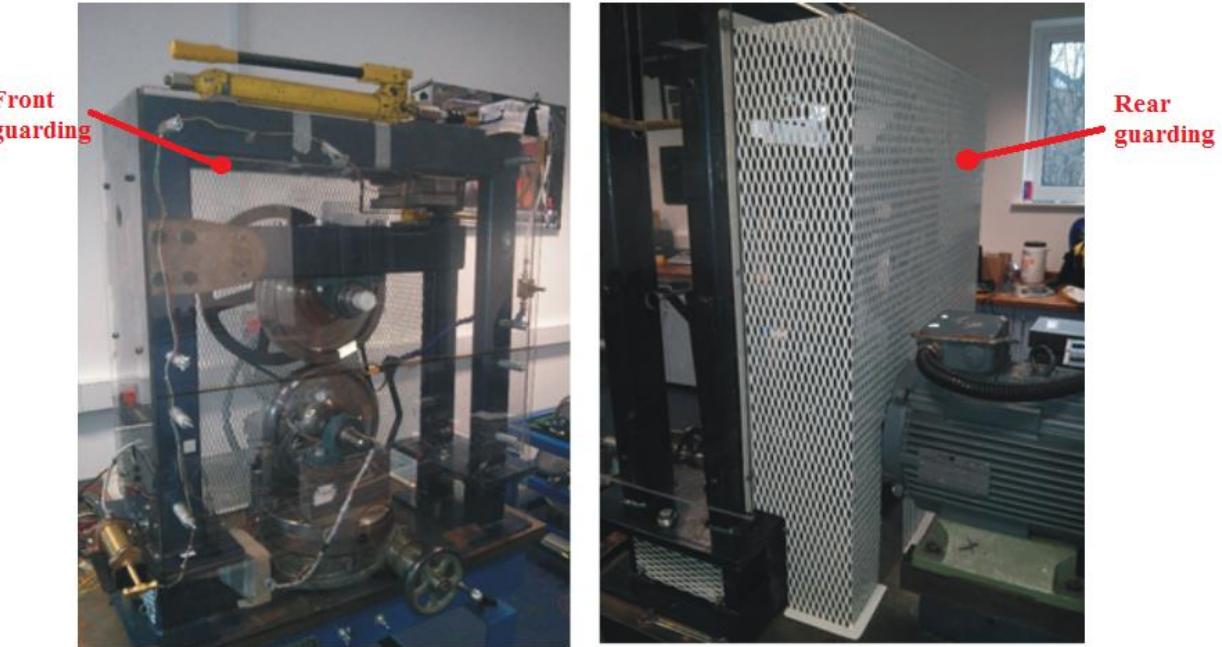
Figure 3.40: Front and rear guard for the test rig

3.8.1 Application of Friction Modifiers on the rollers for curve squeal mitigation

Two different friction modifiers with distinctive chemical properties was used for the experiments on the test rig. They include:

(1) **Friction modifier 1 (FM1)**: This kind of friction modifier contains solids suspended in a water-based solution. The watery solution is designed to evaporate leaving the solid part on the rollers. Therefore, for all tests conducted on the test rig, this friction modifier was applied on the dry rollers for about 3 minutes before testing to allow the evaporation of the water component. FM1 quantity (0.5ml) was applied to the two rollers. This quantity ensured that the rollers was lubricated for the entire experiment duration.

(2) **Friction modifier 2 (FM2):** This type of friction modifier has thick soluble properties. It is greasy and therefore does not have drying time. Tests was therefore conducted immediately after application. For comparison between Friction modifier 1, 0.5ml of FM2 was applied using a syringe to both roller surfaces. Immediately after the application the rollers were rotated by hand to evenly distribute the FM2 on the surface.

For example, Figure 3.41 shows the Friction modifier observed on the wheel anr rail roller surfaces after experiments, the friction modifiers applied on the wheel and rail rollers

73

was degreased using abrasive sand paper to return the roller back to the original dry contact conditions.

Friction modifier 2 applied on the wheel and rail surfaces
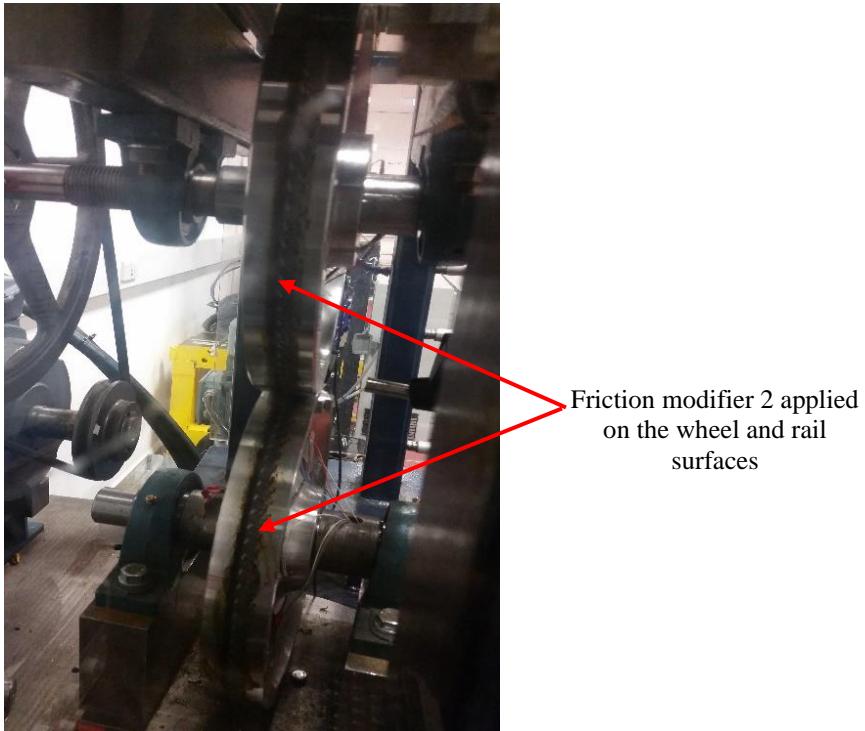
Figure 3.41: Friction modifiers applied to the roller surfaces

3.8.2 Water application on the rollers for curve squeal mitigation

Applying water to the rail roller is required to simulate wet conditions on the rail, which is prevalent in most railway networks in the UK. The rail roller was chosen as the main part for application of water since it represented the rail of the wheel-rail interface (WRI) in a typical UK rail network. It was required that the constructed water applicator provide steady water flow to the rail roller while the test rig tests was conducted. The water applicator consists of a cranked bracket firmly attached to the test rig-rotating table. A nozzle and a flexible hose targeted at the surface of the rail roller was inserted into the cranked bracket. A small reservoir mounted on the test rig top was connected to the flexible hose. This allowed the variable drip-feed mechanism at a steady water flow rate to be applied through the flexible hose to the roller. The applicator is shown in Figure 3.42.
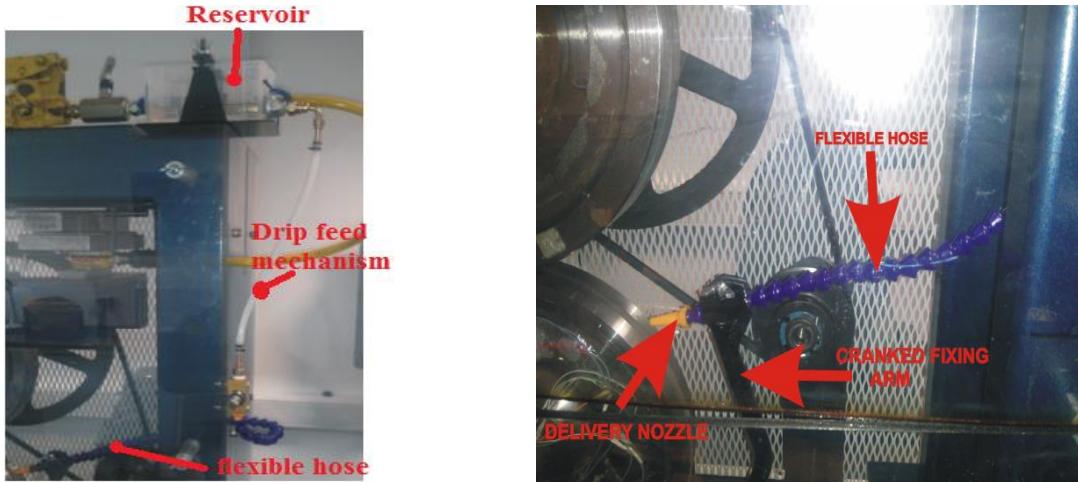
Figure 3.42: Water application system on the twin disc rig

3.8.3   Experimental procedures for the Twin disc rig

The experimental procedures conducted on the twin disc rig can be summarized in the following table

Table 3.10: Experimental parameters for the test rig

Parameters	Measurement range	Equipment resolution
Dry contact measurement	0º – 1.5º	0.1º
Normal load	2.5 kN	-
FM application (FM1 and FM2)	0º – 2º (0.5 ml was applied for each Friction modifier)	0.05º
Water application	0º – 2º (Rate 0.25 – 0.6 ml/min) 0.4ml/min was used for all tests	0.1º

Friction modifiers was applied on the wheel and rail roller surfaces using a syringe. After the application of the friction modifiers, the wheel and rail rollers were rotated by hand to distribute the modifiers on the rollers. Then the friction modifiers was degreased from the rollers using 600 grit emery paper. The specified normal load (2.5kN) was applied to the rollers and test rig was run for about 5 minutes at central position (0 degrees) to ensure that every trace of friction modifier is degreased from the rollers surface.

Summary of the process conducted on the Twin disc rig include:

(a)   Hydraulic jacking mechanism was used to apply the desired load to the rollers.

(b)   The wheel and rail roller were aligned together in a straight position.

(c)   Before any tests was recorded using the data acquisition system, the test rig was started and allowed to run for approximately one minute at 0° yaw angle. This was to ensure that the rig was ready to take measurements.

(d)   Preliminary tests were conducted to determine the desired wheel roller speed and load suitable for monitoring curve squeal on the test rig. These tests were required to ensure reliable, consistent and repeatable results on the test rig. These tests were conducted in dry contact conditions without the influence of water of friction modifiers.

(e)   For water application on the roller surfaces, a steady flow rate of 0.4 ml/min was used for all speeds and all tests. The reason for this choice was that the lowest flow rate (0.25ml/min) possible using the water application system and the maximum flow rate (0.6 ml/min) did not influence the results as the yaw angle of the rollers was increased from zero degrees to 2 degrees.

The two preliminary tests conducted include the effect of varying the normal load on curve squeal and the effect of varying the speed on curve squeal. The test results showed that the normal load influences the occurrence of curve squeal. According to (Hsu et al., 2007) 2.2kN is sufficient to conduct curve squeal experiments on the test rig to replicate real track scenarios. In this work, the wheel and rail profiles were subjected to normal force ranging from 1 kN to 3 kN in 0.5 kN increments. The rollers were aligned together in a central position and the yaw angle was adjusted in 0.1 degrees increments until curve squeal occurs. At normal loads, below 2.5 kN, no curve squeal was heard for yaw angles up to 1.5 degrees. For normal loads greater than 2.5 kN, curve squeal was observed at certain yaw angles. At 3 kN heavy wear on the wheel and rail rollers was observed at the wheel-rail interface with debris falling on Twin disc rig sides. It was also observed that curve squeal occurred at yaw angles as low as 0.2 degrees. In research conducted in literature, must wheels experience curve squeal at angles greater than 0.2 degrees. Therefore, 2.5 kN was chosen at optimal normal load sufficient to generate curve squeal close to what is obtainable in literature. After the determination of the normal load required for measurements, the wheel and rail profiles were re-grinded to ensure that new profiles devoid of wear are used to commence experiments on the Twin disc rig.

Figure 3.43 shows the flow chart for the experimental procedure conducted on the Twin disc rig.
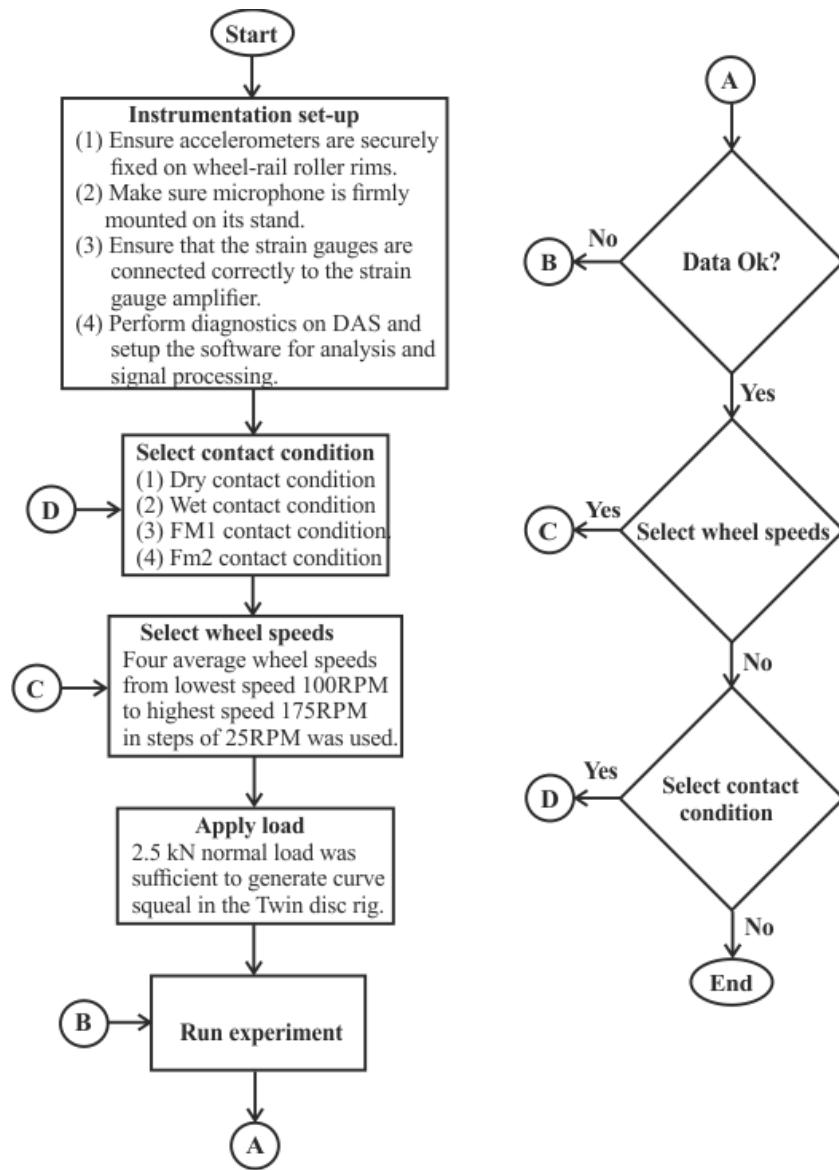
Figure 3.43: Flow chart experiments

The experiment carried out on the twin disc rig was selected carefully to address the main objectives of this research work. The steps chosen was used to reduce errors in measurement. At the start of experiment, the rollers were aligned in central position using the rotary spindle. The accelerometers, microphones and strain gauges were visually inspected to ensure that they are correctly installed for measurements. The next step was to set the wheel roller speed to around 100RPM. This was used as the lowest speed for which the twin disc rig can operate. The next step was to set the normal load to 2.5kN. The sampling frequency was chosen to be over twice the maximum frequency range of the wheel and rail roller natural frequencies set at around 9kHz. The

next step was to select the contact conditions for the set wheel roller speed. The tests were carried out up until the last average wheel speed (175RPM) for the specified contact condition. For each speed, the yaw angle was adjusted from zero degrees up until about 1.5 degrees. Measurements for each yaw angle was taken for 5 seconds. Constraints on the maximum yaw angle was put in place to reduce the amount of wear on the wheel rail surfaces and to provide repeatability of measurements. The highest speed was the maximum speed that can be run to obtain good results from the slip rings since they are limited to operate at about 250RPM in theory. After the dry contact condition measurements was conducted, the wheel-rail contact surfaces were cleaned for any debris and the next contact condition was applied. Experiments were repeated until all measurement results have been obtained.

3.8.4   Initial measurement results from the microphone

In condition monitoring, it is important to obtain baseline measurements that can be used to provide useful insight into the performance of the system at a glance. These measurements are best obtained for new wheel-rail profiles that are not worn to provide benchmark for other measurements on the twin disc rig. Figure 3.44 shows one of the measurements collected from the microphone located 50 mm away from the wheel-rail contact. The recording was done at wheel rolling speed set at 100RPM for two different yaw angles. The first yaw angle is at zero degrees (no curve squeal) while the second yaw angle is at 1.2 degrees (curve squeal occurrence). The results show that for the baseline time domain data at zero degrees yaw angle, the sound magnitude is significantly reduced compared to the sound magnitude at 1.2 degrees. At 1.2 degrees yaw angle, bursts of energy that occurs periodically in the time frame is observed. The periodic bursts of sound energy represent the revolution of the wheel roller. The bursts are distinct as a result of reduction in wheel roller speed. As the yaw angle increases, excessive load on the three-phase induction motor as a result of the excessive friction and vibration in the wheel-rail contact is observed. The causes the wheel roller speed to reduce as the yaw angle increases.
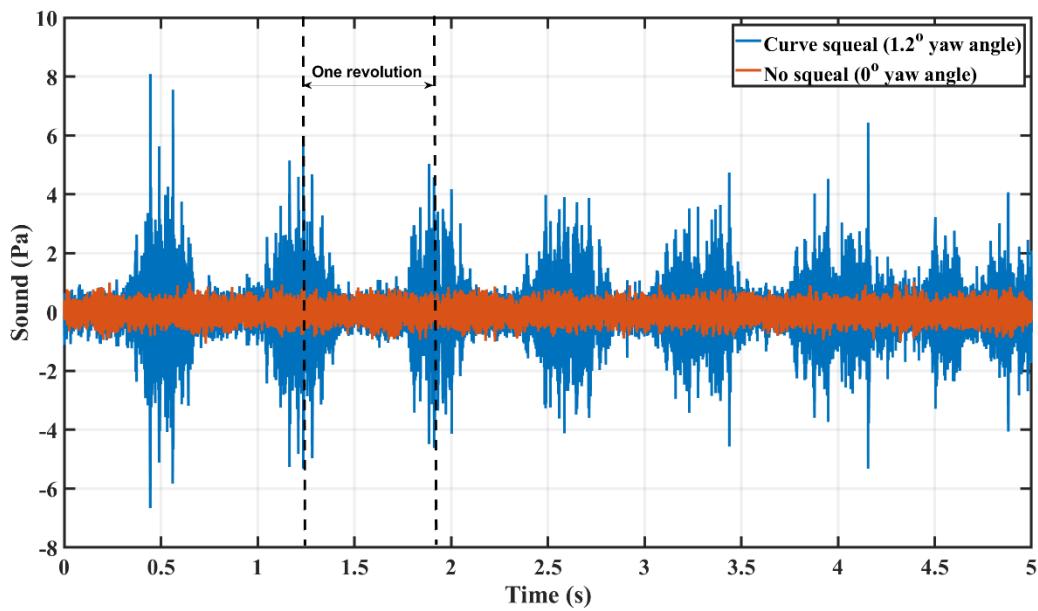
Figure 3.44: Microphone data for the system running at average wheel speed of 100RPM at 2.5kN load in dry contact conditions.

Since the twin disc rig is an open loop system, the three-phase induction motor driving the pulley system did not maintain constant wheel speed as the yaw angle increases. However, the focus of this study is not on the wheel-speed, but rather on the detection and mitigation of curve squeal. The influence of wheel speed and rotation on curve squeal was observed to be of very little effect in studies conducted on twin disc rig by (Meehan and Liu, 2018). According to their study, change in wheel speed did not affect the natural frequency that was excited on the wheel roller responsible for curve squeal.

Figure 3.45 shows the power spectrum of the time domain data for frequencies up to 9kHz for zero yaw angle.
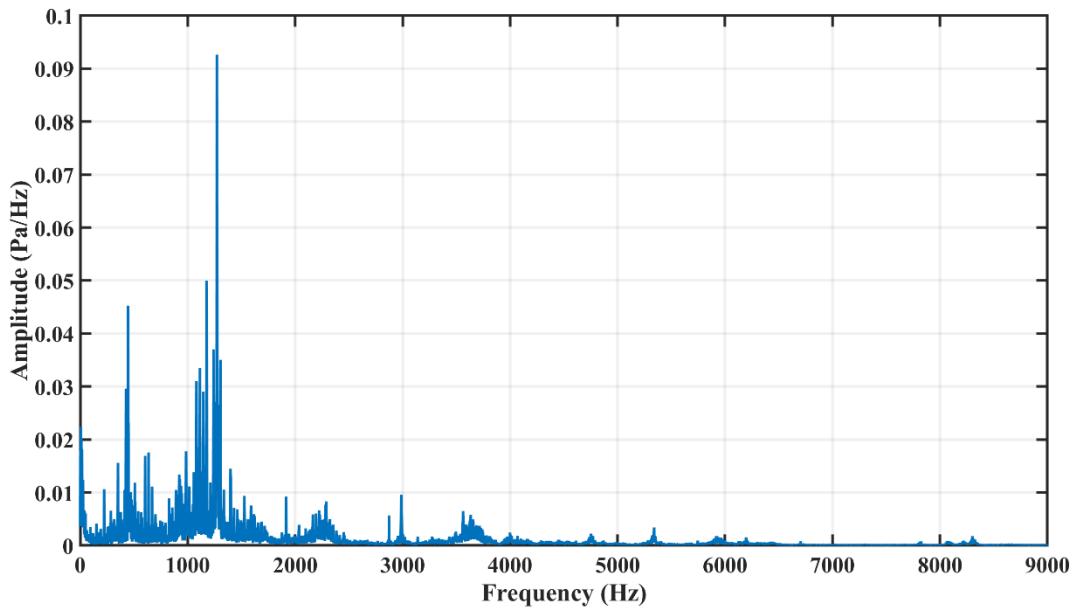
Figure 3.45: Power spectrum from the microphone for the system running at average wheel speed of 100RPM at zero degrees yaw angle.

The results show the maximum power spectral energy occurs between 1kHz and 2kHz. Taking a detailed look at this frequency range from 1kHz to 1.5kHz, the following is shown in Figure 3.46.
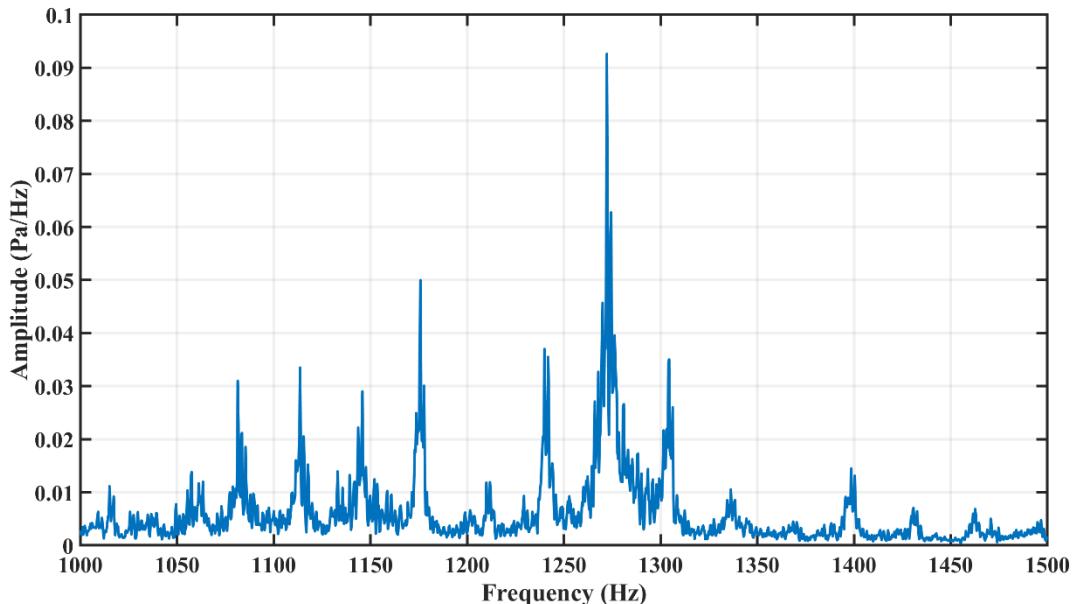
Figure 3.46: Zoomed in power spectrum from the microphone for the system running at average wheel speed of 100RPM at zero degrees yaw angle.

80

The results illustrate that the dominant frequency is around 1270 Hz. This frequency is not seen in the natural frequency results obtained for the wheel and rail rollers. A strong possibility is that this frequency possible represents the rolling contact noise generated as a result of interaction between the wheel and the rail. Further details on the signal processing of the microphone data would be discussed in detail in the next chapter.
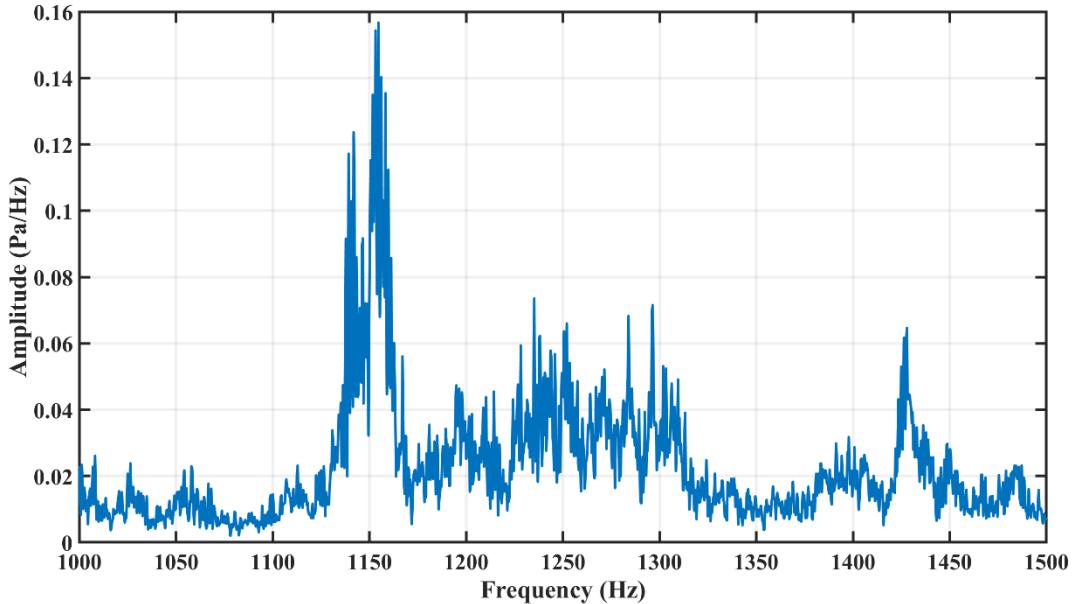
Figure 3.47: Zoomed in power spectrum from the microphone for the system running at average wheel speed of 100RPM at 1.2 degrees yaw angle.

Figure 3.47 shows the zoomed in section of the power spectrum when squeal occurs at 1.2 degrees. The rolling contact noise around 1250 Hz has been suppressed by the dominant curve squeal frequency centred around 1150 Hz. This frequency is about 55 Hz more than the second nodal diameter and natural frequency of the wheel roller. A quick observation of the power spectrum shows that the wheel roller is responsible for curve squeal on the twin disc rig. The peak around 1400 Hz to 1450 Hz band is the second nodal diameter and natural frequency of the rail roller.

3.8.2 Initial accelerometer measurements.

In condition monitoring, it is sometimes imperative that an initial investigation into the nature of the acquired signals be carried out to ensure that they are devoid of noise and the measurements

are correctly taken. The first five seconds of the baseline measurements for the wheel and rail accelerometers at central position (zero degrees yaw angle) is shown in Figure 3.48.
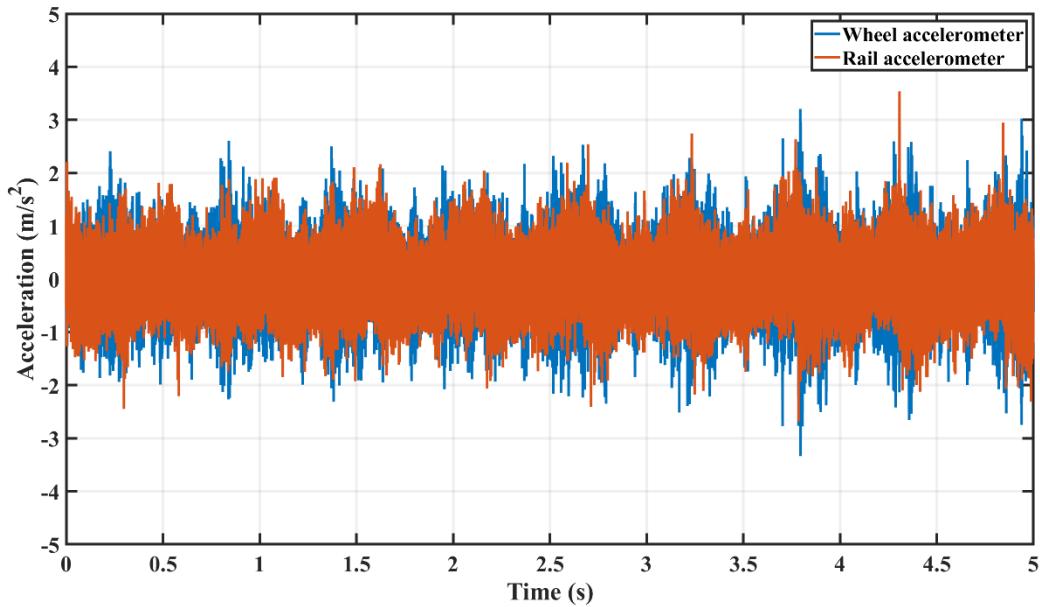
Figure 3.48: Time domain data for the wheel and rail accelerometer at central position

Hardly any difference can be observed between the two signals. Although there are some peaks in the data, it is difficult to tell the performance of the wheel and rail roller with this measurement.
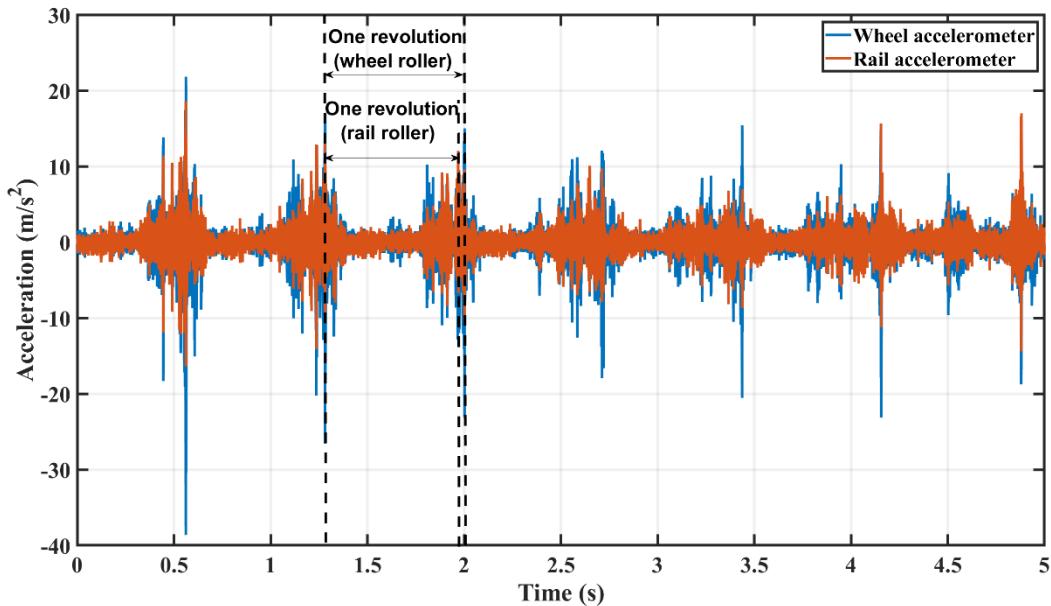
Figure 3.49: Time domain data for the wheel and rail accelerometer at 1.2^O yaw angle

Figure 3.49 shows the time domain data of the wheel and rail accelerometer at 1.2 degrees yaw angle. Similar to the results obtained from microphone data, it can be observed that the set wheel speed (100RPM) at baseline for the experiment has significantly dropped. The wheel and rail rotations are clearly visible. These results indicate that an increase in the yaw angle results in excessive load on the three-phase motor. This leads to a decrease in the speed of the driver pulley connected to the wheel roller shaft and a subsequent decrease in speed of the rail roller. The excessive load is possible due to the increase in the lateral forces at the wheel-rail interface resulting in increased adhesion coefficient. Since no closed loop system is actively installed in place to ensure that the wheel and rail roller speeds are constant regardless of the increased yaw angle, the twin disc rig operates as an open loop system. This is expected for the current design of the test rig.

Figure 3.50 shows the power spectrum obtained from the wheel and rail accelerometers.
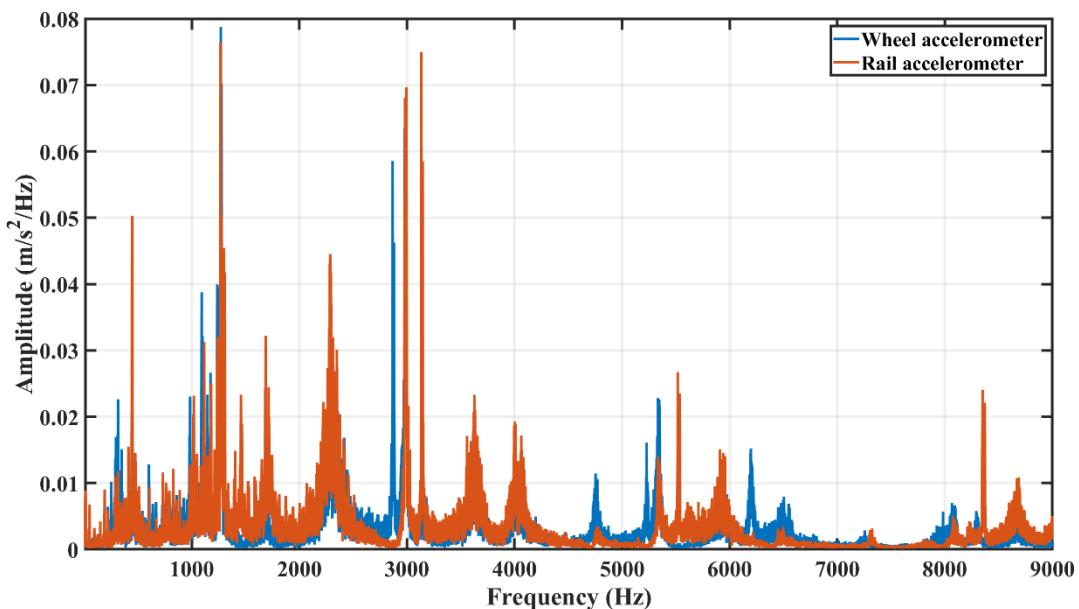
Figure 3.50: Power spectrum from the wheel and rail accelerometer for the system running at average wheel speed of 100RPM at central position.

Maximum peak of the power spectrum plots is observed in the frequency range of 1000 Hz to 2000 Hz. It is not clear what this peak is. However, some of the peaks above the 2000Hz represent the natural frequencies of the wheel and rail roller. Since the focus is on curve squeal condition monitoring on the twin disc rig, emphasis would be given to the maximum peak and the surround

frequencies that result in curve squeal. A section of the power spectrum plot from 1000Hz to 1500Hz is shown in Figure 3.51.
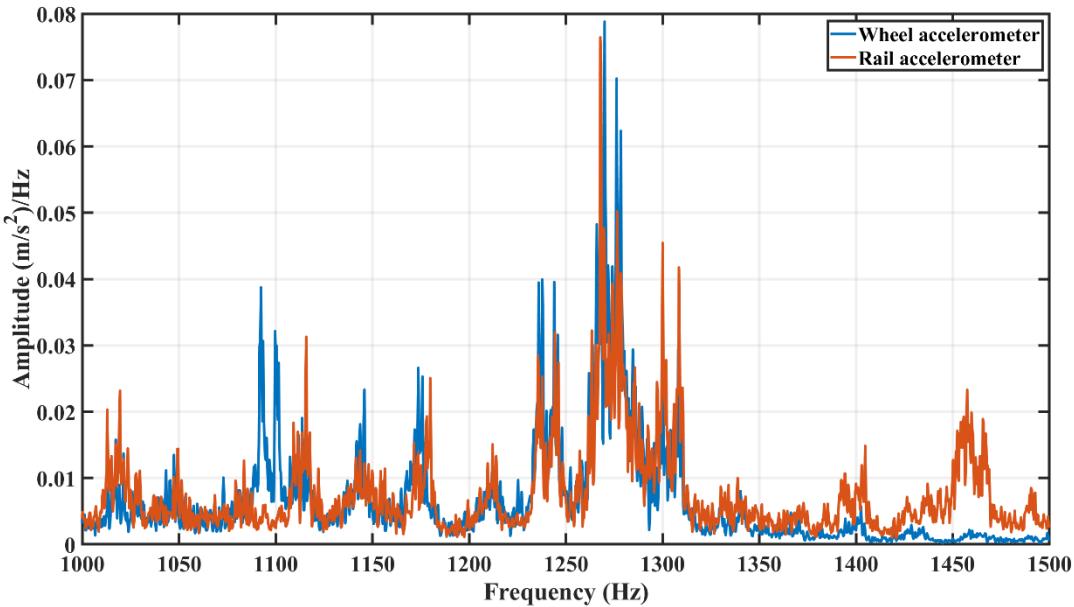
Figure 3.51: Power spectrum of the wheel and rail accelerometer data for the system running at average wheel speed of 100RPM at central position.

The result shows that the maximum peak for the wheel and the rail roller is centred around 1270Hz. This result correlate with the maximum peak obtained from the microphone data. It can therefore be inferred from the results that this is excitation frequency is as a result of the vibration of the wheel and rail data in central position when no yaw angle is applied to the rail roller. This results in rolling contact noise which was heard when the experiments were taken. This frequency has been observed to suppress the natural frequencies of the wheel and rail roller for this frequency range. The peaks around 1100 Hz and 1450 Hz indicate the second nodal diameter and natural frequency of the wheel and rail roller respectively.

Figure 3.52 shows the section of the power spectrum plot of the wheel and rail accelerometer for the frequency band 1000Hz to 1500Hz at 1.2 degrees yaw angle. The results for the wheel and rail accelerometer show a sharp peak around 1150Hz. This definitely represents the curve squeal frequency. This excitation frequency is so dominant that it resonates from the wheel roller to the rail roller. The second nodal diameter and first natural frequency of the wheel roller around 1095 is therefore responsible for curve squeal. The shift of about 55 Hz from the natural frequency of the wheel roller to the around 1150Hz is probably due to the dynamics of the system.
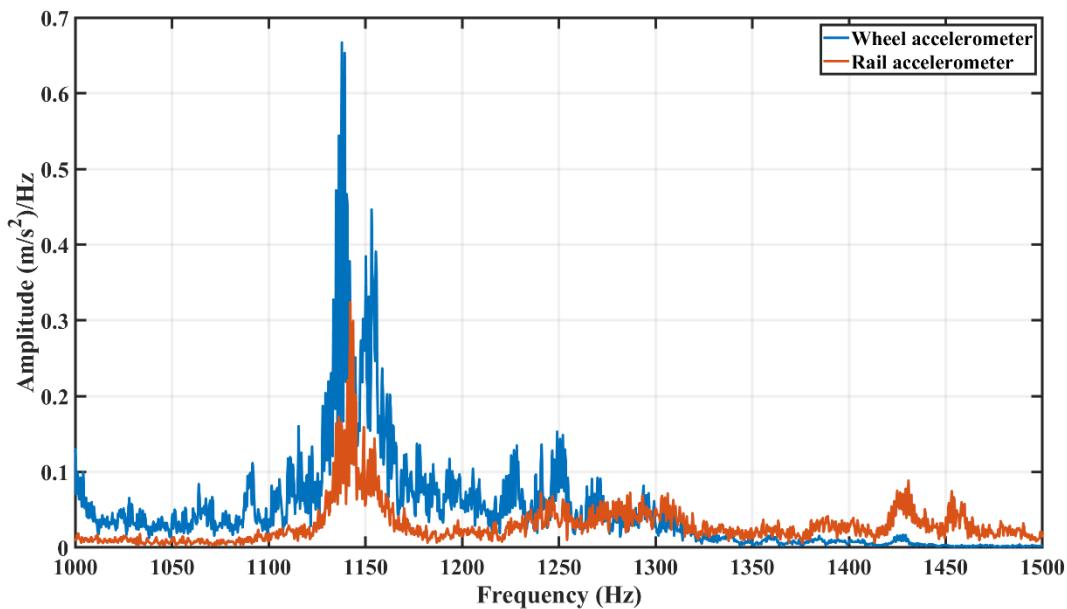
Figure 3.52: Zoomed in power spectrum of the wheel and rail roller data for the system running at average wheel speed of 100RPM at 1.2 degrees yaw angle.

3.9   Summary

This chapter presented a detailed study of the twin disc rig that would be used to investigate and validate the research objectives and aims. A detailed presentation of the instrumentation and measurement equipment has been discussed. There are 4 different contact conditions that would be used in this research to understand what happens in curve squeal mitigation. The Instron 3369 table top system was used to calibrate the lateral and vertical/normal forces that are developed in the wheel-rail interface. The calculated slopes/gradients would be used in this research to obtain the tangential creep curves for various contact conditions and wheel speeds. The impact hammer test was carried out on the wheel and rail rollers to obtain the respective natural frequencies.

Finally, initial baseline measurements using wheel/rail accelerometer and microphone data was carried out to provide useful insight to the performance of the system. The results obtained showed that curve squeal is a strong tonal frequency that resonates from the wheel roller to the rail roller and probably to all structural components of the twin disc rig. A flow chart that detailed the experimental procedure carried out in the twin disc rig for data acquisition was presented.

Chapter 4: Development of curve squeal model for the Twin disc rig

The main aim of this chapter is to develop a mathematical model for curve squeal on the test rig. This model will help in the comprehension of what transpires during the development of curve squeal on the test rig. The test rig comprises of the wheel-rail roller and other components. However, for this case, only the wheel and rail roller would be considered in the model. The equations representing the lateral vibration of the wheel and rail roller are derived from first principles. The inputs to the developed model are the lateral forces, yaw angle and the lateral creepages. The adhesion coefficient functions for the dry, wet, FM1 and FM2 contact conditions are obtained from experimental measurements of the lateral force and curve fitted using Modified Fastsim algorithm. The lateral stiffness and damping coefficient of the wheel and rail roller are obtained from the impact hammer results. The curve squeal vibration amplitudes calculated are then used to determine the squeal noise amplitude in decibels.

4.1 Introduction

An extensive literature review on several curve squeal models have been discussed in Chapter 2. Two main modelling approaches were identified; frequency domain solution obtained by linearization of the wheel-rail contact equations, and time domain solution of the non-linear wheel-rail contact equations. However, curve squeal is a non-linear phenomenon involving the wheel-rail contact dynamics and contact mechanics. The frequency domain solution only determines the stability of the model and its frequency. It does not take into consideration the amplitudes of vibration and the curve squeal, which is characteristic of time domain models. Therefore, based on the limitations of the frequency domain model, this chapter presents a simplified and efficient time-domain curve squeal model for the test rig. This model would integrate the vibration modes of the wheel and rail roller responsible for curve squeal, wheel-rail contact mechanics and curving to predict theoretically the amplitude of the wheel vibration velocity responsible for curve squeal. The lateral stiffness and damping coefficients of the wheel associated with curve squeal would be obtained by curve fitting the impact hammer tests. The rolling contact model and tangential contact model using Fastsim algorithm and adhesion (friction) coefficient model would be used to compute the latera creep forces developed in the wheel-rail roller contact. Finally, the vibration amplitude of curve squeal would then be calculated from the equations of motion of the wheel and then the sound radiation emanating from the wheel would be estimated to compute the curve squeal amplitude in decibels.

The following steps would be used to model and simulate curve squeal on the twin disc rig:

(2) Determine the shape and size of the wheel-rail contact depending on the normal force and yaw angle using Hertz contact theory.

(3) Estimate the lateral creep force developed in the wheel-rail contact using adapted Fastsim algorithm.

(4) Calculate the vibration velocity amplitude of curve squeal from the wheel and then use values to determine the curve squeal amplitude in decibels.

4.2 Hertz contact theory (HCT)

Hertz contact theory is the most extensively used mathematical theory in contact mechanics. It takes into consideration the shape of the contacting bodies and the surrounding contact area. HCT is widely used in wheel-rail contact problems to resolve the normal contact forces, size and shape

of the contact area and the local deformation because of the normal applied load. (Shabana et al., 2004), (Yan and Fischer, 2000).

The summarized assumptions of HCT are stated as follows:

(1)   The contact area is very small compared with the lateral and longitudinal radius of the curvature of the contact surfaces.

(2)   The deformations formed because of the applied normal force are considered elastic.

(3)   The contacting surfaces are assumed frictionless, thus resulting in independent analysis of the tangential and the normal contact problem.

(4)   The contacting surfaces are assumed smooth without surface roughness.

(5)   The contacting surfaces are non-conformal and continuous. A contact is non-conformal if the contacting bodies meet at a point initially and there is no interpenetration of the two surfaces at no applied load.

(6)   The traction distributions and contact pressures are ellipsoidal.

4.2.1   Application of Hertz Contact Theory to the test rig

HCT was applied to the test rig to determine the shape and size of the contact area formed by the wheel and rail roller. The HCT developed for the test rig would take into consideration the effect of yaw angle applied manually by the rotary table and the normal applied load to the wheel-rail interface. The radius of curvature of the wheel and the rail roller (R_{x1}, $Rx2$, R_{y1}, and R_{y2}) is considered as displayed in Figure 4.1 where:

R_{x1} is the wheel roller radius in the longitudinal (x-axis) direction (155 mm)

R_{x2} is the rail roller radius in the longitudinal (x-axis) direction (145 mm)

R_{y1} is the wheel roller radius in the lateral (y-axis) direction (∞)

R_{y1} is the rail roller radius in the longitudinal (x-axis) direction (100 mm)

Since the applied normal load range for the twin disc rig (0 – 4 KN), and the wheel roller does not have flanges as typical railway wheels do, Hertz contact theory was deemed fit for solving the normal contact problem and would be used throughout this thesis.
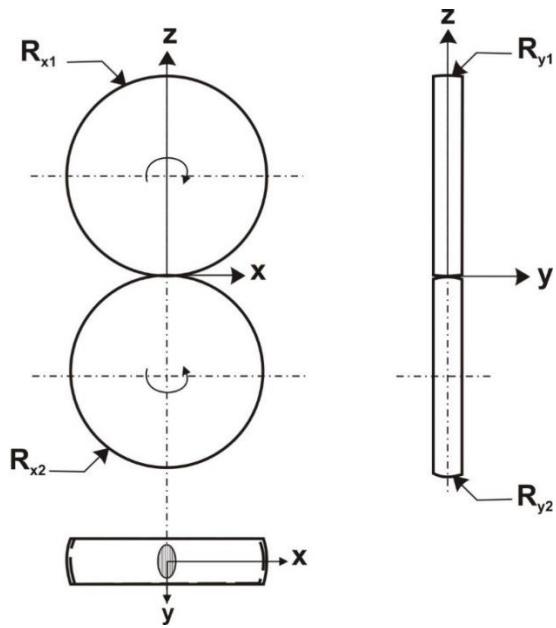
Figure 4.1: Wheel and rail roller geometry showing the principle radius of curvatures and the contact area

Figure 4.2 shows the wheel and roller geometry with the principal radii of curvature in the rolling direction (x) and lateral direction (y) and the inclusion of yaw angle.
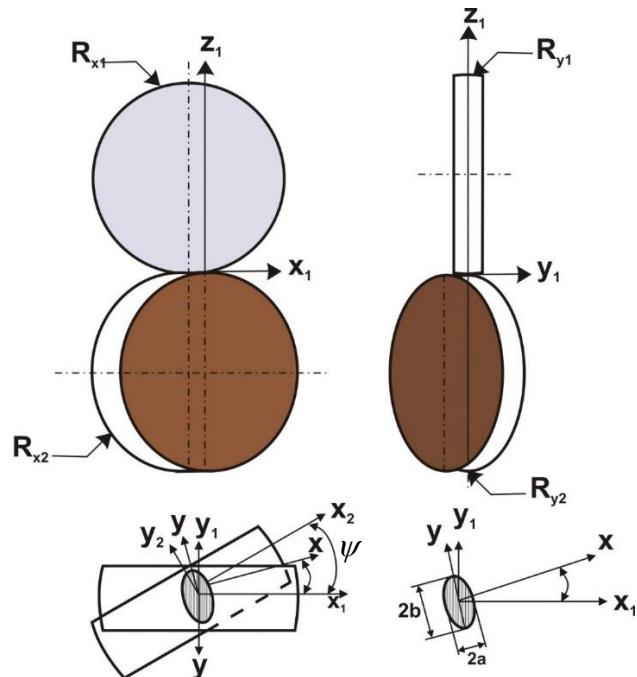
Figure 4.2: Wheel and rail roller with the yaw angle adjusted on the rail roller

Applying Hertz contact theory, the required inputs are the radii of curvature already stated, the normal load F_N and the Young modulus of elasticity, E (Popovic, 2010).

Given that the yaw angle, $\psi = 0$ as is the case in Figure 4.1, the semi-axes of the contact patch ellipse, a and b can be expressed as:

$$a = a' \left(\frac{3F_N R}{E'}\right)^{1/3} \tag{4.1}$$

$$b = b' \left(\frac{3F_N R}{E'}\right)^{1/3} \tag{4.2}$$

where a' and b' are the approximate semi-axes of the contact area and can be expressed as:

$$a' \approx \gamma^{1/3} \left[\frac{2}{\pi} E(m)\right]^{1/3} \tag{4.3}$$

$$b' \approx \gamma^{-2/3} \left[\frac{2}{\pi} E(m)\right]^{1/3} \tag{4.4}$$

R is the resultant radius of curvature expressed as:

$$R = \frac{R_{x1} R_{y1} R_{x2} R_{y2}}{R_{x1} + R_{y1} + R_{x2} + R_{y2}} \tag{4.5}$$

F_N is the normal applied force and E' is the combined young modulus of elasticity. The indentation (δ) as a result of the normal applied force can be expressed as:

$$\delta = \delta' \left(\frac{9F_N{}^2}{8R(E')^2}\right)^{1/3} \tag{4.6}$$

Where δ' is the approximate indentation and can be expressed as:

$$\delta' \approx \gamma^{2/3} \left[\frac{2}{\pi} E(m)\right]^{-1/3} \left[\frac{2}{\pi} K(m)\right] \tag{4.7}$$

The maximum contact pressure (P_m) can be expressed as:

$$P_m = \frac{F_N}{\pi ab} \tag{4.8}$$

While the maximum Hertzian contact pressure can be defined as follows:

$$P_0 = \frac{3}{2} P_m \tag{4.9}$$

The elliptical integrals of the first kind $(E(m))$ and the elliptical integral of the second kind $(K(m))$ can be expressed as:

$$E(m) \approx \frac{\pi}{2}(1 - m)\left[1 + \frac{2m}{\pi(1 - m)} - \frac{1}{8} In(1 - m)\right] \tag{4.10}$$

$$K(m) \approx \frac{\pi}{2}(1-m)\left[1 + \frac{2m}{\pi(1-m)} In\left(\frac{4}{\sqrt{1-m}}\right) - \frac{1}{8}In(1-m)\right]$$ (4.11)

and

$$\gamma \approx \left[1 + \sqrt{\frac{In(16/u)}{2u}} - \sqrt{In(4)} + 0.16In(u)\right]^{-1}$$ (4.12)

m is the dimensionless constant that can be expressed as:

$$m = \sqrt{1-\gamma^2} \text{ and } \gamma = \frac{a}{b} \text{ for } a < b \ \gamma = \frac{b}{a} \text{ for } b > a$$ (4.13)

$$u = \frac{R_x}{R_y} \text{ for } 0 < u < 1$$ (4.14)

Note that γ is the ratio of the semi-axes contact lengths and u is the ratio of the radii of curvature in the longitudinal and lateral direction.

The principal radius of curvature R_x and R_y can be expressed as:

$$\frac{1}{R_x} = \frac{1}{R_{x1}} + \frac{1}{R_{x2}}, \qquad \frac{1}{R_y} = \frac{1}{R_{y1}} + \frac{1}{R_{y2}}$$ (4.15)

When the effect of yaw angle is considered, $\psi \neq 0$ as shown in Figure 4.2, the principal radius of curvature in equation 4.15 can be re-written as:

$$\frac{1}{R_x} = \frac{1}{2}\sum D - \sqrt{\Delta}$$
$$\frac{1}{R_y} = \frac{1}{2}\sum D + \sqrt{\Delta}$$ (4.16)

where;

$$\sum D = \frac{1}{R_{x1}} + \frac{1}{R_{y1}} + \frac{1}{R_{x2}} + \frac{1}{R_{y2}}$$ (4.17)

and

$$\Delta = H_1^2 + H_2^2 + 2H_1 H_2 \cos(2\psi)$$ (4.18)

where;

$$H_1 = \frac{1}{2}\left(\frac{1}{R_{x1}} - \frac{1}{R_{y1}}\right) \text{ and } H_2 = \frac{1}{2}\left(\frac{1}{R_{x2}} - \frac{1}{R_{y2}}\right)$$ (4.19)

where D is the summation of the radius of curvature for the wheel and rail rollers, and H_i is the half radius of curvature of the wheel and rail roller.

4.3 Finite element model (FEM) of the wheel-rail roller system

Having derived HCT equations for the test rig in the previous section, to validate further the elliptical shape is formed in the wheel-rail roller contact, FEM of the wheel and rail roller was designed and simulated. Geometrical modelling was implemented in a CAD environment (SolidWorks). The geometry was imported into Ansys Workbench. Significant amount of time is required for contact problems since they are non-linear. Taking into account that it would be required to carry out different simulations for varying normal load, only a sector of the rail and the whole wheel is considered for analysis to reduce computational time.

The wheel and rail are meshed using Multizone method in as shown in Figure 4.3. The two po
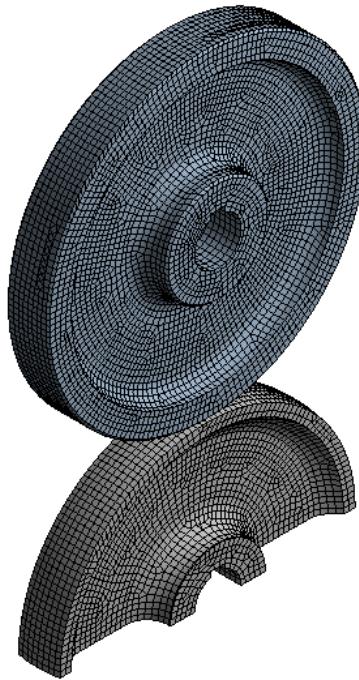
Figure 4.3: Finite element model of the wheel and rail roller

Mesh density in the contact area influences the solution accuracy (Srivastava et al., 2014). Therefore, to ensure greater accuracy of the contact solution, an area (10mm x 10mm) was selected and mesh density was increased such that the element size was 1mm (See Figure 4.4). The same was implemented on the wheel roller. Effects of rotation of the wheel was neglected for this study. The wheel and rail roller were assumed to have properties already specified in Table 3.1. The coefficient of friction of the wheel and rail was set to be 0.3. The base of the half rail was fixed to

prevent rigid body motion of the system. The FEM has a total of 875,543 elements and 232,241 nodes.
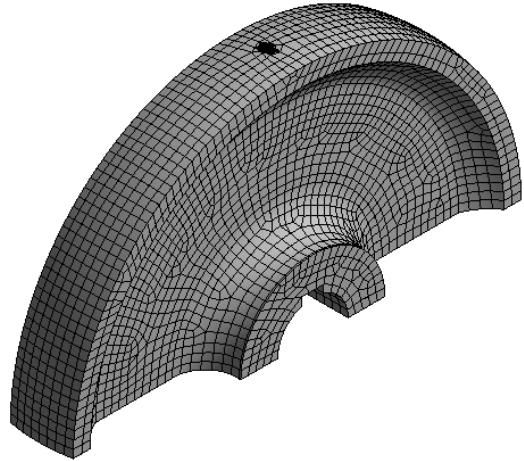
Figure 4.4: Section of the rail roller with mesh density concentrated on the contact area

Normal loads with steps of 500N up to 3000N was applied to the wheel roller to obtain the corresponding contact area. The contact area semi-axes and the normal contact pressure was extracted from the FEM model. For example, the result given that the normal load is 2500N is shown in Figure 4.5
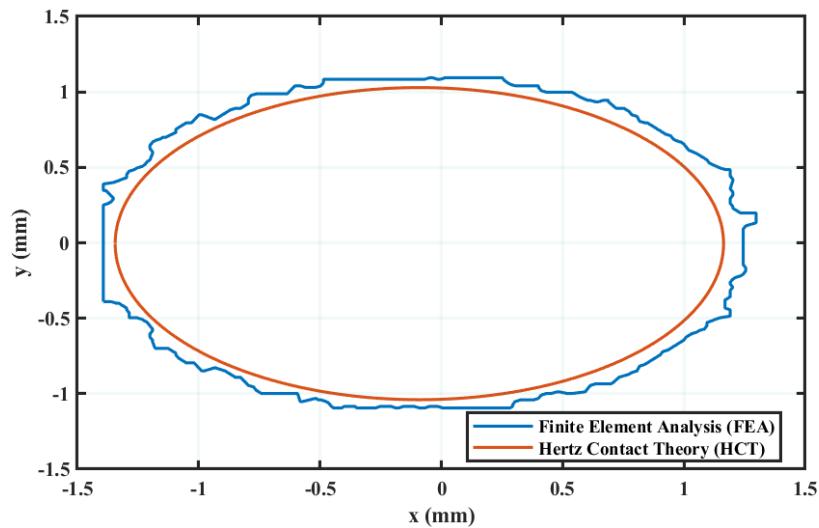
Figure 4.5: Contact area for normal applied load of 2500N – Comparison between HCT and Finite Element Analysis using Ansys workbench.

A noticeable increase in the contact area dimensions for the FEM compared to HCT is observed. The reason for the slight increase in contact area is based on the assumption of conformal contact for FEM methods. Despite the difference, both methods show good correlation which each other. Figure 4.6 shows the contact pressure in the rolling (x) and lateral (y) direction for the HCT and FEM models. It can be observed that the maximum contact pressure of the FEM model is greater that HCT. The reason for this is the fact that HCT assumes that the wheel-rail contact problem is a half space approximation while the FEM method assumes conformity of the wheel and rail profiles. These assumptions imply, that the FEM methods would always produce larger values of normal contact pressure and contact area.

(a)   (b)

(c)
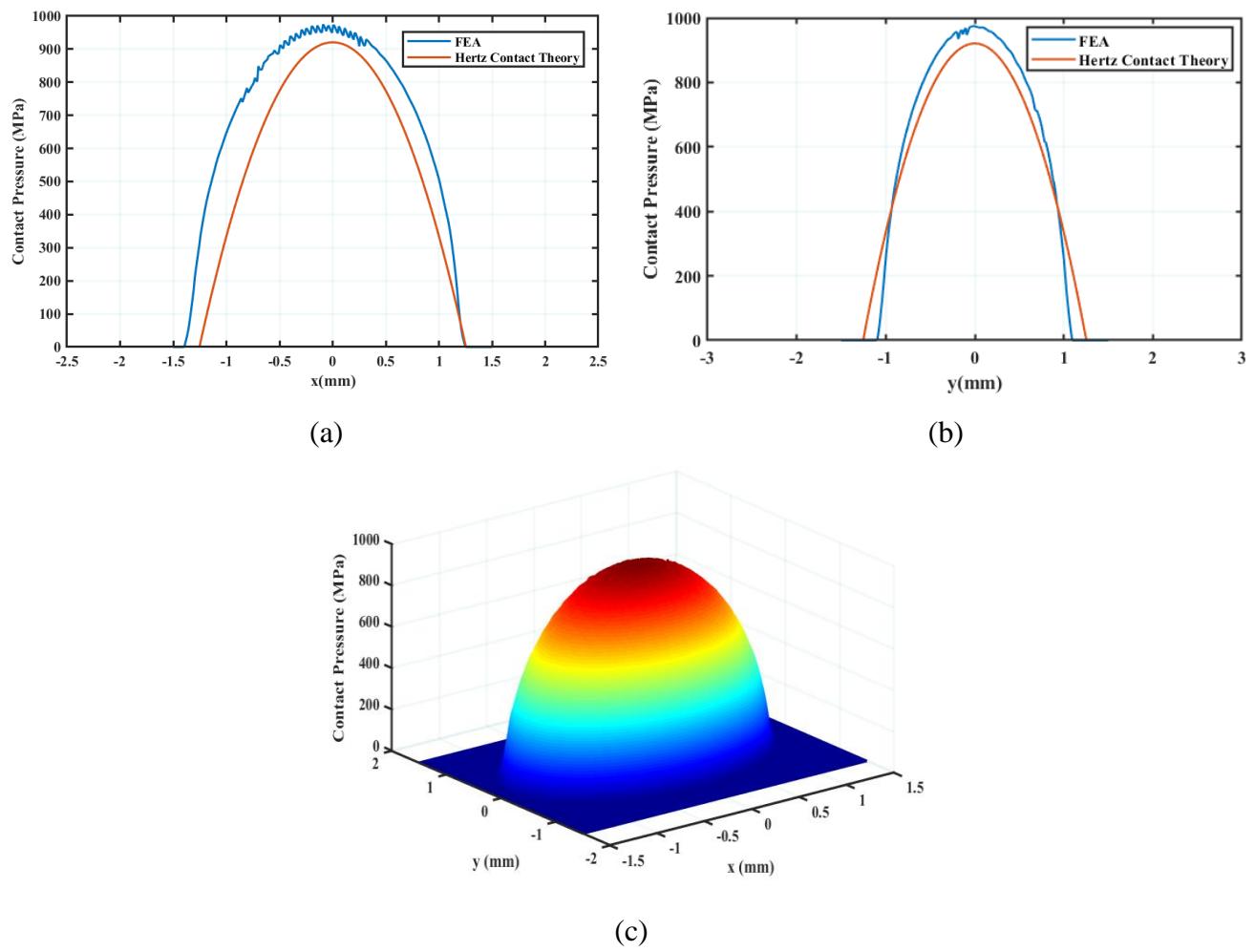
Figure 4.6: Normal contact pressure developed the contact area for normal applied load of 2500N (a) Lateral direction (b) Longitudinal direction (c) 3D plot of the contact pressure obtained from FEA.

Figure 4.7 shows the effect of normal force on the contact area and the normal contact pressure.

(a)

(b)
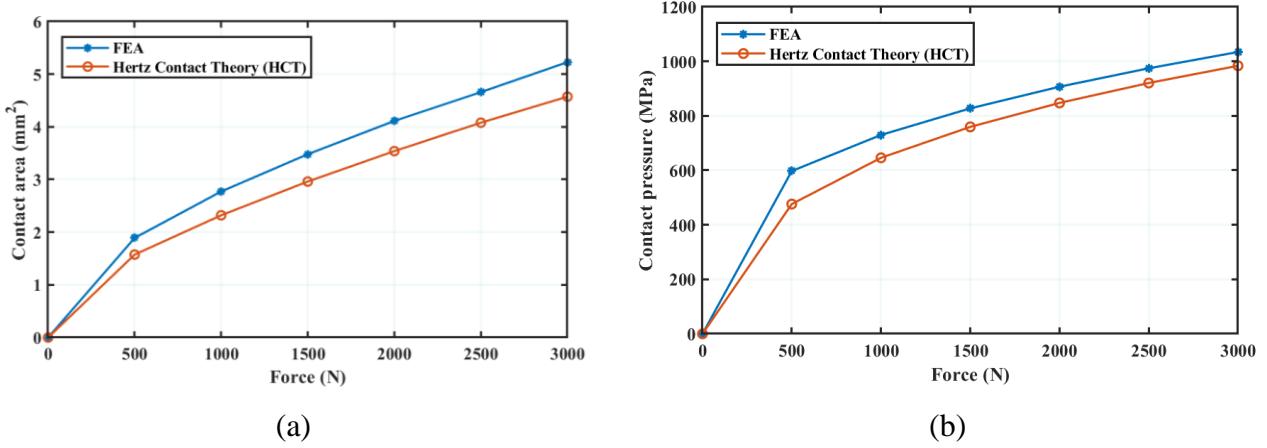
Figure 4.7: Effect of varying the normal applied force on the (a) Contact area and (b) Normal contact pressure

There is a positive correlation between the HCT and the FEM methods. As expected, the FEA method produces larger values of contact area and pressure as a result of the conformal contact assumed in the simulation. Having established the good correlation between HCT and FEM methods, the HCT method would be used to model and simulate curve squeal in the Twin disc rig. The Twin disc rig is designed to operate with loads up to 4000N. Several normal loads up to 2500N was tested to investigate which load is sufficient to generate curve squeal. Normal load 2500 N was chosen as appropriate in this study to produce curve squeal on the test rig. Loads below this value did not produce the required curve squeal as the yaw angle was increased. The chosen load was used therefore used to investigated curve squeal phenomenon on the twin disc rig.

4.4   Tangential contact model for curve squeal.

The computation of creep forces in multibody simulations is usually time-consuming and complex task to deal with. Creep force models that take into consideration large creepages has been developed and studied extensively in literature (Polach, 2005), (Spiryagin et al., 2013). To reduce computation time of creep forces especially for application in the test rig, it is imperative that a fast-simplified algorithm for rolling contact be applied. (Kalker, 1982) developed an algorithm called Fastsim. This algorithm is a fast-computational method that simplifies Kalker's variational theory for rolling contact. It accurately computes the creep forces generated at the contact area of the wheel-rail roller interface by dividing the contact region into different sub-area. It however,

has some disadvantages such that it does not permit creep force-creepage agreement for measurement results obtained from railway systems especially for high creepages.

A modified Fastsim algorithm proposed by (Spiryagin et al., 2013) would therefore be applied to the test rig to determine the creep forces and the creepages developed in the wheel-rail contact. This approach introduces the variable flexibility constant to cater for different adhesion coefficient conditions resulting from contact conditions such as water and friction modifiers.

It has been established in literature that lateral creepage leading to lateral creep forces is the dominant cause of curve squeal in railways (Thompson, 2009), (Liu and Meehan, 2016), (Meehan and Liu, 2018), (Monk-Steel and Thompson, 2003). Therefore, in the development of a model for curve squeal, only the lateral creepage and creep forces would be considered.

4.4.1 Tangential contact force model using the Modified Fastsim algorithm

The Modified Fastsim algorithm is based on the modification of Kalker's original Fastsim algorithm (Kalker, 1982) to take into consideration large creepages developed in low adhesion conditions on the wheel-rail interface. It assumes that the variable friction coefficient reduces with increasing slip velocity below the adhesion limit, thereby predicting negative or positive falling slop of the creep-creepage curve obtained from experimental measurements. It also assumes constant variable adhesion coefficient over the entire contact patch region. The dynamic friction coefficient can be expressed as:

$$\mu = \mu_s((1-A)e^{-Bw} + A) \tag{4.20}$$

Where μ_s is the static coefficient of friction, A is the ratio of the friction coefficient limit at infinity slip to the maximum friction coefficient μ_s, w is the slip velocity vector magnitude and B is the coefficient of exponential friction decrease, s/m.

The slip velocity dependent friction coefficient considers the vector sum of the longitudinal and lateral creepages while neglecting spin. It can be expressed as (Spiryagin et al., 2013):

$$w = V(v_x{}^2 + v_y{}^2) \tag{4.21}$$

where V is the linear speed of the train in m/s, v_x and v_y are the longitudinal and lateral creepages respectively. In the curve squeal model, longitudinal creepage is not considered to be a contributor to curve squeal (Pieringer, 2011), (Zenzerovic et al., 2015). It is therefore neglected in this work.

The factor k, known as the stiffness reduction factor is used to maintain slip ratio to adhesion ratio increase in the contact area. It can be expressed as follows:

$$k = k_0 \left(\beta + \frac{1}{1 - \sigma \varepsilon} \right) \tag{4.22}$$

where k_0 is Kalker's initial reduction factor value at creep values close to zero, β is the fraction of the initial Kalker's reduction factor at creep values tending to infinity, $0 \leq \beta \leq 2$, σ is the non-dimensional parameter concerned with reduction of the contact stiffness with increasing area of slip ($0 \leq \sigma$), ε is the tangential stress gradient in the distribution stress transformed to a hemisphere. The tangential stress gradient can also be expressed as:

$$\varepsilon = 0.25 v \left(\frac{G \pi a b k_0 C_{22}}{\mu F_N} \right) \tag{4.23}$$

where G is the modulus of rigidity, a and b are the semi-axis of the contact area in the lateral and longitudinal direction respectively, C_{22} is Kalker's lateral creep coefficient, F_N is the normal applied force, μ is the adhesion coefficient and v is the total creepage computed as the sum of the lateral and longitudinal creepages defined as ($\sqrt{v_x^2 + v_y^2}$). It is important to note that the influence of longitudinal creepages on curve squeal was investigated in detail by (A. D. Monk-Steel, 2006) using a scale test rig. The results obtained from the experiments concluded that longitudinal creepage has a minimal effect on curve squeal as compared to lateral creepage. Therefore, only lateral creepage would be used to model and monitor curve squeal on the test rig.

Finally, the flexibility constant L used by Kalker can be modified as follows:

$$L' = \frac{L}{k} \tag{4.24}$$

This model would be applied to fit lateral creep force measurement data obtained from experiments on the test rig. To conclude, the modified Fastsim algorithm would be employed to compute the lateral creep forces developed in the test rig for dry, wet and friction modifier 1 (FM1) and friction modifier 2 (FM2) contact conditions. The contact area was discretized using the Kalker's original Fastsim algorithm to model processes for each contact particle. This is preferred to the point-contact model that computes the creep forces on a global contact level. The global contact level does not account for the contact variables throughout the whole contact area unlike the discretization method. For the test rig, the contact area was discretized as shown in Figure 4.8.
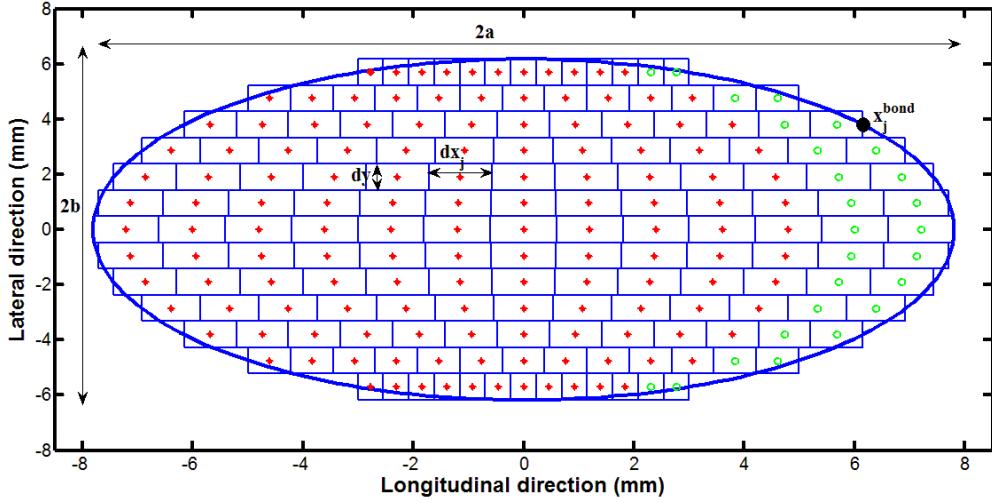
Figure 4.8: Creep force computation using discretization method - Kalker's Fastsim algorithm (Red dot indicates areas of slip while green dots indicates area of adhesion).

The red dots in the figure show the area of adhesion while the green dots show the area of slip in the wheel-rail contact area. The contact area is discretized into *m* x *n* rectangular elements with size *dx* x *dy* as illustrated in Figure 4.8. The equations for the discretization using Fastsim algorithm is shown expressed as follows:

$$dy = \frac{2b}{m}$$

$$y_l = -b + (j - 0..5)dy, j = 1 \dots \dots \dots \dots \dots \dots, m$$

$$x_j^{bnd} = a\sqrt{\left(1 - \left(\frac{y_j}{b}\right)\right)} \tag{4.25}$$

$$dx_j = \frac{2x_j^{bnd}}{n}$$

$$x_{i,j} = x_j^{bnd} - (i - 0.5)dx, i = 1, \dots \dots \dots \dots \dots \dots \dots \dots. n$$

Where *a* and *b* are the semi-axes of the contact area, y_l is the distance in the rolling direction,

The calculation of the total lateral force in the contact area was implemented by summing the integral surface tractions (discretized creep forces for each element).

4.5   Development of curve squeal model for the test rig

Having discussed the wheel-rail contact model and creep forces developed in the twin disc rig, the development of the curve squeal model is presented in this section. The model is designed and simulated in the time domain, as its ability to determine the curve squeal amplitudes is considered paramount in this model. The model is based on the detailed squeal model by (Zenzerovic et al., 2015). The structure of the curve squeal model is shown in Figure 4.9.
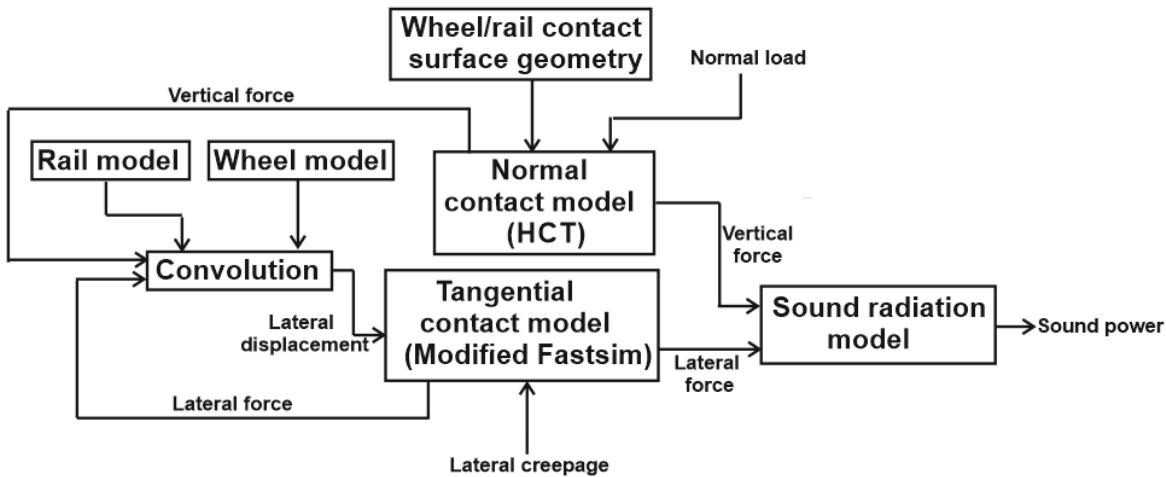
Figure 4.9: Curve squeal model structure

The model comprises of the wheel and rail models, which are the curve fitted frequency response functions from experimental modal analysis conducted in chapter 3. The output from the wheel and rail model is convulsed with the lateral force to obtain the lateral displacement. The normal contact model is the Hertz Contact Theory (HCT) extensively discussed in section 4.2. The tangential contact model used is the modified Fastsim algorithm discussed in detail in section 4.4. The inputs to the model are the wheel/rail contact surface geometry, normal load and the lateral creepage. The lateral creepage is a function of the yaw angle and the lateral velocity. The lateral creepage is expressed as follows:

$$v_y = \psi + \frac{dy}{Vdt} \qquad (4.26)$$

where ψ is the yaw angle, $\frac{dy}{dt}$ is the lateral velocity of the wheel roller and V is the wheel rolling speed.

The sound radiation model is based on the simple model developed by (Zenzerovic et al., 2015). This model used approximations of the boundary element method (BEM) for sound radiation developed by (Pieringer, 2011) and (Monk-Steel and Thompson, 2003). Comparisons between the simple

model for sound radiation and BEM model showed good agreement and correlation. As a result of the fast-computational time of the simple model, it would be applied in this thesis to compute the sound power levels of the dominant curve squeal frequency of the wheel roller. Since the response of the wheel and rail roller to excitation has been obtained from impact hammer tests, curve fitted frequency response functions of the experimental results can be used for the curve squeal model.

4.5.1 Dynamics of the system

The dynamics of the wheel and the rail roller are represented using the curve fitted frequency response function of the frequency response functions obtained in the Chapter 3. Double integration of the frequency response functions for the wheel and rail roller in Figure 3.18 and Figure 3.19 was implemented to obtained the receptances of the wheel and rail roller. Receptance is defined as the ratio between the displacement and the force. It is expressed as follows:

$$G_{i,j}(f) = \frac{d_i(f)}{F_j(f)} \qquad (4.27)$$

Where $d_i(f)$ is the displacement response as a result of excitation force F_j in the coordinate direction i. It is assumed that the wheel-rail system is damped such that the response of the system decays to zero after a certain time period. Having obtained the curve fitted frequency response function, the real part of the receptance is doubled to obtain the frequency spectrum (Zenzerovic et al., 2015):

$$S_{i,j}(f_d) = 2Real(G_{i,j}(f_d)) \qquad (4.28)$$

where the discrete frequency is f_d. The obtain the system response in the time domain, the inverse Fourier transform is applied to equation (4.27).

$$s_{i,j}(n\Delta t) = F^{-1}(S_{i,j}(f_d)) \qquad (4.29)$$

Where Δt represents the discrete time length, and n ranges from 0 to (N -1). The number of samples is represented as N. The time domain signal $s_{i,j}(n\Delta t)$ is represented as follows:

$$C_{i,j}(n\Delta t) = \begin{cases} 0.5\Delta t s_{i,j}(n\Delta t) & for\ n = 0 \\ \Delta t s_{i,j}(n\Delta t) & for\ n = 1 \dots \dots N/2 \end{cases} \qquad (4.30)$$

The frequency response function of the wheel and rail roller is assumed to have decayed to zero at $(N/2)\Delta t$.

Finally, to obtain the displacement of the wheel and rail roller in the time domain, convolution integral of the excitation force and the frequency response functions is applied:

$$d(t) = F \otimes C = \int_0^t F(\tau)C(t - d\tau)d\tau \tag{4.31}$$

The discretization of the convolution integral can be expressed as:

$$d(t_d) = F \otimes C = \sum_{\tau=0}^{t_d} \sum_{j=1}^{3} F(\tau)C(t_d - d\tau) \tag{4.32}$$

Where the discrete time is represented as t_d. The next section presents the wheel and rail dynamics.

4.5.2 Dynamics of the wheel and rail roller

The wheel and rail roller parameters used for the development of the curve squeal model is shown in Table 3.3 and Table 3.4. Finite elements (FE) of the wheel and rail roller have been discussed in chapter 3. The natural frequencies were also determined in the previous chapter for frequencies up to 9kHz. The wheel and rail modes obtained in the previous chapter are all axial with zero nodal circles and nodal diameters. The wheel and rail receptance were determined by double integration of the frequency response functions of the wheel and rail roller in chapter 3. Curve fitting using least of squares rational fraction polynomials method was used to fit the experimental wheel and rail receptances. This method relies on the fact that the frequency response functions of the structure are transfer functions that has poles an zeros. The method fits analytical rational fraction polynomial split between poles and zeros to the transfer function of measured frequency response function. This method is useful when it is required to curve fit a frequency response function that has more than one natural frequencies. The rational fraction polynomial form is given as:

$$H(w) = \frac{\sum_{k=0}^{m} a_k s^k}{\sum_{k=0}^{n} b_k s^k} \tag{4.33}$$

Where is the Laplace transform operator ($s = jw$), m and n are the order of the numerator and denominator polynomials, a_k, and b_k are the numerator and denominator polynomial coefficients. The wheel receptance, $G_{i,j}^W(f)$ and the rail receptance, $G_{i,j}^R(f)$ is shown in Figure 4.11 and Figure 4.12 respectively.
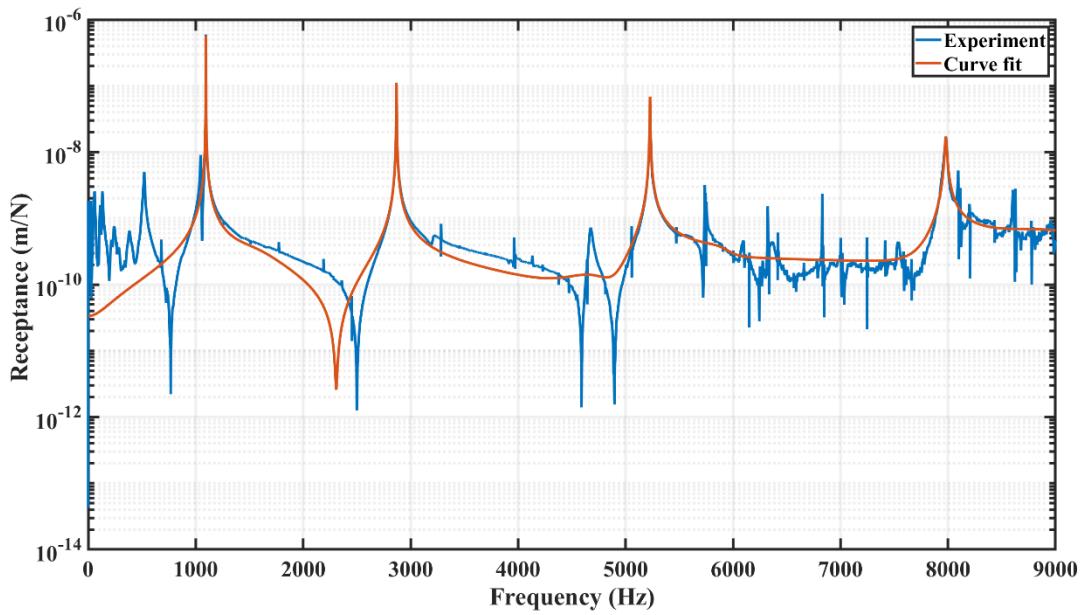
Figure 4.11: Receptance of the wheel roller

The wheel and rail modal damping factors are determined as shown in Table 4.1. The lateral receptance for the wheel and rail roller is assumed to occur at the wheel-rail contact point. In real wheel-rail contact, the lateral receptance varies depending on the contact location between the wheel and the rail
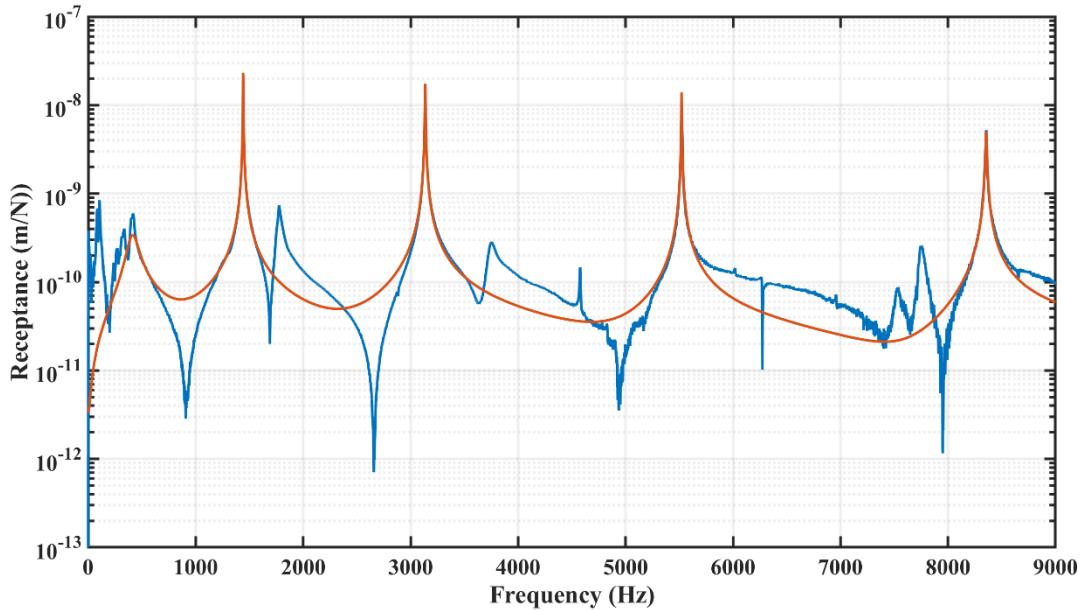
Figure 4.12: Receptance for the rail roller

102

Wheel rotation effect has been neglected in the development of curve squeal. According to (Pieringer, 2011) wheel rotation does not have significant influence on the curve squeal model results. Using equation (4.27) and equation (4.28) the lateral displacement in the time domain can be obtained by taking the inverse Fourier transform of wheel receptance, $G_{i,j}^{W}(f)$ and rail receptance $G_{i,j}^{R}(f)$.

4.6 Model for sound radiation from the wheel

The capability to determine the sound radiated from the system is necessary for the curve squeal model. The reason for this is that squeal is regarded in literature as strong annoying noise and therefore its severity must be evaluated using sound levels. Since it has been established in literature that the wheel roller is the dominant contributor of curve squeal, only the sound amplitude radiated from the wheel roller would be considered. The contributions of the overall sound radiated from the wheel roller are limited for the case of this thesis to only axial motion of the wheel roller. Simple sound model developed by (Zenzerovic et al., 2015) would be used to simulate the sound radiated from the wheel. Sound power radiated from the wheel at a given frequency in a given the wheel velocity field can be expressed as:

$$W(n,f) = \rho c_0 \sigma_j(n,f) \sum_{k=1}^{N_j} \left(S_{jk} \bar{v}_{jk}^2(n,f) \right)$$
(4.34)

Where ρ is the density of air and c_0 is the speed of sound, σ_j is the axial motion radiation efficiency and S_{jk} represents the axial radiation surface cross-section of the wheel roller. The axial surface of the rail roller was divided into N_j annular surfaces with radius $R_1, R_2 \ldots R_k$. The radiation cross section of the wheel roller is shown in Figure 4.13.
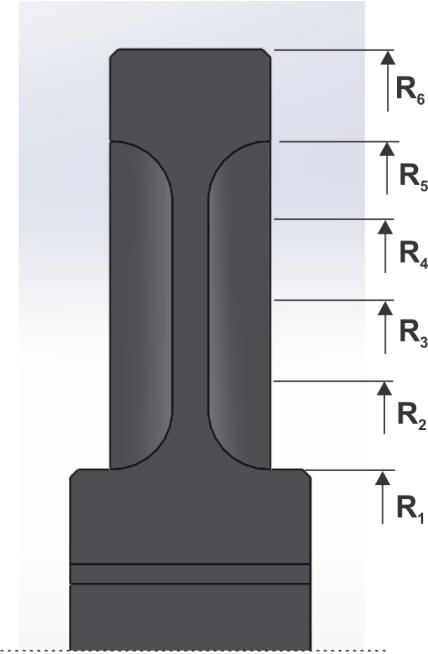
Figure 4.13: Radiation surfaces for the wheel roller

The radiated axial motion of the wheel roller can be expressed as (Vincent et al., 2006):

$$\sigma_j(n,f) = \frac{1}{1 + \left(\frac{f_{cj}}{f}\right)^{2n+4}} \quad (4.35)$$

where f_{cj} is the transition frequency of the wheel roller cross section expressed as:

$$f_{cj} = \frac{c_0 k(n)}{2\pi R} \quad (4.36)$$

The coefficient k can be defined as:

$$k(n) = 1.9 + 1.015 - 0.0189n^2 \quad (4.38)$$

The wheel radiation surface is then divided into 5 annular surfaces S_{jk} with radius $R_1, R_2 \dots R_K$. The annuli of the surface areas are determined as:

$$S_{jk} = 2\pi(R_{k+1} - R_k) \quad (4.37)$$

It is important to note the R is the nominal rolling radius of the wheel roller and both the transition frequency and axial radiation efficiency depend on the number of nodal diameters.

Having established the axial motion of the wheel roller, the wheel velocity field on the wheel roller can be determined depending on the axial direction. Since the radial motion of the wheel roller was not considered, the wheel velocity is expressed as:

$$\bar{v}_{jk}^2(n,f) = 2\pi f((iG(n,f)F_L(f))) \quad (4.39)$$

104

4.7 Results

In this section, the validation of the models for curve squeal based on Figure 4.2 is carried out. The tangential contact model using modified Fastsim, and sound radiation model results is discussed. It is well established that axial wheel modes with nodal diameters and zero nodal circuits are the most excited during curve squeal. It was also discovered that from the initial results obtained from the experiments conducted on the twin disc rig, wheel axial mode with 2 nodal diameters and zero circuits is the dominant contributor of curve squeal. Therefore, the sound validation model is carried out for frequencies around the dominant axial mode. Before the sound radiation mode is validated, the tangential contact point model results would be discussed next.

4.7.1 Measured and curve fitted creep curve result analysis

The model parameters using modified Fastsim algorithm have been obtained from measurements of the lateral force on the Twin disc rig. The parameters are presented in Table 4.1

Table 4.1: Creep force model proposed parameters for the Twin disc rig

Dry contact conditions				
Model parameters	**Average wheel speed (RPM)**			
	100	**125**	**150**	**175**
k_0	0.44	0.34	0.24	0.24
β	0.01	0.09	0.15	0.18
σ	0.30	0.32	0.33	0.35
A	0.23	0.38	0.34	0.32
B	61	61	60	50
μ_s	0.60	0.60	0.38	0.28
k_{inf}	0.44	0.8	0.24	0.24
Wet contact conditions				
Model parameters	**Average wheel speed (RPM)**			
	100	**125**	**150**	**175**
k_0	0.5	0.4	0.44	0.43

	1.5	0.3	0.29	0.2
β	1.5	0.3	0.29	0.2
σ	0.01	0.95	0.95	0.9
A_F	0.77	0.96	9.6	9.6
B_F	60	10	3.1	2.5
μ_s	0.32	0.26	0.2	0.15
k_{inf}	0.5	0.8	0.79	0.79

FM1 contact conditions				
Model parameters	**Average wheel speed (RPM)**			
	100	**125**	**150**	**175**
k_0	0.55	0.45	0.44	0.44
β	1.5	0.3	0.29	0.2
σ	0.01	0.95	0.95	0.9
A_F	0.77	0.96	9.6	9.6
B_F	70	10	3.1	2.5
μ_s	0.15	0.12	0.1	0.06
k_{inf}	0.5	0.8	0.79	0.79

FM2 contact conditions				
Model parameters	**Average wheel speed (RPM)**			
	100	**125**	**150**	**175**
k_0	0.55	0.45	0.44	0.44
β	1.5	0.3	0.29	0.2
σ	0.01	0.95	0.95	0.9
A_F	0.77	0.96	9.6	9.6
B_F	70	10	3.1	2.5
μ_s	0.15	0.13	0.07	0.06
k_{inf}	0.55	0.8	0.79	0.79

Figure 4.14 shows the measured and curve fitted results using Modified Fastsim algorithm for average speed of 100RPM in dry contact conditions. It can be observed from the plot that up to

about 0.5^0 yaw angle, the adhesion coefficient is directly proportional to the yaw angle. This region in the contact area is called the area of adhesion. As the area of adhesion in the contact patch increases for large yaw angles negative friction occurs as is shown in Figure 4.10. The sudden decreasing adhesion coefficient is due to the oscillations in the contact areas of adhesion and slip otherwise called stick-slip of the adhesion curve. The negative slope of the adhesion coefficient agrees with curve squeal models adopted by (Rudd, 1976) to mean instability in the wheel-rail contact. The negative friction is a possible indicator of curve squeal for the test rig.
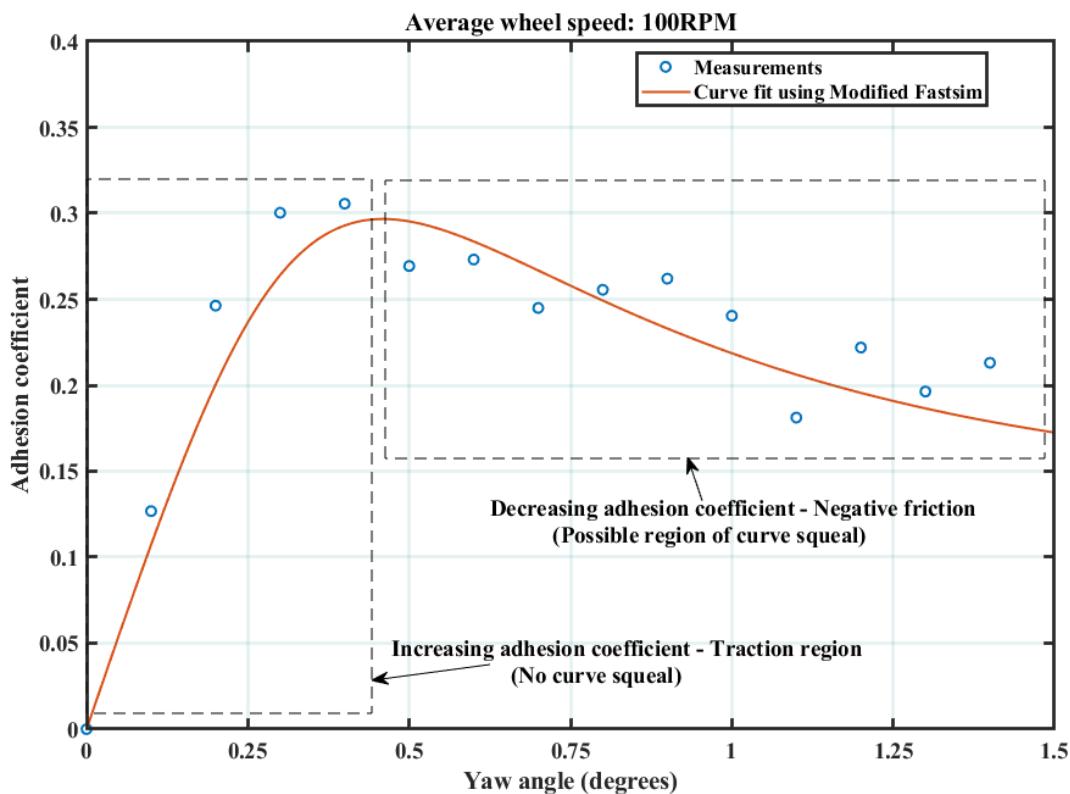
Figure 4.14: Measured and curve fitted results of the adhesion ratio – yaw angle curve for average wheel speed of 100RPM.

Figure 4.15 shows the measured and curved fitted results of the adhesion ratio – yaw angle curve for average wheel speed of 100RPM, 125RPM, 150RPM and 175RPM respectively. The results obtained for average speeds of 100RPM and 125RPM showed the negative adhesion coefficient effect at large yaw angles. This is probably due to the stick-slip oscillations experienced in the contact are as the yaw angle increases. It is important to note that from equation (4.26) that the yaw angle is differently proportional to the lateral creepage. For average wheel speeds of 150RPM

and 175RPM it can be observed that there is a slight reduction in the adhesion coefficient value although there is no significant difference between the curve squeal regions (were a gradual reduction in the adhesion coefficient ratio for increasing yaw angle) and the previous average wheel speeds already mentioned. Peak adhesion ratio at low average wheel speeds (100RPM and 125RPM) was observed from the plots to be about 0.3. This value similar to the value obtained in real track conditions. As the average wheel speed increased from 125RPM up to 175RPM, the peak value of the adhesion coefficient dropped to about 0.2. Although there is a slight reduction in the adhesion coefficient ratio, it is still undesirable to operate the test rig or even real track conditions at very high speeds.
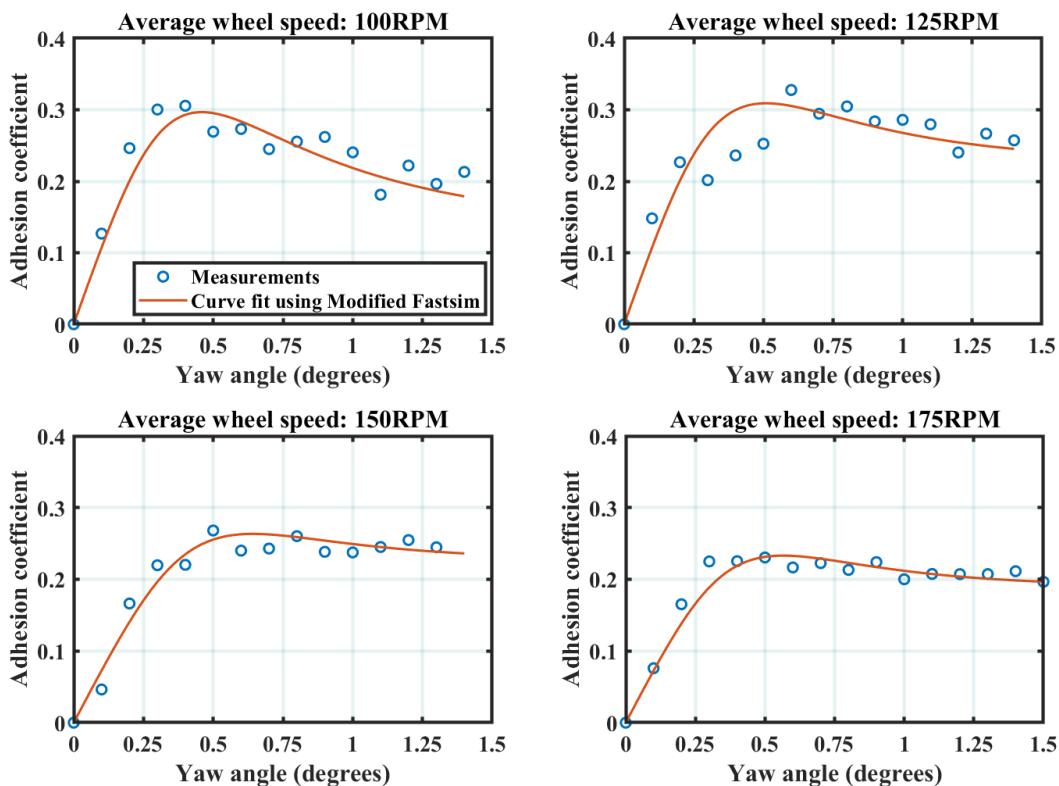
Figure 4.15: Measured and curve fitted friction creep curves for dry contact conditions

Figure 4.16 shows the measured and curve fitted creep curves for wet contact conditions for average wheel speeds of 100RPM, 125RPM, 150RPM and 175RPM. The results showed that for all average wheel speeds, positive increase in the adhesion coefficient was observed after about 0.4^0. This indicates that the application of water at a controlled rate (0.5ml/min) to the wheel-rail interface change the characteristics of the adhesion ratio-yaw angle curves from negative friction

to positive friction. The term positive friction is used here to indicate that after the anticipated curve squeal region (at a particular yaw angle), there was a positive increase in the adhesion coefficient. These results indicate the mitigation of curve squeal. However, the adhesion coefficient values are still high with peak values ranging from 0.15 to 0.2. Although positive friction characteristics was observed with the application of water to the wheel-rail roller interface, the friction coefficient did not reduce as much compared with dry contact conditions. This indicates that in wet contact conditions, curve squeal could still probably occur as the yaw angle is increased beyond 1.5 degrees.
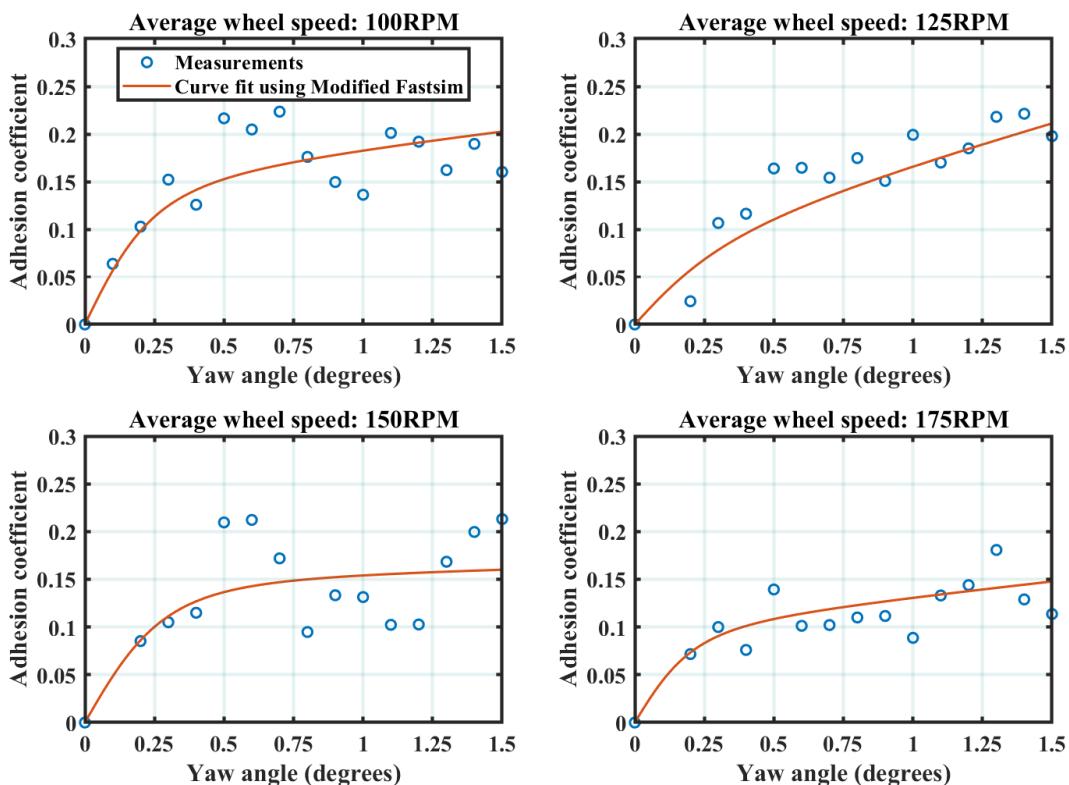
Figure 4.16: Measured and curve fitted friction creep curves for wet contact conditions

Figure 4.17 shows the measured and curve fitted adhesion coefficient – yaw angle creep curves for all average wheel speeds under FM1 contact conditions. Decrease in the adhesion coefficient of FM1 compared with dry contact conditions (see Figure 4.11), and wet contact conditions (see Figure 4.12) is significant. Positive friction is observed for all average wheel speeds. As expected, there is a negative correlation between the adhesion coefficient and the average wheel speed. As the average wheel speed increases, the adhesion coefficient decreases. FM1 exhibits high positive

friction characteristics compared with dry contact conditions and even wet conditions. The reduction in adhesion coefficient is desirable in tight curves but afterwards the train negotiates the curve, the adhesion ratio must be restored to normal conditions of about 0.3 to avoid the railway vehicle skidding off the track.
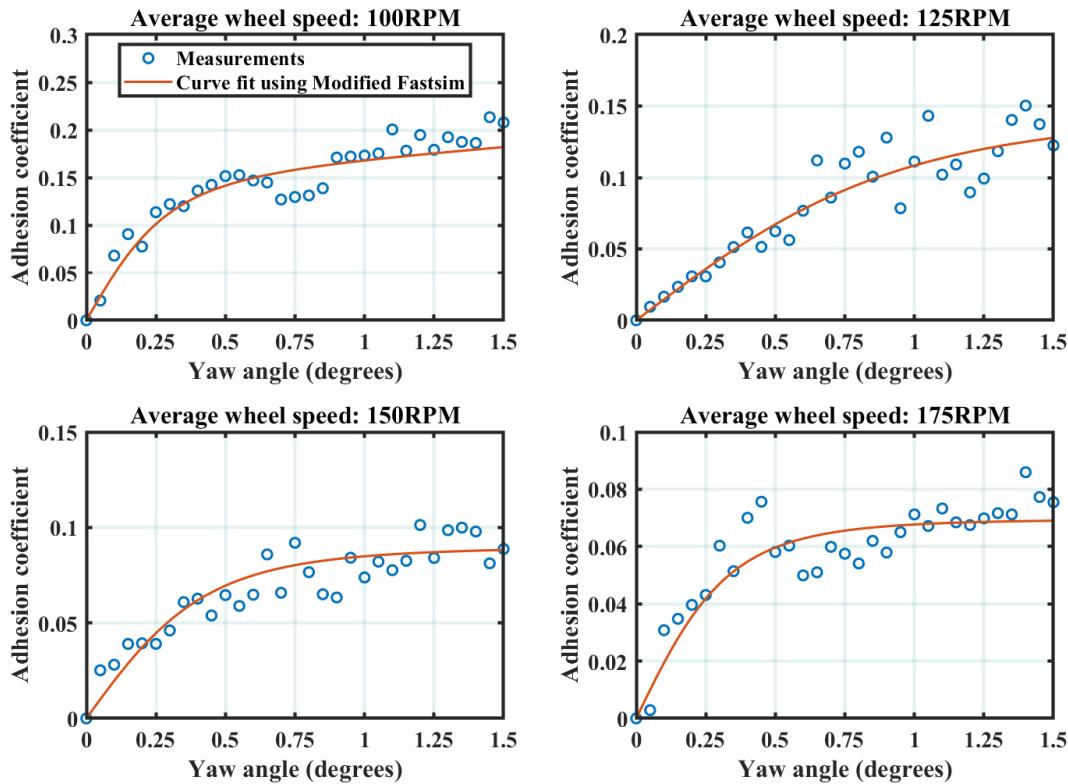
Figure 4.17: Measured and curve fitted friction creep curves for FM1 contact conditions

Figure 4.18 shows the measured and curve fitted creep curves for all average wheel speeds under FM2 contact conditions. An even less reduction in the peak values of the adhesion coefficient ratio is observed using the FM2 due to the probably its viscosity. In addition, the adhesion coefficient decreases as the average wheel speed increases thus showing negative correlation between each other.

To conclude, the introduction of different contaminants (water, FM1 and FM2 to the wheel-rail interface reduces the adhesion coefficient for all average wheel speeds used in this thesis. Mixed results was obtained for wet contact conditions. The reduction in adhesion coefficient was not significant for wet contact conditions. A further increase in the yaw angle beyond 1.5^0 would probably lead to the development of curve squeal on the test rig.
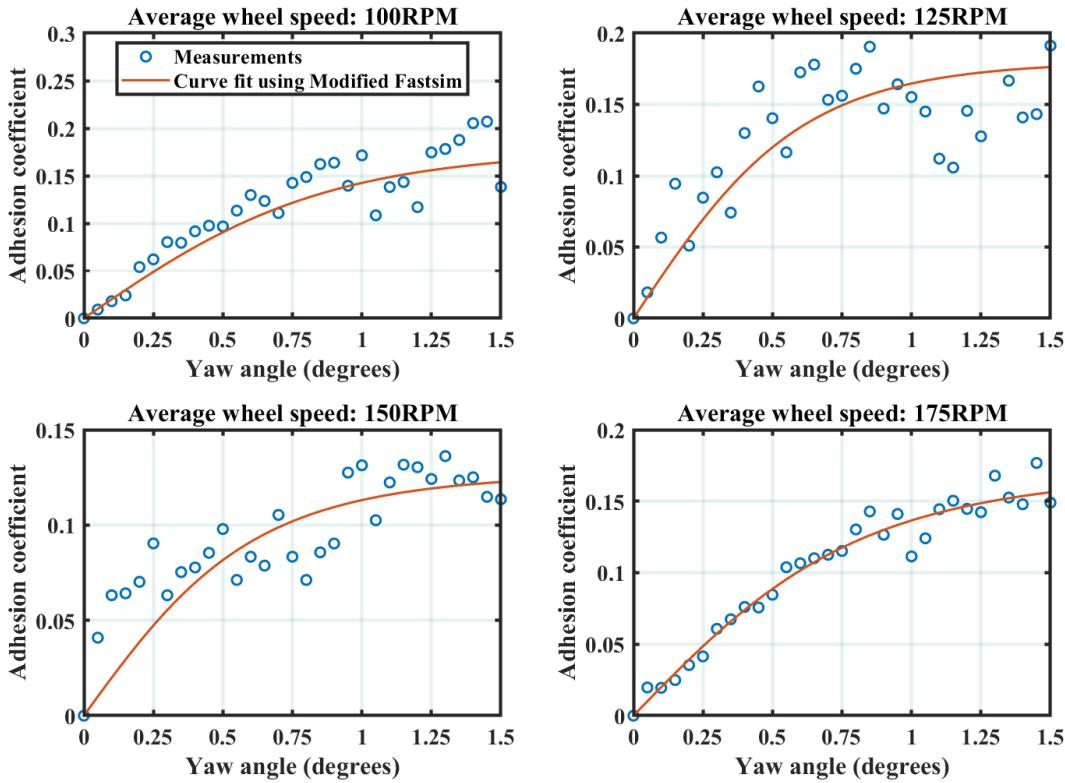
Figure 4.18: Measured and curve fitted friction creep curves for FM2 contact conditions

Having obtained the curve fitted friction creep curves using modified Fastsim algorithm, using Table 4.1, the curve fitted adhesion ratio versus yaw angle curves for all average wheel speeds and all contact conditions is shown in Figure 4.19. The results obtained especially for average speed of 100RPM indicate that at very large yaw angles, the adhesion coefficient values for wet, FM1 and FM2 contact conditions tend to reach the wheel-rail contact. This does not necessarily mean that curve squeal is developed due to the positive increase in the adhesion coefficient value. It is noted that for all average wheel speeds, the effect of negative friction associated with dry contact conditions has been eliminated with the introduction of contaminants to the wheel-rail interface. These adhesion coefficient curves would be substituted in equation 4.27 to determine the lateral creep force developed in the wheel rail contact. The adhesion coefficient value is a function of lateral creepage.
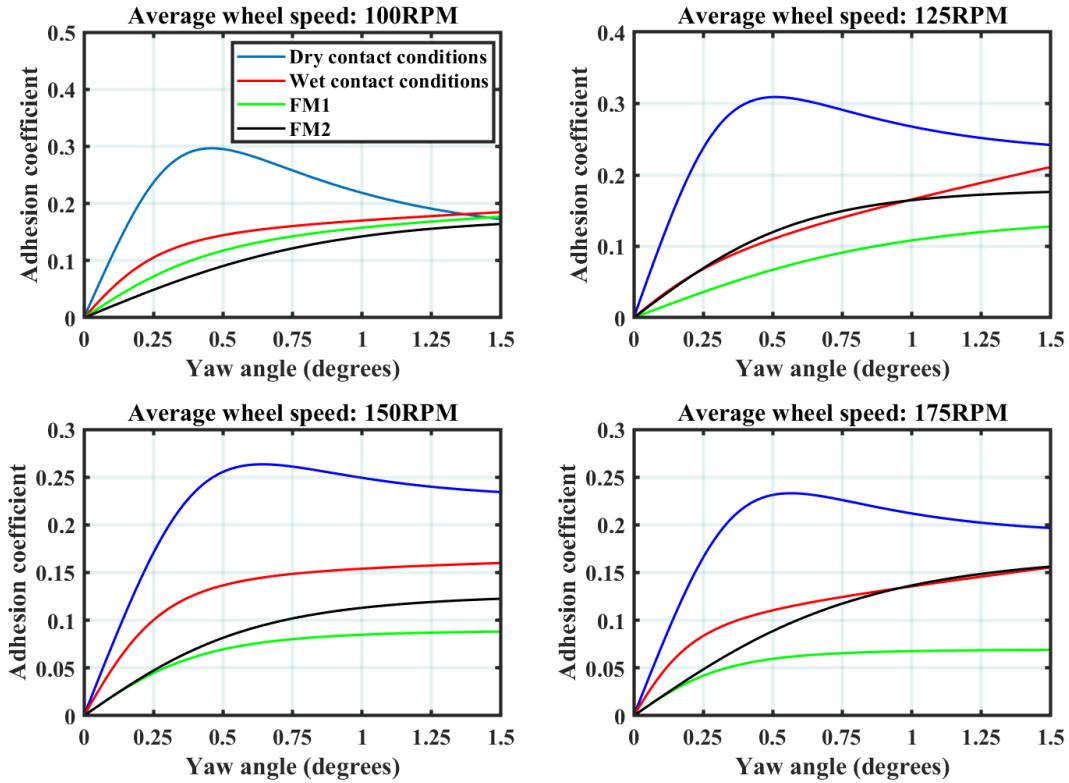
Figure 4.19: Curve fitted friction creep curves for all contact conditions and all average wheel speeds

4.7.2 Analysis of results obtained from curve squeal of vibration model for the test rig

In order to access the performance of the proposed modified Fastsim model for the calculation of lateral creep forces, the developed curve squeal model was solved for various contact conditions. The generation of curve squeal proposed in this thesis due to transverse vibrations of the wheel for large yaw angles. Taking into consideration the dominant curve squeal mode, and its modal parameters, the wheel roller vibration was simulated for average wheel speeds 100RPM, 125RPM, 150RPM and 175RPM. To replicate exactly what happens in the wheel-rail contact, the initial displacement and velocity of the simulations was set depending on the maximum peak values of the measured lateral vibration from the wheel accelerometer. The measured lateral vibration accelerometer values was integrated once and twice to obtain the lateral velocity and displacement of the wheel roller respectively. For each yaw angle, the estimated initial conditions for the initial lateral displacement and velocity was found and used for analysis. The results for dry, wet, FM1 and FM2 contact conditions for all four average wheel speeds is shown in Figure 4.20.
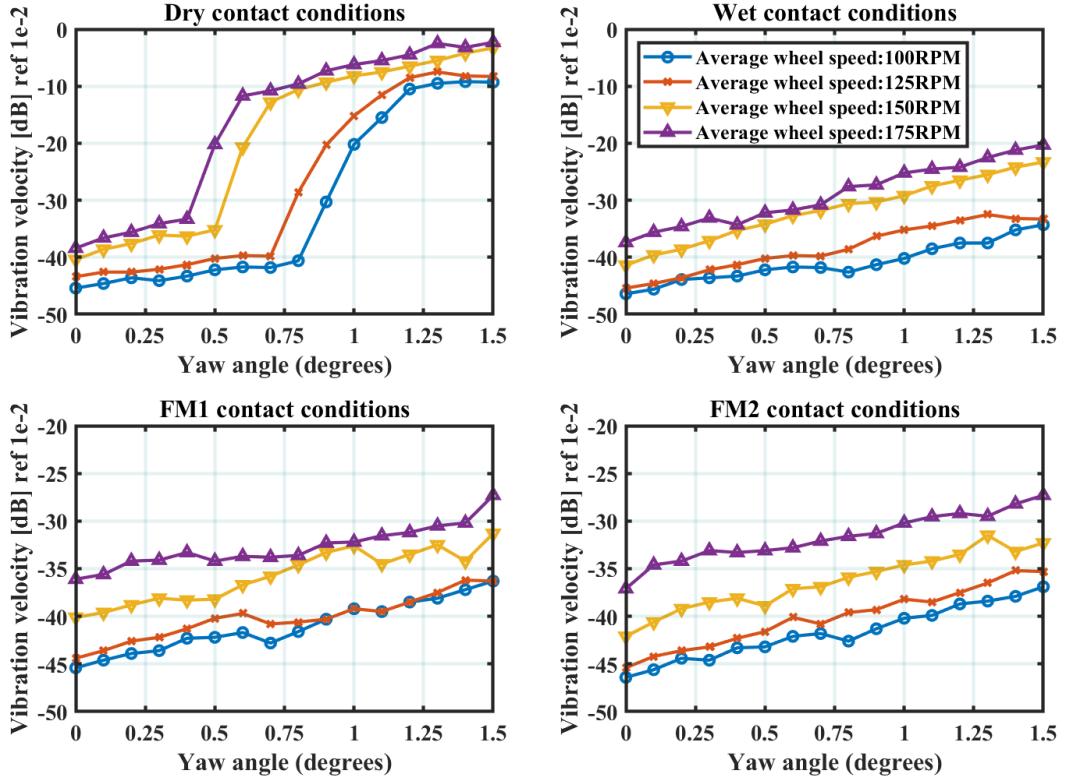
Figure 4.20: Effect of the yaw angle on the simulated transverse vibration velocity

For *dry contact conditions*, the transverse vibration velocity of the wheel roller increases with the yaw angle for all four average wheel speeds. The vibration velocity for average wheel speed of 100RPM, 125RPM, 150RPM and 175RPM increased suddenly at around 0.8^0, 0.7^0, 0.5^0 and 0.4^0 respectively. These angles are the onset development of curve squeal in the test rig for dry contact conditions. In addition, there is an observed negative correlation between the average wheel speed and the onset development of curve squeal. As the average wheel speed increases, the yaw angle corresponding to the onset development of curve squeal decreases. The sudden increase in the vibration velocity at dry contact indicates the existence of negative friction or negative damping in the contact area. This leads to the generation of increasing vibration velocity until large non-linear curve squeal amplitude is reached.

The transverse velocity for *wet contact conditions* increases with increasing yaw angle for all rolling speeds. There is no sudden increase in the vibration velocity amplitude for all yaw angles. This is probably due to the effect of positive friction or positive damping in the wheel-rail contact due to the introduction of water to the interface. When the wet contact condition results is

compared with the dry contact results, it can be found that curve squeal is mitigated for all average wheel speeds.

Similarly, the results obtained for FM1 and FM2 contact conditions showed a further decrease in the vibration velocity of all four average wheel speeds. This is because of the high friction positive characteristics associated with friction modifiers. When the FM1 and FM2 simulated contact conditions is compared with dry contact results, it is evident that curve squeal is mitigated for all average wheel speed values
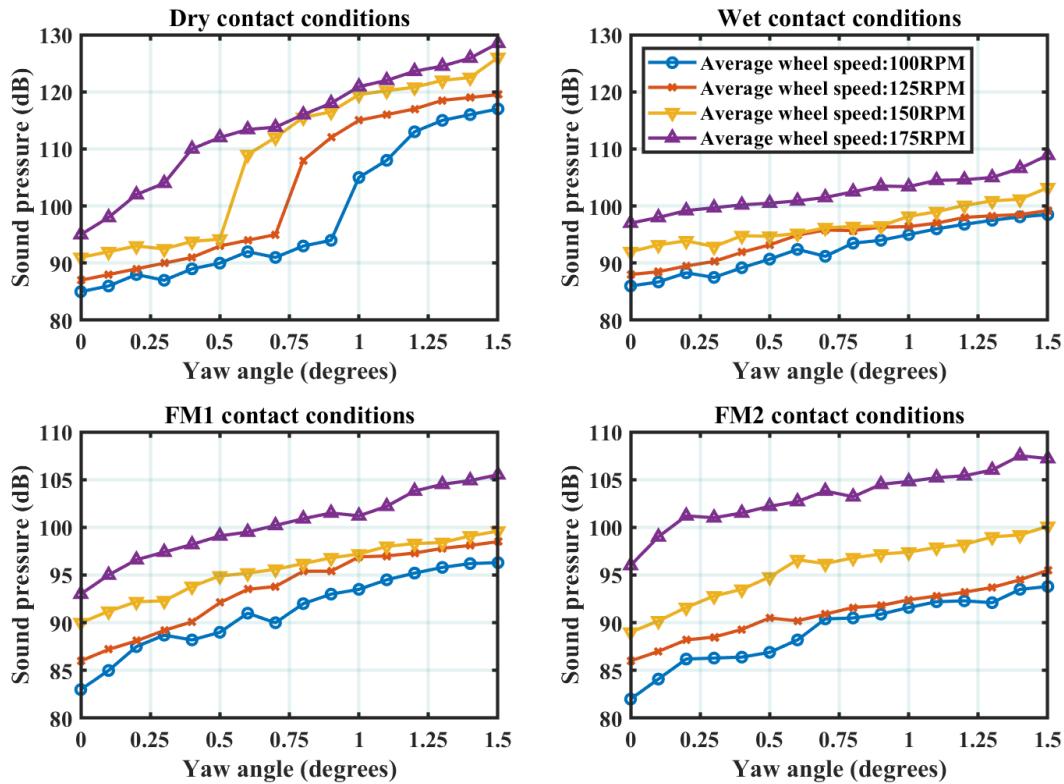
Figure 4.21: Effect of the yaw angle on the simulated transverse vibration velocity

For the *dry contact conditions,* sound pressure level increase with increasing yaw angle for all four average wheel speeds. The sound pressure level for the average wheel speed of 100RPM, 125RPM, 150RPM and 175RPM suddenly increase at around 0.9^0, 0.7^0, 0.5^0 and 0.3^0. These angles represent the onset development of curve squeal on the test rig. Also, there is an observed negative correlation between the average wheel speed and the onset development of the simulated curve squeal amplitude. The same conclusions was realised for the simulated vibration velocity of the wheel roller. For wet, FM1 and FM2 contact conditions plots shown in Figure 4.19, the sound

114

pressure level is influenced by the yaw angle. A rather steady increase in the sound pressure level for contaminated contacts (water, FM1 and FM2) indicate the absence of curve squeal. This shows the positive friction characteristics of water and FM1 and FM2.

4.8   Summary

Curve squeal model for the twin disc rig has been developed and simulated. The model comprised of the wheel and rail models, normal contact model, tangential contact model and sound radiation model. The wheel and rail models are the wheel receptance functions obtained from curve fitting the receptance results obtained from experimental modal analysis. The normal contact model was used to determine the size and shape of the wheel-rail contact. The model depended on the contact geometry and the normal load. The tangential contact model employed the modified Fastsim algorithm to determine the lateral force developed at the wheel-rail contact.

The adhesion ratio (ratio of the lateral force to the vertical force) was measured in the twin disc rig for different yaw angles, wheel rolling speeds and with friction modifiers/water. It was found that when friction modifiers are applied to the wheel-rail contact surface, the adhesion coefficient and the lateral force decrease significantly compared with dry contact conditions without friction modifier. The decrease is more pronounced with friction modifiers (FM1 and FM2). It was observed from the measured adhesion coefficient-creep curve that the curve tilts upwards with increasing wheel speed. This is in contrast to the dry case. It was also observed that water and friction modifiers (FM1 and FM2) tend to significantly reduce or completely mitigate the negative slope associated with dry contacts.

A simple sound radiation model considering only the dominant wheel axial mode (2 nodal diameters and zero circles) was developed and simulated at different yaw angles, wheel speeds and with water and friction modifiers. The results show that the development of curve squeal occurs at different wheel rolling speeds. The increase in wheel rolling speed results in the faster development of curve squeal. The results of the vibration amplitudes of the dominant wheel axial mode exhibited the same phenomenon. However the transition yaw angles (angles between no curve squeal and curves squeal) did not yield satisfactory result for both the simulated vibration velocity and sound pressure levels.

Chapter Five: Curve squeal monitoring using acoustics analysis

This chapter presents the application of acoustic analysis methods for monitoring curve squeal in the twin disc rig. Time, and frequency domain methods would be used to identify the onset development of curve squeal. An introduction is included to emphasize the important of acoustic methods for monitoring curve squeal. The importance of time and frequency domain methods for the feature extraction is discussed in detail. Condition monitoring indicators such as kurtosis and skewness would be used to extract meaningful features about the time domain sound data for different wheel speeds and different contact conditions. In addition, spectrum analysis would be applied to the time domain data to further understand the frequency components that hare responsible for curve squeal and how it can be mitigated. Condition monitoring indicators peak and rms would be applied to the spectrum data to extract useful features about the condition of the wheel-rail contact. These would indicate which frequency component is responsible for curve squeal, the rolling noise frequency and the harmonics that are generated as a result of the dominant curve squeal frequency. Finally, a detailed summary of the results obtained would be presented with insight into its application to detect and characterize curve squeal as well as its mitigation.

5.1   Introduction – Acoustic based condition monitoring for curve squeal

Acoustic based condition monitoring has the advantage of retrieving important information about the condition of a system non-invasively. This advantage has enabled curve squeal to be measured and detected in railway track curves for decades.

Acoustic based condition monitoring has been applied to the measurement of curve squeal in railways (Hanson et al., 2014), (Panulinova et al., 2016), (Fourie et al., 2016), (Liu and Meehan, 2016), (Hsu et al., 2007), (Anderson et al., 2018), (Thompson, 2009). These studies covered in detail the application of frequency domain analysis for identification of curve squeal. Little or no information about the acoustic measurements for identification and characterization of curve squeal was mentioned. Therefore, the objective of this chapter is to identify condition monitoring indicators obtained from acoustic measurements that could be applied to identify and characterize curve squeal in the twin disc rig.

The condition monitoring indicators would be extracted from the acoustic measured data. Time and frequency domain analysis would be applied to investigate and identify curve squeal. The advantage of using time domain analysis is that they can be readily applied in condition monitoring systems online because they depend on single value representation. They are not affected by spectral leakage, signal aliasing and other effects that are characteristic of frequency domain methods. Frequency domain methods, although widely used would be used to identify the natural frequencies of the wheel and rail roller responsible for curve squeal.

The condition monitoring indicators obtained from the acoustic data would be used to analyse the effect of different contact conditions and their influence on curve squeal mitigation. The acoustic data which was measured by variation for four different wheel speeds at different yaw angles would be analysed.

5.2   Acoustic time domain data analysis

The acoustic time domain data measured from the microphone placed at 50 mm from the wheel rail interface was obtained for dry, wet, FM1 and FM2 contact conditions at 2.5kN normal load. Figure 5.1 shows the sound measurements obtained from the microphone at average wheel speed of 100RPM for four main contact conditions. The baseline measurements of the test rig at zero yaw angle (no curve squeal) is used to compare what transpires when curve squeal is detected on the test rig. As would be discovered in the course of this study, curve squeal occurs at higher yaw

angles. It is expected that curve squeal would have occurred at angle greater than 1° for all wheel rolling speeds. For comparison between no curve squeal and curve squeal, 1.2^0 yaw angle has been chosen to distinguish between the two.

From the results in Figure 5.1, a noticeable periodic outburst in the sound data occurs in dry contact conditions at 1.2 degrees yaw angle. This is probably as a result of the decreased wheel speed at the yaw angle. As explained earlier, increase in the yaw angle of the wheel roller results in increase in the lateral forces developed on the wheel rail interface. This increase results in excessive loads on the three-phase induction motor thus leading to reduction in speed. Since the system operates in open loop configuration, a reduction in wheel speed is expected as the yaw angle increases. It can also be observed that for dry contact conditions, a distinct increase in the sound pressure peak is observed when the yaw angle is increased to 1.2 degrees compared to the baseline time domain data at zero degrees yaw angle.

It can also be concluded from the plots that there is no significant difference in the sound amplitude when water, FM1 and FM2 was applied to the rollers. This illustrates at first observation the mitigation effect of water, FM1 and FM2 when applied on the wheel-rail interface.
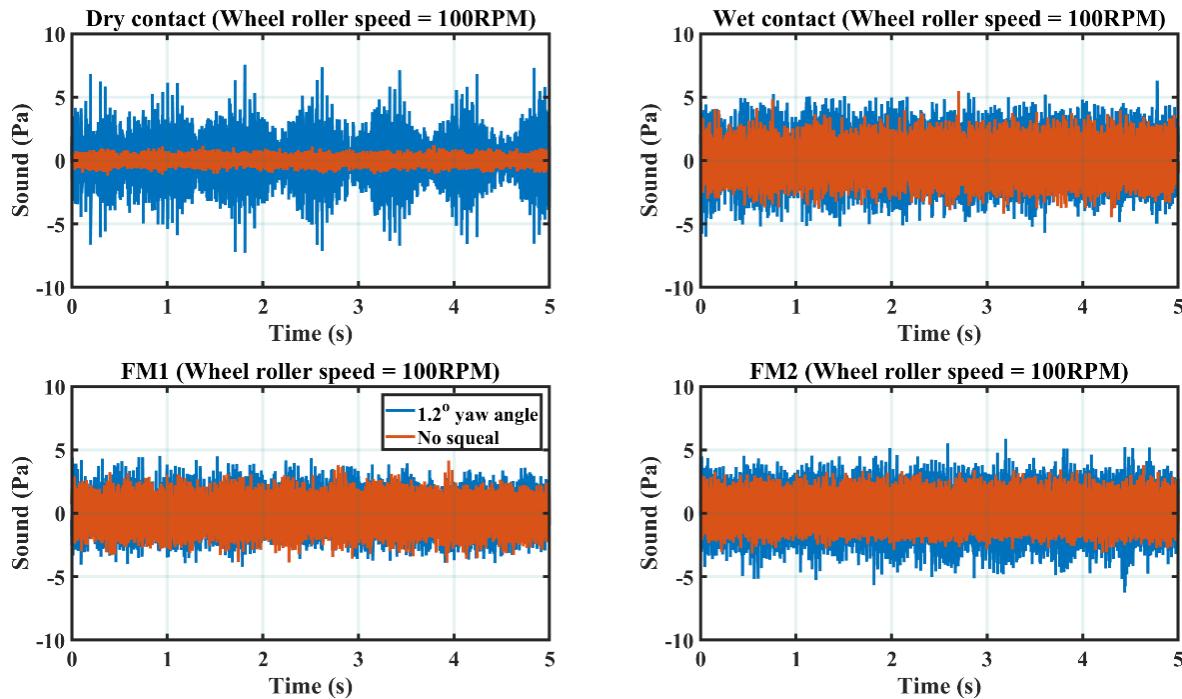
Figure 5.1: Sound pressure time domain data for average wheel speed of 100 RPM

Figure 5.2 shows the acoustic time domain data obtained from the microphone for dry, wet, FM1 and FM2 contact conditions at average wheel speed of 125RPM. For dry contact conditions, significant difference in sound amplitudes between zero degrees and 1.2 degrees yaw angle is observed. This is as a result of the increase in the yaw angle of the rail roller. The sound amplitudes for wet, FM1 and FM2 remain fairly similar for zero degrees and 1.2 degrees yaw angles. The time domain data shows noticeable increase in the amplitudes at zero degrees yaw angles for the contaminants (water, FM1 and FM2) when compared with dry contact conditions at this angle. It can therefore be concluded that at zero degrees yaw angle, the sound pressure amplitudes are slightly for the contaminant are higher compared to dry contact conditions.
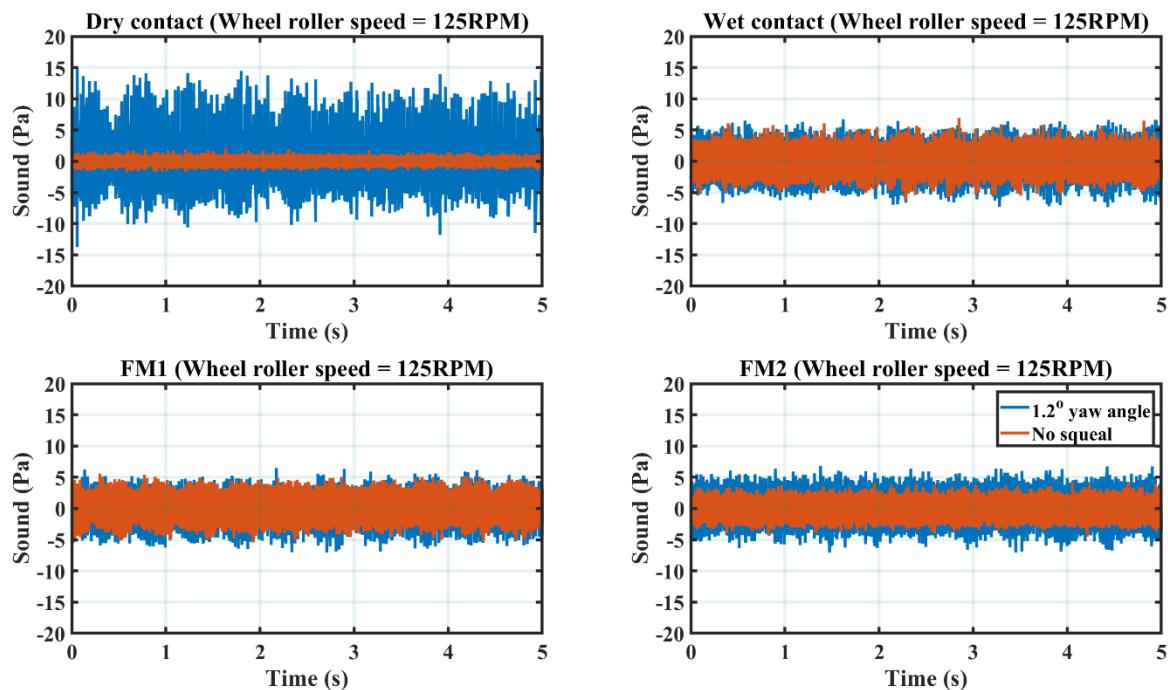
Figure 5.2: Sound pressure time domain data for average wheel speed of 125 RPM

Figure 5.3 shows the acoustic time domain data obtained from the microphone for dry, wet, FM1 and FM2 contact conditions at average wheel speed of 150RPM. The periodic bursts due to reduction of the wheel and rail roller speeds at 1.2 degrees yaw angle is again observed at this wheel speed. A noticeable increase in the sound amplitude is observed at this wheel speed compared to the previous wheel speed. Also, a noticeable increase in the sound amplitudes for wet, FM1 and FM2 contact conditions is observed compared to the previous average wheel speeds of 100RPM and 125RPM. This is purely due to increase in wheel roller speed. It is hard to distinguish

at this stage the cause for the difference between the sound amplitudes of FM1 and FM2 for zero degrees and 1.2 degrees yaw angle.
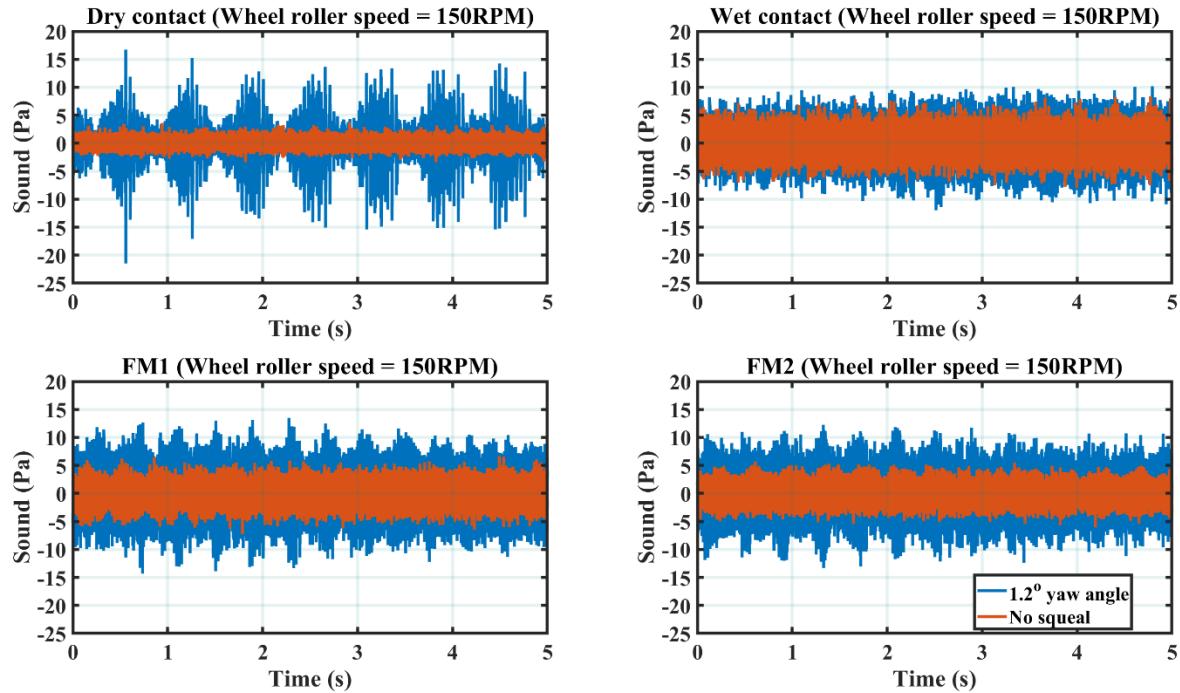
Figure 5.3: Sound pressure time domain data for average wheel speed of 150 RPM

Figure 5.4 shows the acoustic time domain data obtained from the microphone for dry, wet, FM1 and FM2 contact conditions at average wheel speed of 175RPM. The periodic bursts due to reduction of the wheel and rail roller speeds at 1.2 degrees yaw angle is again observed at this wheel speed. A distinguishable feature from the sound signals obtained from the microphone for all contact conditions is the increase in sound amplitude for both no squeal and curve squeal as the wheel roller speed increased. The difference between FM1/FM2 contact conditions and water conditions is the observable increased sound amplitude. This is probably due to the characteristics of the friction modifiers and its effect at high speeds. However, whether this noticeable increase helps in mitigation of curve squeal is not clear at this stage. Further feature extraction and signal processing would be required to understand what transpires in the wheel-rail interface as it is increased.
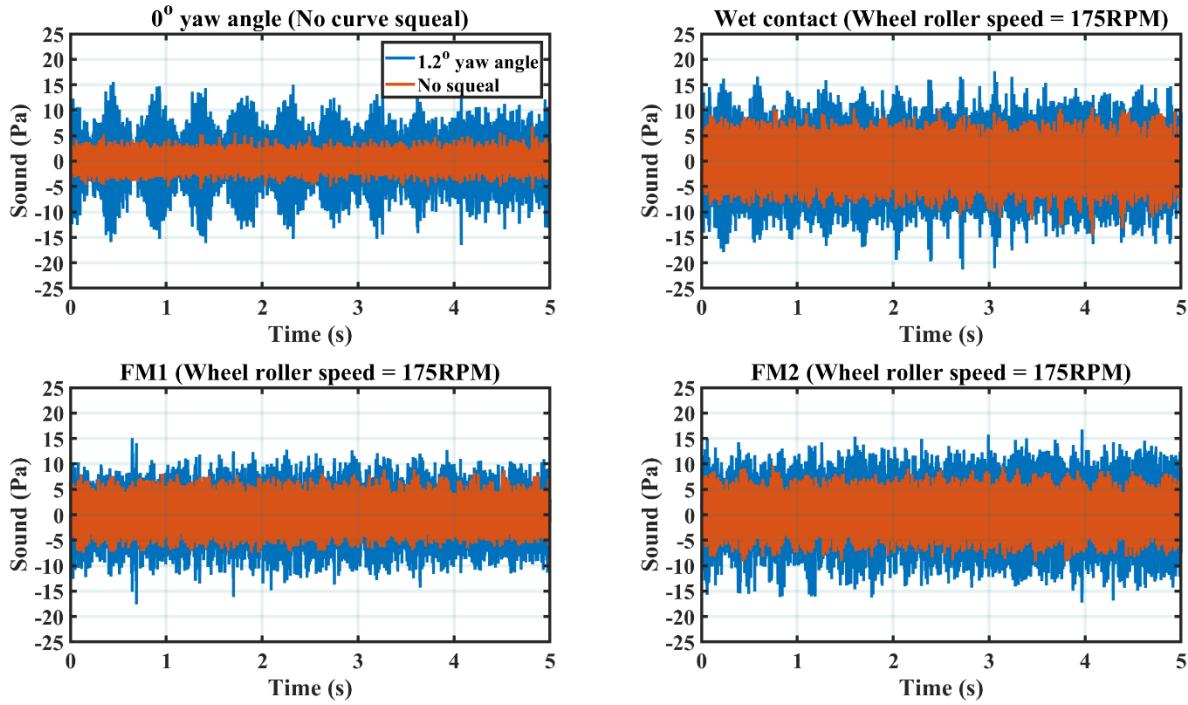
Figure 5.4: Sound pressure time domain data for average wheel speed of 175 RPM

The sound signals represented by Figure 5.1 to Figure 5.4 shows that time domain statistical analysis can be applied to further understand what happens during curve squeal. Condition monitoring indicators would therefore be employed in the next section to investigate and characterize curve squeal and how it can be mitigated.

5.2   Description of curve squeal condition monitoring indicators

The condition monitoring indicators for curve squeal deal use statistical techniques to extract features from the sound signal. Some of the condition monitoring indicators that would be used include RMS, Peak and Crest factor, Kurtosis, Skewness and Probability distribution function (PDF).

5.2.1   Peak

The peak value of a time series data is the absolute or maximum value of the data. It can be expressed as follows:

$$Spectral\ peak = \max(x_n) \tag{5.1}$$

121

5.2.2 RMS

The root mean square (RMS) value is useful in the detection of rotating machine imbalance. RMS value describes the power content of a vibration signal. It is defined as the deviation of distributions from the vibration signal mean value. The mathematical expression for RMS value calculation of a typical vibration data is expressed as:

$$RMS = \left(\frac{1}{N}\sum_{n=1}^{N}x_n^2\right)^{\frac{1}{2}} \tag{5.2}$$

where N is defined as the number of data points for the vibration signal and x is time series data. Where x_n is the time domain series data?

5.2.3 Crest factor

Another important time domain method is crest factor. It is defined as the ratio of the maximum peak value of the vibration signal to the RMS value. Crest factor is important to determine the effects of faults in rotating machines. Crest factor can be expressed mathematically as (Igba et al., 2016):

$$Crest\ factor = \frac{Peak}{RMS} \tag{5.3}$$

A high crest factor indicates the presence of fault in a time series data.

5.2.4 Skewness

Skewness property defines how symmetrical the sound data is compared with the normal distribution. The skewness of a normal distribution function is usually zero. When the vibration data is skewed to the left, then the data is negatively skewed while when the data is skewed to the right then the distribution is positively skewed. Skewness can be calculated as follows (Ovacikli et al., 2013):

$$Skewness = \left(\frac{(x-\mu)}{\sigma}\right)^3 E \tag{5.5}$$

where x, E, σ and μ are the time domain signal, expectation operator, standard deviation and the mean respectively.

5.2.5 Kurtosis

Variability and location characterization are one of the fundamental tasks to undertake in statistical analysis. Kurtosis is used to characterize the measured sound data further. Both methods rely on the normal distribution of the measured data. Kurtosis determines whether the vibration data is light-tailed or heavy tailed relative to the normal distribution. It has been established in most literature that a kurtosis value of three represents a good functioning vibratory system while any value greater that this indicates fault in the system. Kurtosis can be calculated as (Fei, 2016):

$$kurtosis = E\left(\frac{(x-\mu)}{\sigma}\right)^4 \qquad (5.4)$$

where *x, E,* σ and *µ* are the time domain signal, expectation operator, standard deviation and the mean respectively.

5.3   Feature extraction using Peak, RMS and Crest factor

The condition monitoring indicators, Peak and RMS did not yield satisfactory results especially for high wheel speeds. The reason for this being that the as the wheel speed increases, the peak and RMS of the sound signal increases. For low wheel speeds (100RPM), the peak and RMS provided good results. For speeds 125RPM and above, it is difficult to distinguish between curve squeal and no curve squeal. For example, in Figure 5.4, there is no significant difference between the peak amplitudes at zero degrees and 1.2 degrees when dry and contaminant (wet, FM1 and FM2) contact conditions was compared for average wheel speed of 175RPM.

5.4   Feature extraction using kurtosis and skewness

The effect of varying the yaw angle on the kurtosis values was investigated for four average wheel speeds as displayed in Figure 5.5. Comparisons between the dry, wet, FM1 and FM2 contact conditions was investigated for the onset development and mitigation of curve squeal on the test rig. Similar results were obtained for the crest factor value can be inferred from the results for the kurtosis plots. There also exists a negative correlation between the average wheel speed and the yaw angle required for curve squeal to occur. As has been established in literature the kurtosis value for healthy gears in machine systems is 3. Based on this value, it can be inferred from the plots that the average kurtosis value for no curve squeal on the test rig is around the value of 3. This indicates that the test rig is in the rolling contact noise region and thus no curve squeal occurs

in this region. A large disparity in the kurtosis values after yaw angles 0.9^0, 0.7^0, 0.6^0 and 0.6^0 indicate the onset development of curve squeal in the test rig for average wheel speeds 100RPM, 125RPM, 150RPM and 175RPM respectively. It can also be concluded that the average kurtosis value of around 3 for no curve squeal was maintained for all yaw angles and average wheel speeds when water, FM1 and FM2 was applied to the rollers. This indicates that curve squeal was mitigated on the test rig when these contaminants to the wheel rail interface.

The onset development and mitigation of curve squeal in the test rig was also investigated using the skewness values. The effect of varying the yaw angle on the skewness values for all four average wheel speeds is illustrated in Figure 5.6. In the rolling contact noise region, the skewness value has an average of about zero for all average wheel speeds. This value according to the definition of skewness implies that the time domain signal is not skewed either to the left or right but at a central position. This is required condition for all healthy vibratory systems in the industry. In the curve squeal region, the time domain data for sound sharply skewed to the right implying that they are all negatively skewed.
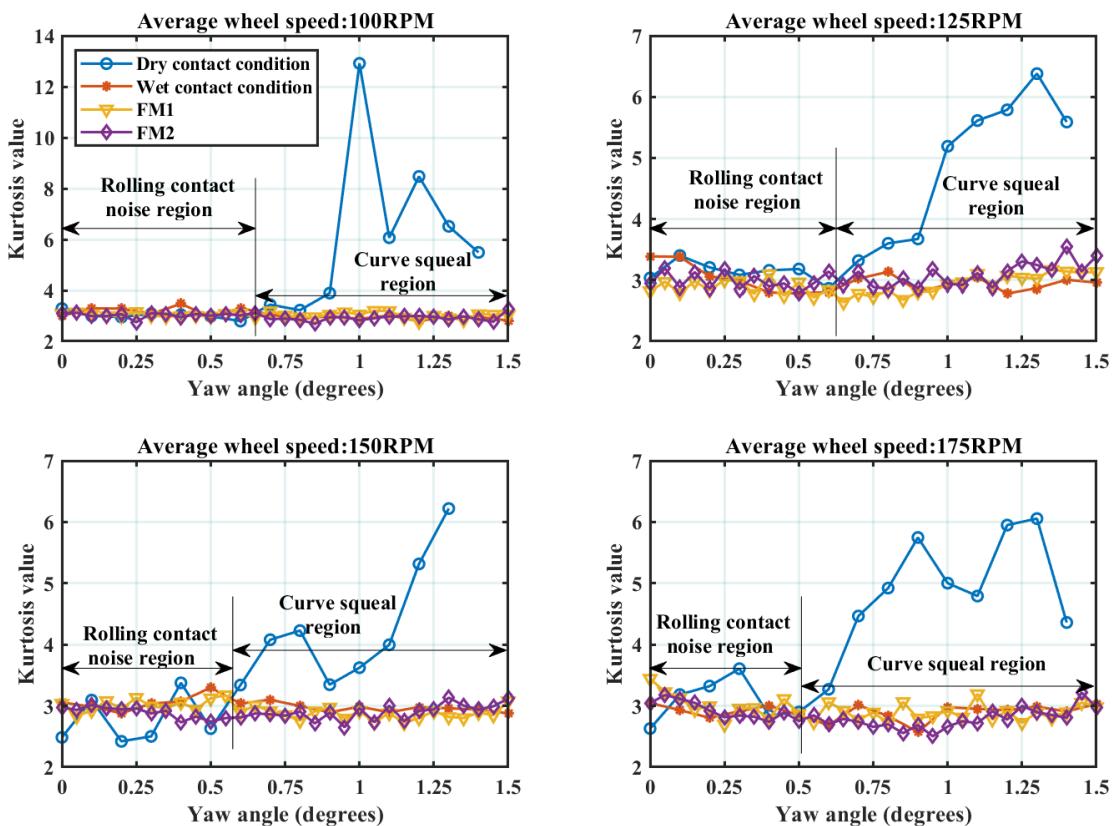
Figure 5.5: Kurtosis versus yaw angle for all four average wheel speeds

This disparity in skewness value beyond 0.7 degrees, 0.7 degrees, 0.6 degrees and 0.5 degrees for average wheel speeds 100RPM, 125RPM, 150RPM and 175RPM respectively, indicates the onset development of curve squeal. It is important to observe that the application of water, FM1 and FM2 maintains the skewness value to about 0 for all yaw angles and all average wheel speeds. This indicates the mitigation effect of water, FM1 and FM2 on the curve squeal in the test rig. However further information on which roller contribute to the development of curve squeal was difficult to predict. Therefore, in the next section the conventional frequency domain analysis would be used to understand which rollers are more dominant in curve squeal development on the test rig.
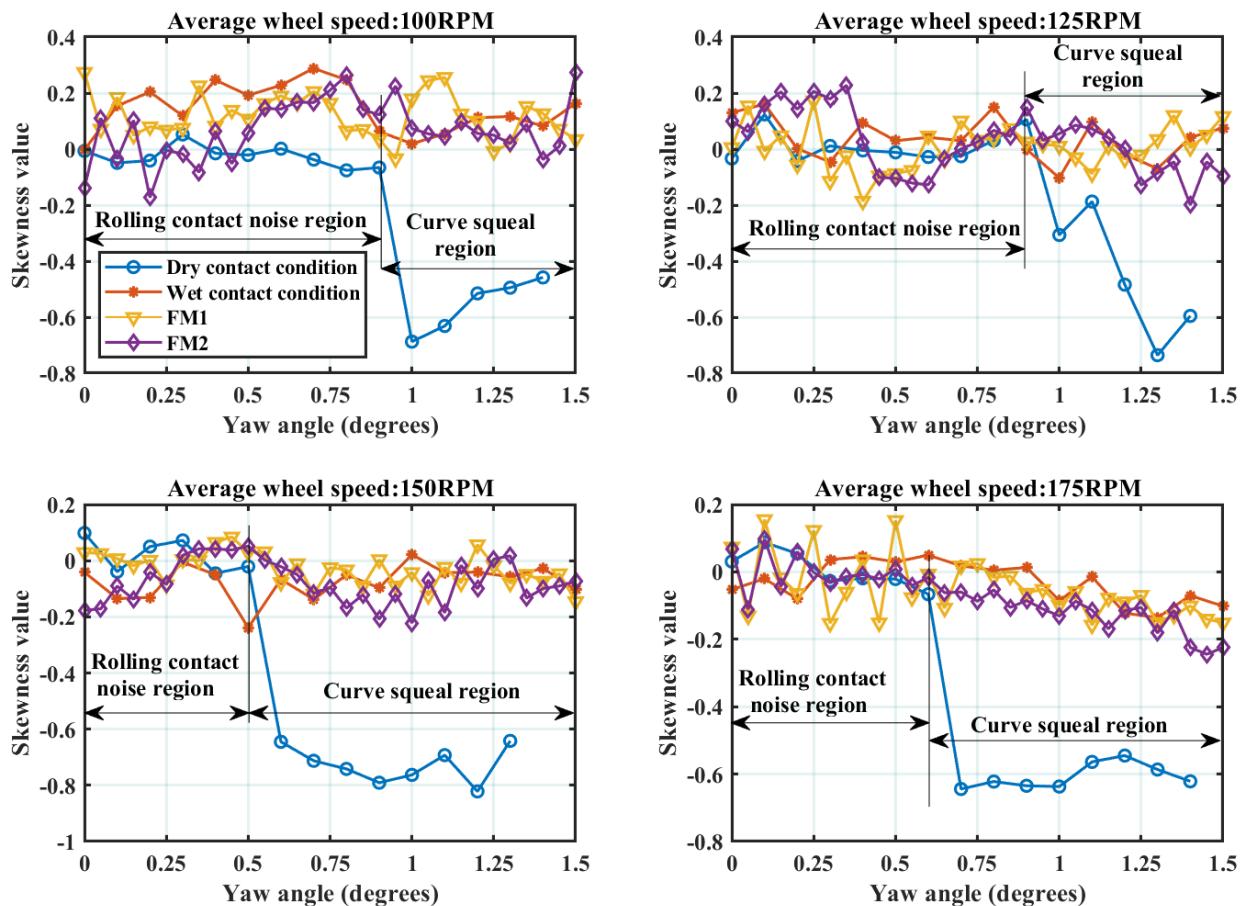
Figure 5.6: Skewness versus yaw angle for all four average wheel speeds.

5.5   Frequency domain analysis

Frequency domain analysis is the foundation for processing signals from several systems in the field of science, engineering and mathematics. Unlike time domain analysis, frequency domain

determines the frequency components of a signal. The frequency components obtained using frequency domain analysis is then used to make observations and conclusions on the condition of the system. Several reasons for the application of frequency domain analysis as itemized by Cohen include; to study the time domain data, identify the frequency components of the signal and its flexibility as a mathematical tool for study purposes. Among all the mathematical tools used in engineering and condition monitoring, frequency domain analysis is the most widely used method for signal processing and condition monitoring and would therefore be used in this research to detect and characterize curve squeal.

Frequency domain analysis are usually conducted on a time domain signal using Fourier transforms. Fourier transforms are used to convert the time domain data to frequency domain comprising of frequency components with different amplitudes. The frequency components determine the condition of the system. One of the main advantages of using frequency domain analysis is the ability to identify and characterize faults in a system by observing the amplitudes of the frequency components. Based on these observations, conclusions can be drawn on where more energy resides. This makes the identification of faults easier to find and study in most engineering systems.

Frequency domain analysis has been widely applied for the monitoring curve squeal in rolling railway vehicles (Vincent et al., 2006), (Liu and Meehan, 2016), (Meehan and Liu, 2018), (Hsu et al., 2007). In conclusion, frequency domain analysis for monitoring curve squeal would be investigated in this section to detect the onset of curve squeal as has been achieved in time domain analysis. In addition, the mitigation of curve squeal using water, and friction modifiers would also be investigated using frequency domain analysis by examining which frequency components have energy that is more spectral and are the dominant cause of curve squeal.

5.5.1 Spectrum analysis

Spectrum analysis is used to obtain the frequency characteristics of the time domain signal using Fourier transform methods. Fast Fourier transform (FFT) is used to determine the frequency components of the time domain signal. Spectrum analysis of a signal can also be defined as the plot of the signal amplitudes as a function of frequency. Fast Fourier transforms are useful in vibration analysis to detect faults in the vibratory system. However, they suffer from limitations based on the length of the time domain signal. Because of the finite nature of time domain signals,

spectral leakage is most likely to occur if FFT is applied directly to the signal. To solve this problem, windowing functions can be applied to the time domain signal before FFT is implemented. Window functions are used to minimize spectral leakage in time domain signals (Oppenheim and Schafer, 1975). Hanning, rectangular, hamming and others are some of the window functions that could be applied to the time domain signal. Assuming that the time domain signal is given as $x(t)$ and the power spectrum is defined as $S_{xx}(\omega)$, then the power spectrum of a signal can be represented as:

$$S_{xx}(\omega) = |F\{x(t)\}|^2 \qquad\qquad (5.6)$$

where F is the Fourier transform of the time domain signal $x(t)$.

Spectrum analysis finds applications in several areas in machine vibratory systems. Despite the advantages of using frequency domain analysis, one of the main issues of its application is the condition that the signal is finite majority of the time. To solve this problem, window function is applied to the time domain data before the application of Fast Fourier Transform (FFT). Spectral leakage can therefore be reduced when window function is applied to the data. Window functions are also useful for the reduction of signal discontinuities by finding the maximum in the signal middle and decreasing both edges of the signal to zero. There are different types of window functions that are utilized for time domain data. However, the common window functions include hanning, rectangular and hamming windows.

For this chapter, the rationale for the application of spectrum analysis is to determine the frequency components of the sound signal in other to establish which of these components is responsible for curve squeal. In addition, the frequency components of the signal for the different contact conditions would be investigated and analysed to investigate the mitigation of curve squeal on the test rig.

5.6   Spectrum analysis to the microphone data

The time domain data for sound obtained in Figure 5.1 to Figure 5.4 describes the changes in the amplitude of the signal from the microphone when wheel speed and various contact conditions were varied. The same sound signals in the time domain were analysed using spectrum analysis. Figure 5.7 illustrates the power spectrum plot for average wheel speed 100RPM. The power spectrum was also plotted for wet, FM1 and FM2 contact conditions. The energy content of the data for both curve squeal (1.2 degrees yaw angle) and no curve squeal (zero degrees yaw angle)

are confined within the frequency range of 0 to 2000Hz. For dry contact condition, there is a magnitude of difference between curve squeal and no curve squeal. At curve squeal, a sharp peak around 1200 Hz can be observed. However, the actual value of the peak is not clearly visible from the plot. A quick glance through the wet, FM1 and FM2 power spectrum plots show more energy confined within 0 to 400Hz for both curve squeal and no curve squeal cases. The high-power spectrum peak observed at his frequency band indicates the high vibrations of the twin disc rig components excluding the wheel and rail rollers.
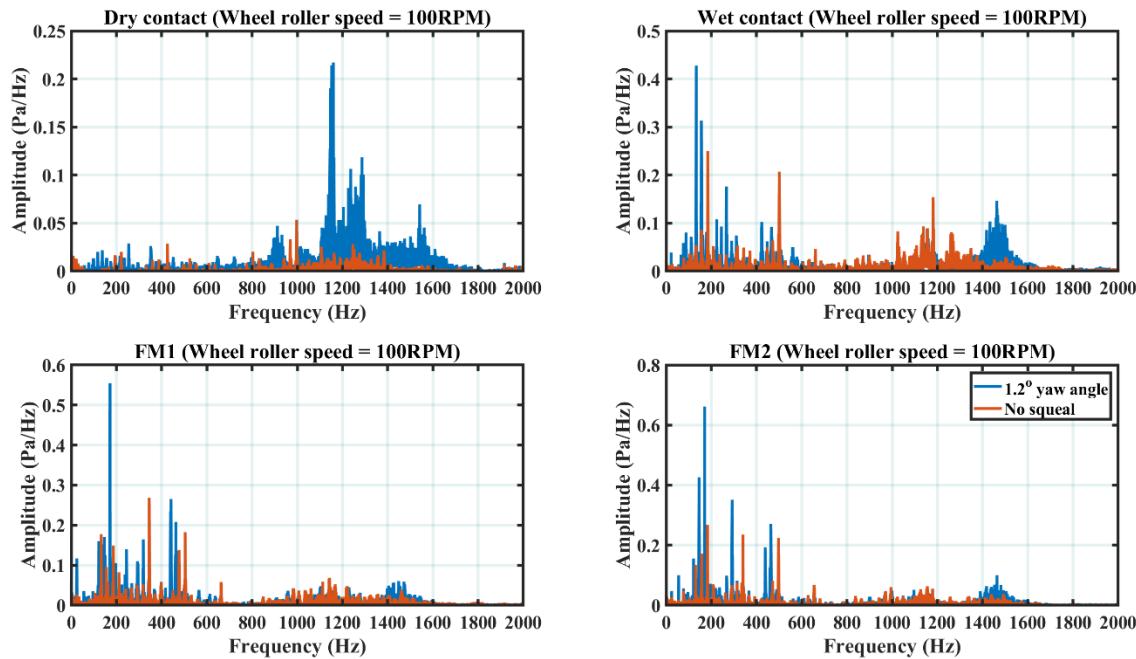
Figure 5.7: Power spectrum plots from the microphone for average wheel speed of 100 RPM

Figure 5.8 shows the section of the plot in Figure 5.7 for dry contact conditions for a frequency range of 1000Hz to 1500Hz. The reason for zooming into this frequency range is to be able to
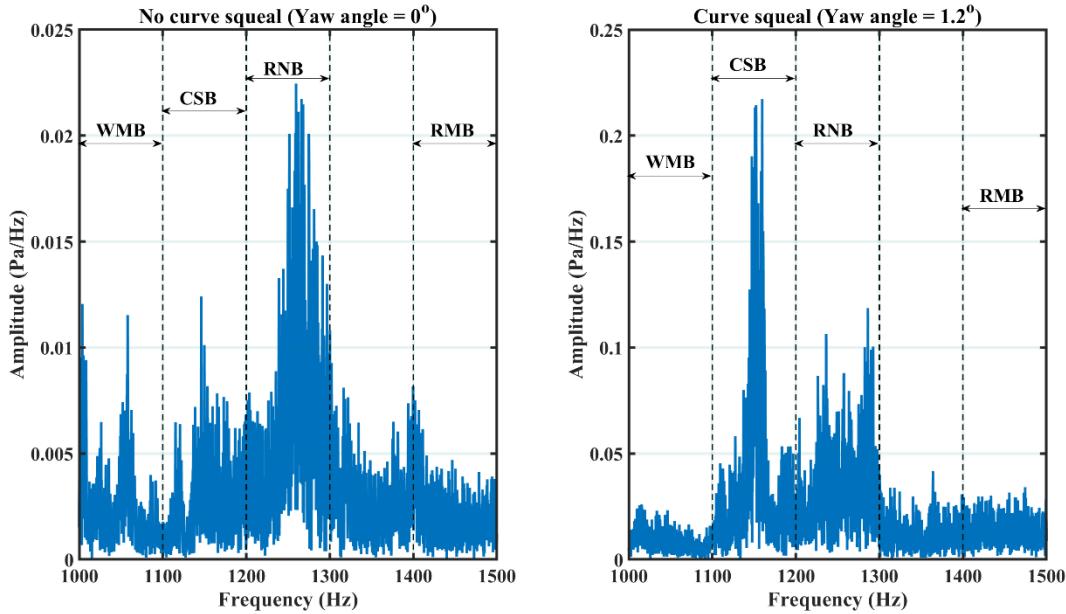
Figure 5.8: Zoomed in section of the power spectrum plots from the microphone for average wheel speed of 100 RPM

Identify what happens at the around the maximum power spectrum for dry contact conditions. Also, since the minimum natural frequency of the wheel and rail roller obtained from impact hammer tests and FEM is approximately 1095Hz, limiting the investigation of the frequency components of the sound signal to 1000Hz to 1500Hz is deemed sufficient to understand and characterize curve squeal. In other to understand the frequency components observed, power spectrum plot was divided into four distinctive regions. These regions include:

(a) Wheel mode band (WMB): This band represents the region where the second nodal diameter and natural frequency of the wheel roller. The excitation frequency of the wheel roller at this frequency is around 1095 Hz as obtained in impact hammer tests and FEM method in chapter 3.

(b) Curve squeal band (CSB): The rolling noise band represents the region where curve squeal is expected to occur. Although the curve squeal frequency tends to be associated with the second nodal diameter and natural frequency around 1095Hz, the dynamics of the system can cause a shift in this excitation frequency to this band. A high peak identified in this region is most likely to be as a result of curve squeal developed at one of the wheels.

129
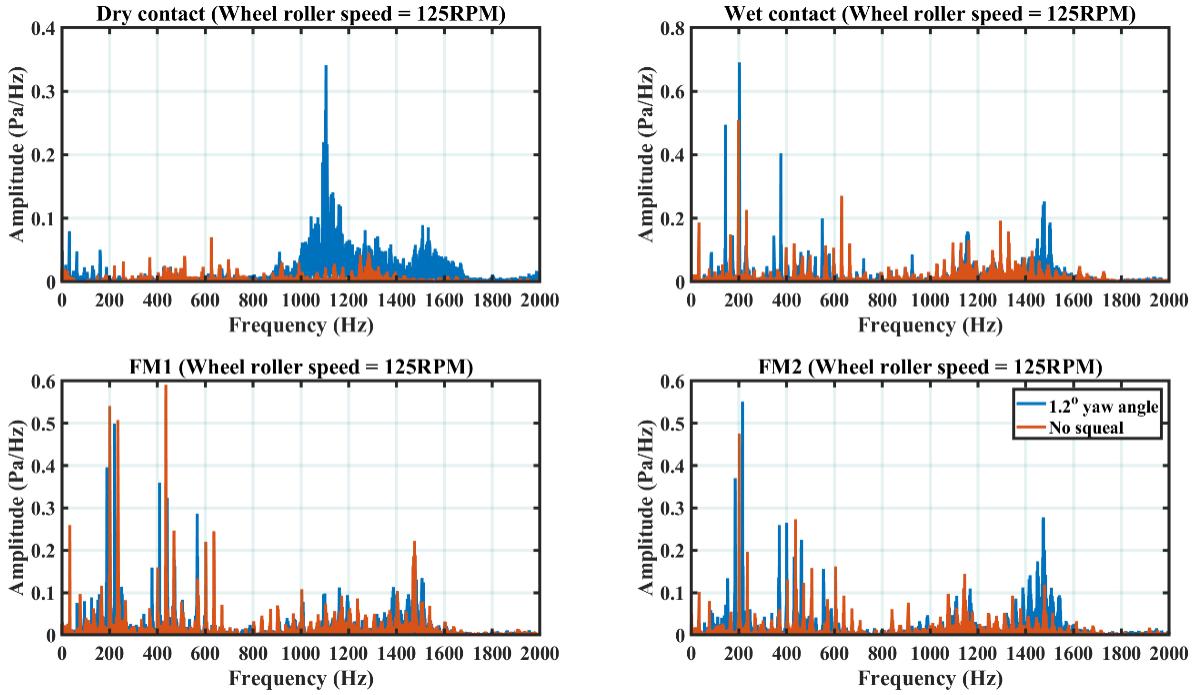
Figure 5.9: Power spectrum plots from the microphone for average wheel speed of 125 RPM

(c)   Rolling noise band (RNB): Rolling noise band represents the type of noise emanating as a result of the interaction between the wheel and rail roller dynamics. This noise dominates other excitation frequencies of the wheel and rail roller at central position.

(d)   Rail modal band (RMB): The rail modal frequency band represents the excitation region where the second nodal diameter and natural frequency of rail roller is located. From the results of the impact hammer tests and FEM, the natural frequency and second nodal diameter of the rail roller is at about 1441Hz. This frequency may change as a result of the system dynamics but however, the band identification allocated to this natural frequency represents this excitation frequency.
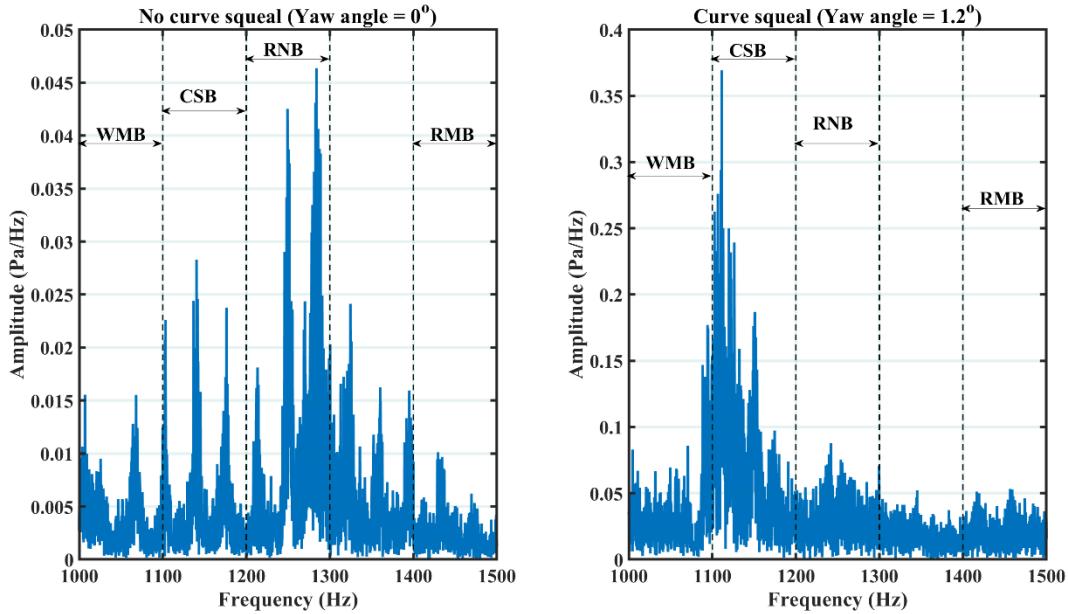
Figure 5.10: Zoomed in section of the power spectrum plots from the microphone for average wheel speed of 125 RPM

Having described in detail the frequency bands of interest for identification and characterization of curve squeal, Figure 5.8 shows the zoomed in section of the power spectrum plots for 100RPM in dry contact conditions. The highest spectral peak at zero degrees yaw of the rail roller is around 1270Hz centered around the RNB frequency range. This indicates that when the wheel and rail rollers are at central position, the noise emanating from the interaction of the wheel and rail roller is predominantly rolling contact noise. This noise does not pose any annoyance to the environment. It dominates other natural frequencies and modes of vibration of the wheel and rail roller. Figure 5.9 shows the power spectrum plots for average wheel speed of 125RPM. For dry contact conditions, a noticeable sharp peak about 1000Hz is observed. Although the actual frequency is not very visible, this peak indicates curve squeal generated by the wheel roller. For the wet, FM1 and FM2 contact condition, large sound peaks are recorded in the lower frequency region 0 Hz to 400Hz. Although this frequency range is not of interest for the development of curve squeal, it does indicate the excessive vibration of the twin disc rig components. A close look of the dry contact conditions results at average wheel speed of 125RPM is observed in Figure 5.10. A zero degrees yaw angle, the rolling noise band (RNB) dominates the other frequency bands. The natural frequency of the wheel roller at the wheel modal band (WMB) region is observed. In addition, the

rail roller natural frequency at the RMB band is also observed. This indicates that at zero degrees yaw angle, the wheel and rail rollers vibrate at their natural frequencies. The dynamics of the wheel and rail roller contact generate rolling noise around 1260Hz which suppresses all the other frequency bands. In Figure 5.10, a strong tonal peak frequency around 1120Hz is observed at 1.2 degrees yaw angle. All the other frequency bands have been suppressed by this excitation frequency. This frequency indicates the presence of curve squeal as a result of excitation of the natural frequency of the wheel roller (second nodal diameter and zero nodal circle).
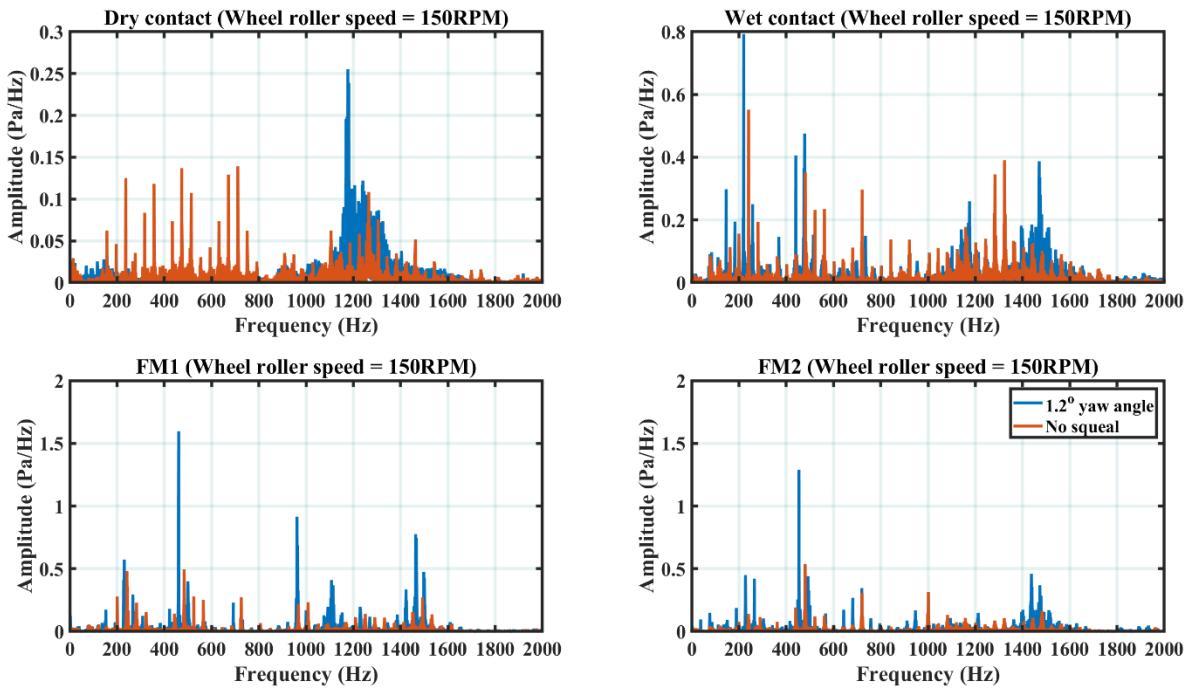
Figure 5.11: Power spectrum plots from the microphone for average wheel speed of 150 RPM

Figure 5.11 shows the power spectrum plots for average wheel speeds of 150RPM. The results obtained show similar trend with the previous wheel speeds. However, the presence of water, FM1 and FM2 in the wheel rail interface attenuates the dominate curve squeal frequency and transfers the vibration to other rig components. While this may not be harmful, it may be useful in future to identify which frequencies in the lower region have been excited as a result of the mitigation of curve squeal on the twin disc rig.

A zoomed in section of the power spectrum for dry contact conditions is shown in Figure 5.12. As has been observed for lower wheel speeds, the rolling noise frequency band dominates the other

frequency bands. The rolling noise as a result of the normal operation of the wheel and rail contact at central position (yaw angle = zero degrees) is around 1280Hz.
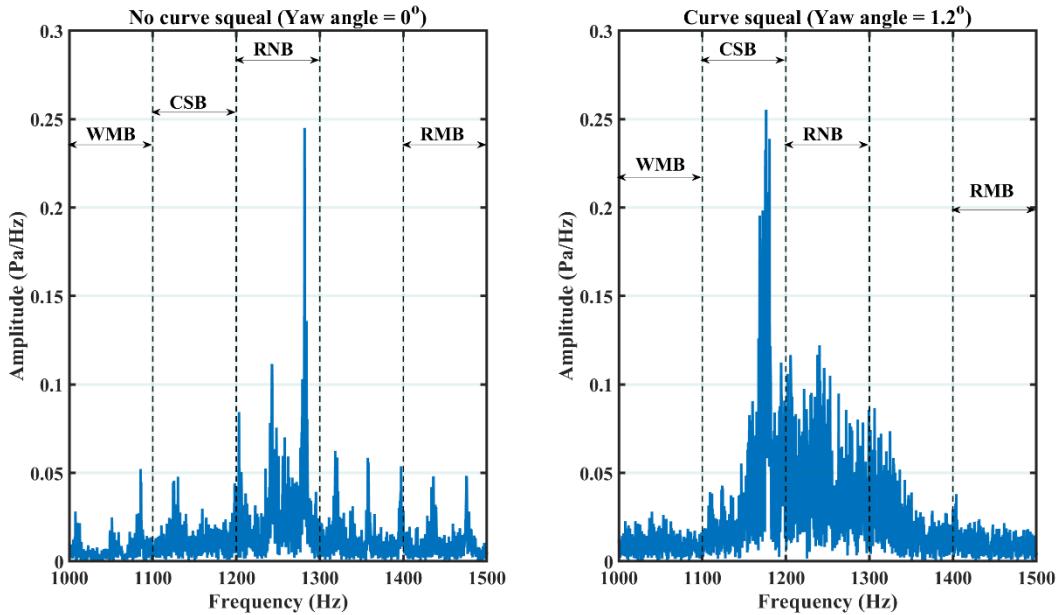
Figure 5.12: Zoomed in section of the power spectrum plots from the microphone for average wheel speed of 150RPM

Figure 5.12 also shows that transpires at curve squeal. A distinct peak at around 1185Hz in the curve squeal band (CSB) dominates and suppresses the natural frequencies of the wheel and rail roller. Figure 5.13 shows the power spectrum plots for average wheel speed of 175RPM. It can be observed from the plots that the dominant peak for dry contact conditions denotes the occurrence of curve squeal. However, it can be also be observed that at the highest speed of 175RPM, the contribution of the rail roller around the rail modal band (RMB) is observed. This indicates that the introduction of water, FM1 or FM2 to the wheel rail interface at high speeds suppresses the curve squeal frequency and amplifies the contribution of the rail roller. This observation is critical for curve squeal mitigation. The noise generated by the rail squeal (amplification of the second nodal diameter and natural frequency of the rail roller) at 175RPM did not cause annoyance as is the case of curve squeal.
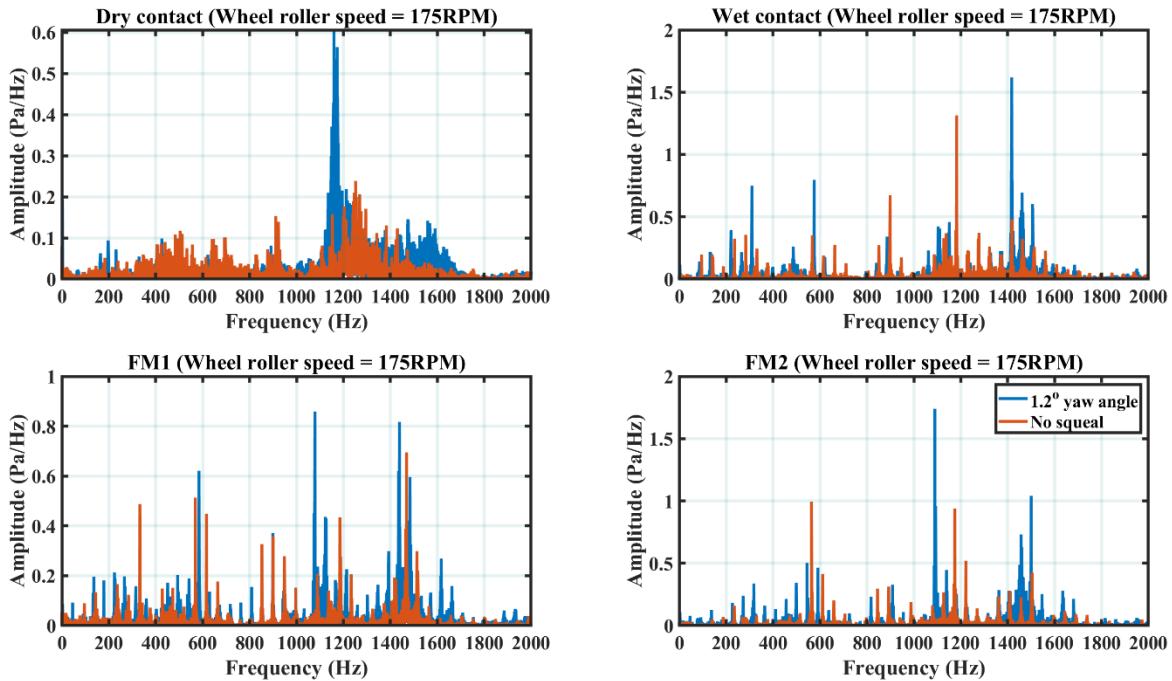
Figure 5.13: Power spectrum plots from the microphone for average wheel speed of 175 RPM

Figure 5.14 shows the closed in view of the power spectrum for average wheel speeds of 175RPM. The results obtained from the study show that the rolling contact frequency excited by the interaction between the wheel and the rail at central position observed in the RNB. In addition, curve squeal frequency around 1160Hz was observed at the CSB when the yaw angle of the rail roller was increased from zero degrees yaw angle to 1.2 degrees.

The application of spectrum analysis to the sound data has emphasized some vital features that where not observed using time domain feature extraction methods. Different excited frequencies were observed from the sound data for the various wheel-rail contact conditions. The clear disparity between the results obtained for zero degrees and 1.2 degrees yaw angle suggests that the spectrum data is suitable for feature extraction. Before feature extraction methods are applied, it is important to investigate in detail what happens during curve squeal mitigation on the twin disc rig.
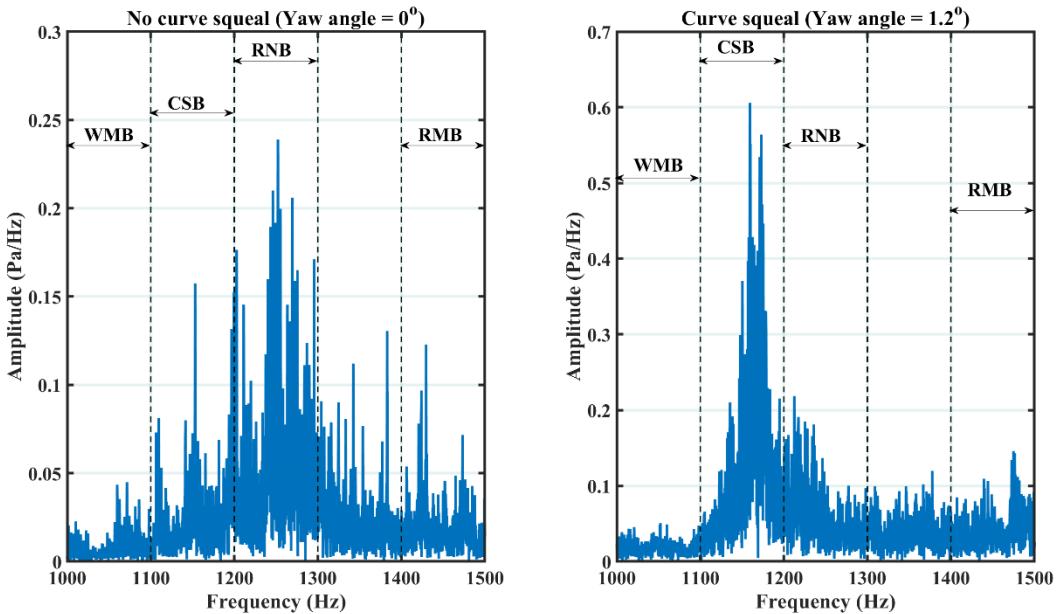
Figure 5.14: Zoomed in section of the power spectrum plots from the microphone for average wheel speed of 175RPM

5.6.2 Curve squeal mitigation understanding using spectral analysis

Having discussed in detail the development of curve squeal as a result of the wheel roller, it is necessary to understand what happens when water, FM1 and FM2 is applied to the wheel-rail interface. This phenomenon has been discussed briefly in the previous chapter. However, there are several key frequency components that are excited in the power spectrum when these contaminants are applied to the wheel-rail interface.

Figure 5.15 show the comparison between the power spectrum for dry and FM1 contact conditions for the four-wheel speeds and yaw angle of 1.2 degrees. At the lowest average wheel speed of 100RPM, the introduction of FM1 mitigated the curve squeal frequency in the CSB. However, the result of this was the excitation of the axial frequency of the rail roller in the RMB around 1450Hz. This indicates that the application of FM1 to the wheel-rail interface leads to rail squeal. This intense vibration as a result of the excitation of the rail roller dominant frequency does not cause annoyance to the environment. The amplitude of the excitation frequency at the RMB band increases with increasing average wheel speed from 100RPM to 175RPM. However, at high speeds, 150RPM and 175RPM, the power spectral amplitude at the CSB is noticeable. However,

the excitation at the CSB frequency does not matter at this point since it is dominated by the excitation frequency of the rail roller.
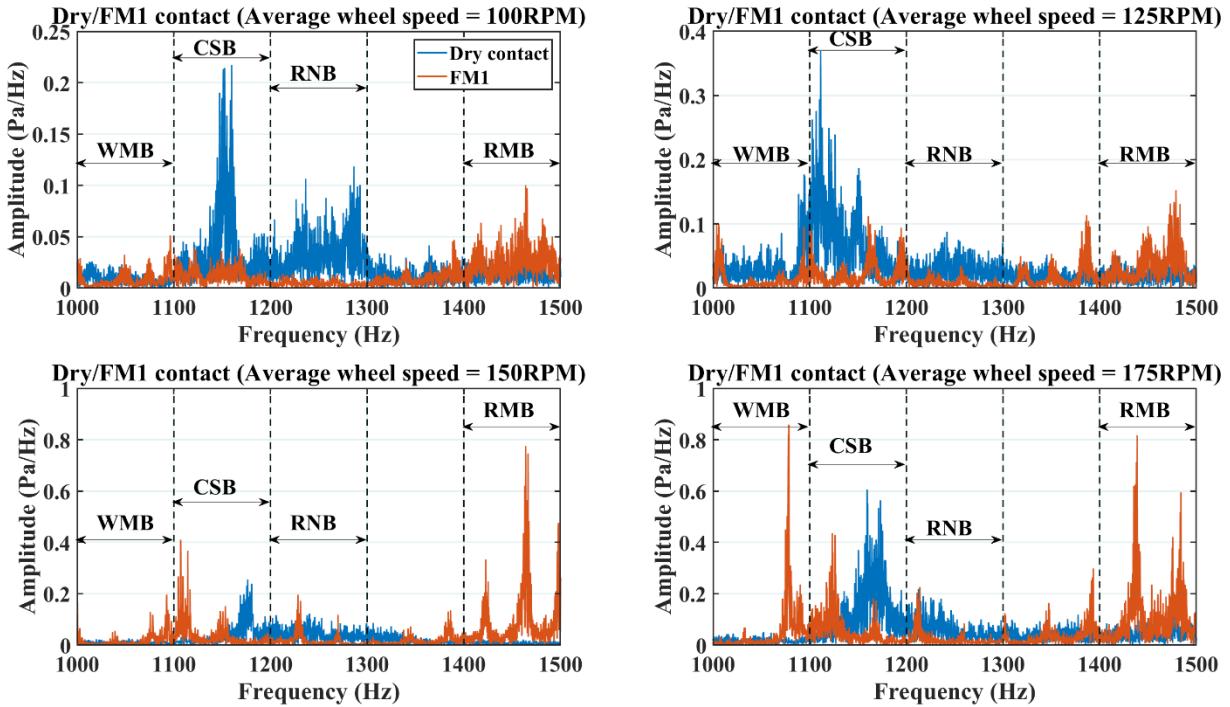
Figure 5.15: Curve squeal mitigation using FM1 contact conditions obtained from spectrum plots for the microphone at 1.2 degrees yaw angle.

Figure 5.16 shows the power spectrum plot comparison between dry contact conditions and FM2. Similar trend is observed by the aforementioned comparison between dry contact and FM1 contact conditions. Therefore, similar conclusions can be drawn from the comparisons made for FM1 and dry contact conditions.
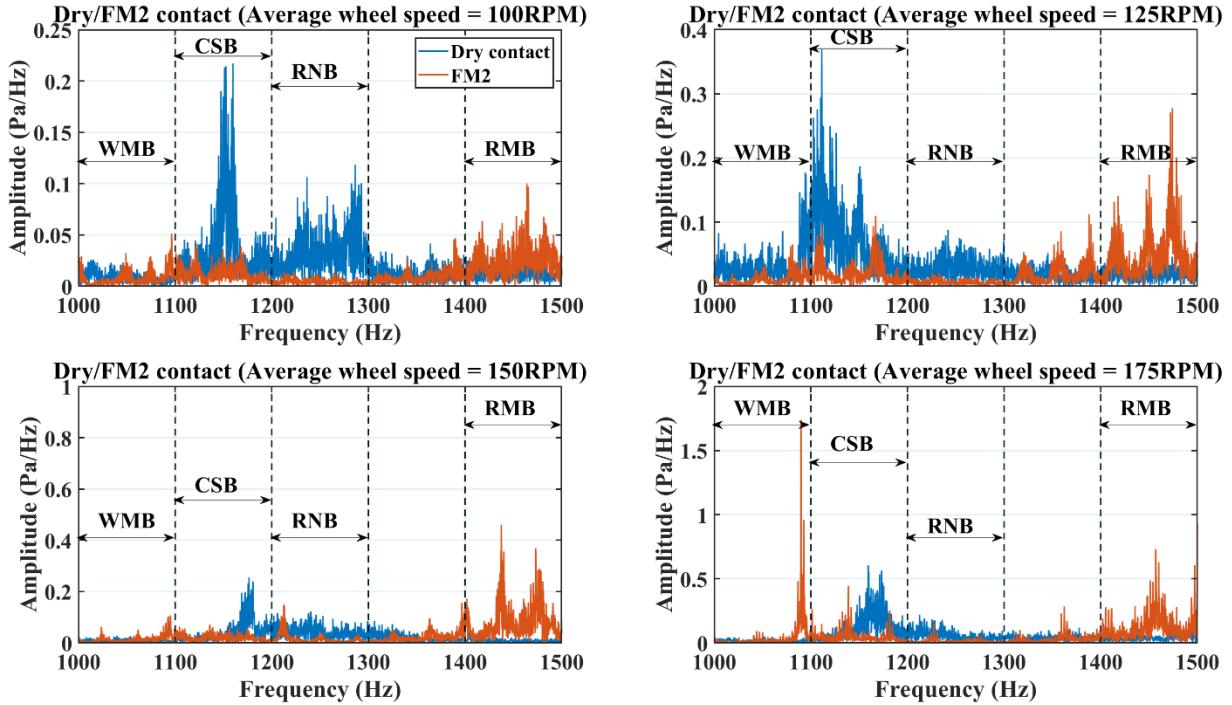
Figure 5.16: Curve squeal mitigation using FM2 contact conditions obtained from spectrum plots for the microphone.

Figure 5.17 shows the power spectrum plots for dry and wet contact conditions at 1.2 degrees yaw angle. It can be observed that for the four average wheel speeds, the introduction of water to the wheel rail interface at a steady rate of 0.4m/min attenuated the excitation frequency responsible for curve squeal at the CSB band. However, as the wheel speed increased from 150RPM to 175RPM, the attenuation of the excitation frequency at the CSB band was not effective. However, this resulted in excessive rail squeal due to the excitation of the second nodal diameter and natural frequency of the rail roller in the RMB band. It can be concluded that the introduction of water at a steady flow rate to the wheel-rail interface succeeded in eliminating curve squeal by increasing the contribution of the second nodal diameter and natural frequency of the rail roller. This balancing effect was sufficient to mitigate curve squeal from the wheel roller.
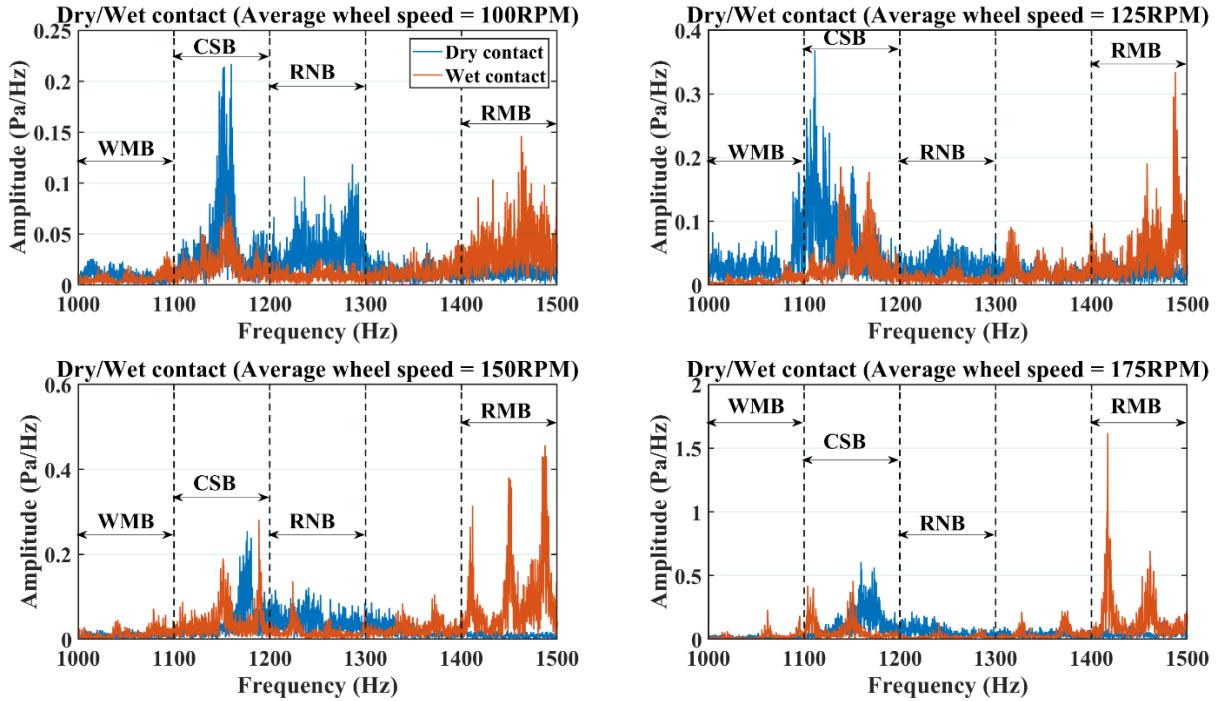
Figure 5.17: Identification of curve squeal mitigation using wet contact conditions obtained from spectrum plots for the microphone.

5.6.3   Curve squeal mitigation understanding using harmonics of the sound data

Rotating machines are known to be source so harmonics in a typical vibratory system. Harmonics are formed as a result of multiples of the dominant frequency. In most bearing applications, harmonics are as a result of unbalance and misalignment of the bearing shafts rotating speed. In the development of curve squeal, harmonics in the data have been identified by several authors in previous research. (Hsu et al., 2007) discovered from their analysis that curve squeal is a result of dominant wheel mode natural frequencies and its corresponding harmonics. (Rudi and Joachim, 2007) also concluded that curve squeal dominant frequency generates corresponding harmonics from the radiated sound and vibration data obtained in real track measurements.

In this study, harmonics of the dominant curve squeal frequency located at the CSB would be extensively discussed. In addition, the mitigation effect of water, FM1 and FM2 in curve squeal would be investigated.

Figure 5.18 show the comparison between the dry and FM1 contact conditions for four average wheel speeds when the rail roller is yawed at 1.2 degrees angle. At 100RPM, the fundamental curve squeal frequency is about 1150hz. The harmonics of this fundamental frequency 2X and 3X

are around 2300Hz and 3450Hz respectively. Similarly, for 125RPM wheel speed, the fundamental frequency is centered around 1130Hz while the 2nd and 3rd harmonics are approximately 2260Hz and 3390Hz respectively. At higher speeds, the 2nd and 3rd harmonic sound amplitudes tend to be attenuated compared to the dominant axial modes of the wheel and rail roller.
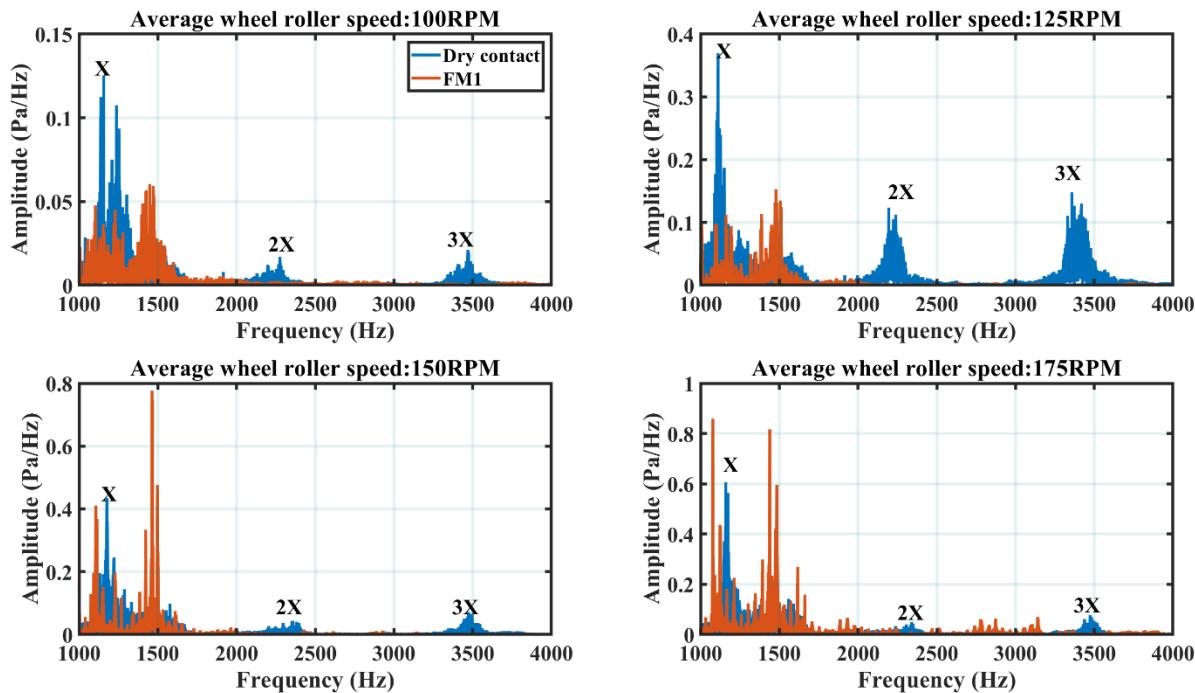
Figure 5.18: Comparison between power spectrum of dry and FMI at 1.2 degrees yaw angle for frequencies ranging from 1000Hz to 4000Hz.

It can be observed from Figure 5.19 that at the higher frequency harmonics sound amplitudes diminish at higher speeds 150RPM and 175RPM. It can also be inferred from the plots that the introduction of FM1 and FM2 eliminates the high frequency harmonics for all four average wheel speeds. However, the friction modifier did not completely attenuate the fundamental frequency. Therefore, this could suggest that the elimination of the harmonics is associated with the positive friction characteristic of the adhesion coefficient associated with friction modifier FM1 as discussed in chapter 4. The positive friction characteristics is synonymous with the reduction of the transverse forces developed at the wheel rail interface.
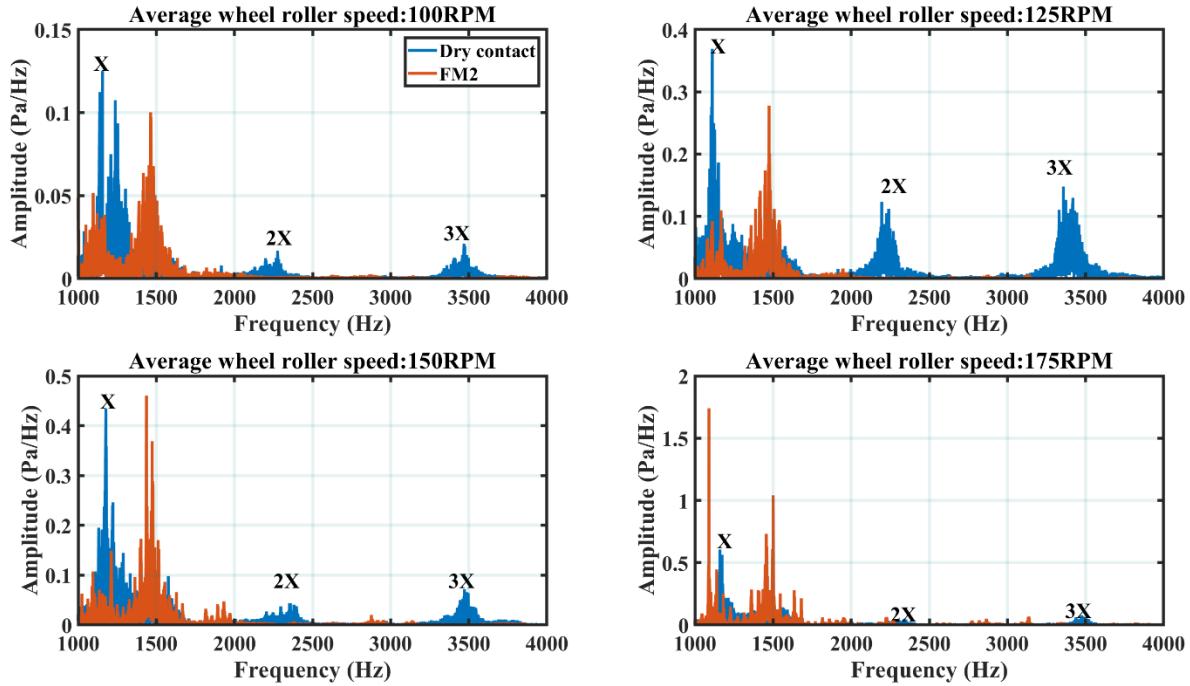
Figure 5.19: Comparison between power spectrum of dry and FM2 at 1.2 degrees yaw angle for frequencies ranging from 1000Hz to 4000Hz.

Figure 5.19 shows the comparison between the power spectrum of dry and FM2 sound data when 1.2 degrees yaw angle is applied to the rail roller. Similar conclusions can be inferred from the analysis of dry and FM1 contact conditions. It is hard to distinguish between the performance of FM1 and FM2 in curve squeal mitigation from the results shown in Figure 5.18 and Figure 5.19. Both friction modifiers attenuate the fundamental dominant curve squeal frequency, amplify the dominant frequency of the rail roller and completely eliminate high frequency harmonics.

Figure 5.20 show the comparison between the power spectrum of dry and water when 1.2 degrees yaw angle is applied to the rail roller. Similar conclusions can be drawn from the comparisons between dry contact and the friction modifiers. However, the application of water to the wheel-rail interface at a does not attenuate the curve squeal frequency at the highest wheel roller speed. It can be observed that the fundamental at X has similar amplitude with sound data at wet contact conditions.
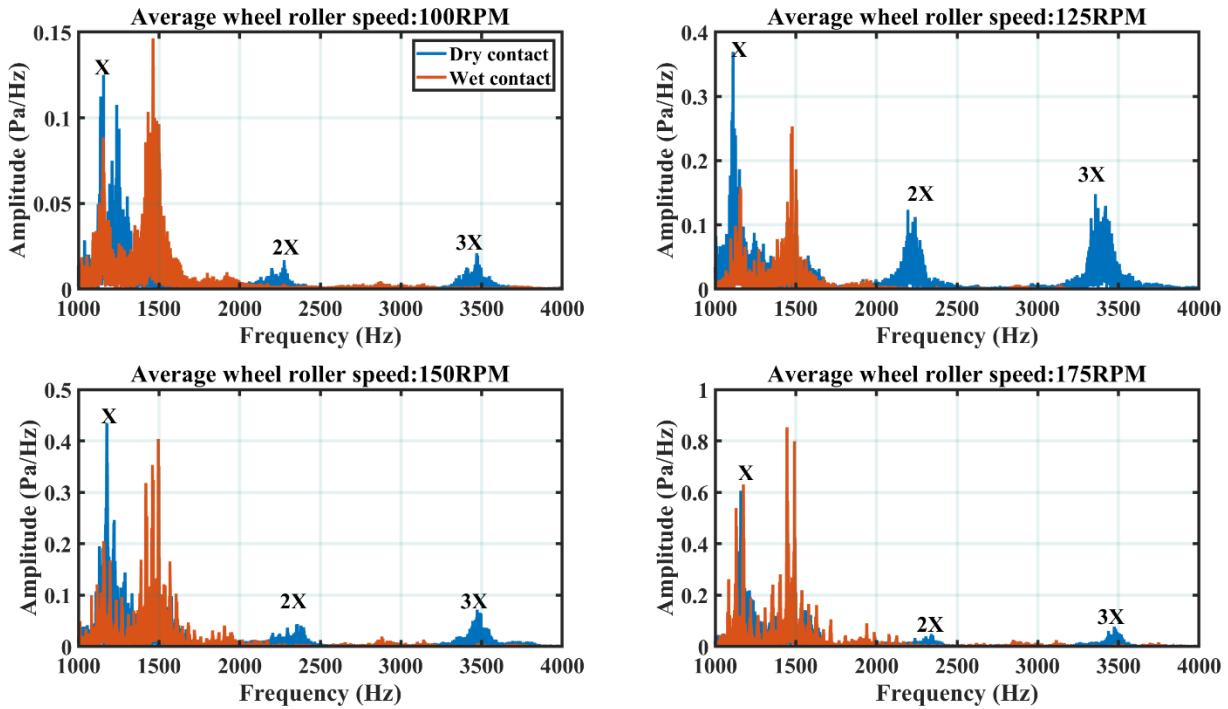
Figure 5.20: Comparison between power spectrum for dry and wet contact at 1.2 degrees yaw angle for frequencies ranging from 1000Hz to 4000Hz.

From Figure 5.14, it can be observed that the transition between the rolling contact noise region and the curve squeal region occur at yaw angles around 0.9^0, 0.8^0, 0.6^0 and 0.5^0 for average wheel speeds 100RPM, 125RPM, 150RPM and 175RPM respectively. Notice that the peak amplitude of the curve squeal frequency changes for each average wheel speed but is within the 1100Hz to 1200Hz band. Also, the rolling contact noise band frequency changes is well for each average wheel speed but lies within the 1200Hz – 1300Hz frequency band range.

5.7   Onset curve squeal determination in using sound data for dry contact condition

The previous section has thoroughly analysed frequency components of the wheel and rail roller using spectral analysis. This section seeks to identify the incipient development of curve squeal. This would help identify the transition between no curve squeal and curve squeal. For dry contact conditions sound data was taken every 5 seconds at 0.1 degrees yaw angle increment up till 1.4 to 1.5 degrees.

Figure 5.21 shows the effect of yaw angle variation on the CSB and RNB. The sound pressure in decibels was measured at the start of experiment for the four average wheel speeds. The measured

sound pressure level for the wheel speeds at dry contact conditions was respectively 80dB, 84dB, 92dB and 100dB. The sound pressure data was converted from pascals to dB and then the measured sound pressure level in dB for the respective average wheel speeds was added to obtain the plots shown in Figure 5.22. As expected, the rolling contact noise dominates when no curve squeal is detected. The transition between no curve squeal and curve squeal for the average wheel speeds 100RPM, 125RPM, 150RPM and 175RPM are respectively 0.95 degrees, 0.9 degrees, 0.6 degrees and 0.5 degrees respectively.
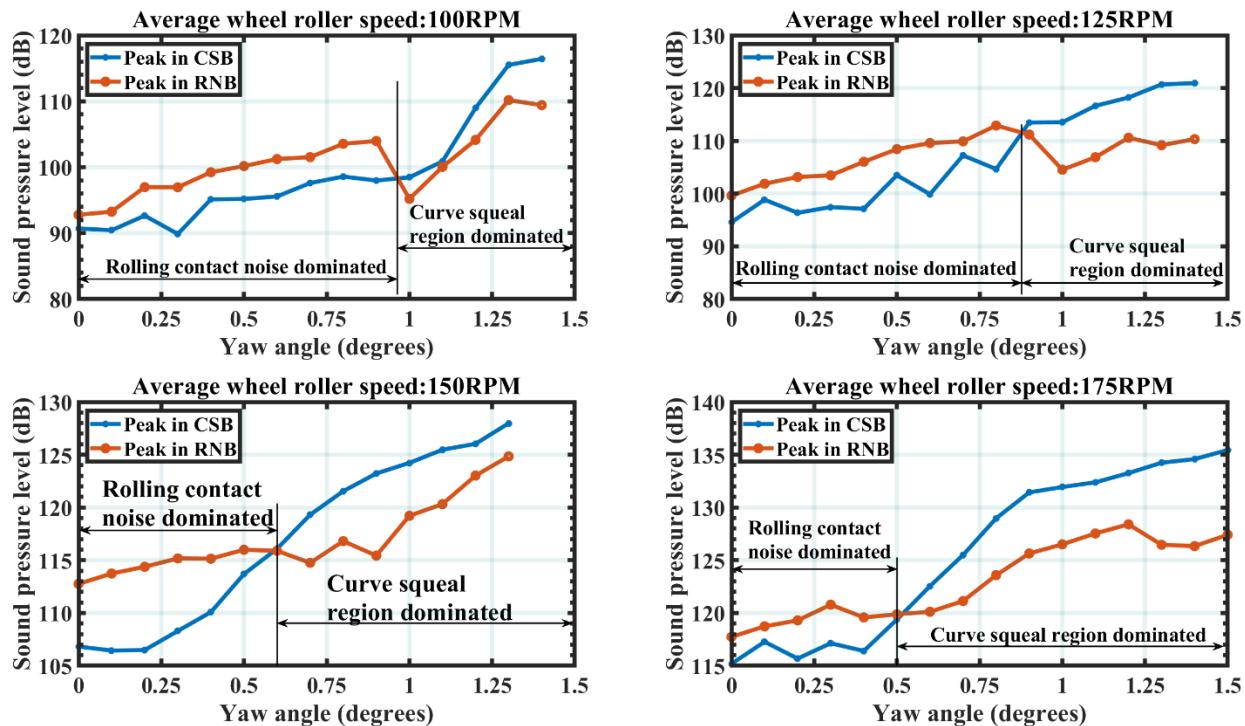
Figure 5.21: The effect of varying yaw angle on spectral peak of sound for the dominant frequency bands for dry contact conditions

The results show that the increase in the wheel rotation speed results in the decrease in the transition between no curve squeal and curve squeal region. (Liu and Meehan, 2013) also obtained similar results whereby the increase in speed is inversely proportional to the transition yaw angle between curve squeal and no curve squeal.

5.8 Feature extraction methods from the acoustic spectrum analysis data

This section presents the application of feature extraction techniques that are relevant in the condition monitoring applications. The feature extraction methods were selected based on their relevance and suitability in detecting and characterizing curve squeal from the sound data. Before feature extraction was carried out, bandpass filter of the frequency bands CSB, RNB and RMB was designed for each sound data and converted to frequency domain using spectrum analysis. Thereafter, the condition monitoring indicators are extracted from the data.

5.8.1 Feature extraction using spectral peak analysis method

This feature represents the maximum sound amplitude of the power spectral density data obtained from the microphone. The spectral peak for each band is expressed as follows:

$$P_{CSB} = \max(|X_{CSB}|)$$
$$P_{RNB} = \max(|X_{RNB}|) \tag{5.5}$$
$$P_{RMP} = \max(|X_{RMB}|)$$

where P_{CSB}, P_{RNB} and P_{RMB} represent the maximum peak at frequency band CSB, RNB and RMB respectively. X_{CSB}, X_{RNB} and X_{RMB} represent the bandpass power spectrum for frequency bands CSB, RNB and RMB.

Figure 5.22 shows the variation of the yaw angle with respect to the spectral peak for the aforementioned frequency bands CSB, RNB and RMB. No curve squeal is observed at yaw angles lower than 1.1 degrees for average wheel speed of 100RPM. The spectral peak obtained from the RNB dominates the other frequency bands. Similarly, no curve squeal occurs for yaw angles less than 0.9 degrees, 0.6 degrees and 0.5 degrees for average wheel speeds 125RPM, 150RPP and 175RPM respectively. The reason for this is as a result of the increase in wheel speed. Above these yaw angles for all average wheel speeds, the spectral peak in the CSB band dominates. This indicates that the wheel roller is responsible for curve squeal. The shift in dominant axial mode of the wheel roller to the CSB band is as a result of the wheel-rail contact dynamics.

The application of spectral peak as a feature extraction method for early detection of curve squeal has effectively presented the difference between no curve squeal and curve squeal from the microphone data.
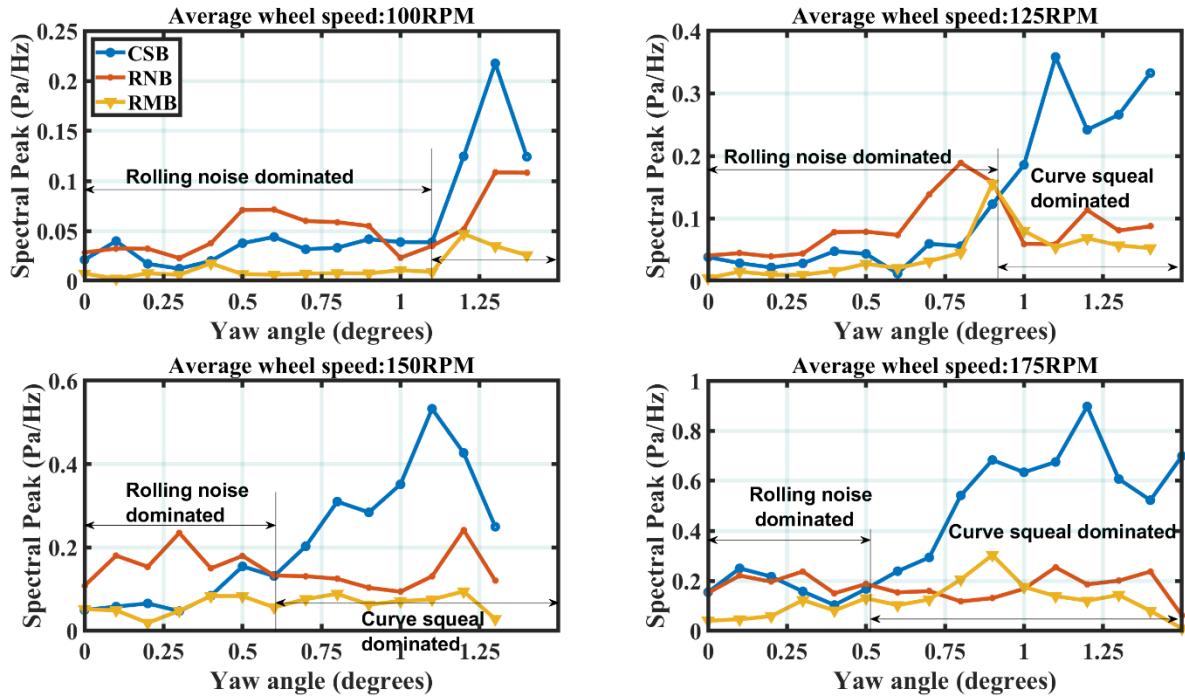
Figure 5.22: Effect of varying yaw angle on bandpass filtered rms values from the dominant frequency bands for dry contact conditions

5.8.2 Feature extraction using spectral rms analysis method

The spectral root mean square (RMS) feature utilizes the same expression as equation (5.2). The spectral rms of the band pass filtered rms values are calculated as follows:

$$RMS_{CSB} = \left(\frac{1}{N} \sum_{n=1}^{N} |X_{CSB}|^2 \right)^{\frac{1}{2}}$$

$$RMS_{RNB} = \left(\frac{1}{N} \sum_{n=1}^{N} |X_{RNB}|^2 \right)^{\frac{1}{2}} \tag{5.5}$$

$$RMS_{RMB} = \left(\frac{1}{N} \sum_{n=1}^{N} |X_{RMB}|^2 \right)^{\frac{1}{2}}$$

Where RMS_{CSB}, RMS_{RNB} and RMS_{RMB} represent the spectral RMS of the frequency bands CSB, RNB and RMB respectively. N represents the sample size of the sound data.

Figure 5.23 shows the spectral RMS statistical feature applied to the average sound data for the average wheel speed of 100RPM, 125RPM, 150RPM and 175RPM. It can be observed that the

144

transition between the rolling contact noise region and the curve squeal region occur at yaw angles around 1.1^0, 0.9^0, 0.6^0 and 0.6^0 for average wheel speeds 100RPM, 125RPM, 150RPM and 175RPM respectively. The slight changes in the transition between the rolling contact noise region and the curve squeal noise region obtained from the previous section is increase in wheel rolling speed. As the wheel roller speed increases, the transition between curve squeal and no curve squeal reduces. This implies that wheels are more likely to squeal at higher wheel speeds. There is a clear difference between spectral RMS at curve squeal and spectral RMS at no curve squeal (rolling noise dominated).
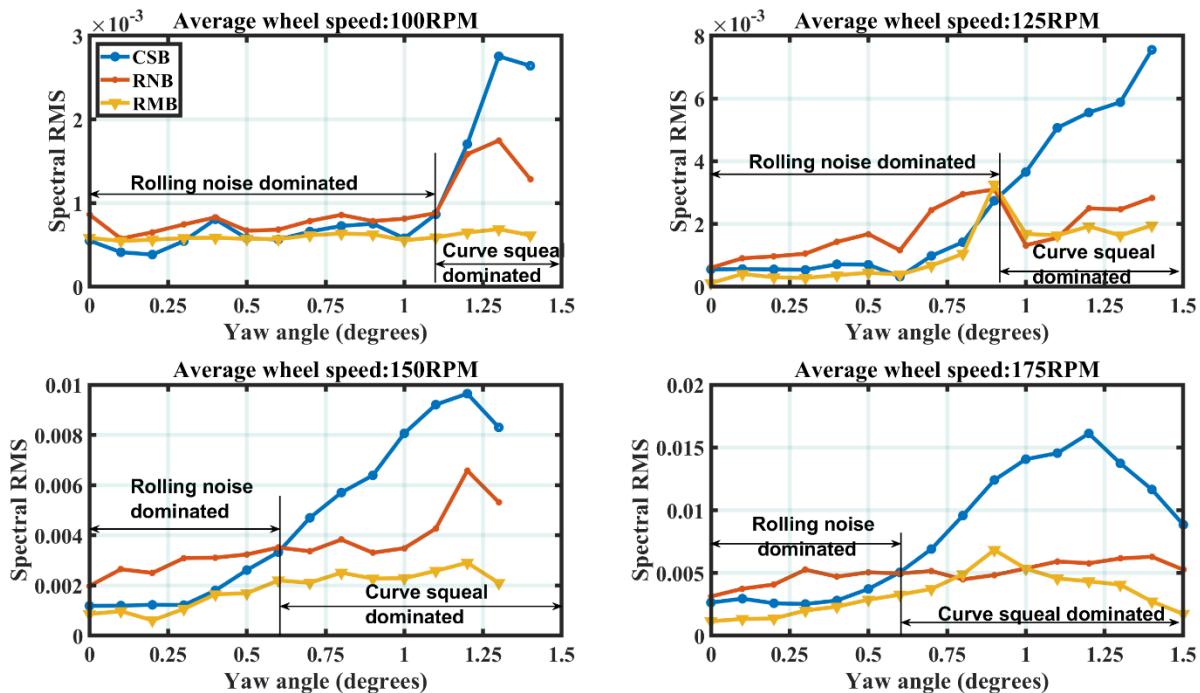
Figure 5.23: Spectral RMS analysis for the three frequency bands under four average wheel speeds.

Figure 5.24 shows the statistical spectral RMS for average wheel speed of 100RPM, 125RPM, 150RPM and 175RPM respectively under four different contact conditions. The spectral RMS of the CSB frequency band was taken for each yaw angle. The yaw angle resolution for FM1 and FM2 was 0.05 degrees. The results obtained show a clear disparity between dry contact conditions and water, FM1 and FM2 spectral rms at the transition yaw angles between no curve squeal and curve squeal. The transition yaw angles between no curve squeal and curve squeal is 1 degree, 0.9 degrees, 0.75 degrees and 0.5 degrees respectively.
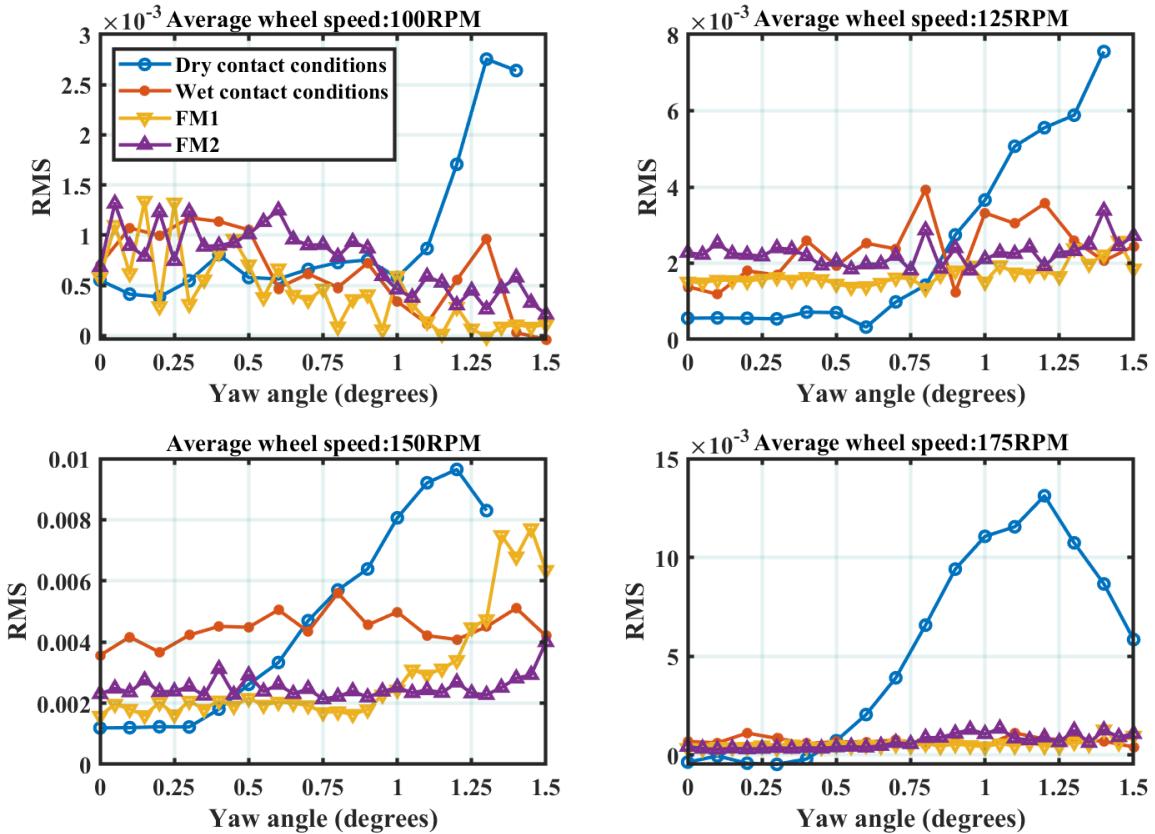
Figure 5.24: Spectral RMS analysis for the CSB frequency band four different contact conditions.

Figure 5.25 shows the spectral RMS of the second harmonics (2X) frequency band (2200Hz to 2400Hz) for all four contact conditions and four average wheel speeds. The results obtained show a clear difference between no curve squeal and curve squeal. The transition yaw angles can be observed as approximated 1.1 degrees, 0.9 degrees, 0.5 degrees, and 0.5 degrees respectively. Beyond the transition yaw angles, a sharp increase in the spectral RMS is observed. This signifies that the development of curve squeal in the test rig.

Figure 5.26 shows the spectral RMS of the third harmonics (3X) frequency band (3400Hz to 3600Hz) for all average wheel speeds and four contact conditions. The transition yaw angles between curve squeal/curve squeal mitigation and no curve squeal are 1.1 degrees, 0.9 degrees, 0.5 degrees and 0.5 degrees for average wheel speeds of 100RPM, 125RPM, 150RPM and 175RPM. There is a positive correlation between the spectral rms obtained for the second harmonics and the spectral RMS obtained for the third harmonics in terms of the transition yaw angles.
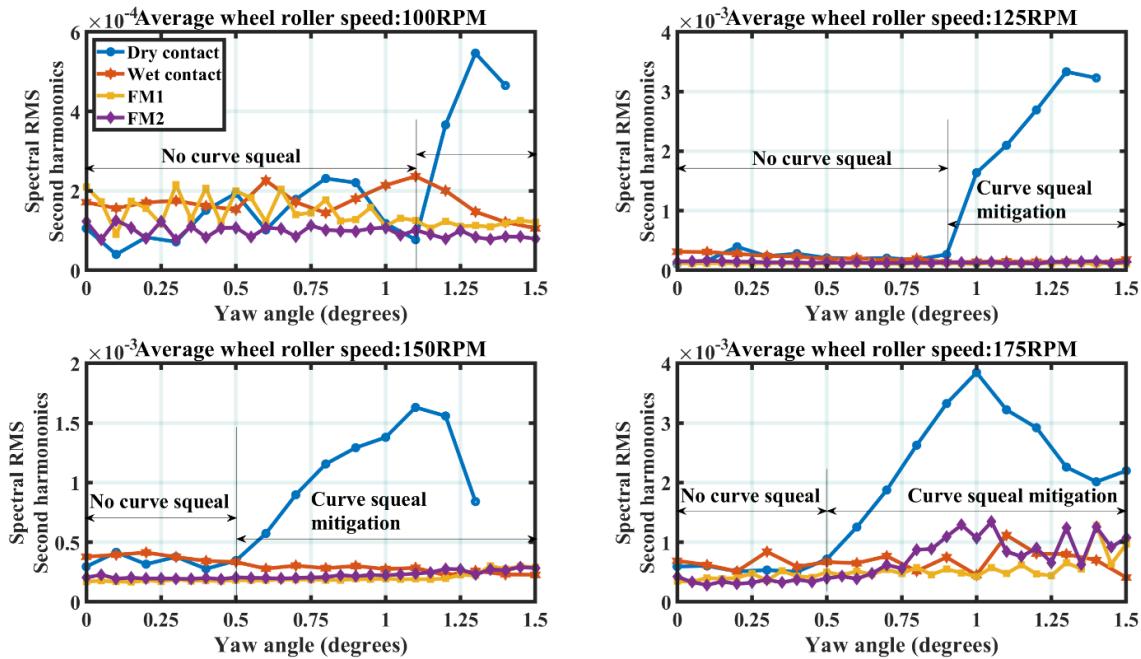
Figure 5.25: Spectral RMS analysis for the second harmonics for four different contact conditions and four average wheel speeds.

This signifies that the spectral RMS of the second and third harmonics using the specified 200Hz bandwidth is provides a strong indication of the onset development of curve squeal and the
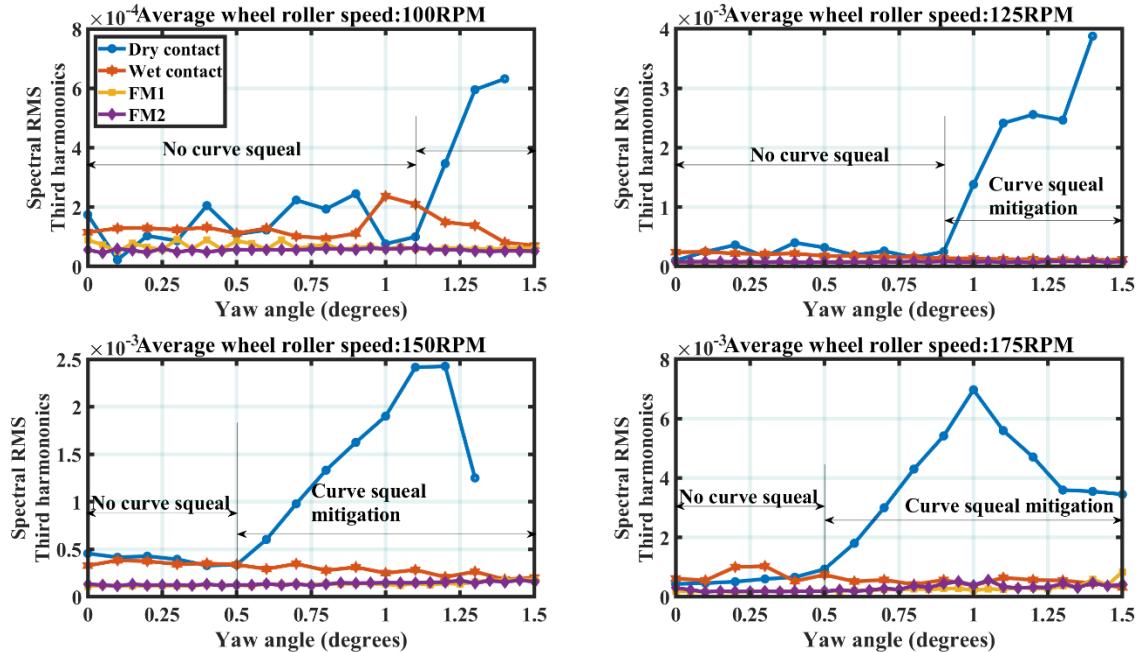
Figure 5.26: Spectral RMS analysis for the third harmonics for four different contact conditions and four average wheel speeds.

mitigative influence of the water, FM1 and FM2 to curve squeal in the test rig. To conclude, the application of spectral RMS feature extraction method for the determination of onset development of curve squeal and curve squeal mitigation is suitable for the intended application. Even with the variation of the wheel speed and yaw angle, this feature extraction method performed efficiently.

5.9   Summary of acoustic analysis performed on the test rig

The application of time domain methods and spectrum analysis has been applied to the sound data. For dry contact conditions, the sudden periodic outputs of the sound data in the time domain at large yaw angles is an indication of wheel speed reduction as the yaw angle increases. This trend was a result of the excessive load demand applied to the three-phase induction motor as the yaw angle of the rail roller increases. The load is as result of the increase in the transverse (lateral) vibration and force developed at the wheel rail contact for large yaw angles.

Five condition monitoring indicators were applied to the sound data for feature extraction. The five condition monitoring indicators; peak, rms, crest factor, kurtosis and skewness clearly differentiate between regions of rolling contact noise (no curve squeal) and curve squeal region. A clear disparity between curve squeal and no curve squeal was observed when peak and rms features were extracted from the sound data for four average wheel speeds and yaw angle variation from zero degrees to 1.5 degrees. The inclusion of the four contact conditions help to differentiate between no curve squeal and curve squeal region. A kurtosis value greater than three indicated the development of curve squeal for the sound data as the yaw angle increased. In addition, skewness extreme negative skewness of the sound data at high yaw angles indicated the development of curve squeal, while skewness values around zero indicated no curve squeal. The kurtosis and the skewness conclusions were drawn from the comparison of the dry, wet, FM1 and FM2 contact conditions as the yaw angle increased from zero degrees to 1.5 degrees for four average wheel speeds. Increase in average wheel speed resulted in decrease in the transition yaw angle (yaw angle between no curve squeal and curve squeal region).

Spectral analysis was applied to the sound data to investigate the frequency components of the wheel and rail roller responsible for curve squeal. The result showed that the wheel is the main contributor of curve squeal and that the curve squeal frequency is located at the curse squeal band (CSB) ranging from 1100Hz to 1200Hz. Four frequency bands were used to identify and characterize curve squeal and it mitigation for all four wheel speeds as the yaw angle was increased

from zero to 1.5 degrees yaw angles. For the spectral peak and spectral RMS, an initial bandpass filter was designed for four frequency band positions WMB (1000Hz to 1100Hz), CSB (1100Hz to 1200Hz), RNB (1200Hz to 1300Hz) and RMB (1400Hz to 1500Hz). This was necessary to extract the natural frequencies and second nodal diameter of the wheel roller (located in the WMB) and rail roller (located in RMB). The curve squeal band (CSB) had the highest spectral energy and was therefore used to indicate onset and development of curve squeal on the twin disc rig. The actual frequencies in the CSB band responsible for curve squeal are slight deviations of the actual axial frequency of the wheel roller around 1095Hz obtained from impact hammer tests and FEM analysis.

The strong tonal frequency in the CSB band extracted using spectral analysis was observed to develop second and third harmonics. This indicates that curve squeal is a strong tonal noise that resonates throughout the whole test rig along with its corresponding harmonics. Further investigation to the onset development of curve squeal was investigated using initial bandpass filter applied at the harmonic locations on the power spectrum. The second and third harmonic bandpass filter frequency bands are 2200Hz to 2400Hz and 3400Hz to 3600Hz. The spectral peak and RMS of the second and third harmonic frequency bands were computed for yaw angle variation from zero to 1.5 degrees for all four-wheel speeds and four different wheel rail contact conditions. The transition yaw angles obtained are exactly the same for each harmonic band. This indicates that the utilization of the harmonic bands is a strong indicator for investigating and analysing the early development of curve squeal and curve squeal mitigation.

Finally, the introduction of water, FM1 and FM2 to the wheel rain interface completely eliminated the second and third harmonics developed from the dominant frequency component responsible for curve squeal. In addition, the introduction of these contaminants attenuated the dominant frequency in the CSB and increased the contribution of the rail roller dominant frequency in the RMB.

Chapter Six: Curve squeal monitoring using vibration analysis methods

This chapter covers the application of vibration analysis methods for detecting and monitoring curve squeal in the test rig. Time domain methods would be used to investigate and characterize curve squeal. Some of the feature extraction techniques that would be employed in this chapter include rms, kurtosis, skewness, and crest factor. Initially the time domain methods such as rms, crest factor, kurtosis and skewness are used to characterize curve squeal. Then the probability density function was then applied to the time domain data. The sudden difference in the pdf heights is used to detect and characterize curve squeal. Frequency domain methods was then used to also characterize and monitor curve squeal for the test rig. Baseline spectrum analysis and power spectral density of the vibration data was applied to the data to extract vital information through their respective plots.

6.1 Introduction – Vibration analysis for condition monitoring of curve squeal

The application of vibration analysis has been widely utilised in the field of condition monitoring especially for fault diagnosis of rotating machines. Most machines and industrial systems have some form of vibration, which might be considered as abnormal or normal. It is understood in literature that excessive or abnormal vibration in a machine could be caused by several reasons. When a fault is observed in a typical dynamic system, the amplitude of vibration changes depending on the fault magnitude. These vibration amplitudes are detected using several sensors such as velocity transducers, proximity sensors and accelerometers. Accelerometers are widely utilised for vibration analysis amongst the mentioned sensors (Vishwakarma et al., 2017).

However, in railways excessive vibration of wheelset as it negotiates round a tight curve has been associated to result in annoying tonal noise (curve squeal). It is a well-established fact in literature that unsteady lateral creepage is the main cause for generation of curve squeal while flange rubbing and longitudinal creepage are not relevant to curve squeal (Liu and Meehan, 2013), (Liu and Meehan, 2016). Based on this conclusion from literature, accelerometers where installed to measure lateral vibrations of the wheel and rail roller for varying yaw angles with the aim of identifying and characterizing curve squeal. Two accelerometers mounted laterally on the wheel and rail roller (see Chapter 3 for full description of mounting) would therefore be used to extract features from the vibration data that relate to curve squeal development as the yaw angle between the rollers is increased. In addition, the effect of changing the characteristics of the wheel-rail roller interface by the application of water and friction modifiers would be investigated in detail. The mitigation measures used to minimize curve squeal in the wheel would be investigated using vibration analysis. Several vibration analysis methods would for studying curve squeal phenomena would be employed in this chapter. These methods are grouped into three main classes, time domain, frequency domain and time-frequency domain. In each class, various range of methods are presented and used to characterize curve squeal. The advantages and disadvantages of each vibration analysis methods would be highlighted and conclusions would be drawn based on the results obtained.

6.2 Time domain analysis

Time domain methods have been widely applied in condition monitoring fields for several systems. The main aim of this vibration analysis method is to determine the statistical

characteristics of the vibration data. Time domain analysis assumes that the vibration data is random and possesses unique statistical characteristics. The main merit of applying time domain analysis is their relative ease of implementation in online condition monitoring systems. They are also free of picket-fence effect, sampling rate, spectral leakage and signal aliasing. Figure 6.1 to Figure 6.4 displays the vibration data measured from the wheel and rail roller accelerometers. The measurements were taken for average wheel speeds of 100 RPM, 125 RPM, 150 RPM and 175 RPM respectively. Also, different wheel-rail contact conditions such as dry, wet, FM1 and FM2 was measured for each speed and yaw angle. For the vibration measurements, only yaw angles where noticeable curve squeal was observed for each average wheel speed was displayed. As was stated in Chapter 3, the wet contact conditions comprised of constant application of water through a flexible hose to the rail roller at speeds 0.5 ml/min. In addition, 0.5 ml of FM1 and FM2 was applied using syringed tube to the rail roller surface. The test rig was then run for approximately 3 minutes before vibration measurements commenced. For each yaw angle, measurements were taken for a time length of 5 seconds to ensure that adequate time representation of vibration data is measured. This time is not too short to miss vital information from the data and at the same time not too long which could lead to excessive wear and corrugation of the wheel and rail rollers at higher yaw angles.

Figure 6.1 shows the vibration time series data of the wheel and rail roller on the test rig operating at an average speed of 100 RPM. At this speed, for zero yaw angle, it is evident that the magnitude of the acceleration signal for dry contact is significantly lower compared to wet contact conditions. This is also the case when FM1 and FM2 is applied to the wheel-rail contact. It can be inferred from this development that the application of contaminants to the wheel-rail interface reduces the wheel-rail contact stiffness and therefore causes the wheel and rail roller to vibrate more compared to dry contact conditions. This explains why the friction coefficient is significantly reduced when water or friction modifier is applied to the wheel-rail interface. While this is an undesirable phenomenon for a typical wheel-rail interface, the application of water of friction modifiers is required to mitigate curve squeal in tight curves by reduction of the friction coefficient and the lateral creep forces developed. However, once the railway vehicle has negotiated the sharp curve, it is necessary to degrease the friction modifier from the wheelset to restore the friction coefficient and the lateral stiffness back to its original value to maintain traction. Also, from Figure 6.1, at 1.2 degrees yaw angle, the magnitude of vibration data obtained from the mounted wheel and rail

accelerometers increased compared to zero degrees yaw angle between the rollers. This yaw angle was chosen as one of the angles where curve squeal is predicted to occur. For dry contact conditions it is discovered that there is a significant increase in amplitude of vibrations for zero degrees yaw angle when compared with 1.2 degrees yaw angle envisaged as one of the angles for which curve squeal occurs. This is not the case with wet conditions and the application of the FM1 and FM2 to the wheel-rail contact interface.
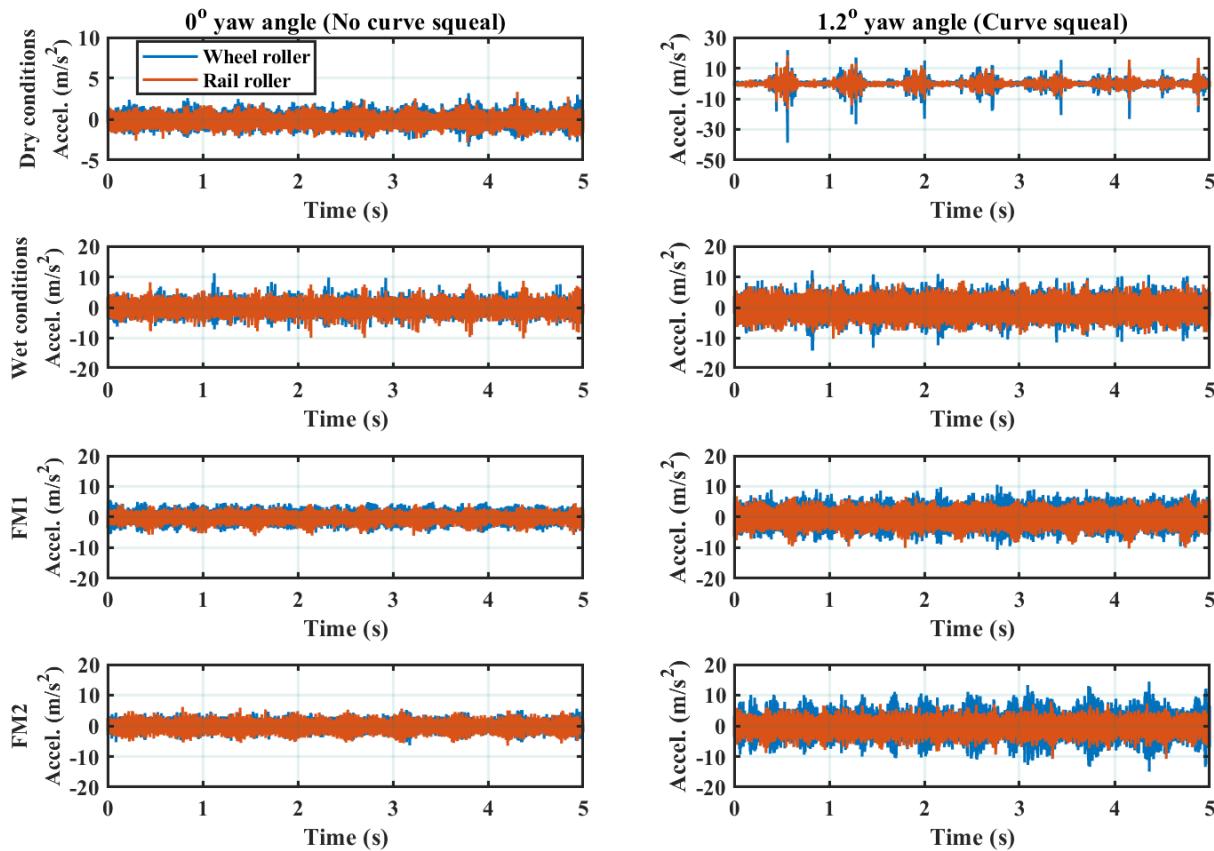
Figure 6.1: Wheel and rail lateral vibration data for average wheel speed of 100 RPM

As the average wheel speed increases from 100 RPM to 125 RPM, the magnitude of vibration measured from the wheel and rail roller accelerometers increases (See Figure 6.2). There is also a significant increase in the wheel and rail accelerometer vibrations as the yaw angle between the rollers is increased from zero degrees to 1.2 degrees for dry contact conditions. For wet conditions, the amplitude of vibrations on the wheel and rail roller is large compared to the dry contact conditions and even the application of FM1 and FM2 on the wheel-rail interface. This is possibly due to the reduction of the lateral stiffness of the wheel-rail rollers, which then causes the vibration

153

magnitude to increase. (Meierhofer et al., 2014) also arrived at the same conclusion that the introduction of contaminants to the wheel-rail interface results in a reduction in stiffness of the anisotropic surface layer between the two contacting surfaces. The vibration amplitude for FM1 and FM2 friction modifiers are slightly lesser than that of the wet contact conditions at zero degrees yaw angle. This explains why it is preferable to apply friction modifiers to the wheel-rail contact rather than water to mitigate curve squeal. For the overall plots in Figure 6.2, an increase in vibration magnitude at zero degrees is observed compared to the 100RPM average wheel speed.
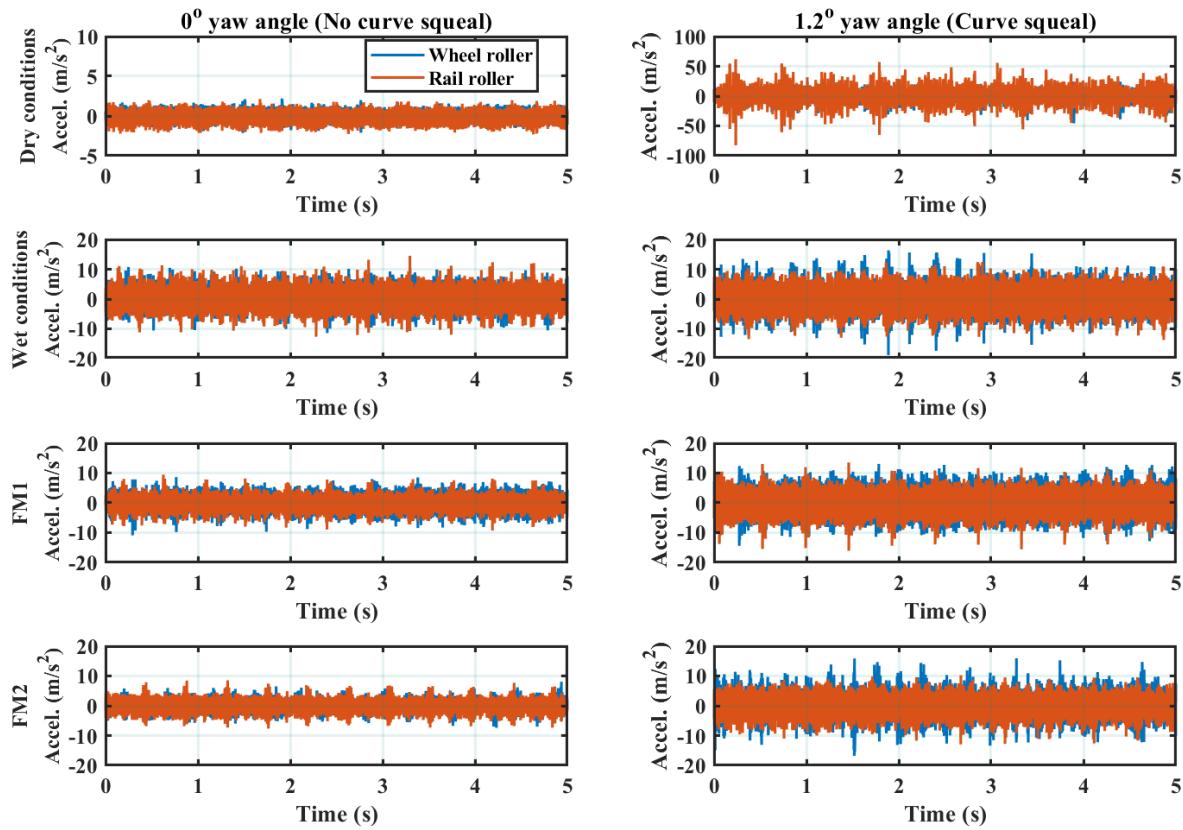
Figure 6.2: Wheel and rail lateral vibration data for average wheel speed of 125 RPM

Figure 6.3 displays the wheel and rail accelerometer data for average wheel speed of 150 RPM. Comparing Figure 6.3 and Figure 6.2, for zero yaw angle (absence of curve squeal), a noticeable increase in the vibration magnitude of the plots for dry, wet, FM1 and FM2 contact conditions was observed at speed of 150 RPM. As is the case for lesser wheel speed of 125 RPM, there a significant increase in the magnitude of vibration of the wheel and rail accelerometer data when the yaw angle was increased from zero degrees to 1.2 degrees (angle associated with curve squeal). However, for wet, FM1 and FM2 contact conditions, there is a slight increase in vibration

154

magnitude as the yaw angle increased from zero degrees to 1.2 degrees. It is noted that again the vibration amplitudes of wet, FM1 and FM2 for zero degrees are significantly higher at zero degrees yaw angle when compared with dry contact conditions. The reason for this is possibly due to the reduction of the lateral stiffness and friction coefficient thus leading to increased vibration magnitude.
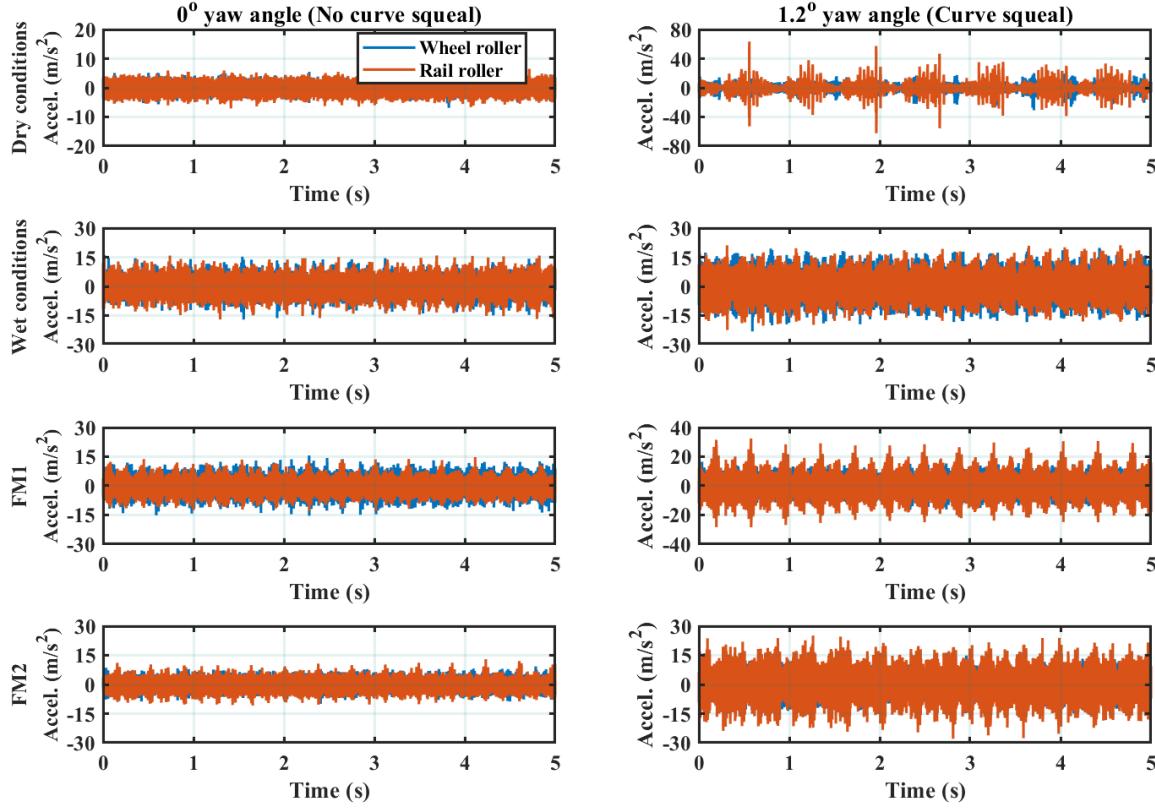
Figure 6.3: Wheel and rail lateral vibration data for average wheel speed of 150 RPM

Finally, Figure 6.4 displays the plots of the measurements obtained from the wheel and rail accelerometers for an average wheel speed of 175 RPM. The vibration magnitude measured for zero yaw angles at dry contact conditions is significantly lesser than wet, FM1 and FM2 contact conditions. This is due to the change in lateral stiffness and the friction coefficient as the wheel-rail interface conditions changes. A large disparity between vibration amplitude at zero degrees and 1.2 degrees is observed. This at first observation shows that the curve squeal occurs due to the excessive increase in vibrations of the wheel and rail rollers. Minimal differences in the vibration amplitudes at zero degrees and 1.2 degrees are observed for wet, FM1 and FM2 contact conditions.

Comparing Figure 6.4 and Figure 6.3 in overall, there is a slight increase in the vibration amplitude as the speed increased from 150 RPM to 175 RPM for zero degrees yaw angle.
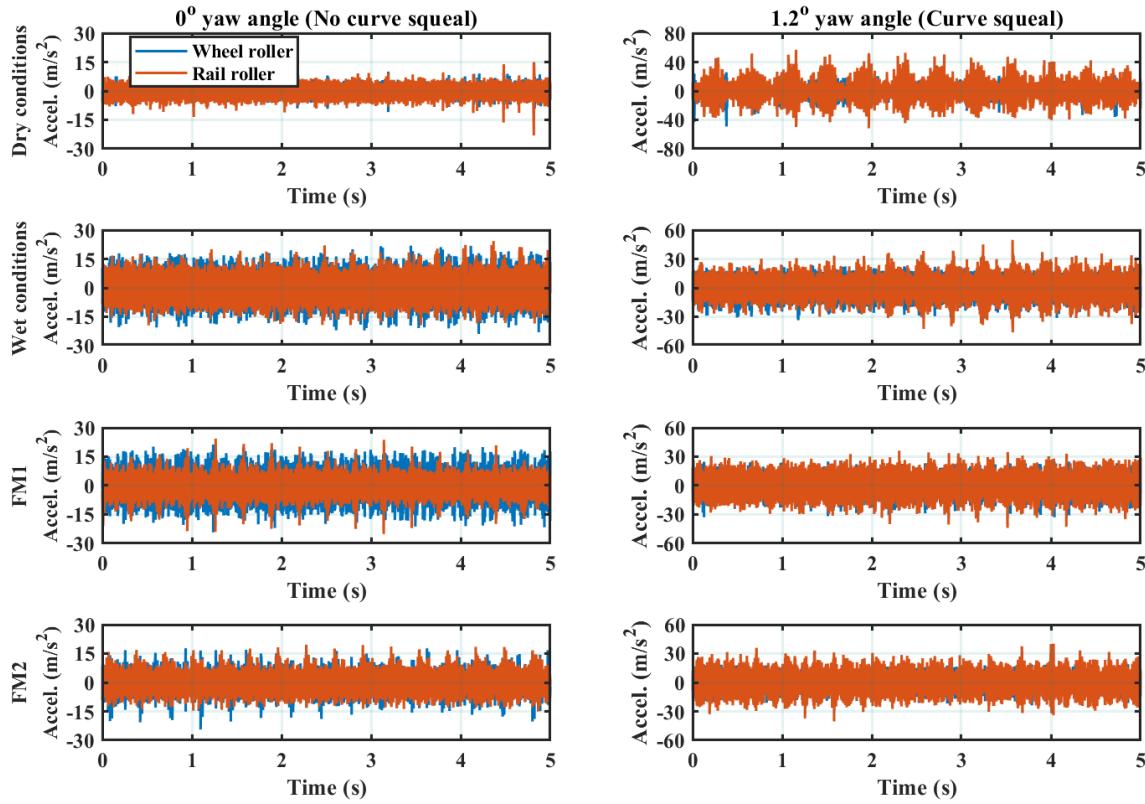
Figure 6.4: Wheel and rail lateral vibration data for wheel average speed of 175 RPM

The vibration results presented in Figure 6.1 to 6.4 shows that they perform reasonably well in time domain analysis. It can be deduced from the plots that the application of water and friction modifiers to the wheel-rail interface reduces the vibration amplitude significantly when the yaw angle is increased from zero degrees to 1.2 degrees. The problem with using only the time domain vibration results is the fact that very little information is provided as to which of the rollers is actually squealing. The time domain statistical methods employed in the next section would be used to investigate which of the roller is prone to curve squeal and how the application of water, FM1 and FM2 to the wheel-rail contact mitigate curve squeal.

Finally, to conclude, the time domain results obtained for the wheel and rail accelerometer showed a decrease in the wheel speed as the yaw angle increased. The periodic bursts at 1.2 degrees yaw angle of the rail roller indicates the reduced speed of the wheel roller from the set speed of 100RPM at central position (zero degrees yaw angle). The average wheel speed of the wheel rollers was

calculated as approximately 100RPM, 125RPM, 150RPM and 175RPM. There was no noticeable decrease in wheel speed when water and friction modifiers was applied to the wheel rail interface.

6.2.1   Feature extraction using Peak, RMS and Crest factor

Peak, RMS and crest factor time domain method were applied to the wheel and rail roller vibration data of the wheel and rail accelerometer using equation (5.1), (5.2) and (5.3). The problems associated with using these condition monitoring indicators in sound measurements are different for the case of the wheel and rail rollers. This is because the lateral vibration of the wheel rollers increases with increasing yaw angle. This is illustrated in the wheel and rail accelerometer time domain data in Figure 6.1 to Figure 6.4 for all average wheel speeds and in dry contact conditions. By obtaining the relationship between the condition monitoring indicators and the yaw angle variation for the wheel and rail accelerometers, it may be possible to differentiate between regions of squeal and curve squeal.

Figure 6.5 shows the calculated peak values for each yaw angle obtained from the vibration data of the wheel and rail accelerometer discussed previous in the last section. The results obtained show that at low wheel speed (100RPM), the peak values of the wheel accelerometer data are greater than the peak values of the rail accelerometer data at yaw angle greater than 0.9 degrees. This angle is called the transition yaw angle defined as the boundary between rolling contact noise and curve squeal. For average wheel speeds, 125RPM, 150RPM and 175RPM, the peak values of the rail roller are found to be greater than that of the wheel roller beyond the transition yaw angles 0.9 degrees, 0.6 degrees and 0.5 degrees respectively.
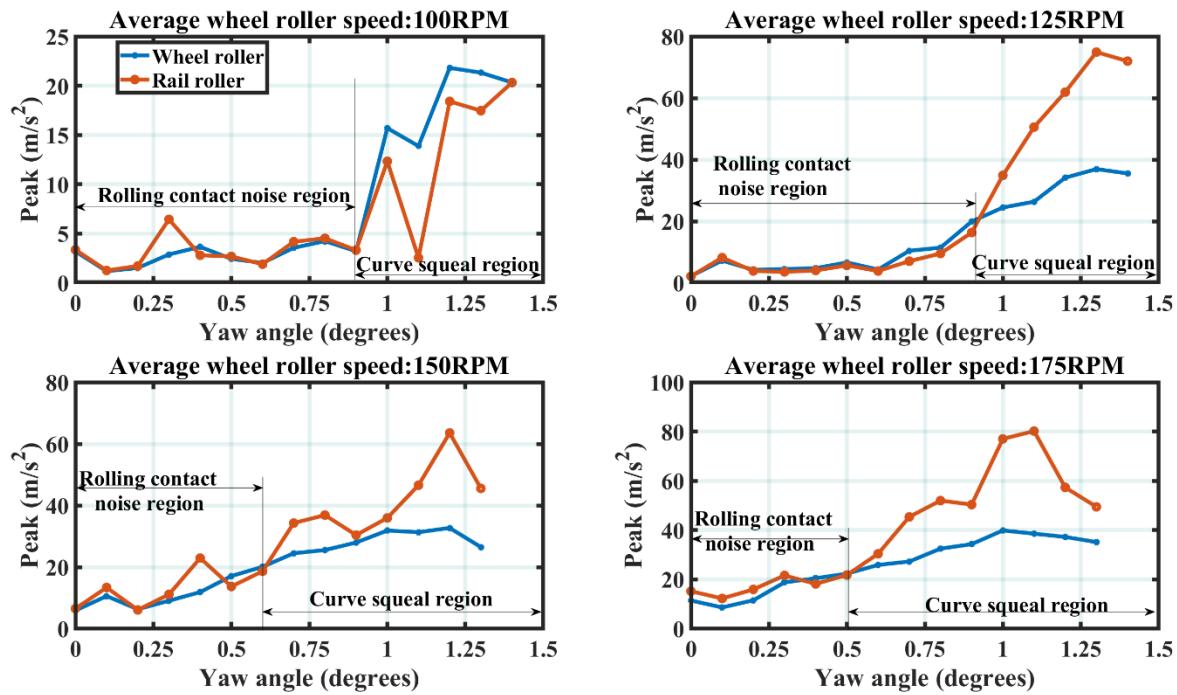
Figure 6.5: Effect of yaw angle on Peak value for the wheel and rail accelerometer for four average speeds and applied load of 2.5 kN.

The results obtained from the peak value indicate the region of rolling contact noise (no curve squeal) and region of curve squeal. However, the peak values do not indicate which of the wheels is the dominant contributor of curve squeal for dry contact conditions.

Figure 6.6 shows the plot of the calculated RMS values for the wheel and rail roller data for varying average wheel speed and yaw angles ranging from zero to 1.5 degrees. The motivation for applying RMS to the accelerometer data was to detect when curve squeal occurs. The results show that the energy content increases as the yaw angle increases for both the wheel and rail roller results. However, for all average speed cases, it is observed that at lower yaw angles, the energy content of the wheel and rail roller data remain constant while a significant increase in the wheel accelerometer rms value is observed after a particular yaw angle is reached.
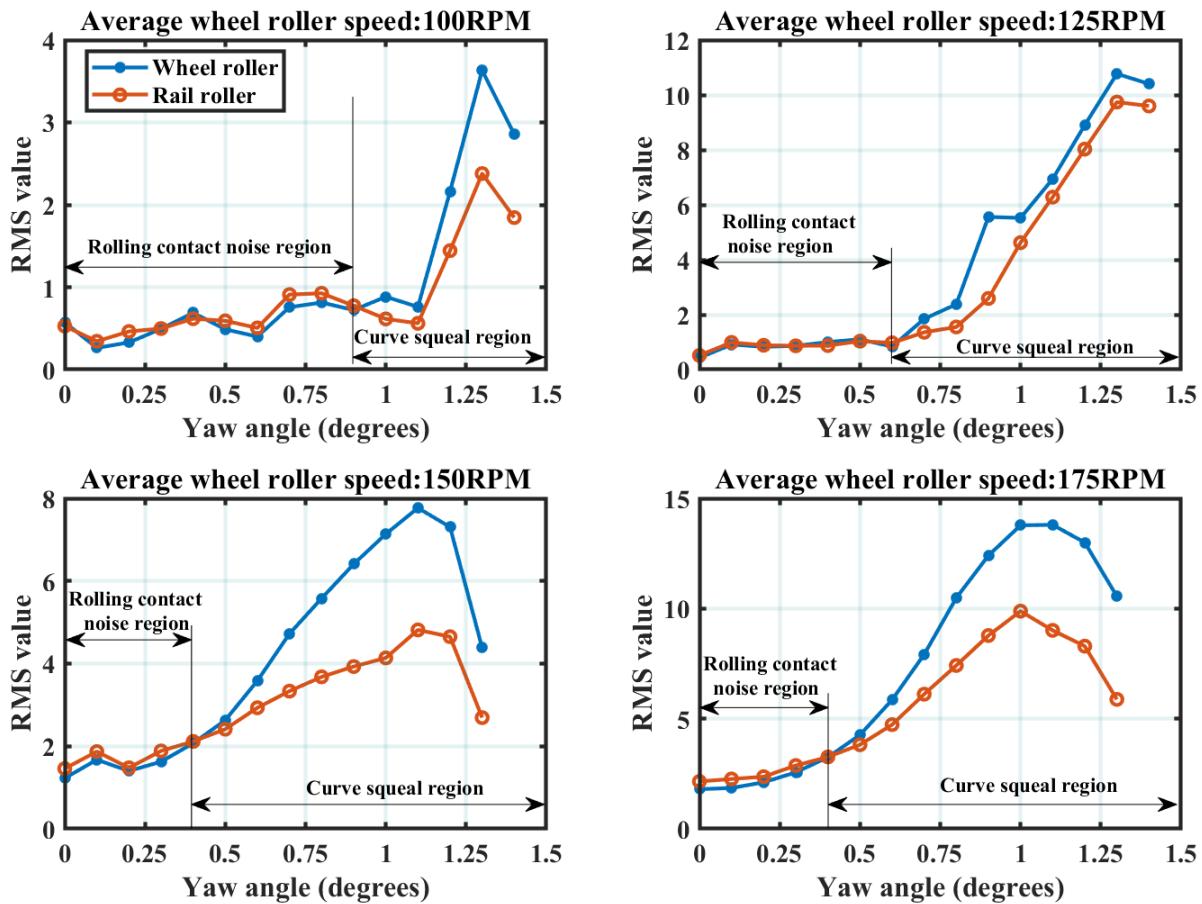
Figure 6.6: Effect of yaw angle on RMS value for the wheel and rail accelerometer for four average speeds and applied load of 2.5 kN in dry contact conditions

The rather larger rms values of the wheel accelerometer when compared to the rail accelerometer indicates more energy content in the wheel roller vibration especially at large yaw angles. For average speed of 100 RPM, 125 RPM, 150 RPM, and 175 RPM, the large value of the RMS of the wheel accelerometer when compared with the rail accelerometer occurred at yaw angles 1^0, 0.7^0, 0.5^0 and 0.5^0 respectively. The resultant disparity of the energy content of the wheel accelerometer compared to the rail accelerometer at these yaw angles indicates that the wheel roller is responsible for curve squeal rather than the rail roller. The rail roller is therefore not the dominant contributor to sound radiation leading to curve squeal as can be inferred from the Figure 6.5. This is in agreement with the results obtained by (Vincent et al., 2006) although they established this fact using frequency domain analysis.

Figure 6.7 shows the crest factor value plots for a given load of 2.5 kN, for average wheel speeds ranging from 100 RPM to 175 RPM. It is worth noting that crest factor is inversely proportional to the RMS value therefore curve squeal is detected when the crest factor of the rail accelerometer data is greater than that of the wheel accelerometer data. It can also be observed from Figure 6.6 that for the average speed of 100 RPM, 125 RPM, 150 RPM and 175 RPM, the yaw angle after which curve squeal is detected are 1^0, 0.8^0, 0.6^0 and 0.6^0. The discovered angles for which curve squeal is identified compares well with the angles obtained in Figure 6.6. The higher crest factor values of the rail roller after the detection of curve squeal indicates that at certain large yaw angles, the wheel vibrates more than the rail at the curve squeal region. This rationale is reached since the crest factor is directly proportional to the peak values of the wheel and rail accelerometer data. It is important to note from Figure 6.5 and 5.6 that the likelihood of curve squeal occurring for earlier yaw angles is higher with increasing average wheel speed. It is therefore imperative that at steep curves in railway tracks, low average wheelset speeds is desired to decrease the changes of curve squeal occurring.

160
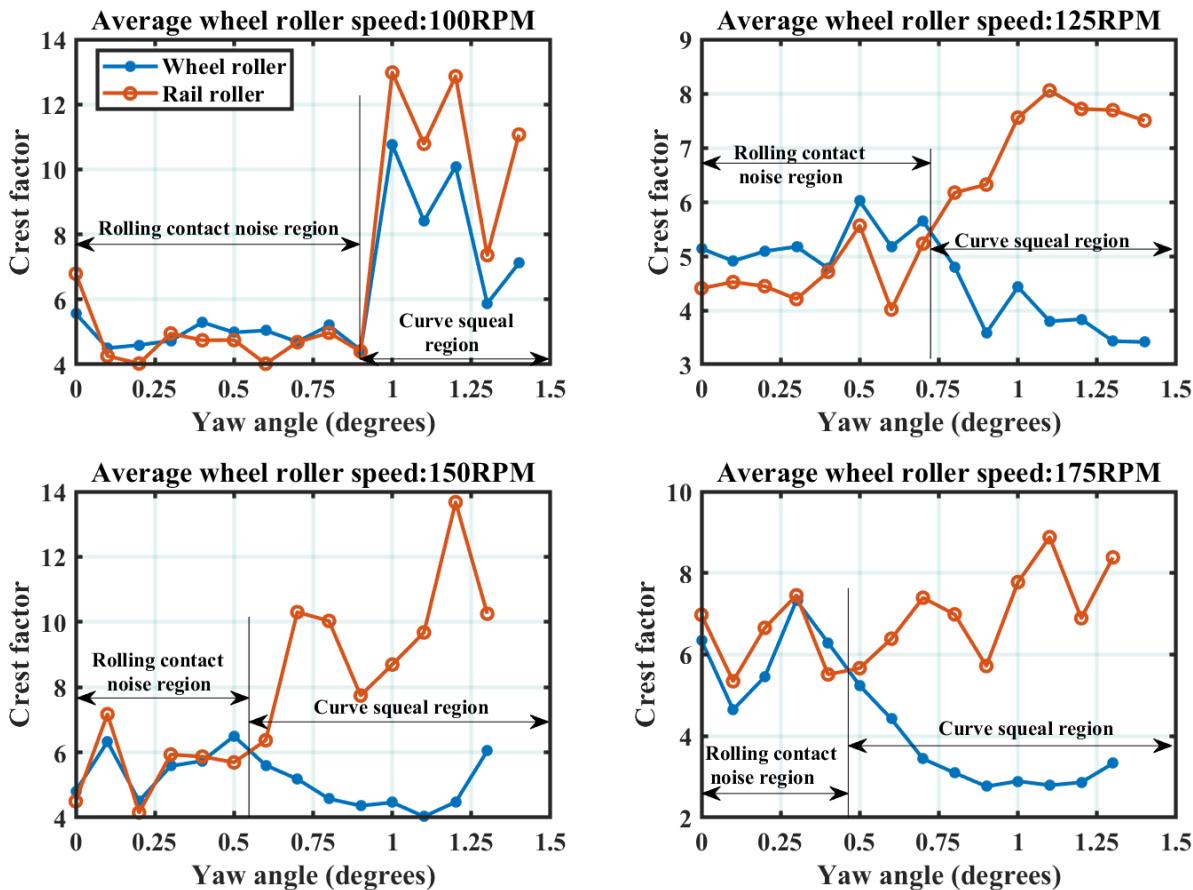
Figure 6.7: Effect of yaw angle on crest factor value for the wheel and rail accelerometer for four average speeds and applied load of 2.5 kN.

From the statistical time domain methods applied (RMS and Crest factor) for feature extraction to identify and detect curve squeal, the results obtained showed that average wheel speed of important for the development of curve squeal. In addition, for the three condition monitoring indicators relationship with the yaw angle, no further signal processing was required to establish the potential regions of curve squeal and no curve squeal.

6.2.3   Feature extraction using Kurtosis and Skewness

Kurtosis and skewness were applied to the wheel and rail vibration data to investigate and detect curve squeal. Equation 5.4 and 5.5 was used to generate the kurtosis and skewness values for the wheel and rail accelerometer respectively.

Figure 6.8 illustrates the kurtosis values for the wheel and rail accelerometer data. The kurtosis amplitude of the wheel and rail vibration data for average wheel speed of 100 RPM ranges from 2 to 3.8 up to yaw angle of 0.9^0. Although the required kurtosis value for a fault free system is below 3, the oscillations of these amplitudes between 2 and 4 for the wheel and rail roller at this speed suggest in this case that the test rig is operating at the no curve squeal region (or pure rolling contact noise).
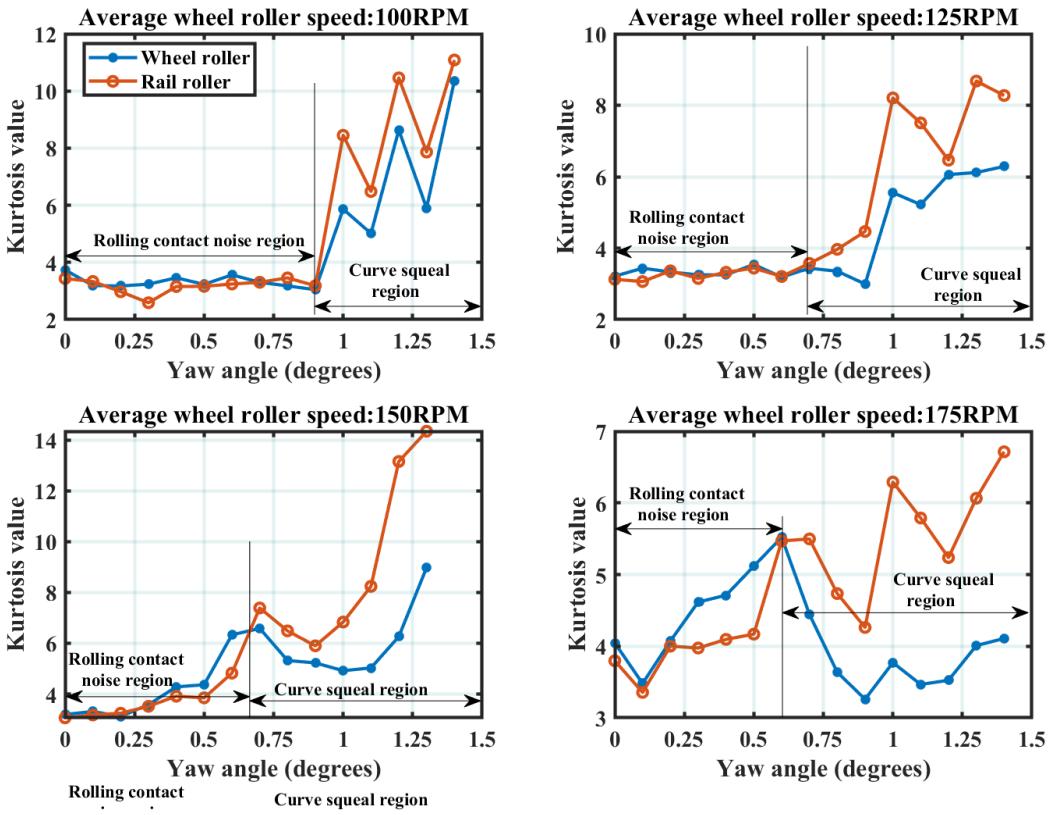
Figure 6.8: Effect of yaw angle on kurtosis values for the wheel and rail accelerometer data operating for four average wheel speeds.

A sharp increase in the kurtosis value for the wheel and rail accelerometer after 0.9^0 indicates the region of curve squeal. For average wheel speeds of 125 RPM, 150 RPM and 175 RPM, the rolling contact noise region ranges from zero degrees to 0.7^0, 0.7^0 and 0.6^0 respectively. The kurtosis amplitude increased sharply after these angles for both the wheel and rail accelerometer data but the rail accelerometer data increased in value more than the wheel accelerometer. The sudden change in the kurtosis value of the wheel and rail accelerometer from its steady state value for all average wheel speeds indicates the identification of curve squeal.
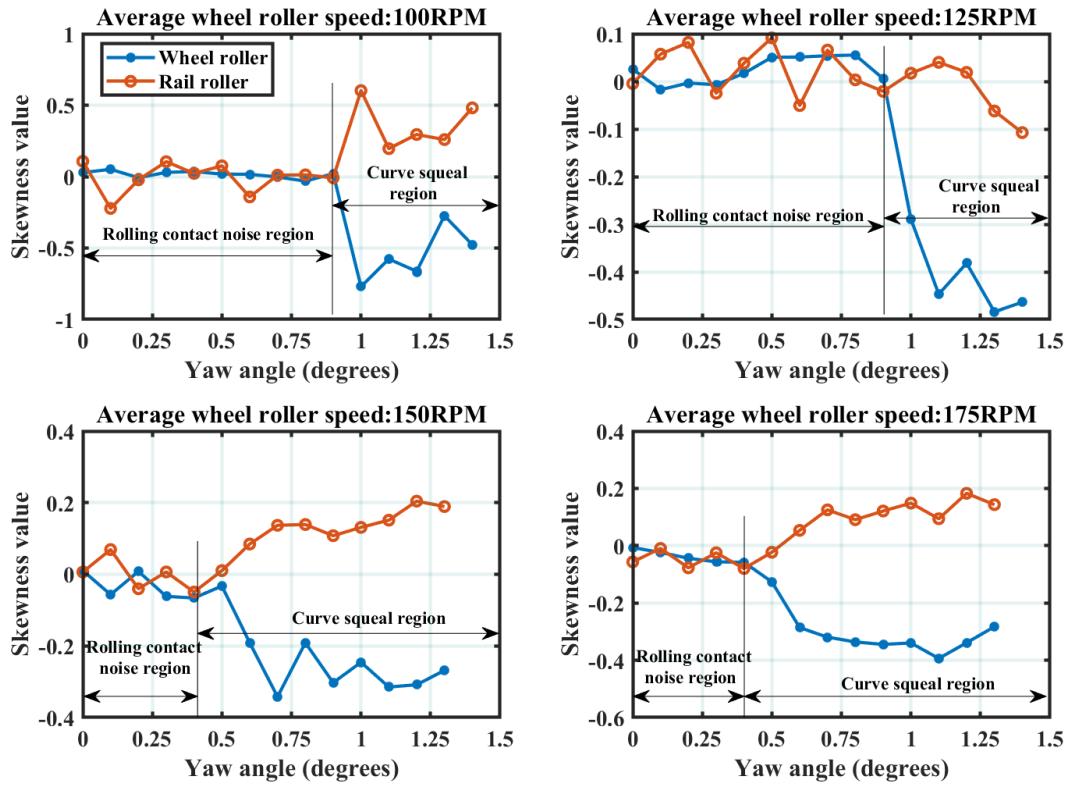
Figure 6.9: Effect of yaw angle on the skewness values for the wheel and rail accelerometer data using four average speeds

Figure 6.9 shows the effect of the yaw angle on the skewness values for the wheel and the rail accelerometer data. It is evident from observations that the for the four average wheel speeds that the skewness value ranges from -0.1 to 0.1 for the rolling contact noise region for the wheel and rail roller. The wheel accelerometer data for all four average wheel speeds is negatively skewed meaning that the data is skewed to the left. It can also be observed that the rail accelerometer data is positively skewed meaning that the value is skewed to the right. The rolling contact region for the four average wheel speeds can be clearly observed to be between zero degrees and 0.9^0, 0.9^0, 0.5^0 and 0.4^0 for speeds 100 RPM, 125 RPM, 150 RPM and 175 RPM respectively. It can thus be concluded that when curve squeal is detected on the rig, the wheel accelerometer data is negatively skewed while the rail accelerometer data is more positively skewed. Although this disparity in skewness values at the curve squeal region is not the case for average wheel speed of 125 RPM, however the significant different in the values of the skewness indicates the detection of curve squeal from the vibration data.

163

6.3 Feature extraction methods for curve squeal mitigation

The previous section discussed in details with the aid of plots several statistical methods that could be used to detect curve squeal in the test rig. Figure 6.1 to Figure 6.4 displayed the time domain of the wheel and rail accelerometer signal for dry, wet, FM1 and FM2 contact conditions operating at four varying speeds. However, it was observed from these figures that the amplitude of vibration for dry contact at zero degrees yaw angle for all four average wheel speeds is significantly less than the amplitudes of wet, FM1 and FM2 contact conditions. The reason for this was explained such that the introduction of contaminants (water and friction modifiers) to the wheel-rail interface changes the contact stiffness of the contact thereby causing the wheel and rail roller to vibrate more when compared in dry contact conditions.

With his main conclusion in mind, it is very difficult to investigate the mitigation effect observed by the application of water and friction modifiers on the wheel-rail contact interface in the time domain. However, the best results were obtained by investigating the effect of the yaw angle on the skewness values for all wheel-rail contact scenarios (See Figure 6.10). The results obtained for average wheel speeds of 100 RPM, 125 RPM and 150 RPM shows the effect of the application of water, FM1 and FM2 on the wheel and rail rollers. It is observed that the skewness values of the wheel accelerometer for instance was observed to tend to zero after the application of water, FM1 and FM2 for average wheel speed of 100 RPM. The skewness was thus shift from being negatively skewed to tending to zero skewness. The same effect was observed for average wheel speeds of 125 RPM, 150 RPM and 175 for the wheel accelerometer data. However, since the wheel roller contributes more to curve squeal compared with the rail roller, the skewness values of the rail roller did not change considerably much for all contact conditions for all speeds as observed in Figure 6.10. This enforces the fact that the wheel roller is the dominant contributor of curve squeal in the test rig.
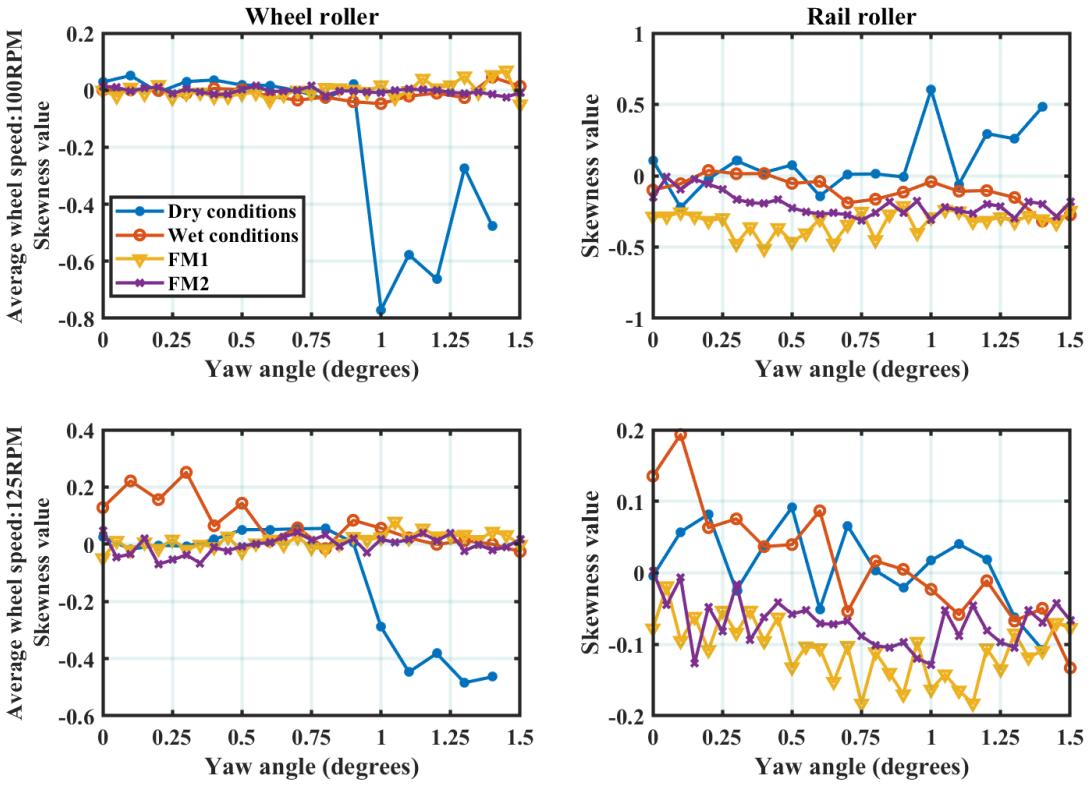
Figure 6.10: Skewness plot of the wheel and rail accelerometer data for two average speeds (100 RPM and 125 RPM) for dry, wet, FM1 and FM2 contact conditions

For higher average wheel speeds as observed in Figure 6.10, there is no significant change in the skewness values for the rail roller. Large disparities in the skewness values are observed in the wheel roller data for average speeds 150 RPM and 175 RPM. This again suggests that the wheel roller is a greater contributor to curve squeal as established in literature. It is important to note that for the average wheel speed of 175 RPM, curve squeal was not eliminated as the yaw angle increased. The skewness values for wet, FM1 and FM2 contact conditions was observed to increase as the yaw angle increases. No significant change was observed for the rail accelerometer results.
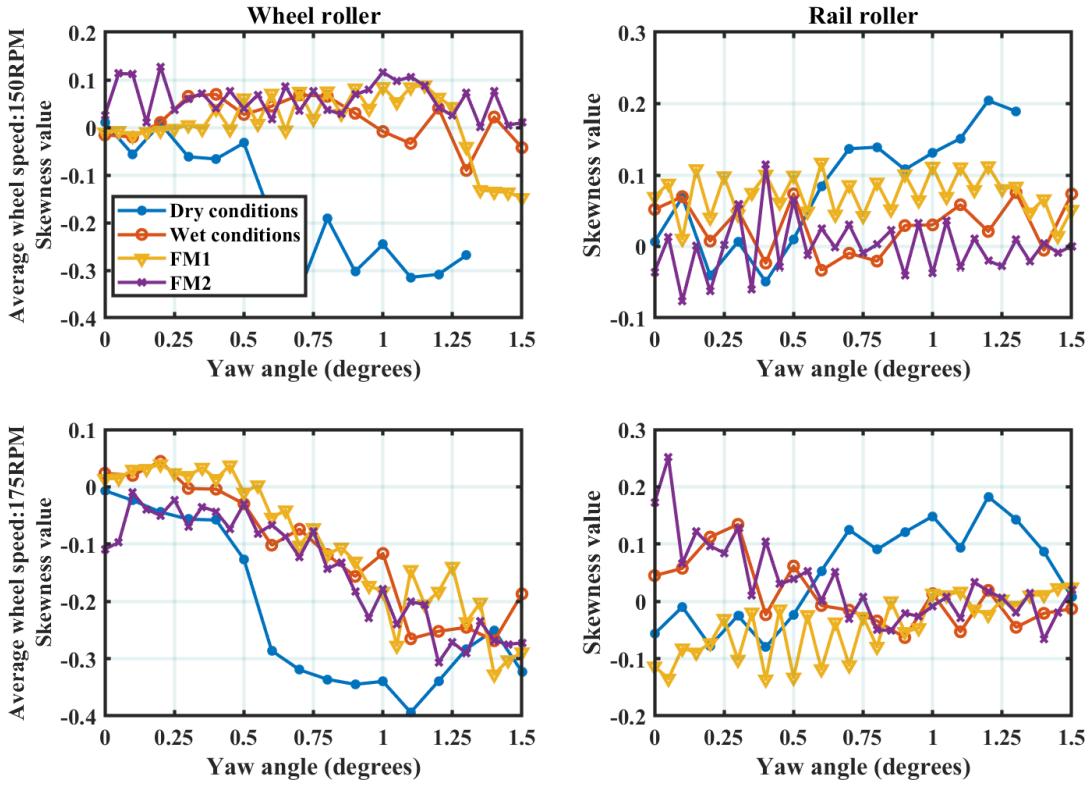
Figure 6.11: Skewness plot of the wheel and rail accelerometer data for two average speeds (150 RPM and 175 RPM) for dry, wet, FM1 and FM2 contact conditions

6.4 Curve squeal identification and characterization using spectrum analysis

The raw time domain data obtained from the wheel and rail accelerometer in Figure 6.1 to Figure 6.2 only described the changes in signal amplitude from the two accelerometers when the wheel speed and the contact conditions are varied. For power spectrum analysis, the same time domain data was analysed.

Figure 6.12 shows the power spectrum plots of the wheel and rail accelerometer data at average wheel speed of 100RPM. The spectrum is obtained for zero degrees and 1.2 degrees yaw angle applied to the rail roller. The frequency range was constrained from 500Hz to 4000Hz as this represents the region were more energy is found on the spectrum data.

At zero degrees yaw angle, some peaks can be observed from the power spectrum plot for the wheel and rail roller. Most of the peaks observed are the natural frequencies of the wheel and rail roller obtained from impact hammer test results. At 1.2 degrees yaw angle, the curve squeal frequency (X) is observed around 1150Hz. It is not very clear from the plot exactly which value it is. The spectral amplitude from the wheel accelerometer data is much greater than the spectral

166

amplitude obtained from the rail roller. This indicates that the wheel is the main contributor of curve squeal in the twin disc rig.
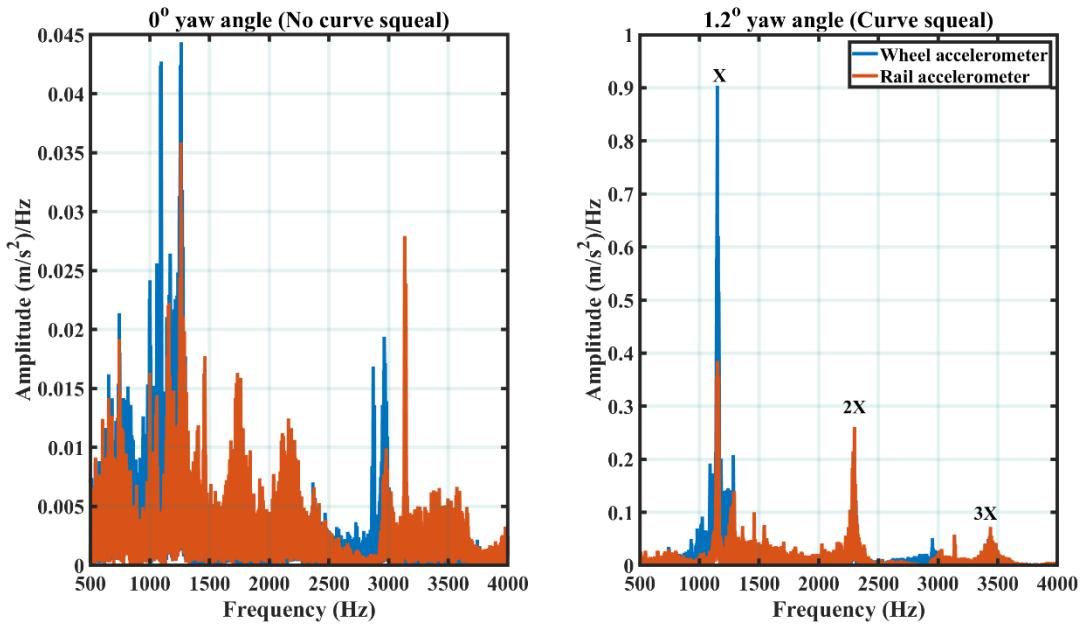
Figure 6.12: Wheel and rail lateral vibration spectrum plots for average wheel speed of 100 RPM in dry contact conditions

The harmonics of the dominant curve squeal frequency are observed at 2X (2300Hz) and 3X(3450Hz) respectively. This signifies that curve squeal produces harmonics of the fundamental curve squeal frequency.
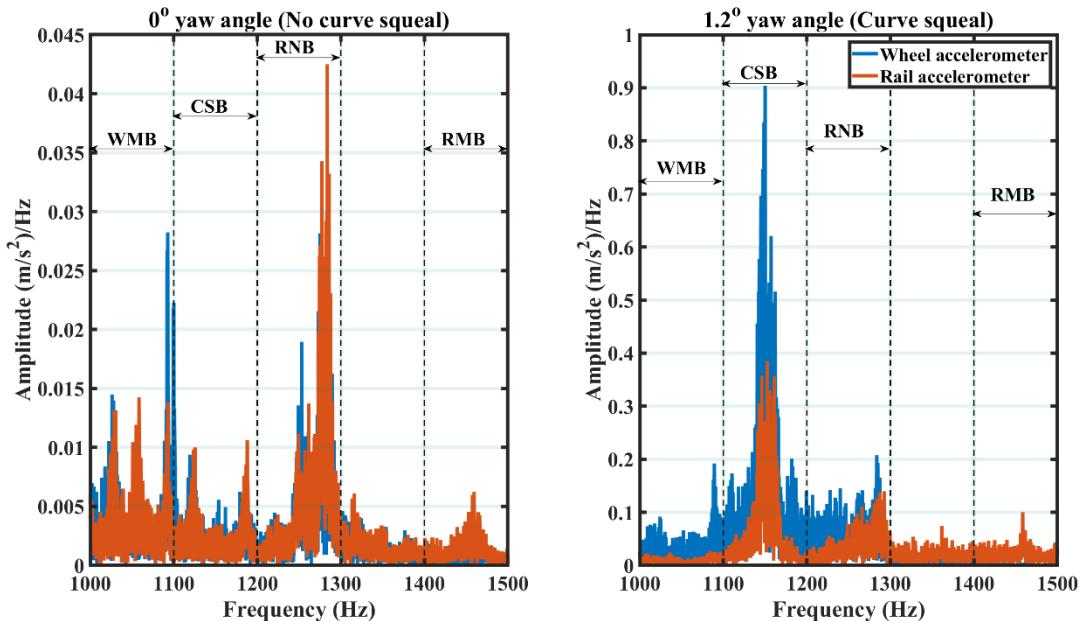
Figure 6.13: Section of the wheel and rail lateral vibration spectrum plots for average wheel speed of 100 RPM in dry contact conditions

Figure 6.13 shows the zoomed in power spectrum plot of the wheel and rail accelerometer data for frequency range of 1000Hz to 150Hz. This range was chosen to identify in detail the frequency components of the wheel and rail vibration spectrum responsible for curve squeal. As defined previous in Chapter 5, the frequency bands WMB, CSB, RNB and RMB was defined for the wheel and rail vibration spectrum. The results obtained shows that the dominant frequency for no squeal is around 1280Hz. This frequency is in the rolling noise band (RNB). This probably indicates the rolling noise frequency generated as a result of the dynamics of the wheel-rail interface at wheel speed of 100RPM. The wheel power spectrum plot identified the second nodal diameter with natural frequency of around 1095Hz while the second nodal diameter and natural frequency of the rail roller can be observed to be excited at zero degrees yaw angle. A sharp peak at the CSB frequency band of about 1150Hz is observed when the rail roller is yawed to the angle of 1.2 degrees. This frequency has been observed to drown all the wheel and rail natural frequencies. This strongly indicates the presence of curve squeal in the test rig.
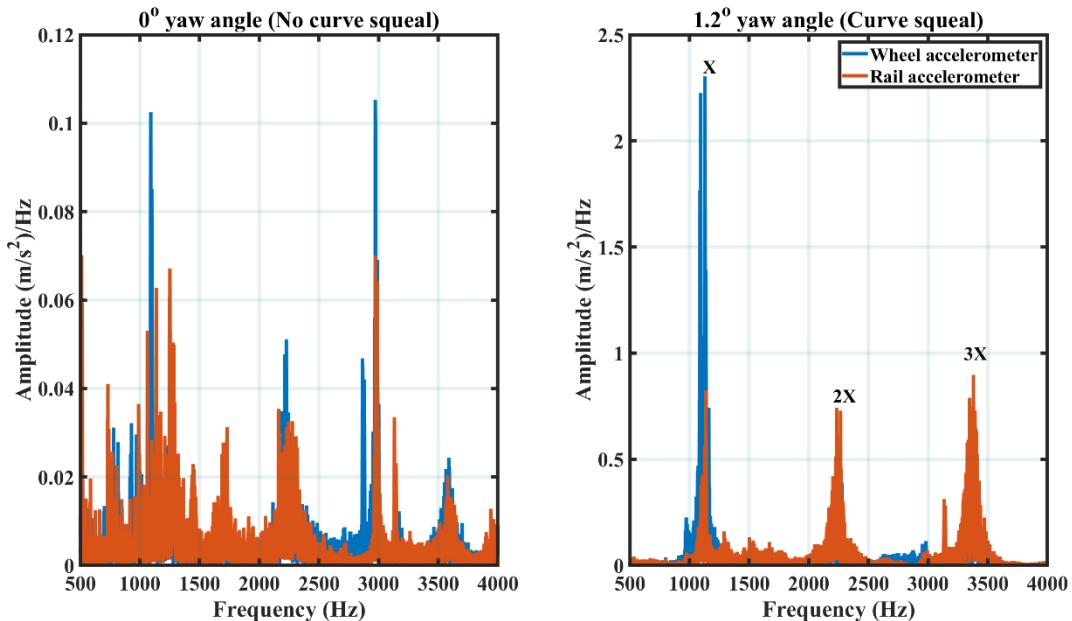
Figure 6.14: Wheel and rail lateral vibration spectrum plots for average wheel speed of 125 RPM in dry contact conditions.

Figure 6.14 shows the power spectrum of the wheel and rail accelerometer time domain data at average wheel speed of 125RPM and in dry contact conditions. The results indicate that are dry contact conditions the wheel and rail roller are vibrating at their natural frequency as obtained from impact hammer test results. The sharp peak around 3000Hz is the third nodal diameter and natural frequency of the wheel roller. At 1.2 degrees yaw angle, the vibration amplitude of the wheel and rail roller is observed at around 1150Hz. This peak frequency (X) or the dominant frequency is the curve squeal frequency as a result of the excitation of the second nodal diameter and natural frequency of the wheel roller. The large disparity between the peaks of the wheel and rail roller indicate that the wheel roller is the main contributor of curve squeal. This dominant curve squeal frequency generates 2nd(2X) and third harmonics at around 2300Hz and 3450Hz respectively.
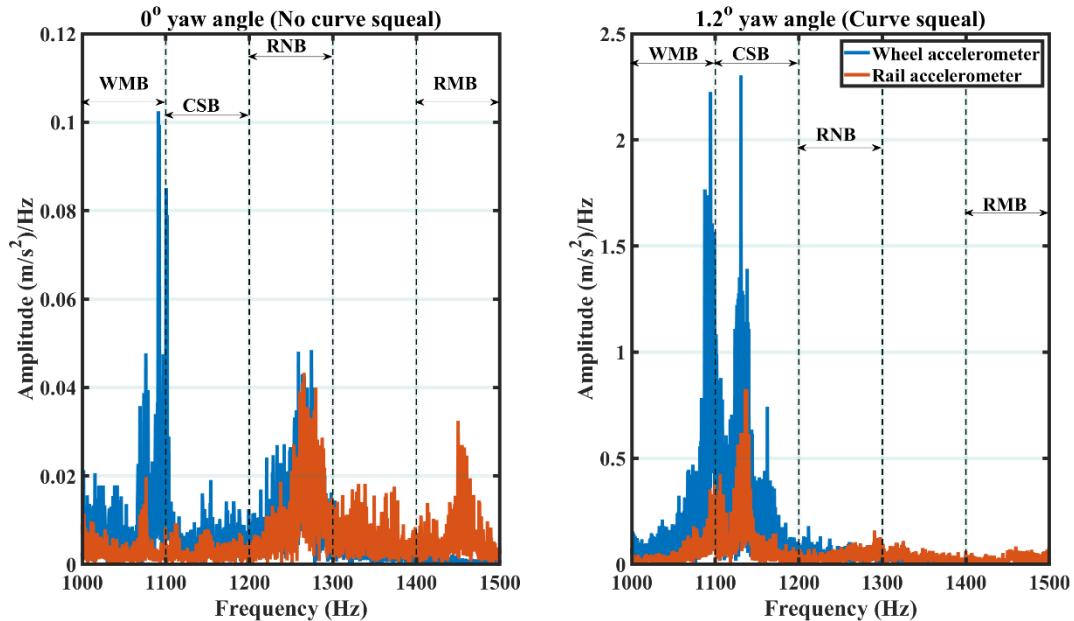
Figure 6.15: Section of the wheel and rail lateral vibration spectrum plots for average wheel speed of 125 RPM (Dry, wet, FM1 and FM2 contact conditions)

Figure 6.15 shows a section of the plot in Figure 6.14 for a frequency range of 1000Hz to 1500Hz. The sharp peak in the WMB band indicates the excitation of the wheel natural frequency around 1095Hz. The excitation of this frequency is normal especially when there is no curve squeal developed on the test rig. The rolling contact noise region has peaks around 1250Hz for both the wheel and rail roller accelerometer data. A noticeable peak amplitude in the RMB region indicates the excitation of the rail roller natural frequency (second nodal diameter and zero nodal circles). At 1.2 degrees the dominant peak observed in the CSB frequency band is the curve squeal

frequency. The dominant spectral amplitude is greater than the wheel natural frequency in the WMB. This indicates that the wheel is the main contributor of curve squeal in the twin disc rig. The same is the case for the rail roller spectrum at 1.2 degrees yaw angle.
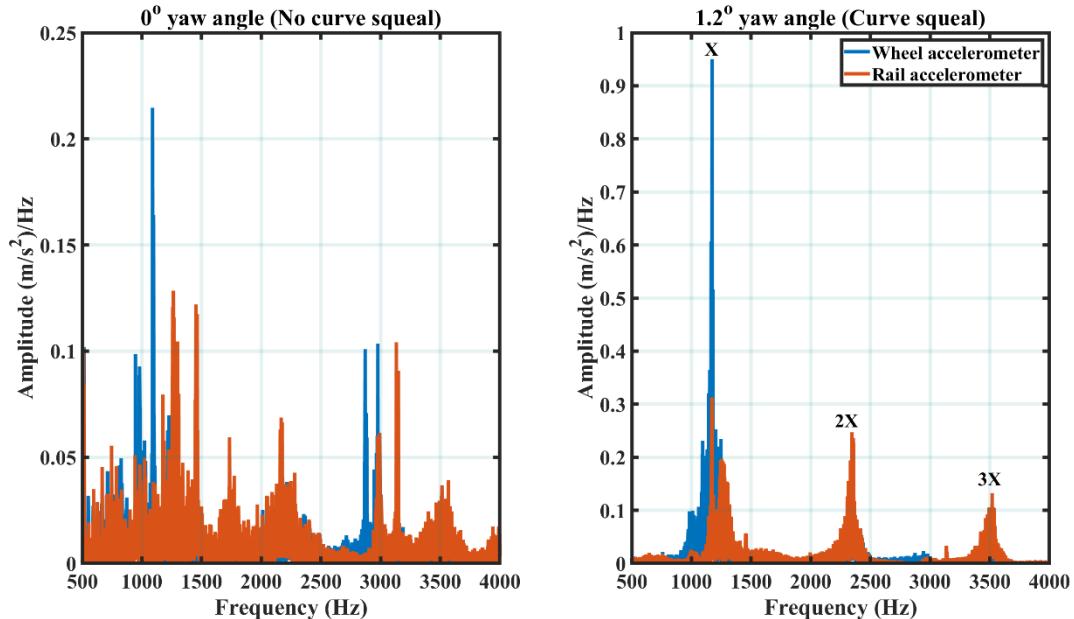
Figure 6.16: Wheel and rail lateral vibration spectrum plots for average wheel speed of 150 RPM in dry contact conditions.

Figure 6.16 shows the wheel and rail spectrum plots for average wheel speed of 150RPM. The dominant peak amplitude for zero degrees yaw angle indicates noise generated as a result of wheel and rail contact dynamics at wheel speed of 150RPM. The other frequency components represent the excitation of the wheel and rail roller at their natural frequencies. The fundamental dominant curve frequency (X approximately equal to 1130Hz) and its corresponding harmonics are observed when the yaw angle is set to 1.2 degrees. This indicates the presence of curve squeal development in the twin disc rig with the wheel being the most dominant contributor.

Figure 6.17 shows the section of the wheel and rail lateral vibration spectrum plots for the wheel and rail roller for a constrained frequency range of 1000Hz and 1500Hz. A closer look shows that the excitation of the natural frequencies of the wheel and rail roller occurs in the WMB and RMB frequency band respectively. The rolling contact noise developed in the RNB band is also present. The sharp peak amplitude of the power spectrum plot at around 1180Hz indicates curve squeal. However, the disparity between the wheel and rail peak amplitudes at 1.2 degrees yaw angle signifies that the wheel roller is responsible for curve squeal.

170
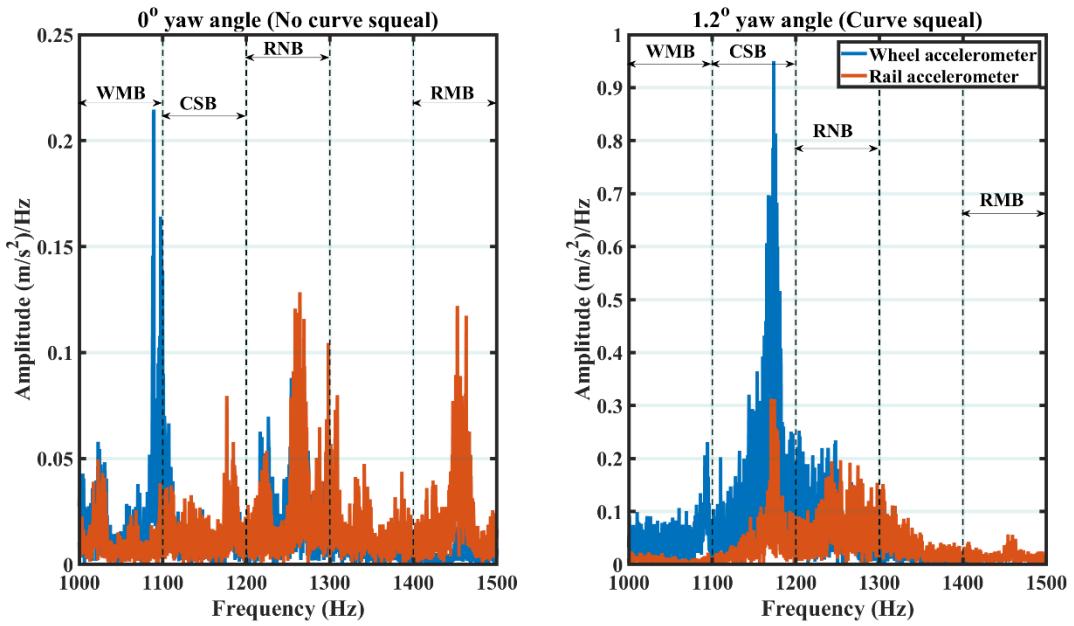
Figure 6.17: Section of the wheel and rail lateral vibration spectrum plots for average wheel speed of 150 RPM in dry contact conditions.

Figure 6.18 shows the spectrum of the wheel and rail roller accelerometer data for average wheel
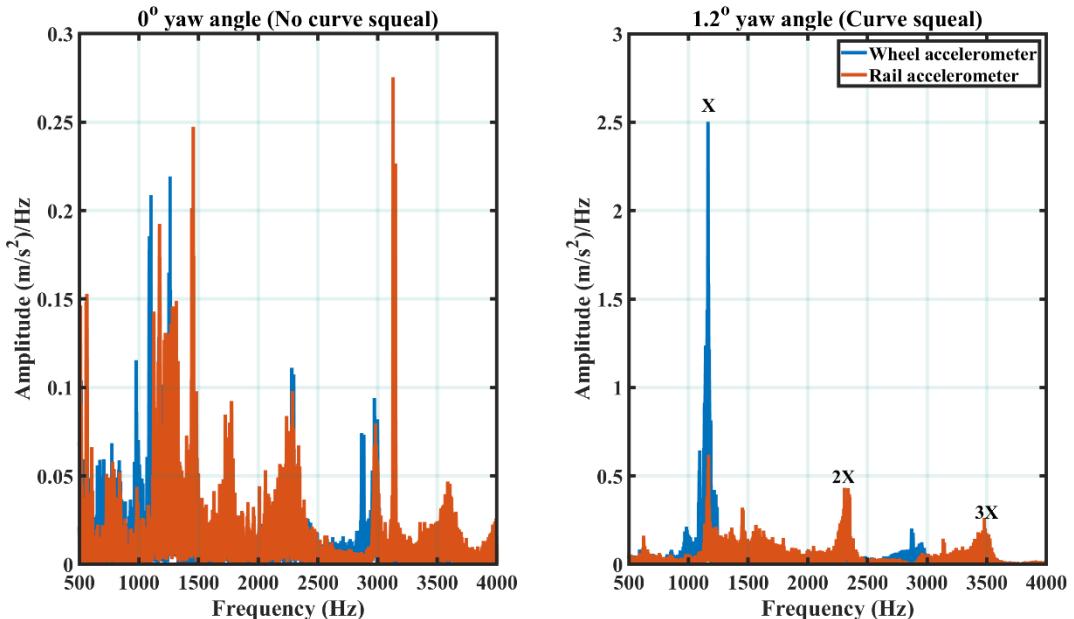
Figure 6.18: Wheel and rail lateral vibration spectrum plots for average wheel speed of 175RPM in dry contact conditions

speed of 175RPM. The sharp peak amplitude from the spectrum plots for zero degrees yaw angle indicate the excitation of the rail roller natural frequency around 3135Hz. The other spectral peaks although not clearly visible indicate the presence the excitation of the wheel and rail natural frequencies within the specified frequency range of 500Hz to 4000Hz. As has been the case with the previous wheel speeds, the dominant curve squeal frequency and the associated harmonics (2X and 3X) where X is around 1150Hz is observed in Figure 6.18. This indicates the presence of curve squeal in the twin disc rig.
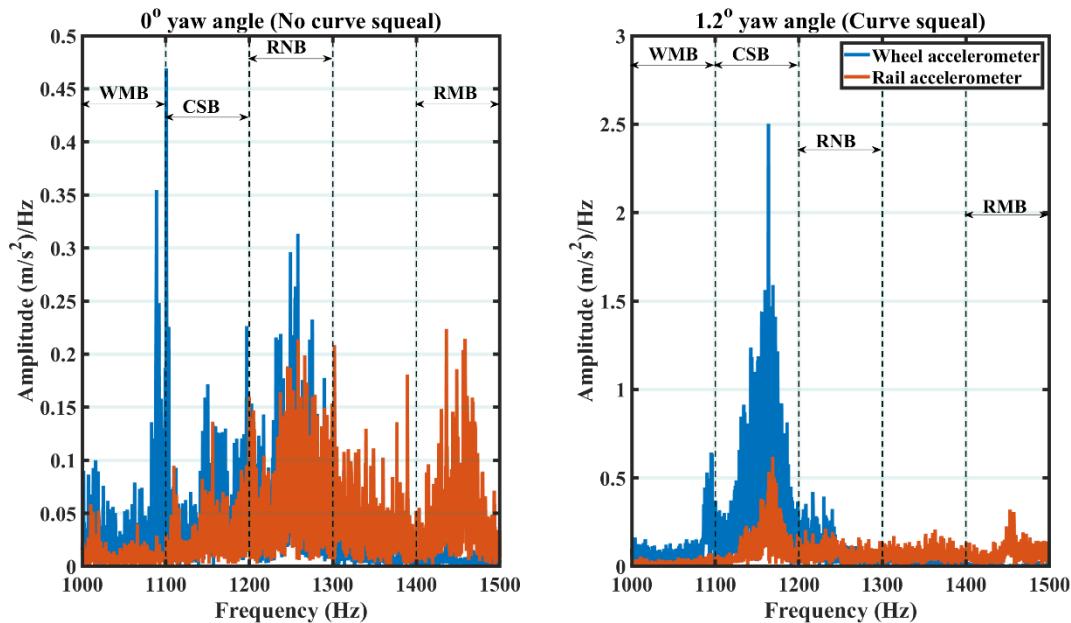

Figure 6.19: Section of the wheel and rail lateral vibration spectrum plots for average wheel speed of 175 RPM in dry contact conditions.

Figure 6.19 show the section of wheel and rail roller spectrum for frequency range of 1000Hz to 1500Hz. The respective frequency bands of interest are clearly defined showing the frequency components of the wheel and rail roller excited at their natural frequencies. The only distinct frequency from the rest is the rolling contact frequency centred around the RNB frequency band at zero degrees yaw angle. When the yaw angle is changed to 1.2 degrees, the dominant curve squeal frequency in the wheel and rail roller spectrum plot is excited. This indicates the presence of curve squeal with the wheel roller being the main contributor.

The application of spectrum analysis to the wheel and rail accelerometer data has specified some key elements that were not easily observed with the application of time domain feature extraction

methods. The respective frequency bands that clearly defines what transpires in the dynamics of the wheel rail contact has been observed.

6.5 Curve squeal mitigation using spectrum analysis

Spectrum analysis would be applied to the wheel and rail accelerometer data for dry, wet, FM1 and FM2 contact condition to investigate how curve squeal is mitigated.
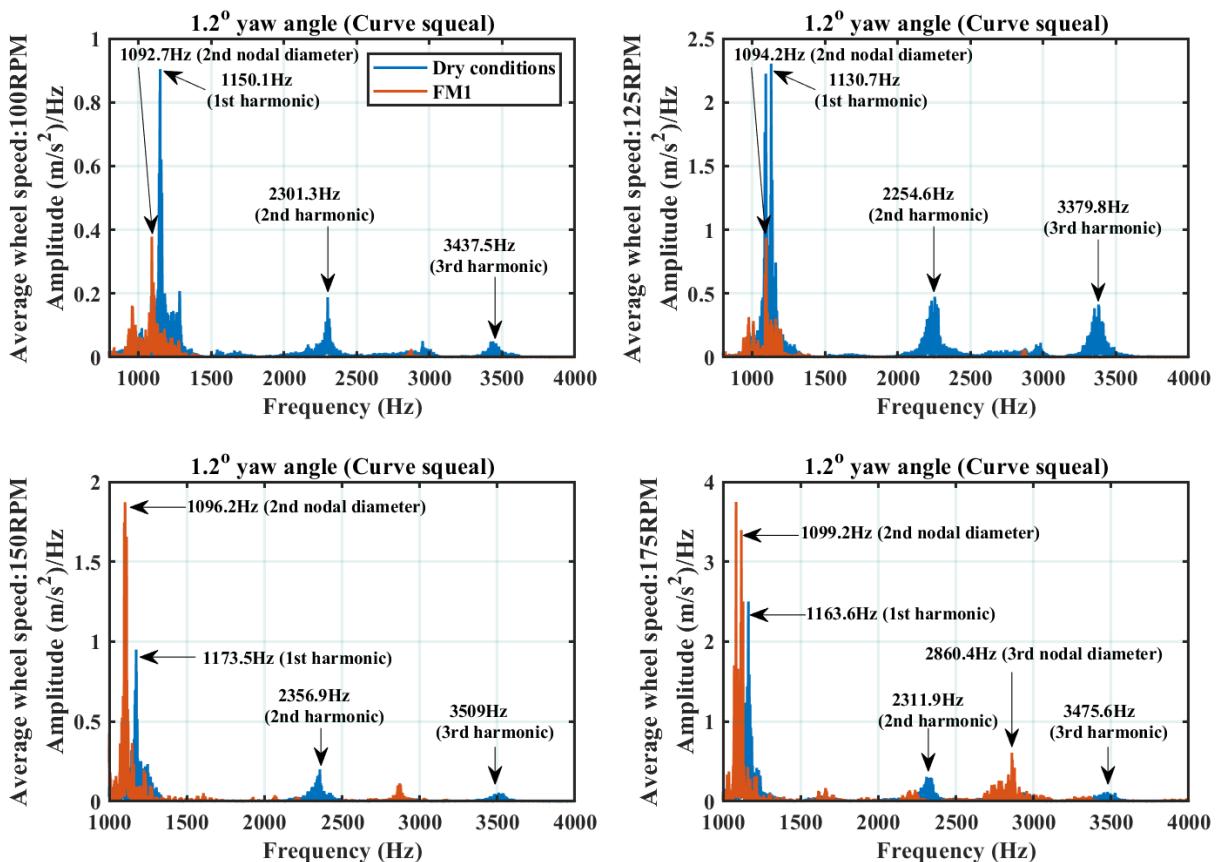
Figure 6.20: Spectrum plots from wheel accelerometer illustrating curve squeal mitigation using FM1 applied on the wheel-rail interface for varying wheel speeds

Figure 6.20 shows the spectrum plots of dry and FM1 wheel accelerometer data for average wheel speed of 100RPM, 125RPM, 150RPM and 175RPM. 1.2^{0} yaw angle was chosen to illustrate curve squeal mitigation since at this value curve squeal has commenced for all average wheel speeds. It can be observed from Figure 6.20 the fundamental or dominant excitation frequency for curve squeal is 1150.1Hz, 1130.7Hz, 1173.5Hz and 1163.6Hz for average wheel speeds of 100RPM,

125RPM, 150RPM and 175RPM respectively all contained in the CSB frequency band. It can also be observed from the plots that the second and third harmonics of the dominant curve squeal frequency are evident as shown in Figure 6.20. The introduction
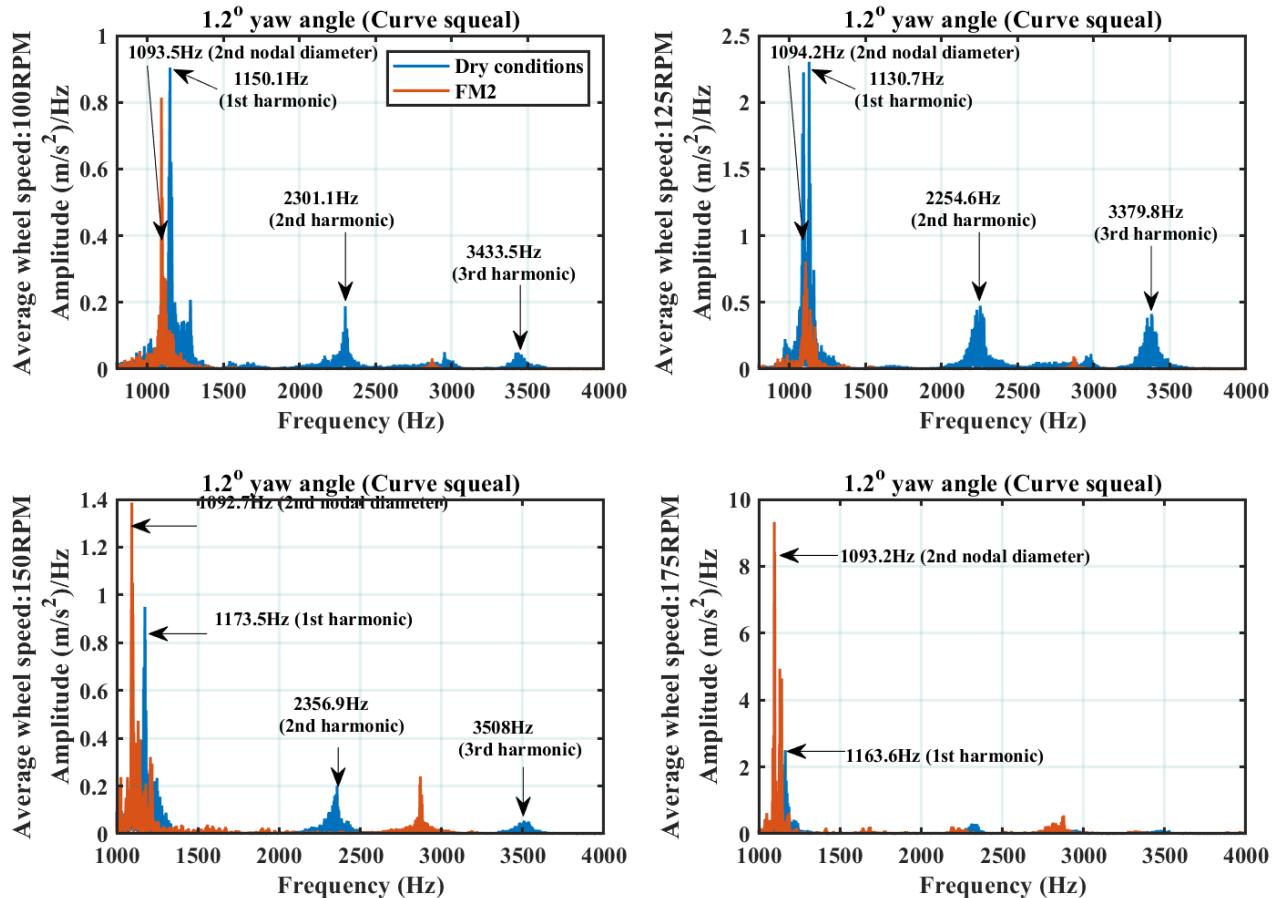
Figure 6.21: Spectrum plots from wheel accelerometer illustrating curve squeal mitigation using FM2 applied on the wheel-rail interface for varying wheel speeds

Curve squeal for test rig can therefore be defined as a strong tonal vibration in the CSB frequency band, and its corresponding harmonics. It is important to note that when curve squeal is detected, the influence of the other natural modes of vibration of the wheel and rail roller (nodal diameters greater than 2) is non-existent. It is also important to observe that FM1 eliminates the second and third harmonic frequency components for all four average wheel speeds. In addition, a reduction in the amplitude of the fundamental frequency is also observed when FM1 is applied to the wheel-

rail roller interface. FM1 causes the wheel roller to vibrate at its natural modes while eliminating the corresponding harmonics associated with curve squeal in dry contact conditions.

Figure 6.21 shows the effect of FM2 on the spectrum plots obtained from the wheel accelerometer for four varying wheel speeds.
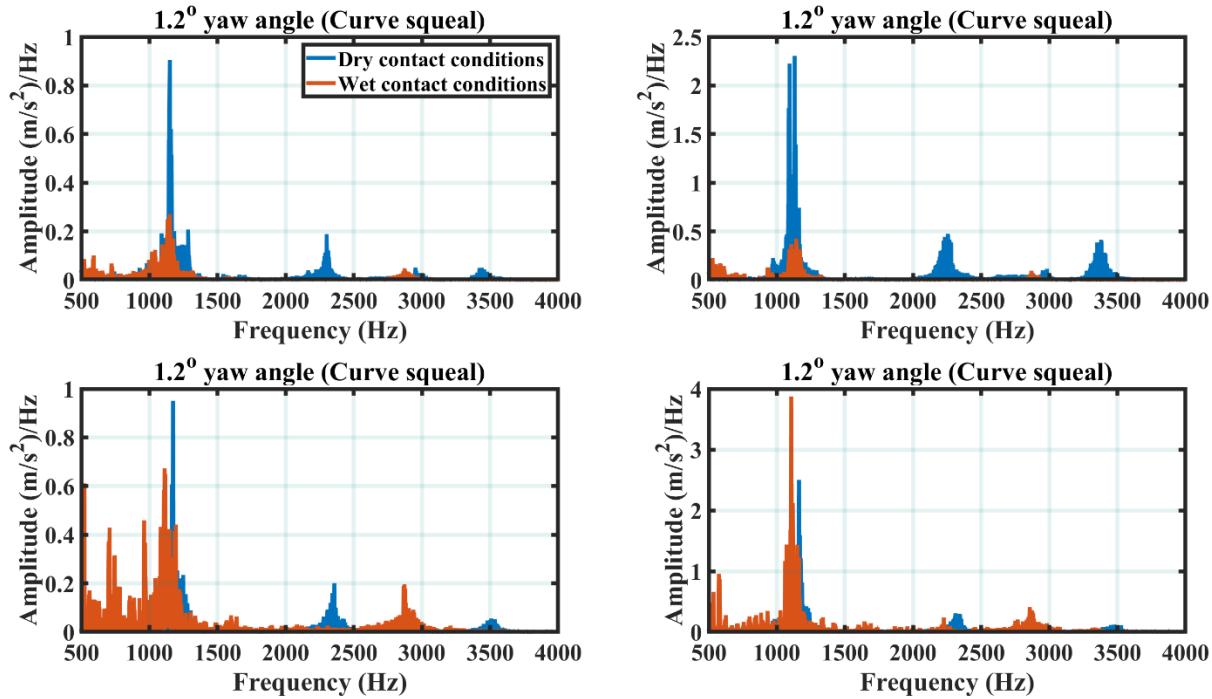
Figure 6.22: Spectrum plots from wheel accelerometer illustrating curve squeal mitigation using water applied on the wheel-rail interface for varying wheel speeds

The same conclusions stated for the effect of the application of FM1 on the wheel-rail contact can be inferred for plot in Figure 6.21. There is no significant difference in the mitigation effect when using FM2 as compared with FM1. It is however, necessary to note that for higher average wheel speeds (150RPM and 175RPM); there is a notable increase in the amplitude of vibrations around the axial modes of the wheel roller (second nodal diameter). This is greater than the fundamental frequency associated with curve squeal. Despite the larger amplitude of the axial modes of the wheel roller second nodal diameter frequency (centred at around 1093.5 Hz), the main aim of application of FM1 and FM2 is to eliminate the high frequency harmonics and allow the wheel roller to vibrate at its natural modal frequencies as obtained in the impact hammer test results.

Finally, Figure 6.22 shows the spectrum plots for varying wheel speeds obtained from the wheel accelerometer in wet contact conditions. The application of water on the wheel-rail roller interface was investigated. Similar conclusions for FM1 and FM2 results shown in Figure 6.22 and Figure 6.23 can be applied as well. Curve squeal and its associate harmonics was eliminated for the application of water on the wheel-rail interface. It is also important to note that the water application made the wheel roller to start to vibrate at its natural modes as well.
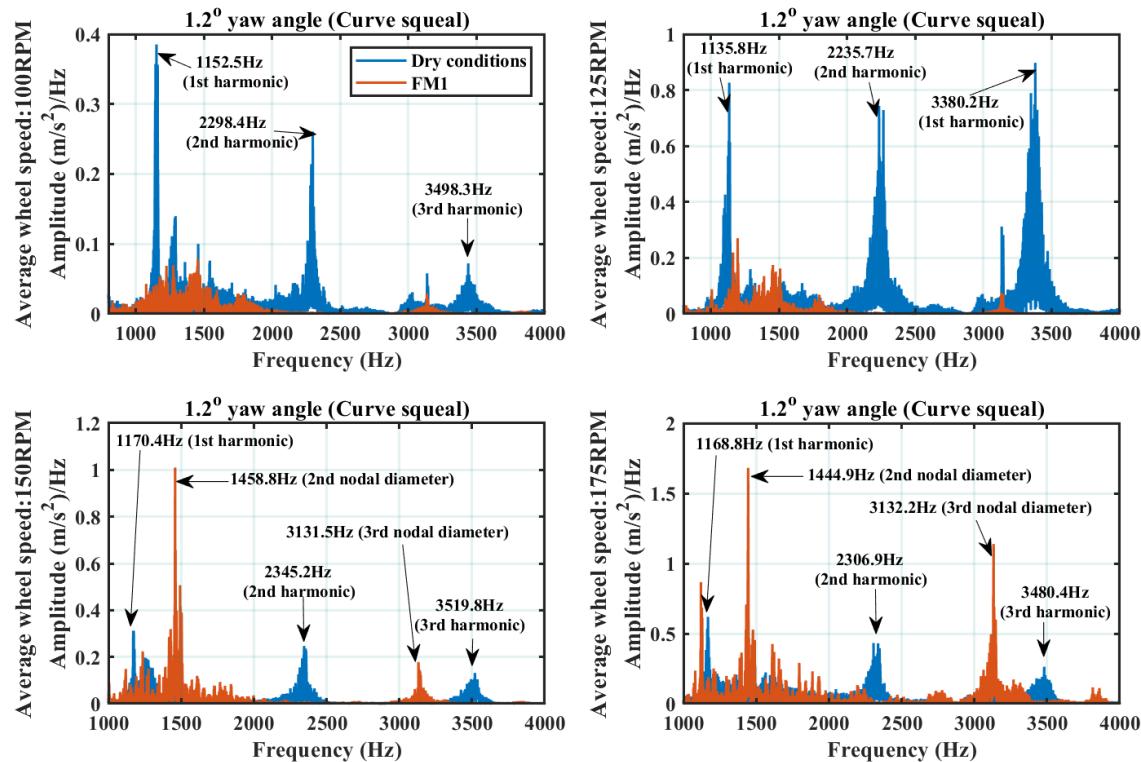
Figure 6.23: Spectrum plots from rail accelerometer illustrating curve squeal mitigation using FM1 applied on the wheel-rail interface for varying wheel speeds

Figure 6.23 shows the spectrum plots obtained from the rail accelerometer when FM1 was applied on the wheel-rail interface. Although the rail roller is not the major contributor to curve squeal, it is important or the overall test rig that curve squeal on the rail roller is mitigated as well. It can be observed that the application of FM1 eliminates the harmonics associated with curve squeal for all four average wheel speeds. As the average wheel speed increases, the amplitude of the harmonics reduces while the amplitudes of the rail roller natural modes increase considerably. The increase in the vibration amplitudes of the natural frequencies of the rail roller as the speed increases does

not imply that curve squeal exists since the rail roller is just vibrating at its respectively frequencies.
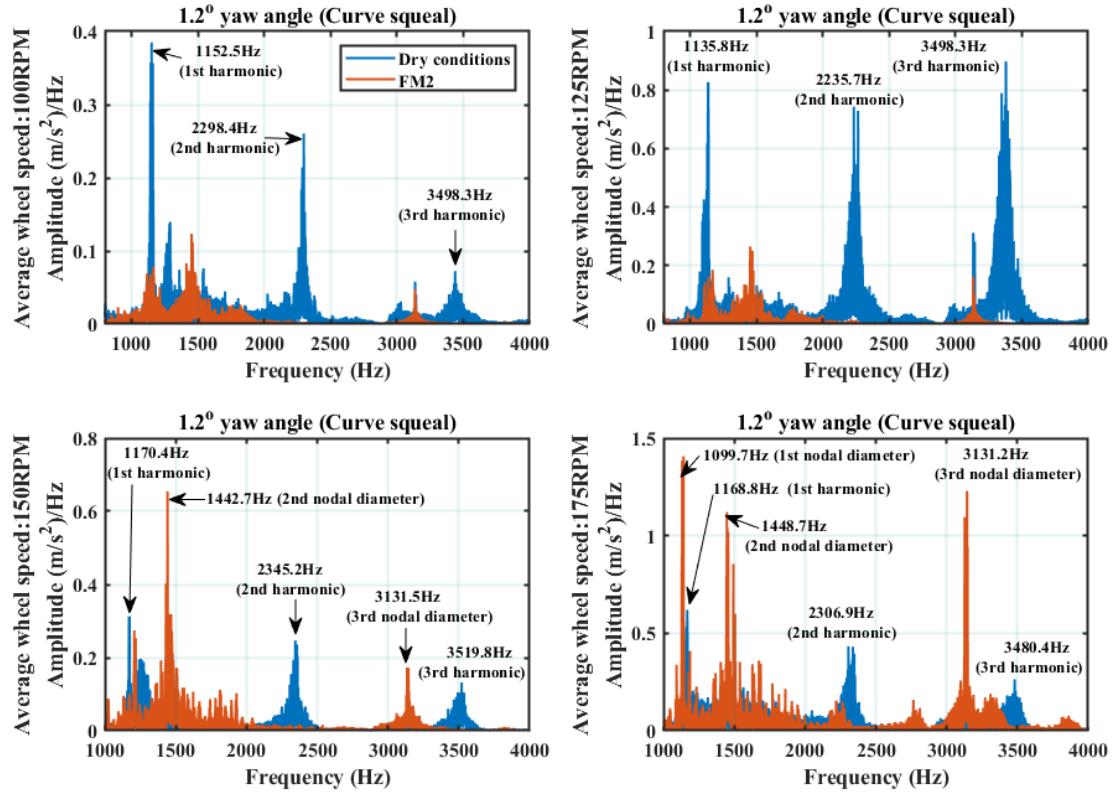
Figure 6.24: Spectrum plots from rail accelerometer illustrating curve squeal mitigation using FM2 applied on the wheel-rail interface for varying wheel speeds

Similar results are obtained for the spectral plots shown in Figure 6.24 and Figure 6.25 for the application of FM2 and water to the wheel-rail roller interface.
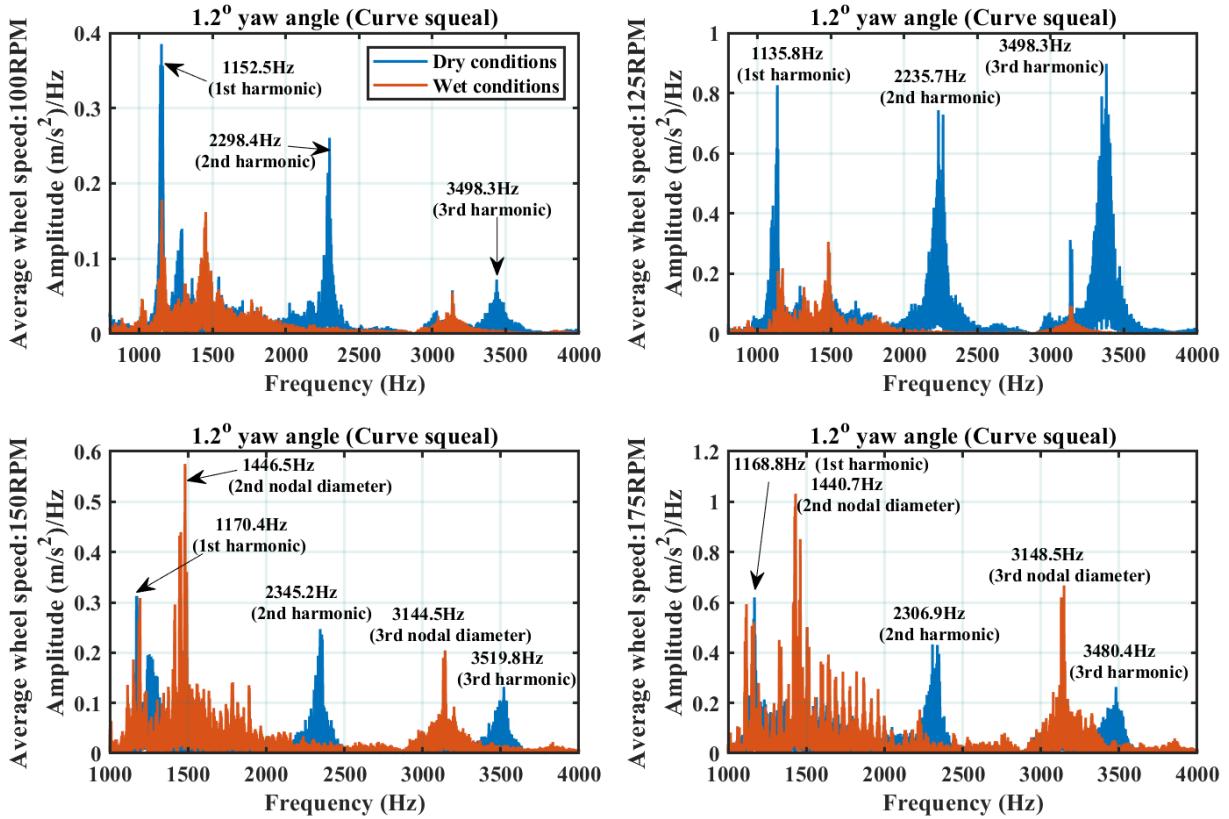
Figure 6.25: Spectrum plots from rail accelerometer illustrating curve squeal mitigation using water applied on the wheel-rail interface for varying wheel speeds

To conclude, the effect of water, FM1 and FM2 on the wheel-rail interface mitigated curve squeal in the wheel and rail roller. Although the wheel roller is dominate cause of curve squeal due it's higher vibration amplitude for all average wheel speeds when compared with the rail roller spectral plots, it is evident that the harmonics associated with curve squeal of both rollers was removed. It is therefore important to note the strong vibration centered at the fundamental frequency for curve squeal and its harmonics (second and third harmonics) are responsible for curve squeal.

6.5 Curve squeal detection using the frequency bands

The frequency bands of interest that are associated with curve squeal are the WMB, CSB, RNB and RMB. However, to determine the onset development of curve squeal, that is the transition between no curve squeal and curve squeal regions, the spectrum plots of the CSB, RNB and RMB are a useful feature. The spectral peak in the CSB, RNB and RMB obtained from the power spectrum plots in dB/Hz, is plotted for each respective yaw angle.

Figure 6.26 shows the effect of varying yaw angle on the peak power spectral density for the three frequency bands CSB, RNB and RMB for all four average wheel speeds. The spectrum plots was generated from the wheel accelerometer data.
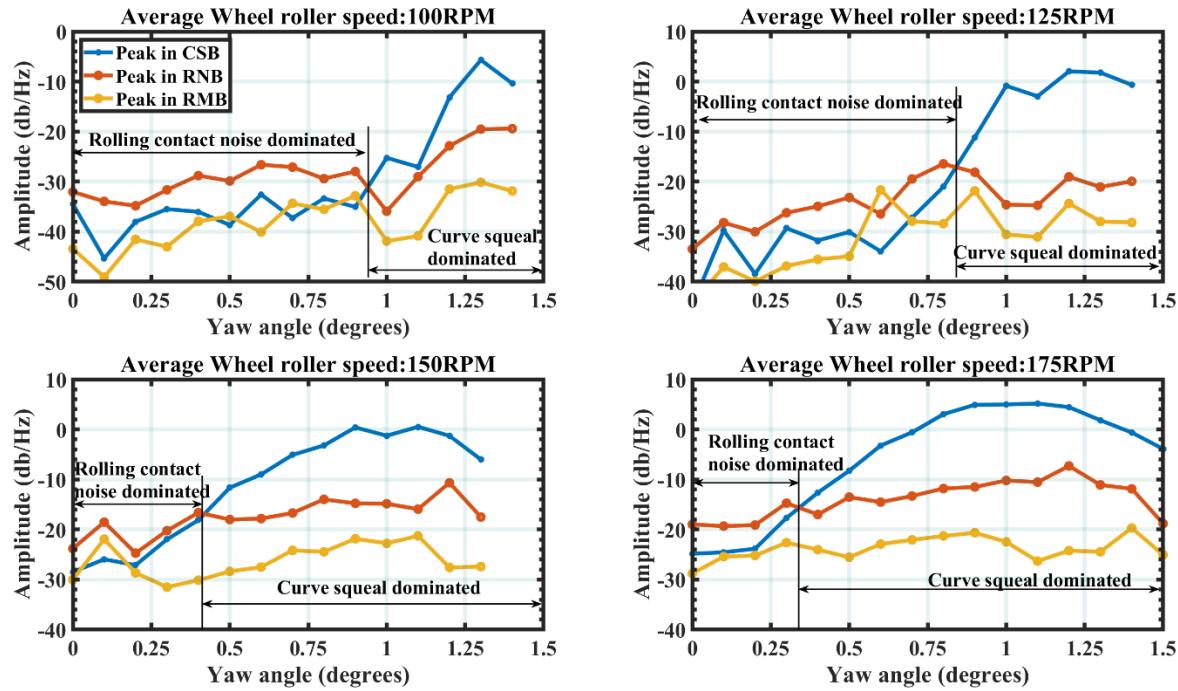
Figure 6.28: The effect of varying yaw angle on the peak power spectral density for the wheel accelerometer for three main frequency bands (CSB, RNB and RMB).

It can be observed from the plots that the rolling contact noise region is dominated by the frequency CSB when no curve squeal is observed for all average wheel speeds. The onset development of curve squeal starts at about 0.9^0, 0.85^0, 0.4^0 and 0.35^0 for average wheel speeds 100RPM, 125RPM, 150RPM and 175RPM respectively. The curve squeal region can be observed from Figure 6.26 as dominated by the CSB region. The actual curve squeal frequency for the average wheel speeds varies within this region. It can be concluded from the results obtained that wheel speed is an important factor for the onset development of curve squeal. As the wheel speed increases, the chances of curve squeal developing increases. This implies that the actual yaw angle required for the development of curve squeal reduces as the wheel speed increases. This explains why in actual railway curves, wheelset speeds are crucial to minimize the incipient development of curve squeal.
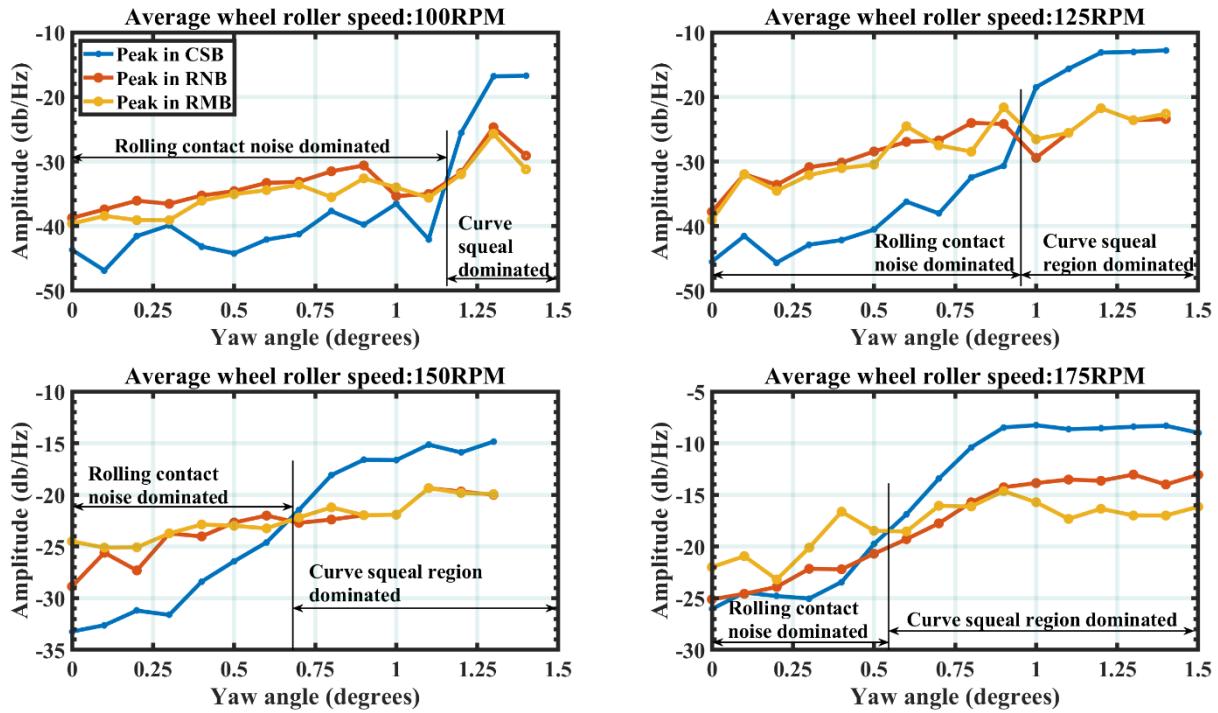
Figure 6.27: The effect of varying yaw angle on power spectral density for the rail accelerometer for three main bands (CSB, RNB and RMB)

Figure 6.27 shows the peak power spectral density obtained from the rail accelerometer for varying average wheel speeds. The onset yaw angle after which curve squeal is developed are about 1.15^0, 0.95^0, 0.7^0 and 0.55^0 for average wheel speeds of 100RPM, 125RPM, 150RPM and 175RPM. There is small disparity in the onset yaw angles for the rail accelerometer results when compared with the wheel accelerometer results in Figure 6.27. This is probably due to the mounting positions of the accelerometers. This explains why there is a delay in the onset detection of curve squeal in the rail accelerometer when compared with the wheel accelerometer results. It is also worthy of mention that the peak power spectral density values for the wheel accelerometer data for all speeds is greater than that of the rail roller. This again explains that the wheel roller is the main contributor to curve squeal on the test rig.

6.6   Feature extraction methods applied to the wheel and rail accelerometer spectrum data

In this section, feature extraction methods would be applied to the wheel and rail accelerometer spectrum data.

Peak and RMS condition monitoring indicators have been selected as the feature extraction methods in this chapter due to their ability to precisely detect and characterize curve squeal. Kurtosis and skewness condition monitoring indicators was applied to the wheel and rail accelerometer spectrum data. They were not presented in this thesis as they did not yield satisfactory results.

6.6.1 Spectral peak condition monitoring indicator application for curve squeal detection

Figure 6.28 shows the spectral peak analysis obtained from the wheel accelerometer spectrum data for the three frequency bands (CSB, RNB and RMB). The RNB and RMB spectral peaks values remained low for all yaw angles. There is a clear difference between the rolling contact noise dominated region and the curve squeal dominated region for all four average wheel speeds. A sharp increase in the CSB spectral peak frequency is an indication of early development of curve squeal. The transition yaw angles between rolling noise dominated region and curve squeal dominated region are 0.9 degrees, 0.8 degrees, 0.35 degrees and 0.35 degrees.
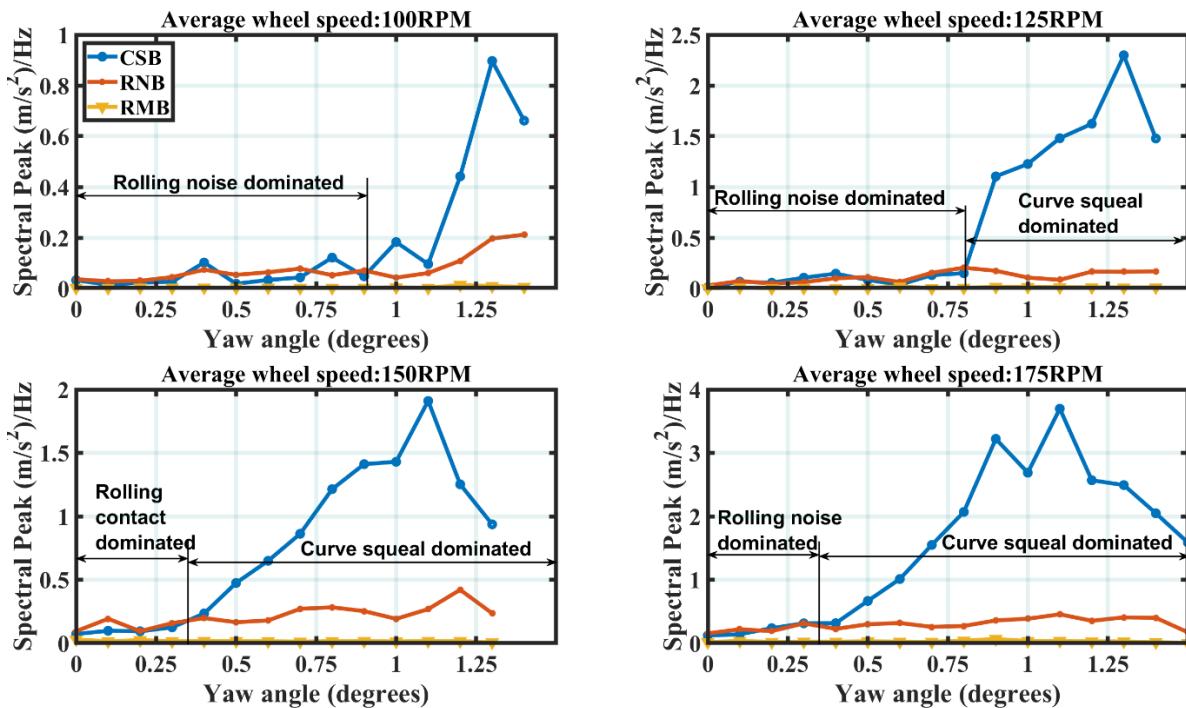
Figure 6.28: Spectral peak analysis obtained from the wheel accelerometer spectrum data for the three frequency bands (CSB, RNB and RMB).

These values show that a decrease in the transition yaw angles is as a result of the increase in the average wheel speed.

Figure 6.29 shows the increase of the spectral peak analysis plots obtained for the rail accelerometer spectrum data for the three frequency bands. The results obtained shows that the transition yaw angles are located at around 1.1 degrees, 0.95 degrees, 0.7 degrees, and 0.5 degrees for average wheel speeds of 100RPM, 125RPM, 150RPM and 175RPM. The spectral peak condition monitoring indicator clearly differentiated between the rolling noise dominated region and the curve squeal dominated region.
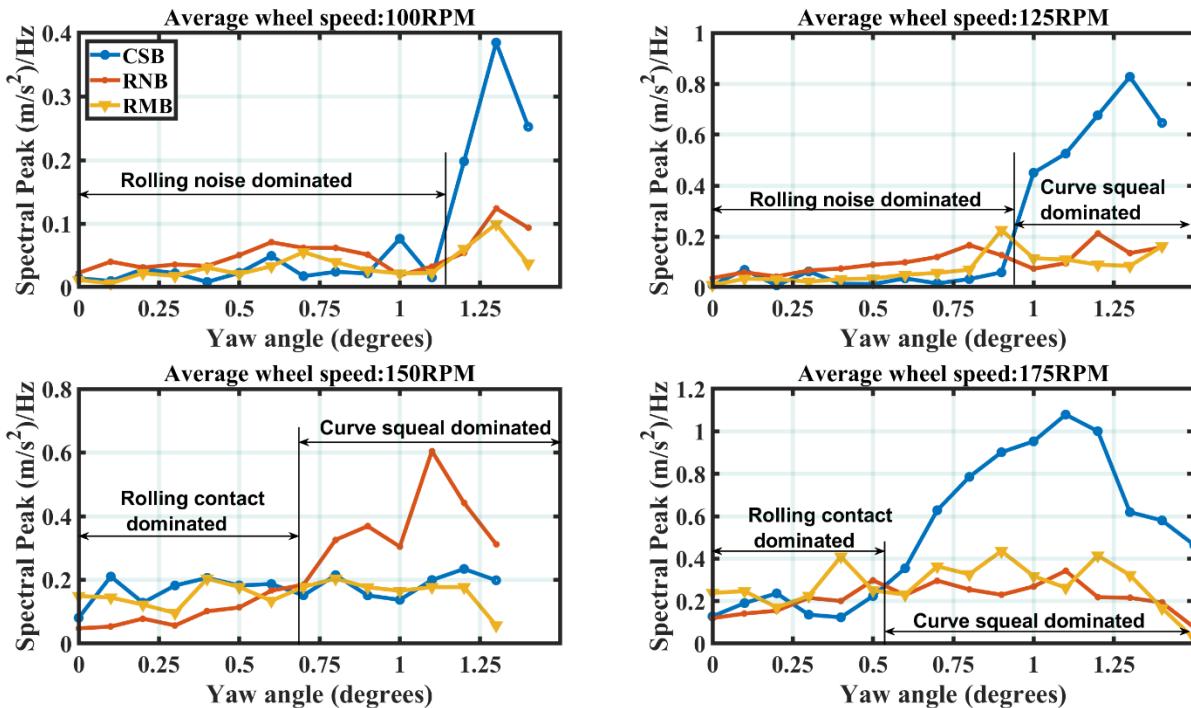
Figure 6.29: Spectral peak analysis obtained from the rail accelerometer spectrum data for the three frequency bands (CSB, RNB and RMB).

6.6.2 Spectral RMS condition monitoring indicator application for curve squeal detection

This condition monitoring indicator was applied in similar manner the microphone data. The same procedure was applied to the wheel and accelerometer spectrum data. Bandpass filter was designed around the RMB, CSB and RMB frequency bands. The spectral RMS was calculated using equation 5.6, 5.7 and 5.8 for the respective frequency bands.

Figure 6.30 shows the spectral RMS obtained from the wheel accelerometer spectrum for the three frequency bands of interest. The transition yaw angles that demarcate between rolling noise dominated region and curve squeal dominated region are approximately equal to 0.9 degrees, 0.8

degrees, 0.35 degrees and 0.35 degrees for average wheel rolling speeds of 100RPM, 125RPM, 150RPM and 175RPM.
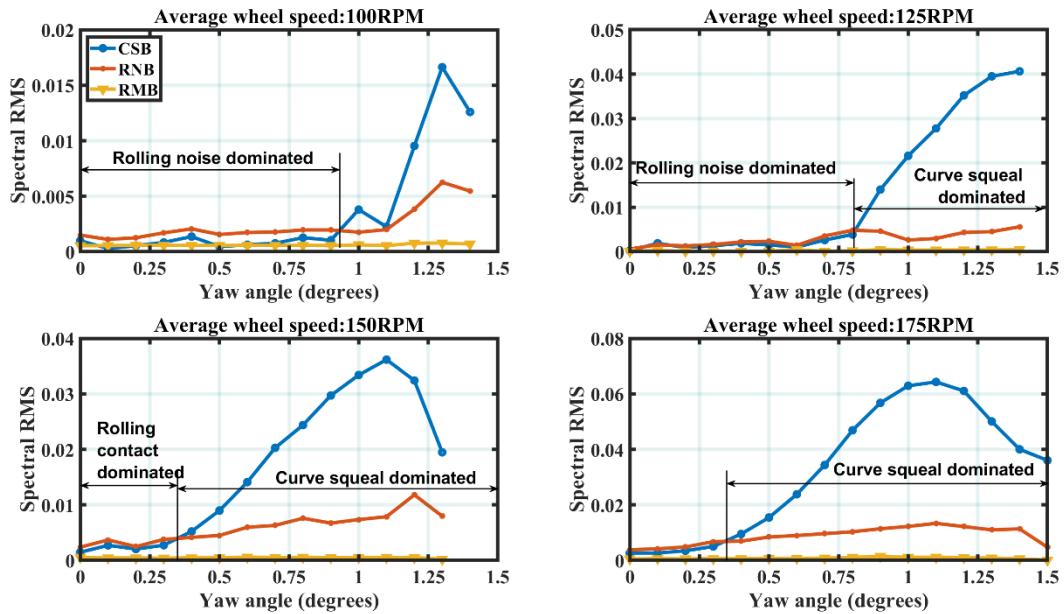
Figure 6.30: Spectral RMS analysis obtained from the wheel accelerometer spectrum data for the three frequency bands (CSB, RNB and RMB).

Similarly, for the rail accelerometer spectrum plots in Figure 6.31, the transition yaw angle results, are around 1.15^0, 0.95^0, 0.7^0 and 0.55^0 for average wheel speeds of 100RPM, 125RPM, 150RPM and 175RPM respectively.

The transition yaw angles obtained from the wheel and rail roller spectrum are slightly different from each other. The wheel roller identifies the onset development of curve squeal earlier than the rail roller. It may be advantageous to use the transition yaw angles of the wheel roller as a yardstick for the early detection and characterization of curve squeal.
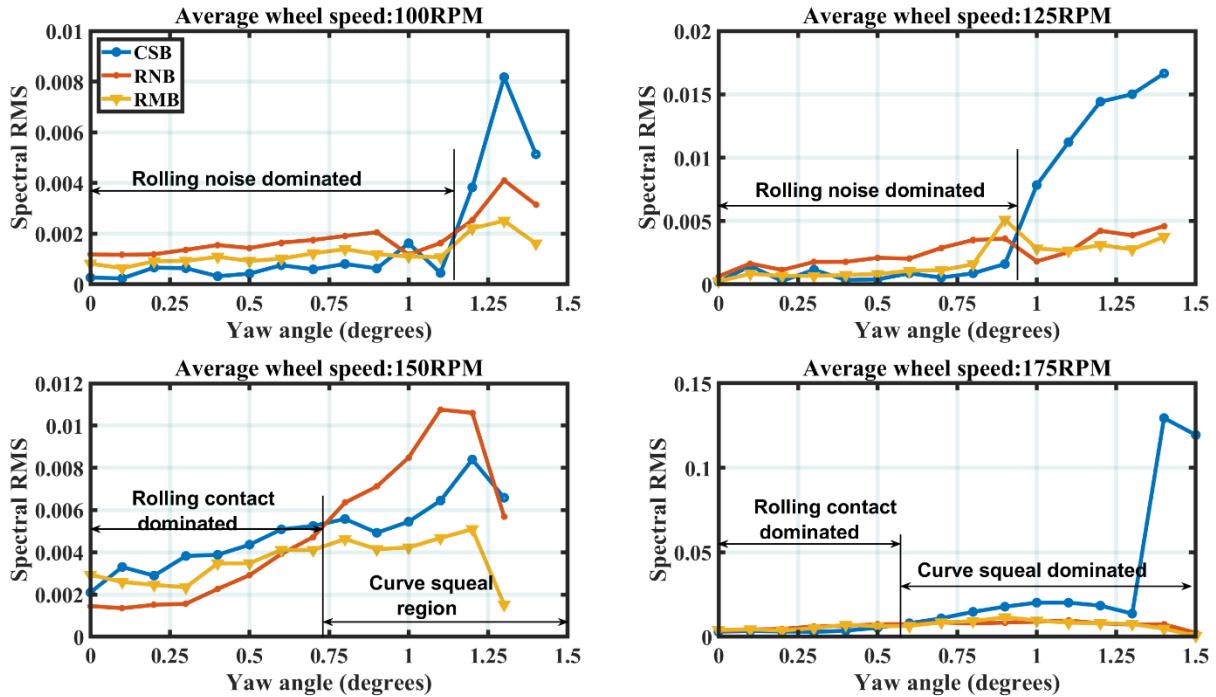
Figure 6.31: Spectral RMS analysis obtained from the rail accelerometer spectrum data for the three frequency bands (CSB, RNB and RMB).

6.7 Curve squeal detection and mitigation using harmonics

Figure 6.32 shows the effect of varying the yaw angle on the spectrum of for the dominant squeal band (CSB). It can be observed that for average wheel speeds 100RPM, 125RPM and 150RPM, curve squeal was mitigated in this frequency band to an extent. However, it is difficult to tell if curve squeal was mitigated for average wheel speed of 175RPM. The spectral RMS value increased for increasing yaw angle for dry, wet, FM1 and FM2 contact conditions. For average speeds of 100RPM, 125RPM and 150 RPM, the yaw angles were curve squeal mitigation was observed are around 1.2^0, 0.9^0 and 0.6^0 respectively.

The spectral RMS plots for average wheel speed of 175RPM shows the spectrum of the wheel accelerometer for wet, FM1 and FM2 contact conditions increasing in the curve squeal region with increasing yaw angle. This trend was observed for the average wheel speed of 150RPM. The results show that are high yaw angles, it is not always the case that the application of FM1, FM2 and water would attenuate the dominant curve frequency of the wheel roller at higher speeds (150RPM and 175RPM). A useful indicator to understand curve squeal mitigation is to investigate

184

what happens to the bandpass spectrum of the second and third harmonics of the wheel and accelerometer spectrum when water, FM1 and FM2 is applied to the wheel-rail interface.
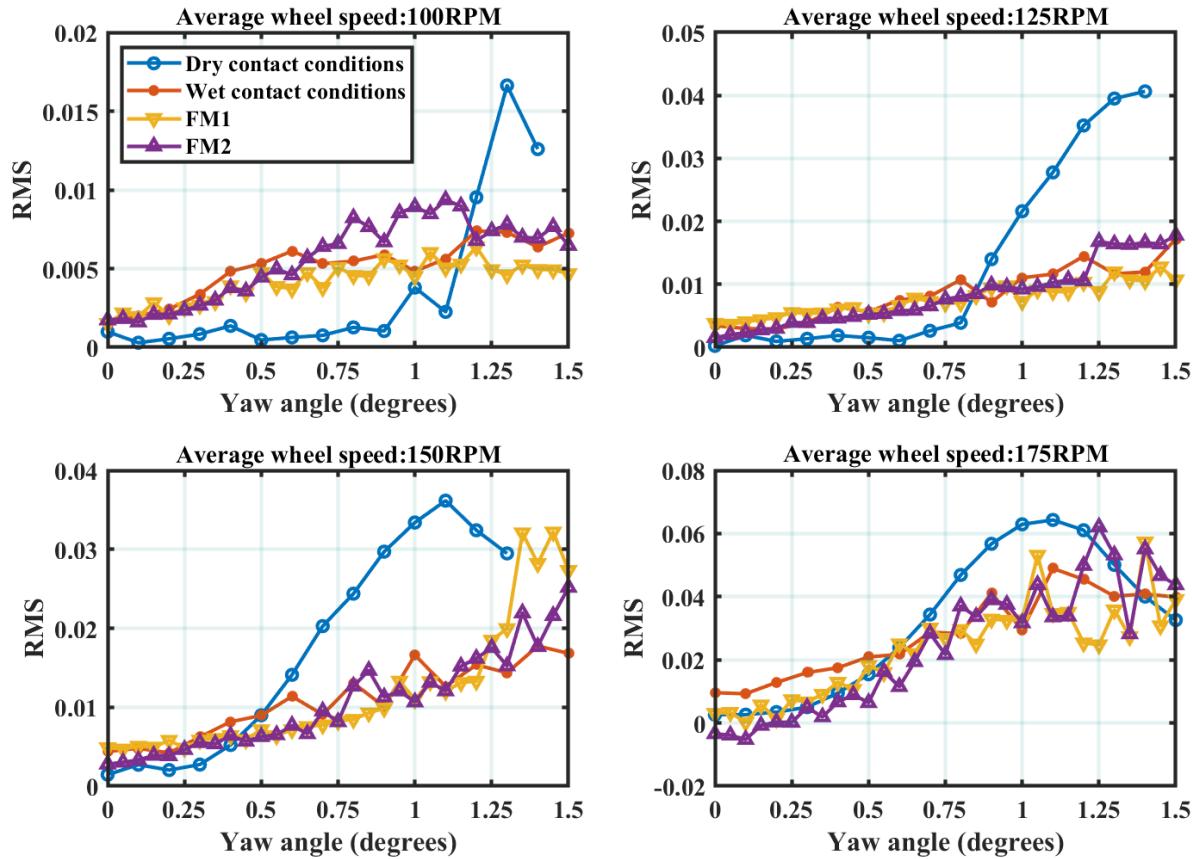
Figure 6.32: Spectral RMS of frequency band (CSB) obtained from the wheel accelerometer spectrum

Figure 6.33 for instance shows the effect of varying the yaw angle on the bandpass filtered RMS second harmonic frequency band (2200Hz – 2400Hz). The 200Hz frequency band range has been chosen to accommodate the total energy spectra associated with the harmonic frequencies.

It is observed that for wet, FM1 and FM2 contact conditions, for all average wheel speeds, curve squeal was mitigated completely. It is also observed from the plots that the transition yaw angles for 100RPM, 125RPM, 150RPM and 175RPM are observed at 1.1^0 0.9^0, 0.5^0 and 0.5^0 respectively. The application of water, FM1 and FM2 mitigated curve squeal for all four average wheel speeds.
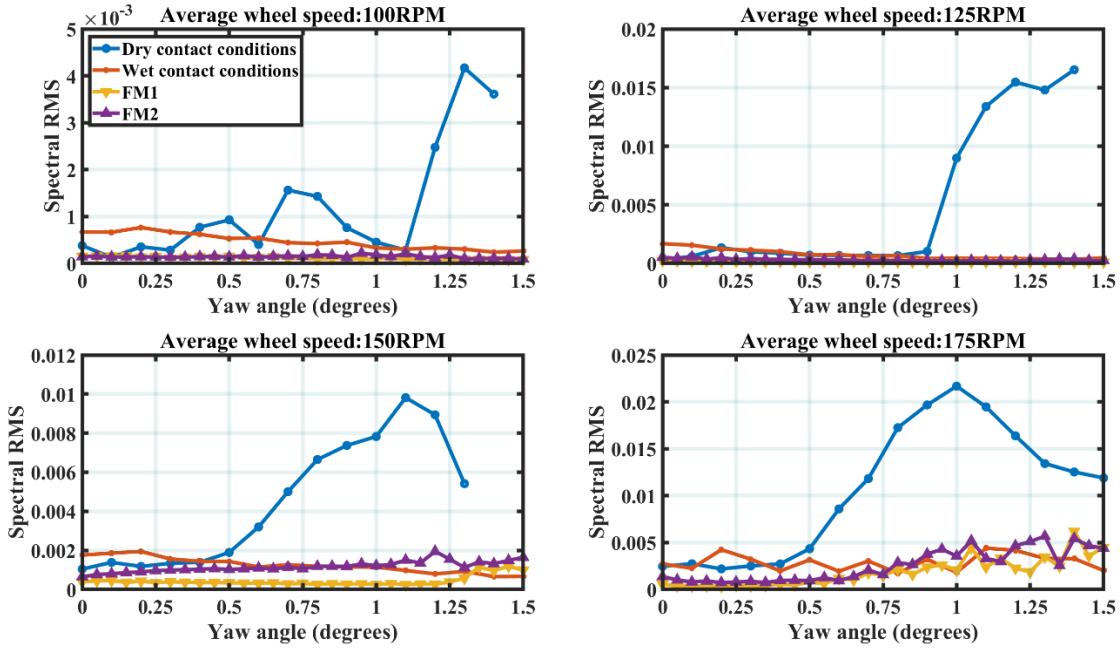
**Figure 6.33: Spectral RMS of the 2ⁿᵈ harmonic frequency band (2200Hz – 2400Hz)
obtained from the wheel accelerometer spectrum**

Figure 6.34 displays the bandpass filtered spectral RMS values for the 3rd harmonics computed at the frequency range of (3400 – 3600Hz) from the wheel accelerometer spectrum.
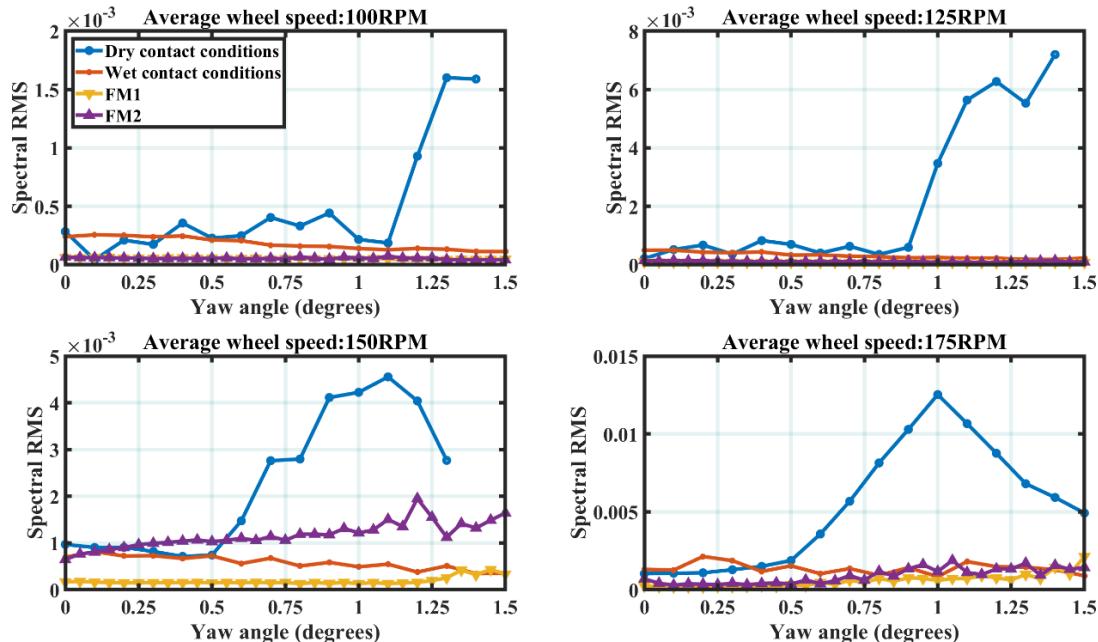
**Figure 6.34: Spectral RMS of the 3ʳᵈ harmonic frequency band (3400Hz – 3600Hz)
obtained from the wheel accelerometer spectrum**

186

The same transition yaw angles that differentiates between curve squeal and no curve squeal obtained from Figure 6.33 is observed. It can also be concluded that the application of water, FM1 and FM2 to the wheel-rail interface mitigated curve squeal completely for all yaw angle variations. Figure 6.35 displays the bandpass filtered spectral RMS values for the dominant curve squeal frequency located at the CSB frequency band. For average wheel speeds of 100RPM, 125RPM and 150RPM, a clear difference between the region of curve squeal and no curve squeal is observed. However, at the highest average wheel speed, the differentiation between the no curve squeal and curve squeal region is not clear. The reason for this that the introduction of water, FM1 and FM2 to the wheel-rail interface does not completely attenuate the spectral RMS values at the highest average wheel speed. It can therefore be inferred from this result that the understanding of how curve squeal is mitigated is not dependent solely on what transpires at the dominant curve squeal frequency. Further investigation as the case maybe on the harmonics produced as a result of the dominant curve squeal frequency provides more insight to the mitigation property of water, FM1 and FM2 applied to the wheel-rail interface.
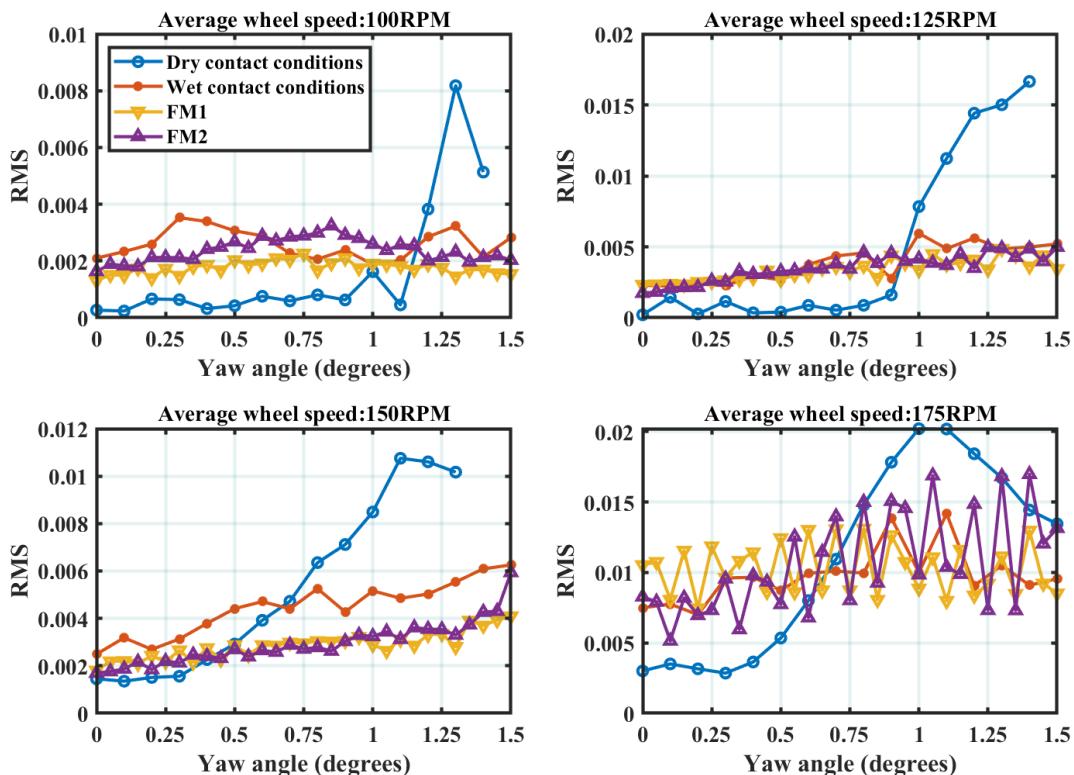
Figure 6.35: Spectral RMS of the fundamental frequency band (CSB) obtained from the rail accelerometer spectrum

Figure 6.36 displays the bandpass filtered spectral RMS values for the 3rd harmonics computed at the frequency range of (2200 – 2400Hz) from the wheel accelerometer spectrum.

The same transition yaw angles obtained from the wheel accelerometer spectrum are observed in the spectral RMS results of the rail accelerometer spectrum. The spectral RMS of the 2nd harmonics obtained from the rail accelerometer spectrum is a strong indicator that illustrates early development of curve squeal and its mitigation on the twin disc rig. The results clearly show that curve squeal has been eliminated for all average wheel speeds as the yaw angle increases for wet, FM1 and FM2 contact conditions. The transition yaw angles are 1.1^0, 0.9^0, 0.5^0, and 0.5^0 for average wheel speeds 100RPM, 125RPM, 150RPM and 175RPM respectively.
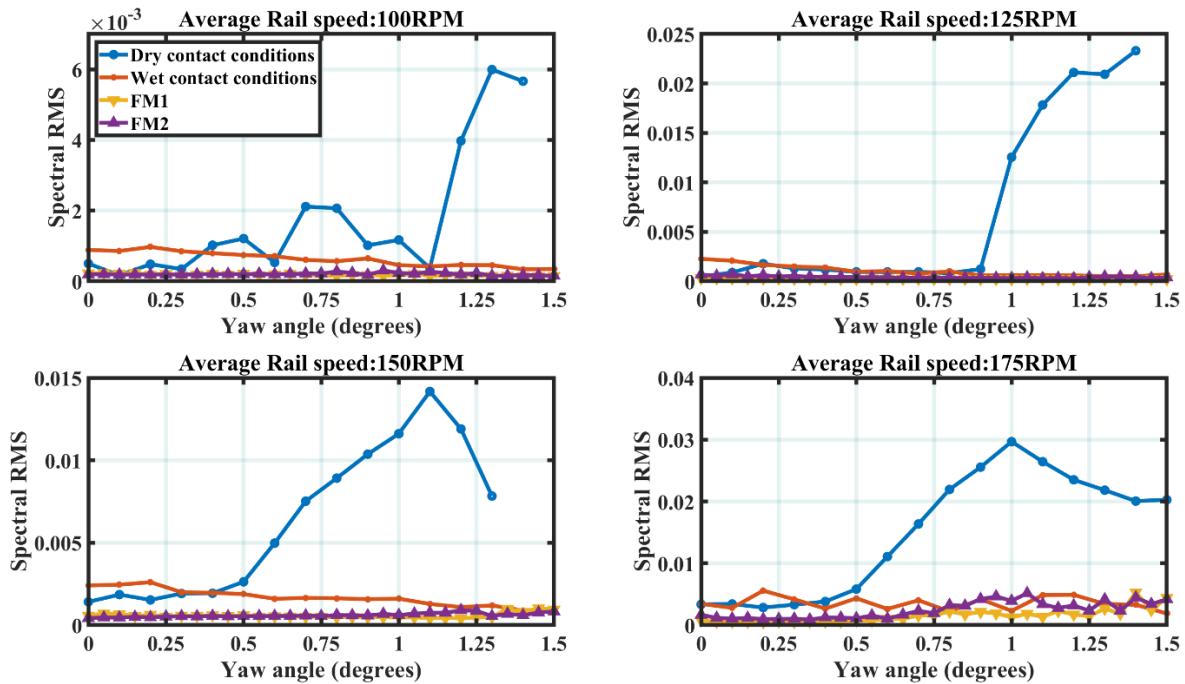
Figure 6.36: Spectral RMS of the second harmonics band (2200Hz – 2400Hz) obtained from the rail accelerometer spectrum.

Finally, Figure 6.37 shows the spectral RMS calculated from the third harmonic band (3400 Hz to 3600Hz) obtained from the rail accelerometer spectrum. The transition yaw angles are observed to be similar to the spectral RMS plots of the second harmonics obtained from the rail accelerometer spectrum in Figure 6.36. This implies that the transition yaw angles obtained from the spectral RMS of the wheel and rail accelerometer spectrum have a high positive correlation.

188
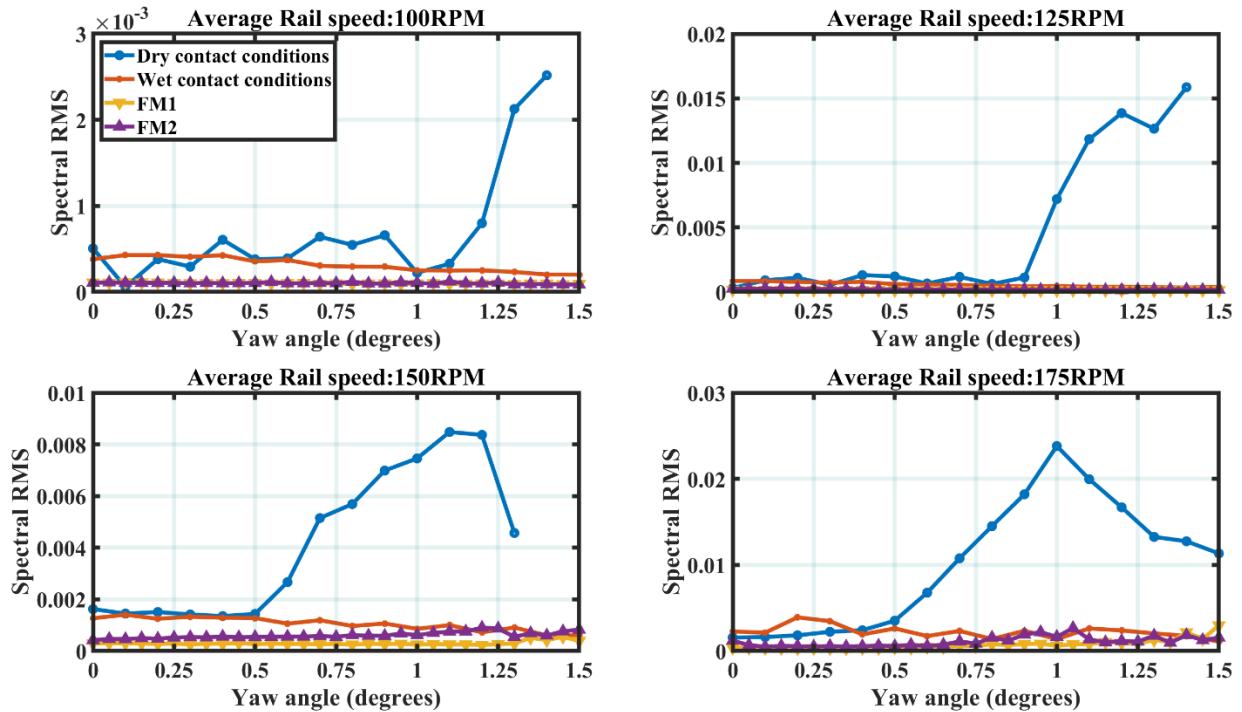
Figure 6.37 Spectral RMS of the third harmonics band (3400Hz – 3600Hz) obtained from the rail accelerometer spectrum.

The application of the spectral RMS condition monitoring indicator to determine the onset development of curve squeal and how it is mitigated is a suitable feature extraction method. Even for the variation of the average wheel speed and contact conditions, this condition monitoring indicator performed effectively.

6.8   Summary

This chapter has presented a signal processing tool that can be used to analyse the vibration data obtained from the wheel and rail accelerometer. From the raw signal plots of the time domain data, it was observed that there was clear acceleration magnitude difference between data obtained when the rollers are at central position to the data obtained when yaw angle is applied to the rail roller in dry contact conditions. The vibration amplitudes of the time domain data when water, FM1 and FM2 data was applied to the wheel-rail interface was observed to have slightly higher amplitudes for all average wheel speeds compared to the vibration amplitudes for dry contact conditions.

189

However, the decrease in wheel speed when water, FM1 and FM2 was applied to the wheel rail surfaces was not significant even at high yaw angles due to the change in the wheel-rail contact conditions compared to dry contact conditions. The average wheel speed of the wheel roller was estimated by finding the mean of all the individual wheel speeds obtained from the time domain data at dry contact conditions. Even though the wheel speed was set to operate the twin disc rig, the wheel speed was not constant due to the variation in the contact conditions and increase in yaw angle. As the yaw angle increases, the lateral creepages increase thereby leading to an increase in the lateral forces. This causes unsteady adhesion coefficient thus transferring excessive load to the three-phase induction motor. Despite these challenges, curve squeal was investigated using condition monitoring indicators for feature extraction applied to the accelerometer data. It was possible to identify the transition yaw angle for which curve squeal occurs using the peak, rms, crest factor, kurtosis and skewness. The main conclusion established from the five condition monitoring indicators is that the accelerometer data for the wheel and rail presented a difference between curve squeal and no curve squeal experienced on the twin disc rig. Kurtosis and skewness of the data presented a clear difference curve squeal and no curve squeal. Kurtosis values ranging from 3 to 5 indicate the pure rolling noise caused by the vibration of the wheel and rail rollers. Kurtosis values greater than this range indicated the development of curve squeal in the test rig. Skewness values around zero signified the lack of curve squeal. Negative skewness exhibited by the wheel accelerometer data for all four-wheel speeds indicate the development of curve squeal. Though the condition monitoring indicators provided slightly different transistor yaw angles, they were able to estimate the occurrence of curve squeal. However, time domain methods were not able to identify the frequency that is responsible for curve squeal.

The application of spectrum analysis to the wheel and rail accelerometer data was therefore necessary to determine the excitation frequency responsible for curve squeal and understand how curve squeal is mitigated with the introduction of contaminants to the wheel-rail interface. Four frequency bands as was the case with the spectrum analysis of the acoustic data was applied to the wheel-rail roller data. The four bands were chosen around the maximum spectral energy of interest from the accelerometer spectrum where the dominant curve squeal frequency is located. The four bands specified in a band frequency of 500Hz include WMB, CSB, RNB and RMB.

The results obtained from spectral analysis of the wheel and rail accelerometer data in dry contact conditions shows that the dominant frequency responsible for curve squeal is excited when the

yaw angle increases beyond a certain value for all four average wheel speeds. This value is called the transition yaw angle. This transition yaw angle decreases as the average wheel speed increases. The dominant curve squeal frequency was observed to be located in the CSB for all four average wheel speeds in dry contact conditions. When the wheel and rail roller is not squealing, the spectrum analysis of the results show the excitation of the axial vibrations of the wheel and rail roller. This normal trend characterizes the dynamics of the wheel-rail contact for yaw angles less than the transition angle. The excitation of the curve squeal frequency beyond the transition yaw angle results in the development of harmonics. The harmonics identified were the 2nd and 3rd harmonics for the wheel and rail roller accelerometer spectrum results.

Condition monitoring indicators, peak and RMS was applied to the frequency bands of the wheel and rail accelerometer spectrum to extract useful features such as detect curve squeal and investigate curve squeal mitigation. It was also useful to understand what happens when water, FM1 and FM2 is introduced to the wheel-rail interface. The application of these contaminant was observed to attenuate curve squeal dominant frequency for all average wheel speeds, excite the rail roller natural frequency located in RMB and completely eliminate the 2nd and 3rd harmonics generated from the dominant curve squeal frequency. Therefore, spectral analysis of the harmonics band specified in this study to have a bandwidth of 200Hz around the region of interest is a useful feature for understanding the development and mitigation of curve squeal on the test rig. Without any reasonable doubt, there was a positive correlation between the spectral analysis obtained from the wheel and rail accelerometer spectrum data when the spectral RMS was analysed. To conclude, the transition yaw angles for the four average wheel speeds 100RPM, 125RPM, 150RPM and 175RPM are 1.1 degrees, 0.9 degrees, 0.5 degrees and 0.5 degrees respectively.

The next chapter presents a detailed comparison between acoustic and vibration results. Correlation between the acoustic and vibration data is used to establish a reliable relationship between the two data. An online scheme would be suggested that could be applied for curve squeal detection and mitigation.

Chapter Seven: Comparison of acoustic and vibration measurement methods for the condition monitoring of curve squeal

This chapter presents the comparison between acoustic and vibration measurements methods for condition monitoring of curve squeal on the twin disc rig. Condition monitoring of progressive curve squeal and early diagnosis of possible wear as a result is crucial to railways to avoid annoyance in the environment characterized by increase in vibration and/or noise levels. Using microphones for acoustic measurement has its unique non-contact advantage of condition monitoring of curve squeal. The principal condition monitoring indicator that can be used for characterizing incipient development of curve squeal and the correlation between non-contact acoustic signal and vibration spectra is unknown. In this chapter the spectrum analysis results of the acoustic and vibration data would be compared in the time and frequency domain using signal processing techniques. Correlation and reliable relationship between acoustic and vibration results would be established. Finally, comparison of what happens when contaminants are introduced to the wheel-rail interface would be investigated using acoustic and vibration sensors. A suitable online scheme for condition monitoring of curve squeal on the twin disc rig that could be applied in the railway industry.

7.1   Introduction

Curve squeal in railways results in associated with interaction between the wheel and the rail. It is strongly tonal and associated with the intense lateral vibration of the wheel in its dominant curve frequency together with its corresponding high frequency harmonics. Curve squeal is caused by the development of unsteady lateral forces developed at the wheel-rail contact occurring at high yaw angles or during curving in railways. The development of the unsteady transverse force is as a result of lateral creepage developed in the wheel-rail interface.

Acoustic measurement methods have been applied for decades to identify and detect curve squeal in curves. This measurement technique is used because of its low cost and non-contact feature. However, spurious noise from the environment from people, passing trains and doppler effect can lead to difficulties in feature extraction of the sound data obtained from the microphone. (Kim et al., 2019) and (Hanson et al., 2014) pointed out some of the challenges of using only microphones for curve squeal measurement. One of the key challenges is in the identification of which wheel is responsible for curve squeal in any given train pass on the railway track. One of the main propositions for identification of which wheel is squealing was to add an accelerometer mounted on the underside of each rail on the railway track. Comparison between the vibration levels from each squeal proved to be a reliable differentiator to identify the rail for which curve squeal occurs. However, it is difficult to use vibration measurements from accelerometers installed on the wheel and rail to monitor curve squeal because of the restrictions of contact sensor installation and high cost of vibration system. With the development of cheaper and cost-effective accelerometers, the integration of multiple sensors is advantageous to have than information derived solely from one sensor alone (Krishnakumar et al., 2018).

This chapter presents the comparison between the acoustic and vibration measurement features obtained from the microphone and accelerometers installed at the wheel and rail. The extracted features applied on both sensors have already been obtained from previous chapters. Correlation method would be used to establish a reliable relationship between acoustic and vibration data for detection and characterization of curve squeal. Correlation in its wide sense is a measure of relationship between two variables. In a highly correlated data, the magnitude change of one variable is related to a change in another variable either in terms of positive or negative correlation. In most cases correlation is used to establish a linear relationship between two variables. Further details on the correlation methods used are discussed in the next section.

7.2 Correlation coefficient methods for establishing relationship between two variables

Correlation is defined as a measure of monotonic association between two variables. The application of correlation is used to determine the strength of relationship between two variables. According to the theory of correlation, a monotonic relationship can be established if; the variable of one data increase as the other variable, or if the value of the variable decreases and the other variable increases. The magnitude change of one variable is associated with a magnitude change in another variable. When the values of one variable increases as the other variable increases, a positive correlation is established between the two variables. Also, when the values of one variable decreases as one variable decreases, then negative correlation is established between the two variables. The degree for which the variation in one variable is related to the variation in another variable can be defined mathematically in terms of the covariance variables. Covariance is an important property that is used to establish how two variables change together. The measurement scale of the variables influences the covariance values (Schober et al., 2018).

There are different methods used to establish correlation between two continuous variables. Some of the main methods include Pearson correlation coefficient, Spearman's correlation coefficient and Kendall correlation coefficient. Pearson correlation coefficient is the most widely used method for fast interpretation of the covariance scaled from -1 to 1. This correlation method is therefore preferred compared to the Spearman and Kendal correlation coefficient methods.

The definition of Pearson's correlation coefficient obtained for two random variables to measure their linear dependence is expressed as follows (Archdeacon, 1994):

$$p(X,Y) = \frac{1}{N-1} \sum_{i=1}^{N} \left(\frac{\overline{X_i - \mu_X}}{\sigma_X} \right) \left(\frac{Y_i - \mu_X}{\sigma_Y} \right) \tag{7.1}$$

Where σ_X and μ_X are the standard deviation and mean of continuous variable X and σ_Y and μ_Y are the standard deviation and mean of continuous variable Y. Pearson correlation coefficient $p(X,Y)$ can also be expressed in terms of the covariance as:

$$p(X,Y) = \frac{cov(X,Y)}{\sigma_X \sigma_Y} \tag{7.2}$$

Where the covariance of the two variables *X and Y* is given as:

$$cov(X,Y) = \frac{1}{N-1} \sum_{i=1}^{N} (\overline{X_\iota - \mu_X}) (Y_i - \mu_X) \tag{7.3}$$

The Pearson correlation coefficient $p(X,Y)$ returns a correlation coefficient matrix which is defined as the matrix for each combination variable.

$$R = \begin{pmatrix} p(X,X) & p(X,Y) \\ p(Y.X) & p(Y,Y) \end{pmatrix} \tag{7.4}$$

Since the variables *X* and *Y* are correlated directly among themselves, the diagonal matrix can be expressed as 1 while the correlation coefficient value is expressed as:

$$R = \begin{pmatrix} 1 & p(X,Y) \\ p(Y.X) & 1 \end{pmatrix} \tag{7.5}$$

The correlation matrix in equation 7.5 derived from Pearson correlation coefficient equation in 7.1 is used to define the strength of correlation between the two continuous variables *X* and *Y*.

The assumptions of Pearson's correlation are stated as follows (Schober et al., 2018):

(1)   As the case may be for statistical inference, data obtained from representative or random sample that do not represent the intended application or population of interest cannot give meaningful results.

(2)   Pearson's correlation method requires that both variables are jointly normal distributed random variables and continuous. This implies that they must fulfil bivariate normal distribution in the intended population sampling.

The table for the interpretation of Pearson's correlation coefficient is defined as follows:

Table 7.1: Conventional method to for Pearson's correlation coefficient interpretation

Correlation coefficient value range	Interpreted value
0.00 – 0.1	Negligible correlation
0.1 – 0.39	Weak correlation
0.4 – 0.69	Moderate correlation
07 – 0.89	Strong correlation
0.9 – 1.00	Very strong correlation

One of the attractive features of correlation coefficient is its ability to translate the coefficient values into descriptors like strong correlation, very strong correlation, weak correlation as shown in Table 7.1. However, based on this table, the correlation coefficient can be easily disputable. For example, it would be unpredictable to classify a correlation coefficient of say 0.69 as moderate correlation and 0.7 as strong correlation. Rather than using this simplistic approach, the correlation coefficient would be interpreted in context with the intended application. Despite the uncertainty in the correlation coefficient value range, it can still be used to indicate the strength of correlation between the two variables.

7.3   The application of Pearson's correlation coefficient to the time domain feature extraction methods.

The application of the Pearson's correlation coefficient for the purpose of condition monitoring presents a efficient and effective approach in classification and detection of curve squeal. The time domain condition monitoring indicators obtained from the microphone and accelerometers data is applied in used to establish the correlation between the two sensor measurements to characterize and detect curve squeal. The features extracted from the time and frequency domain for the identification of curve squeal was first filtered using moving average filter. The reason for the application of moving average filter was to smoothen out the features extracted in the time and frequency domain to enable the proper application of Correlation method without any ambiguity in the data. Given a feature as G the equation for the moving average filter is expressed as follows:

$$D[i] = \frac{1}{M} \sum_{j=0}^{M-1} G[i+j] \tag{7.6}$$

Where *D* is the filtered output data, *G* is the input data and *M* represents the number of points in the average. A five-point moving filter was sufficiently applied to the features extracted from time and frequency domain to smooth out the data.

To fulfil the criteria of normalized continuous variables as specified in the assumptions using Pearson's correlation coefficient, the filtered extraction data are normalized beforehand using the expression as follows (Archdeacon, 1994):

$$N_{cm} = \frac{D - \mu}{\sigma} \tag{7.7}$$

Where *D* is the extracted features obtained from either the acoustic of accelerometer time domain data, μ is the mean of the extracted features for *D* and σ is the standard deviation of *D*.

After the normalization of the features extracted in in time domain, correlation coefficient is computed for the two variables. It is assumed that the features for the microphone data is stored in variable X while the features for wheel or rail accelerometer variable is stored in Y. The correlation coefficient R is calculated for the combinations of acoustic features and vibration features from the wheel accelerometer and acoustic features for the rail acoustic accelerometer.

For the condition monitoring indicators used for feature extraction application to the time domain data of acoustic and vibration signals, only skewness condition monitoring indicator was used for evaluation of the Correlation coefficient. The reason for this is that the other extracted features such as rms and peak did not detect or characterize curve squeal. There was no significant difference between the time domain peak and rms obtained using curve squeal and that of no curve squeal.

Only skewness and kurtosis condition monitoring indicators for the wheel roller was suitable for the application of Pearson's correlation coefficient method. The reason for this is that the skewness feature obtained for the wheel accelerometer is negatively skewed at the curve squeal region for all average wheel speeds. This was the same for the skewness obtained from the microphone data. However, the skewness for the rail roller was positively skewed when curve squeal was detected and identified. Therefore, the skewness feature obtained for the wheel roller can be correlated further with the skewness feature obtained from the microphone region to identify and characterize curve squeal. Also, the Kurtosis values obtained for the wheel and rail accelerometer had different transition yaw angles compared with the kurtosis values of the microphone data. Therefore, the kurtosis feature extraction results cannot be used for correlation between the sensors.

7.3.1 Application of Correlation coefficient to the Skewness Time domain feature.

Figure 7.1 represents the application of Pearson's correlation method applied to the wheel accelerometer and microphone data for various contact conditions and various all average wheel speeds. Skewness feature obtained from the microphone time domain data in dry contact conditions in the region of no squeal was correlated with the skewness feature obtained from the wheel accelerometer in dry, wet, FM1 and FM2 contact conditions. The transition yaw angles for curve squeal used are 1.1 degrees for 100 RPM, 0.9 degrees for 125RPM, 0.5 degrees for 150RPM and 0.5 degrees for 175RPM. The transition yaw angles were extracted from the skewness feature of the microphone and wheel accelerometer data discussed in previous chapters. In dry contact conditions, the correlation coefficient between the microphone data in no squeal region (DryMicNoSqueal) and correlation coefficient of the wheel accelerometer data in the curve squeal region (DryWheelAccSqueal) exhibits negligible correlation (see Table 7.1 for correlation rank) compared to the other contact conditions. However, the correlation coefficient of the microphone data in dry contact conditions in the no squeal region correlated with wheel accelerometer skewness feature in wet, FM1 and FM2 contact conditions show high moderate to strong correlation.
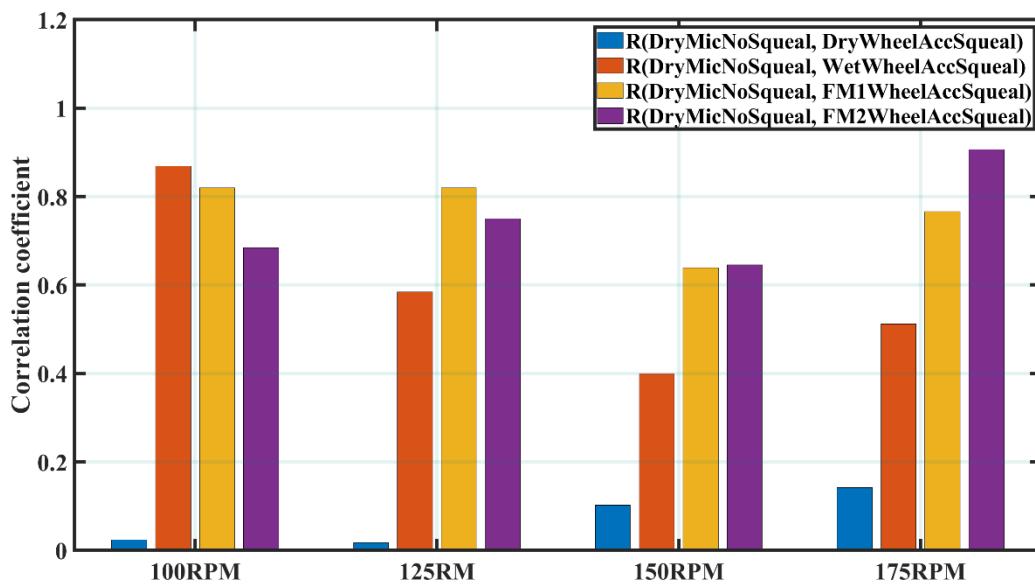
Figure 7.1: Correlation method applied to the skewness feature values from the microphone and wheel accelerometer data.

This distinctive difference at 100RPM indicates the difference between curve squeal and no curve squeal region. Similar trend is observed for average wheel speeds 125RPM, 150RPM and 175RPM respectively. For 125RPM, 150RPM and 175RPM, the correlation coefficient for dry contact conditions between the wheel and microphone accelerometer data exhibited negligible to weak correlation. This value indicates that development of curve squeal in dry contact conditions. The correlation coefficient between the skewness feature of the microphone and the rail accelerometer data did not provide satisfactory results. As explained, this is because of the positively skewness exhibited by the rail accelerometer skewness data. The correlation between the skewness values of the rail accelerometer data and other contact conditions yield confusing values that could not be used to detect the development and characterization of curve squeal in the twin disc rig.

The correlation feature has been applied between the skewness feature of the microphone and wheel accelerometer data to detect and characterize curve squeal. The disparity in the correlation coefficient between the dry contact conditions and the wet, FM1 and FM2 contact conditions shows the possible development of curve squeal.

7.3.2 Application of Correlation method to the spectral Peak and RMS of the dominant curve frequency in Frequency domain.

The application of the correlation method to the spectral peak and RMS feature values between the microphone and the wheel accelerometer is shown in Figure 7.2. At a glance, it is observed that the correlation coefficient of the spectral peak obtained for the microphone and wheel accelerometer spectrum in dry contact conditions has a weak correlation for all average wheel speeds. Transition yaw angles where used to establish the correlation between the spectral peak feature variables. It can also be inferred from the result that there is a clear distinction between the correlation coefficient values obtained when the spectral peak of the microphone data spectrum at dominant curve squeal band (CSB) is compared with wet, FM1 and FM2 contact conditions. There is a strong correlation between the spectral peak feature obtained from the microphone data at no squeal region and the wheel accelerometer spectrum at curve squeal region for wet, FM1 and FM2 contact conditions. This indicates that at dry contact conditions for all average wheel speeds, curve squeal can be identified and detected using the correlation method.
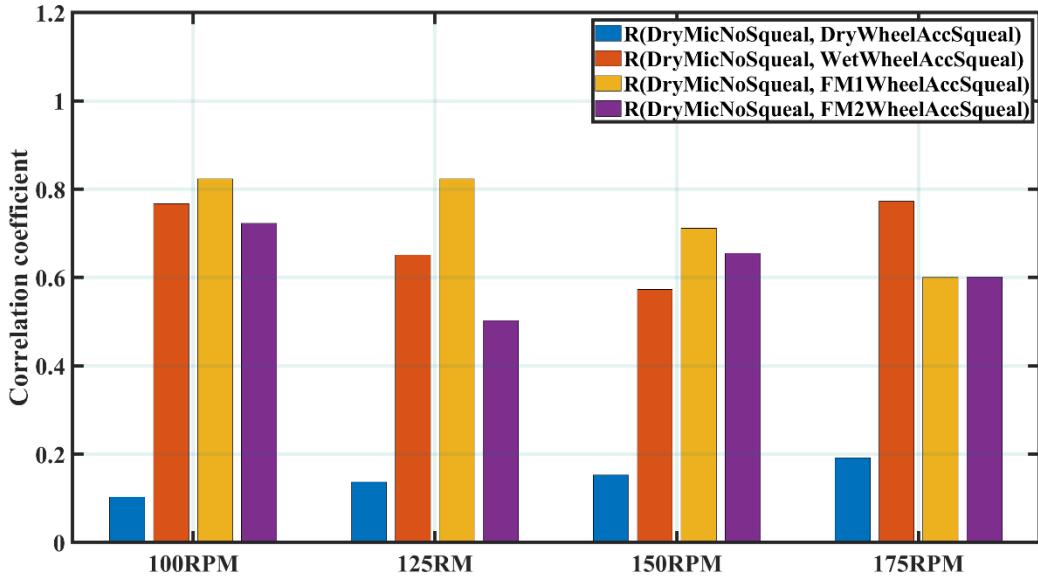
Figure 7.2: Correlation method applied to the dominant curve squeal spectral peak features obtained from the microphone and wheel accelerometer spectrum

Figure 7.3 shows the correlation method applied to the dominant curve squeal peal feature obtained from the microphone and rail accelerometer spectrum. The results obtained is similar to the results obtained in Figure 7.2.
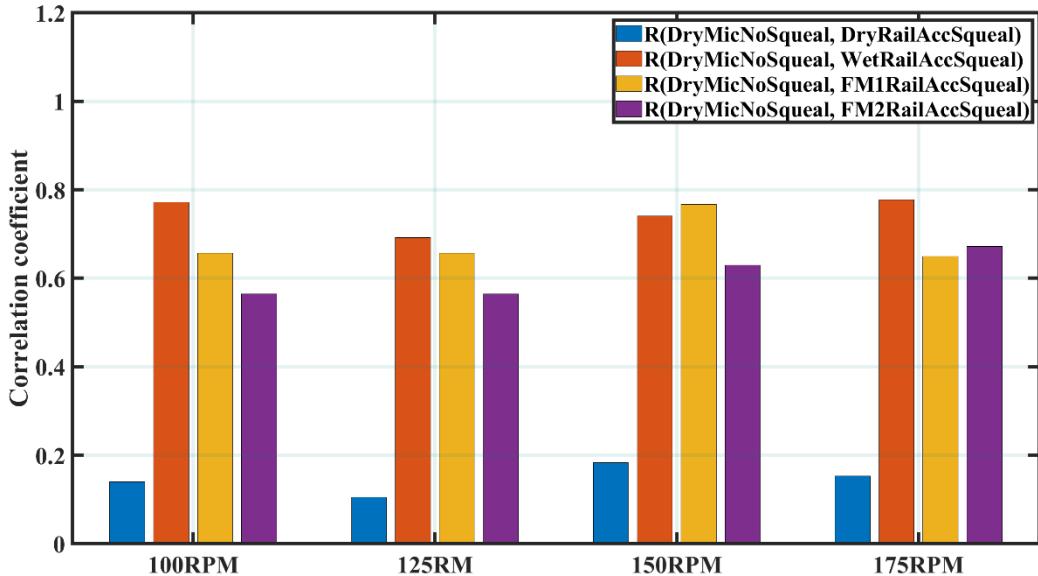
Figure 7.3: Correlation method applied to the dominant curve squeal spectral peak features obtained from the microphone and wheel accelerometer spectrum

The weak correlation coefficient for the dry contact conditions of the microphone and rail accelerometer variables provide weak correlation. A strong correlation between the variables is observed using the spectral peak feature for the microphone data and the accelerometer data. This indicates the development of curve squeal at dry contact conditions. A strong correlation coefficient in dry contact conditions for the variables indicate the lack of curves squeal in the twin disc rig.

Figure 7.4 shows the application of the correlation method to the dominant curve squeal spectral RMS feature comparing the microphone and wheel accelerometer spectrum. Addressing the statistical significance of the results, the spectral RMS feature values for the microphone and wheel accelerometer values exhibit weak correlation. This shows that there is very little relationship between the spectral RMS feature variables. This possibly suggests the occurrence of curves squeal in dry contact conditions.
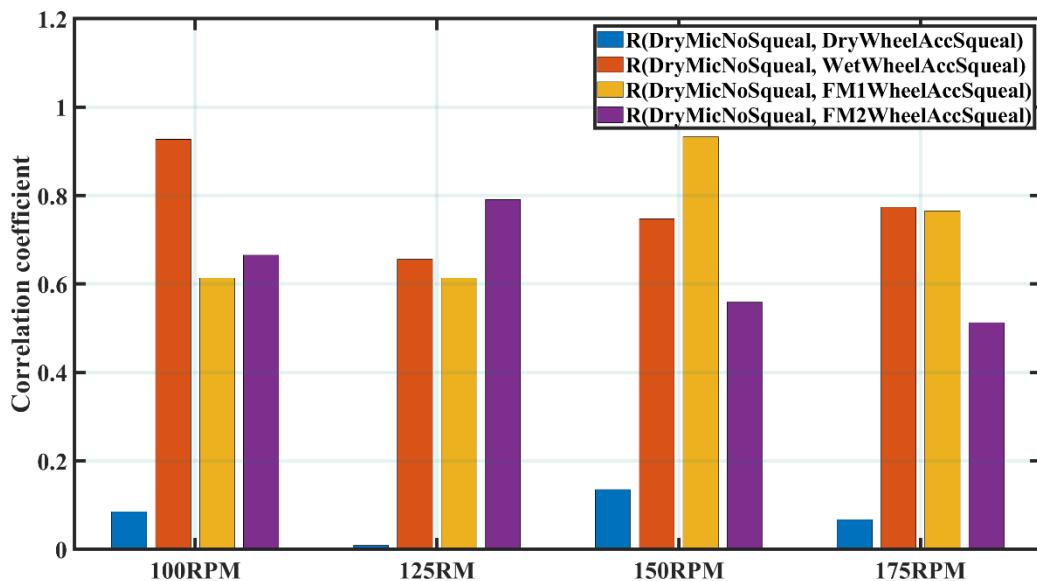
Figure 7.4: Correlation method applied to the dominant curve squeal spectral RMS features obtained from the microphone and wheel accelerometer spectrum

A moderate to strong correlation is observed for the correlation of the spectral RMS features of the microphone data at no curve squeal region and spectral RMS features of the wheel accelerometer at the curve squeal region for wet, FM1 and FM2 contact conditions. This result suggests the possible mitigation of curve squeal in the twin disc rig. The presence of high correlation in dry contact conditions suggests that no curve squeal is detected.

Figure 7.5 shows the application of the correlation method to the dominant curve squeal spectral RMS feature comparing the microphone and the rail accelerometer spectrum. A measure of negligible to weak monotonic relationship between the spectral RMS features of the microphone and rail accelerometer spectrum in dry contact conditions suggests the detection and characterization of curve squeal. This presupposes that in when curve squeal is detected in dry contact conditions, weak correlation exists between the two variables for all four average wheel speeds. This amplitudes of the correlation coefficient in dry contact conditions is redundant for all average wheel speeds. The sharp distinction between the correlation coefficients is a clear indication of curve squeal development on the twin disc rig.
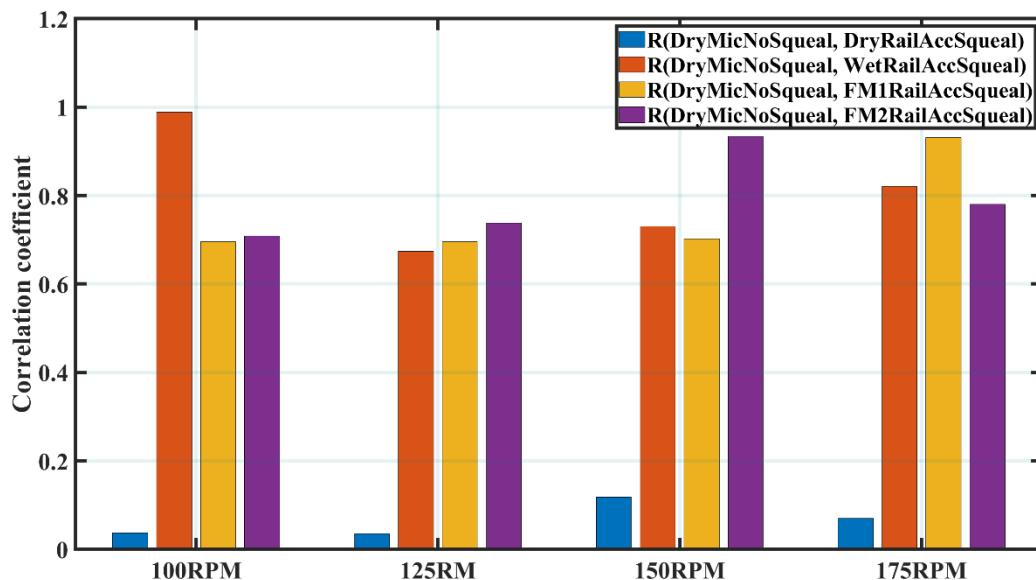

Figure 7.5: Correlation method applied to the dominant curve squeal spectral RMS features obtained from the microphone and rail accelerometer spectrum

The application of the correlation method to the spectral peak and RMS features is useful for not only determination of curve squeal in the twin disc rig, but also the valuable for curve squeal mitigation. This method can be applied in condition monitoring systems to characterize regions of curve squeal in the railway track using the correlation of the microphone and wheel and accelerometer data.

7.3.3 Application of Correlation method to the spectral RMS harmonics in the Frequency domain.

Figure 7.6 presents the application of correlation method to spectral RMS harmonic features obtained from the microphone and wheel accelerometer power spectrum. The results show that the correlation coefficient obtained for dry contact conditions for the two spectral RMS 2nd harmonic features are weakly correlated. This implies that there is little or no monotonic relationship between the two variables. This confidence interval for the correlation coefficient can be used to establish the occurrence of curve squeal detected in the twin disc rig. In addition, a moderate to strong relationship exists between the spectral RMS 2nd harmonic features of the microphone and wheel accelerometer exist for wet, FM1 and FM2 contact conditions. This possibly suggests the mitigation of curve squeal in the twin disc rig.
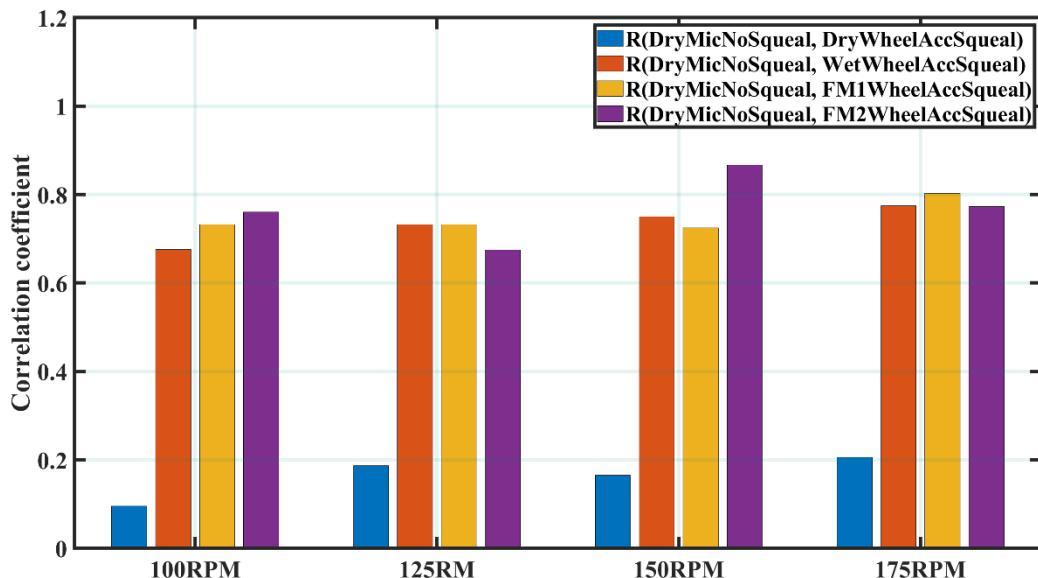
**Figure 7.6: Correlation method applied to the 2nd harmonics spectral RMS features obtained from the microphone and wheel accelerometer spectrum**

Figure 7.6 presents the application of correlation method to spectral RMS 3rd harmonic features obtained from the microphone and rail accelerometer power spectrum. Similar conclusions can eb drawn from Figure 7.6. From table 7.1, there is a moderate to strong relationship between the spectral RMS 3rd harmonic amplitude features of the microphone and the rail accelerometer spectrum when contaminants are introduced to the wheel-rail interface. This is not the case in dry

contact conditions whereby negligible to weak monotonic relationship exists between the two variables.
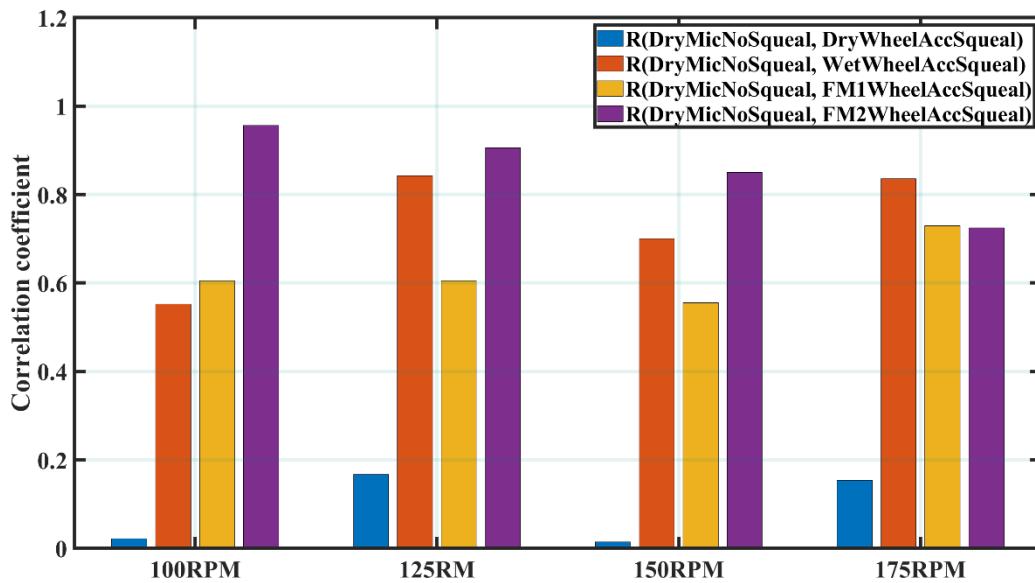
**Figure 7.7: Correlation method applied to the 3rd harmonics spectral RMS features obtained from the microphone and rail accelerometer spectrum**

The performance of the correlation method in the identification of curve squeal was satisfactory for the selected features used. In signal processing, as has been applied in this chapter, it was necessary to select only condition monitoring indicators that produced satisfactory results in curve squeal detection and mitigation. The application of correlation method for statistical feature extraction has presented some attribute that would make it useful to be implemented on a typical conditional monitoring system for curve squeal.

7.4   Proposed condition monitoring system for curve squeal.

The suggested structure of the condition monitoring scheme that could be implemented online that uses the correlation coefficient of the acoustic and vibration data to identify and characterize curve squeal is illustrated in Figure 7.8
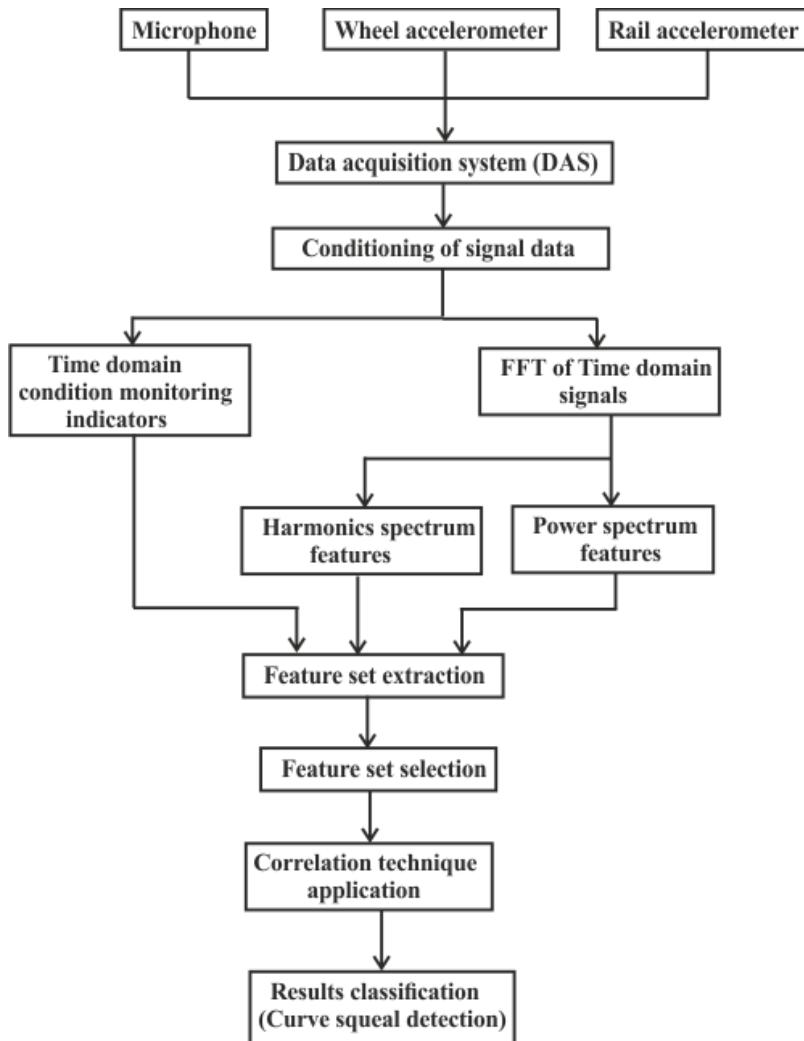
Figure 7.8: Proposed condition monitoring scheme that uses Correlation method for detection an identification of curve squeal

This condition monitoring system was developed in other to be able to provide the characteristic condition of wheel and rail in a typical twin disc rig setup. The scope of most railway systems is to detect possible curve squeal areas in the railway tracks. To determine the suitability of the developed condition monitoring system concept, several tests were developed to evaluate the performance of the system. The twin disc rig main components; wheel and rail roller was studied to investigate which of the rollers contribute to curve squeal under dry contact conditions. Curve squeal mitigation was also investigated using different contaminants introduced to the wheel rail interface.

However, the functionality of the condition monitoring system depends on the measurement signals obtained from the acoustic and vibration measurements. The signals from both are captured using data acquisition systems (DAS). In a typical online system, it is required to dynamically measure the yaw angle as the train negotiates the track. The twin disc rig currently uses manual methods to apply yaw angle to the rollers. For online condition monitoring systems, this should not be the case. For the condition monitoring system to be effective, it is suggested that measurements begin at zero degrees yaw angle. The reason is to establish a baseline to differentiate between curve squeal and no curve squeal. This condition can only work if the wheels are centrally aligned on a straight railway track.

It is suggested that integration of microphone and accelerometers be used to investigate the effect of curve squeal on the track. Accelerometers installed on the wheel rim surface or embedded in the railway track web do not suffer from doppler effect characterized by measurements from the microphone. It is well established in literature that the integration of information obtained from different sensors is better than information derived separately. The fusion of microphone and accelerometers would provide better signal to noise ratio, reliability in case of failure of one of the sensors, higher resolution and reduced uncertainty.

Having explained the justification for use of two different sensors for identification and characterization of curve squeal, the measured data obtained is detrended before being passed for data analysis. Condition monitoring indicators are then extracted from the data for feature extraction using time and frequency domain methods. The condition monitoring indicators applied for microphone data include, kurtosis and skewness while the condition monitoring indicators applied for the accelerometer time domain data are peak, rms, crest factor, kurtosis and skewness. The feature extraction using these condition monitoring indicators and stored for correlation. Only correlation of the condition monitoring indicators used in both acoustic and time domain data is used for analysis.

The signals obtained from the acoustic and vibration data is converted to frequency domain for feature extraction using condition monitoring indicators. The condition monitoring indicators suitable for the time domain data include peak and rms values. The extracted features are used to determine the early development of curve squeal and how it can be mitigated. The spectral peak and rms condition monitoring indicators of the dominant curve squeal and its harmonics are used

to determine onset development of curve squeal and the effect of application of contaminants in curve squeal mitigation.

Correlation coefficient of the extracted features for the acoustic and wheel/rail accelerometer is then determined after the condition monitoring indicators data have been normalized. The rationale for the use of correlation coefficient was to determine the correlation between the normalized values for acoustic and wheel and rail accelerometer to determine curve squeal. A moderate correlation between microphone rail accelerometer features compared with weak correlations of the same features differentiates between no curve squeal and curve squeal regions.

It is suggested from the results that either wheel or rail accelerometer is can be used together with microphone to identify and characterize the development of curve squeal on the twin disc rig as the yaw angle increases. This condition monitoring system can be extended to real railway track conditions to determine and detect curve squeal and how it can be mitigated. This system can also be used to solve the challenges of using only one sensor (microphone) for curve squeal detection and characterization. The use of added accelerometers installed on the wheel or rail can determine which exactly which wheel is responsible for curve squeal. With the reduction in installation costs of accelerometers due to better improved technologies used for its manufacture, the fusion of this sensor with microphone proves to be a reliable alternative for accurate detection and characterization of curve squeal to reduce annoyance and wear on the wheels as the train negotiates a sharp curve. It is important to note that is very difficult to install an online condition monitoring system to analyse in real time the huge amount of data obtained from the sensors installed for curve squeal detection. It is therefore suggested that the results be taken for a short section of the curve track and measurement results from the sensors analysed offline to ascertain the development of curve squeal. Based on the results obtained, a friction modifier applicator system should be installed on the Bogie system. Based on the feature extraction of curve squeal using the offline results obtained, the friction modifier applicator system should only be activated at the transition yaw angles just before curve squeal occurs to ensure curve squeal mitigation. A cheaper alternative can also be explored using a water applicator system installed on the bogie frame for application of water to the wheel-rail interface at the transition yaw angles in the curve that lead to curve squeal development.

Chapter Eight: Conclusion

8.1   Review of objectives for this thesis

In this thesis, condition monitoring of acoustic and vibration signals to characterize curve squeal has been presented in this research work. The study has emphasized the effectiveness of condition monitoring on the twin disc rig. Experimental studies have been put together with theoretical analysis of the characteristics of acoustic and vibration signal in relation to curve squeal detection has been studied. The main achievements of this thesis include:

(1)   **Gain understanding of condition monitoring of curve squeal using vibration and acoustic based signal processing tools.**

With reference to chapter 1 and chapter 2, the author has gained sufficient understanding of vibration and acoustic condition monitoring systems for curve squeal. However, the vibration and acoustic data baseline for all four average wheel speeds is studied in Chapter 6. The author examined the frequency components of the acoustic and vibration data responsible for curve squeal and rolling contact noise on the twin disc rig. The author is of the opinion that it is a useful attempt to utilise the acoustic and vibration baseline data using high speeds and loads to identify the presence of curve squeal on the test rig.

(2)   **To further detail the disadvantages of traditional signal processing and methods for analysis of in time and frequency domains and identify which method is most suitable for analysing vibration and acoustic signals from the wheel rail interface.**

Signal processing methods that can be applied to measured acoustic and vibration signals have been reviewed by the author for the condition monitoring of the twin disc rig. Power spectrum analysis was sufficient to identify the frequency components of the acoustic and vibration signals to characterize curve squeal. This has been explained in detail in chapter 5 and chapter 6.

(3)   **Investigate acoustic and vibration generation and its characteristics in identification of curve squeal on the twin disc rig.**

Chapter 4 presented a time domain-based curve squeal model for the twin disc rig. The vibration amplitudes and the sound pressure level results were obtained for various yaw angle variation and high speeds. The results obtained did not

(4)   Develop a realistic experimental method in situ with adequate system to study acoustic and vibration signals for curve squeal characterization.

Two accelerometers were attached to the wheel and rail roller and microphone was placed at close proximity to the wheel rail interface to measure lateral vibration and sound from the whele rail interface.

(5)   Investigate the condition monitoring performance of acoustic and vibration signals using time and frequency domain analysis.

(6)   identify suitable condition monitoring indicators in time and frequency domain that can be used to predict the incipient development of curve squeal.

(7)   Investigate the effect of water and friction modifiers using acoustic and vibration data for curve squeal mitigation.

(8)   Investigate the condition monitoring performance of using vibration and acoustic signals using Correlation method for curve squeal identification.

(9)   Propose a condition monitoring system based on the developed Correlation method for curve squeal identification.

8.2   Conclusion

Contributions

(1)   Spectral RMS and Peak of the 2nd and 3rd harmonics extracted from the sound and vibration spectrum are sufficient to detect and characterize curve squeal as the yaw angle increased for four average wheel speeds.

(2)   The introduction of water and friction modifiers (FM1 and FM2) completely mitigated curve squeal in the wheel-rail interface. This was observed in the complete attenuation of the spectral RMS and Peaks of the 2nd and 3rd harmonics of the acoustic and vibration spectrum.

(3)   A negligible or weak correlation coefficient of sound and vibration features in dry contact conditions is an indication of curve squeal development on the wheel-rail interface.

(4)   A moderately or strong correlation coefficient using the correlation method of sound and vibration is a strong indicator of no curve squeal developed on the wheel rail interface.

7.3   Suggestions for future work

Suggestions for future work include:

(1)   Develop a FEM model to simulate and characterize curve squeal on the twin disc rig.

(2)   Develop machine learning methods to study and characterize curve squeal using the fusion of acoustic and vibration signals.

Appendix

Appendix 1: Sinocera model YE6232B

YE6232B V/IEPE Input Data Acquisitions

Name: YE6232B V/IEPE Input Data Acquisitions

No: YE6232B

Browse similar products

Previous   YE6231 V/IEPE Input Data Acquisitions

Page :

Next :   YE6231B V/IEPE Input Data Acquisitions

Detail

Model	YE6232B
Channels	16
A/D bits	24bit($\sum-\triangle$)
Input Mode	V/IEPE
IEPE Power Supply	4mA/+24VDC
Signal Input Range	$\leq\pm 10VP$
Signal Frequency Range	DC-30kHZ(-3dB$\pm$1dB)
Gain	×1 , ×10, ×100
Filter	Independent Anti-filtering
Accuracy	±0.5%
Sample Rate (Max.)	96kHz/CH, Parallel
Interface	USB2.0
Trigger Modes	Signal Trigger
Dimensions (mm)	236W×88H×277D
Software	YE7600
Weight	4 Kg
Power Supply	AC: 220V 50Hz 110V 60Hz

Appendix 2: Dytran 3035BG IEPE Accelerometer

SPECIFICATIONS
MODEL 3035B & 3035BG LIVM ACCELEROMETERs

SPECIFICATION	VALUE	UNITS
PHYSICAL		
WEIGHT	2.5	grams
SIZE, HEX x HEIGHT	.281 x .33	inches
MOUNTING PROVISION, 3035B	5-40 integral stud	
MOUNTING PROVISION, 3035BG	flat surface for adhesive mount	
CONNECTOR, RADIALLY MOUNTED	5-44 coaxial	
MATERIAL, HOUSING AND CONNECTOR	300 series stainless steel	
PERFORMANCE		
SENSITIVITY, ± 10% [1]	100	mV/g
RANGE F.S. FOR ± 5 VOLTS OUTPUT	± 50	g
FREQUENCY RANGE, ± 5%	0.5 to 10k	Hz
RESONANT FREQUENCY, NOM.	45	kHz
EQUIVALENT ELECTRICAL NOISE FLOOR	.007	g rms
LINEARITY [2]	± 1%	% F.S.
TRANSVERSE SENSITIVITY, MAX.	5	%
STRAIN SENSITIVITY	.002	g/$\mu\epsilon$ @ 250$\mu\epsilon$
ENVIRONMENTAL		
MAXIMUM VIBRATION/SHOCK	600/3000	± g pk
TEMPERATURE RANGE	-60 to +250	°F
SEAL, HERMETIC	Glass-to-metal and welds	
COEFFIEICNT OF THERMAL SENSITIVITY	.04	%/°F
ELECTRICAL		
SUPPLY CURRENT [3]	2 to 20	mA
SUPPLY COMPLIANCE VOLTAGE RANGE	+18 to +30	volts
OUTPUT IMPEDANCE, TYP.	100	ohms
BIAS VOLTAGE, +10.5 VOLTS NOM.	+9 to +12	Vdc
DISCHARGE TIME CONSTANT, NOM.	0.5	seconds
OUTPUT SIGNAL POLARITY		
FOR ACCELERATION TOWARD TOP	positive	
CASE GROUNDING	case is grounded to electrical power ground	

[1] Measured at 100 Hz, 1g rms per ISA RP 37.2.
[2] Measured using zero-based best straight-line method, % of full scale (F.S.) or any lesser range.
[3] Do not apply power to this device without current limiting, 20 mA MAX. To do so will destroy the integral IC amplifier.

Appendix 3: Instron 3369 Tabletop test system

Features

- 100:1 force range (i.e. use the load cell to 1.0% of capacity with no loss of accuracy)
- Load accuracy of 0.5% of indicated load
- 500Hz data acquisition rate (Bluehill² 3)
- 100Hz data acquisition rate (Bluehill & Bluehill Lite)
- Full software control (cyclic capability optional)
- Automatic transducer recognition
- Thousands of optional grips and fixtures
- Optional temperature chambers
- Full CE compliance
- Color: Grey base with white columns

3369

- 50 kN (11,250 lbf) capacity
- Maximum speed 500 mm/min (20 in/min)
- 1193 mm (47 in) vertical test space

Appendix 4: Impact hammer datasheet (Sinocera model version)

SINOCERA

GST Global Sensor Technology

Impact Hammers

Model LC series

FEATURES
- Selectable force range: 2kN, 5kN, and 60kN
- Wide frequency response
- Small size and low weight
- Experimental modal analysis
- Resonant measurement
- A variety of tips and extender masses

SUPPLIED WITH
- Steel, aluminium, nylon and rubber tips
- Extender mass
- Force transducer

Model	LC-01A	LC-02A	LC-04A
Hammer image			
Sensitivity (pC/N)	4	4	4
Max. shock force (kN)	2	5	60
Head diameter (mm)	Φ16	Φ25	Φ30
Head mass (g)	40	200	300
Extender mass (g)	100	120	150
Hammer length	250	280	300
Force transducer	CL-YD-303	CL-YD-302	CL-YD-305
Frequency responses		See graph below	

Typical Frequency Responses for Tips
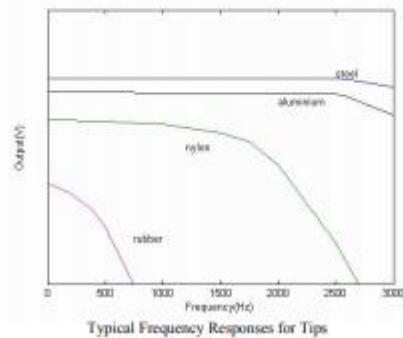
Appendix 5: FLA-3-11 Foil strain gauge

Gauge pattern	Type	Gauge length (mm)	Gauge width (mm)	Backing length (mm)	Backing width (mm)	Resistance (Ω)
FLG-1-11	FLG-02-11 FLG-02-17 FLG-02-23	0.2	1.4	3.5	2.5	120
	FLG-1-11 FLG-1-17 FLG-1-23	1	1.1	6.5	2.5	120
	FLA-03-11 FLA-03-17 FLA-03-23	0.3	1.4	3	2.0	120
	FLA-05-11 FLA-05-17 FLA-05-23	0.5	1.2	5	2.2	120
	FLA-1-11 FLA-1-17 FLA-1-23	1	1.3	5	2.5	120
	FLA-1-350-11 FLA-1-350-17 FLA-1-350-23	1	1.6	4.7	3.6	350
	FLA-2-11 FLA-2-17 FLA-2-23	2	1.5	6.5	3	120
	FLA-2-350-11 FLA-2-350-17 FLA-2-350-23	2	1.9	6.1	3.5	350
	FLA-3-11 FLA-3-17 FLA-3-23	3	1.7	8.8	3.5	120
FLA-3-11	FLA-3-60-11 FLA-3-60-17 FLA-3-60-23	3	1.2	8	3	60

References

A. D. Monk-Steel, D.J.T. (2006). An investigation into the influence of longitudinal creepage on railway squeal noise due to lateral creepage. J. Sound Vib. - J SOUND VIB *293*, 766–776.

ABB (2010). Three-phase asynchronous motors Generalities and ABB proposals for the coordination of protective devices.

Anderson, D., Gautier, P.-E., Iida, M., Nelson, J.T., Thompson, D.J., Tielkes, T., Towers, D.A., Vos, P. de, and Nielsen, J.C.O. (2018). Noise and Vibration Mitigation for Rail Transportation Systems: Proceedings of the 12th International Workshop on Railway Noise, 12-16 September 2016, Terrigal, Australia (Springer).

Archdeacon, T.J. (1994). Correlation and Regression Analysis: A Historian's Guide (Univ of Wisconsin Press).

Arias-Cuevas, O., Li, Z., Lewis, R., and Gallardo-Hernández, E.A. (2010). Rolling–sliding laboratory tests of friction modifiers in dry and wet wheel–rail contacts. Wear *268*, 543–551.

de Beer, F.G., Janssens, M.H.A., and Kooijman, P.P. (2003). Squeal noise of rail-bound vehicles influenced by lateral contact position. J. Sound Vib. *267*, 497–507.

Brunel, J.F., Dufrénoy, P., Naït, M., Muñoz, J.L., and Demilly, F. (2006). Transient models for curve squeal noise. J. Sound Vib. *293*, 758–765.

Chen, X., and Liu, Y. (2014). Finite Element Modeling and Simulation with ANSYS Workbench (Boca Raton: CRC Press).

Cigada, A., Manzoni, S., and Vanali, M. (2008). Vibro-acoustic characterization of railway wheels. Appl. Acoust. *69*, 530–545.

Curley, D., Anderson, D.C., Jiang, J., and Hanson, D. (2015). Field Trials of Gauge Face Lubrication and Top-of-Rail Friction Modification for Curve Noise Mitigation. In Noise and Vibration Mitigation for Rail Transportation Systems, J.C.O. Nielsen, D. Anderson, P.-E. Gautier, M. Iida, J.T. Nelson, D. Thompson, T. Tielkes, D.A. Towers, and P. de Vos, eds. (Springer Berlin Heidelberg), pp. 449–456.

Eadie, D.T., and Santoro, M. (2006). Top-of-rail friction control for curve noise mitigation and corrugation rate reduction. J. Sound Vib. *293*, 747–757.

Eadie, D.T., Kalousek, J., and Chiddick, K.C. (2002). The role of high positive friction (HPF) modifier in the control of short pitch corrugations and related phenomena. Wear *253*, 185–192.

Eadie, D.T., Santoro, M., and Powell, W. (2003). Local control of noise and vibration with KELTRACK[TM] friction modifier and Protector® trackside application: an integrated solution. J. Sound Vib. *267*, 761–772.

Eadie, D.T., Santoro, M., and Kalousek, J. (2005). Railway noise and the effect of top of rail liquid friction modifiers: changes in sound and vibration spectral distributions in curves. Wear *258*, 1148–1155.

Eadie, D.T., Santoro, M., Oldknow, K., and Oka, Y. (2008). Field studies of the effect of friction modifiers on short pitch corrugation generation in curves. Wear *265*, 1212–1221.

European Environment Agency (2017). Annual European Union greenhouse gas inventory 1990-2012 and inventory report 2014. Technical Report 09/2014 (European Environment Agency).

Fei, S. (2016). Kurtosis prediction of bearing vibration signal based on wavelet packet transform and Cauchy kernel relevance vector regression algorithm. Adv. Mech. Eng. *8*, 1687814016645979.

Fingberg, U. (1990). A model of wheel-rail squealing noise. J. Sound Vib. *143*, 365–377.

Fourie, D.J., Gräbe, P.J., Heyns, P.S., and Fröhling, R.D. (2016). Experimental characterisation of railway wheel squeal occurring in large-radius curves. Proc. Inst. Mech. Eng. Part F J. Rail Rapid Transit *230*, 1561–1574.

Global Sensor Technology (2007). ICP Microphone Preamplifier Model YG-201.

Glocker, Ch., Cataldi-Spinola, E., and Leine, R.I. (2009). Curve squealing of trains: Measurement, modelling and simulation. J. Sound Vib. *324*, 365–386.

Hannah, R. L., and Reed S. E. (1992). Strain Gage USERS' HANDBOOK. (Great Britain: Elseviier Science), pp. 1–100.

Hanson, D., Jiang, J., Dowdell, B., and Dwight, R. (2014). Curve Squeal: Causes, Treatments and Results. In Inter-Noise 2014, (Australia), pp. 1–8.

Heckl, M., A. (2000). Curve Squeal of train wheels, part 2: which wheel modes are prone to squeal? J. Sound Vib. *229*, 695–707.

Heckl, M.A., and Abrahams, I.D. (2000). Curve squeal of train wheels, part 1: mathematical model for its generation. J. Sound Vib. *229*, 669–693.

Hsu, S., Huang, Z., Iwnicki, S., Thompson, D., Jones, C., Xie, G., and Allen, P. (2007). Experimental and theoretical investigation of railway wheel squeal. Proc. Inst. Mech. Eng. Part F J. Rail Rapid Transit *221*, 59–73.

Huang, Z.Y., Thompson, D.J., and Jones, C.J.C. (2008). Squeal Prediction for a Bogied Vehicle in a Curve. In Noise and Vibration Mitigation for Rail Transportation Systems, B. Schulte-Werning, D. Thompson, P.-E. Gautier, C. Hanson, B. Hemsworth, J. Nelson, T. Maeda, and P. de Vos, eds. (Springer Berlin Heidelberg), pp. 313–319.

Igba, J., Alemzadeh, K., Durugbo, C., and Eiriksson, E.T. (2016). Analysing RMS and peak values of vibration signals for condition monitoring of wind turbine gearboxes. Renew. Energy *91*, 90–106.

Jiang, J., Anderson, D.C., and Dwight, R. (2015). The Mechanisms of Curve Squeal. In Noise and Vibration Mitigation for Rail Transportation Systems, J.C.O. Nielsen, D. Anderson, P.-E. Gautier, M. Iida, J.T. Nelson, D. Thompson, T. Tielkes, D.A. Towers, and P. de Vos, eds. (Springer Berlin Heidelberg), pp. 587–594.

KALKER, J.J. (1979). Survey of Wheel—Rail Rolling Contact Theory. Veh. Syst. Dyn. *8*, 317–358.

Kalker, J.J. (1982). A Fast Algorithm for the Simplified Theory of Rolling Contact. Veh. Syst. Dyn. *11*, 1–13.

Kalker, J.J. (1990). Three-Dimensional Elastic Bodies in Rolling Contact (Springer).

Kim, J.C., Yun, Y.S., and Noh, H.-M. (2019). Analysis of Wheel Squeal and Flanging on Curved Railway Tracks. Int. J. Precis. Eng. Manuf. *20*, 2077–2087.

Knothe, K., and Groß-Thebing, A. (2008). Short wavelength rail corrugation and non-steady-state contact mechanics. Veh. Syst. Dyn. *46*, 49–66.

Koch, J.R., Vincent, N., Chollet, H., and Chiello, O. (2006). Curve squeal of urban rolling stock—Part 2: Parametric study on a 1/4 scale test rig. J. Sound Vib. *293*, 701–709.

Krishnakumar, P., Rameshkumar, K., and Ramachandran, K.I. (2018). Feature level fusion of vibration and acoustic emission signals in tool condition monitoring using machine learning classifiers. Int. Jounral Progn. Health Manag. 15.

Liu, X., and Meehan, P.A. (2013). Investigation of the effect of lateral adhesion and rolling speed on wheel squeal noise. Proc. Inst. Mech. Eng. Part F J. Rail Rapid Transit *227*, 469–480.

Liu, X., and Meehan, P.A. (2014). Investigation of the effect of relative humidity on lateral force in rolling contact and curve squeal. Wear *310*, 12–19.

Liu, X., and Meehan, P.A. (2016). Investigation of squeal noise under positive friction characteristics condition provided by friction modifiers. J. Sound Vib. *371*, 393–405.

Meehan, P., and Liu, X. (2018). Modelling and mitigation of wheel squeal noise amplitude. J. Sound Vib. *413*, 144–158.

Meierhofer, A., Hardwick, C., Lewis, R., Six, K., and Dietmaier, P. (2014). Third body layer—experimental results and a model describing its influence on the traction coefficient. Wear *314*, 148–154.

Monk-Steel, A., and Thompson, D.J. (2003). Models for railway curve squeal noise.

Muller, B., and Oertli, J. (2006). Combating Curve Squeal: Monitoring existing applications. J. Sound Vib. *293*, 728–734.

Ngigi, R.W., Pislaru, C., Ball, A., Gu, F., and Anyakwo, A. (2011). Predictive control strategies used to solve challenges related to modern railway vehicles. In 5th IET Conference on Railway Condition Monitoring and Non-Destructive Testing (RCM 2011), pp. 1–5.

Oppenheim, A.V., and Schafer, R.W. (1975). Digital Signal Processing (Englewood Cliffs, N.J: Pearson).

Ovacikli, A.K., Pääjärvi, P., and LeBlanc, J.P. (2013). Skewness as an objective function for vibration analysis of rolling element bearings. In 2013 8th International Symposium on Image and Signal Processing and Analysis (ISPA), pp. 462–466.

Panulinova, E., Harabinová, S., and Argalášová, L. (2016). Tram squealing noise and its impact on human health. Noise Health *18*, 329.

Papini, S., Pugi, L., Rindi, A., and Meli, E. (2013). An integrated approach for the optimization of wheel–rail contact force measurement systems. J. Mod. Transp. *21*, 95–102.

Periard, F.J. (1998). Wheel-rail noise generation: Curve Squealing by Trams (Delf University of Technology, Netherlands: PhD Thesis).

Pieringer, A. (2011). Time-domain modelling of high frequency wheel/rail interaction, PhD thesis, Department of Civil and Environmental Engineering. (Sweden, Chalmers University of Technology).

Pieringer, A. (2014). A numerical investigation of curve squeal in the case of constant wheel/rail friction. J. Sound Vib. *333*, 4295–4313.

Pieringer, A., Torstensson, P.T., Giner, J., and Baeza, L. (2018). Investigation of Railway Curve Squeal Using a Combination of Frequency- and Time-Domain Models. In Noise and Vibration Mitigation for Rail Transportation Systems, D. Anderson, P.-E. Gautier, M. Iida, J.T. Nelson, D.J. Thompson, T. Tielkes, D.A. Towers, P. de Vos, and J.C.O. Nielsen, eds. (Springer International Publishing), pp. 83–95.

Piotrowski, J., and Chollet, H. (2005). Wheel–rail contact models for vehicle system dynamics including multi-point contact. Veh. Syst. Dyn. *43*, 455–483.

Polach, O. (2005). Creep forces in simulations of traction vehicles running on adhesion limit. Wear 992–1000.

Popovici, R. (2010). Friction in Wheel-Rail Contacts. University of Twente, Enschede.

Railway noise Technical Measures Catalogue (2013). Technical Report UIC003-01- 04fe, (UIC International Union of Railways).

Remington, P.J. (1987). Wheel/rail squeal and impact noise: What do we know? What don't we know? Where do we go from here? J. Sound Vib. 339–353.

Robert, P., and Tata, P.E. (2014). Ball Bearing Design and Applications.

Rockwell Automation Allen-Bradly (2013). Poweflex750 Series datasheet.

Rudd, M.J. (1976). Wheel/rail noise—Part II: Wheel squeal. J. Sound Vib. *46*, 381–394.

Rudi, V., and Joachim, F. (2007). Noise and Vibration measurements of curve squeal noise due to trams on teh track. In International Congress on Acoustics, (Madrid), p. 5.

van Ruiten, C.J.M. (1988). Mechanism of squeal noise generated by trams. J. Sound Vib. *120*, 245–253.

Schneider, E., Popp, K., and Irretier, H. (1988). Noise generation in railway wheels due to rail-wheel contact forces. J. Sound Vib. *120*, 227–244.

Schober, P., Boer, C., and Schwarte, L.A. (2018). Correlation Coefficients: Appropriate Use and Interpretation. Anesth. Analg. *126*, 1763–1768.

Schwarz, B.J., and Richardson, M.H. (1999). Experimental Modal Analysis. In Vibrant Technology, Inc., (Orlando, Florida), pp. 1–12.

Setsohhonkul, S., and Kaewunruen, S. (2016). Life cycle analysis of railway noise and vibration mitigation methodologies with respect to curve squeal noises.

Shabana, A.A., Zaazaa, K.E., Escalona, J.L., and Sany, J.R. (2004). Development of elastic force model for wheel/rail contact problems. J. Sound Vib. *269*, 295–325.

SHEN, Z.Y., HEDRICK, J.K., and Design, J.A.E.M. of T. (1983). A Comparison of Alternative Creep Force Models for Rail Vehicle Dynamic Analysis. Veh. Syst. Dyn. *12*, 79–83.

Spiryagin, M., Polach, O., and Cole, C. (2013). Creep force modelling for rail traction vehicles based on the Fastsim algorithm. Veh. Syst. Dyn. *51*, 1765–1783.

Squicciarini, G., Usberti, S., Thompson, D.J., Corradi, R., and Barbera, A. (2015). Curve Squeal in the Presence of Two Wheel/Rail Contact Points. In Noise and Vibration Mitigation for Rail Transportation Systems, J.C.O. Nielsen, D. Anderson, P.-E. Gautier, M. Iida, J.T. Nelson, D. Thompson, T. Tielkes, D.A. Towers, and P. de Vos, eds. (Springer Berlin Heidelberg), pp. 603–610.

Srivastava, J.P., Sarkar, P.K., and Ranjan, V. (2014). Contact Stress Analysis in Wheel–Rail by Hertzian Method and Finite Element Method. J. Inst. Eng. India Ser. C *95*, 319–325.

Stefanelli, R., Dual, J., and Cataldi-Spinola, E. (2006). Acoustic modelling of railway wheels and acoustic measurements to determine involved eigenmodes in the curve squealing phenomenon. Veh. Syst. Dyn. *44*, 286–295.

Thompson, D.J. (2009). Railway Noise and Vibration: Mechanisms, Modelling and Means of Control (Amsterdam ; Boston: Elsevier).

Thompson, D.J., and Jones, C.J.C. (2002). Sound Radiation from a vibrating Railway wheel. J. Sound Vib. *253*, 401–419.

Thompson, D.J., Janssens, M.H.A., and de Beer, F.G. (1999). Track-Wheel Interaction Noise Software Theoretical Manual. TNO-report HAG-RPT-990211, TNO Institute of Applied Physics.

Vermeulen, P.J., and Johnson, K.L. (1964). Contact of Nonspherical Elastic Bodies Transmitting Tangential Forces. J. Appl. Mech. *31*, 338–340.

Vincent, N., Koch, J.R., Chollet, H., and Guerder, J.Y. (2006). Curve squeal of urban rolling stock—Part 1: State of the art and field measurements. J. Sound Vib. *293*, 691–700.

Vishwakarma, M., Purohit, R., Harshlata, V., and Rajput, P. (2017). Vibration Analysis & Condition Monitoring for Rotating Machines: A Review. Mater. Today Proc. *4*, 2659–2664.

WHO (2011). Burden of disease from environmental noise - Quantification of healthy life years lost in Europe. Technical report, (WHO).

Xie, G., Allen, P.D., Iwnicki, S.D., Alonso, A., Thompson, D.J., Jones, C.J.C., and Huang, Z.Y. (2006). Introduction of falling friction coefficients into curving calculations for studying curve squeal noise. Veh. Syst. Dyn. *44*, 261–271.

Yan, W., and Fischer, F.D. (2000). Applicability of the Hertz contact theory to rail-wheel contact problems. Arch. Appl. Mech. *70*, 255–268.

Zeng, W., Yang, Y., Qiu, W.-S., Xie, H., and Xie, S.-C. (2017). Optimization of the target profile for asymmetrical rail grinding in sharp-radius curves for high-speed railways. Adv. Mech. Eng. *9*, 1687814016687196.

Zenzerovic, I., Pieringer, A., and Kropp, W. (2015). Towards an Engineering Model for Curve Squeal. In Noise and Vibration Mitigation for Rail Transportation Systems, J.C.O. Nielsen, D. Anderson, P.-E. Gautier, M. Iida, J.T. Nelson, D. Thompson, T. Tielkes, D.A. Towers, and P. de Vos, eds. (Springer Berlin Heidelberg), pp. 433–440.